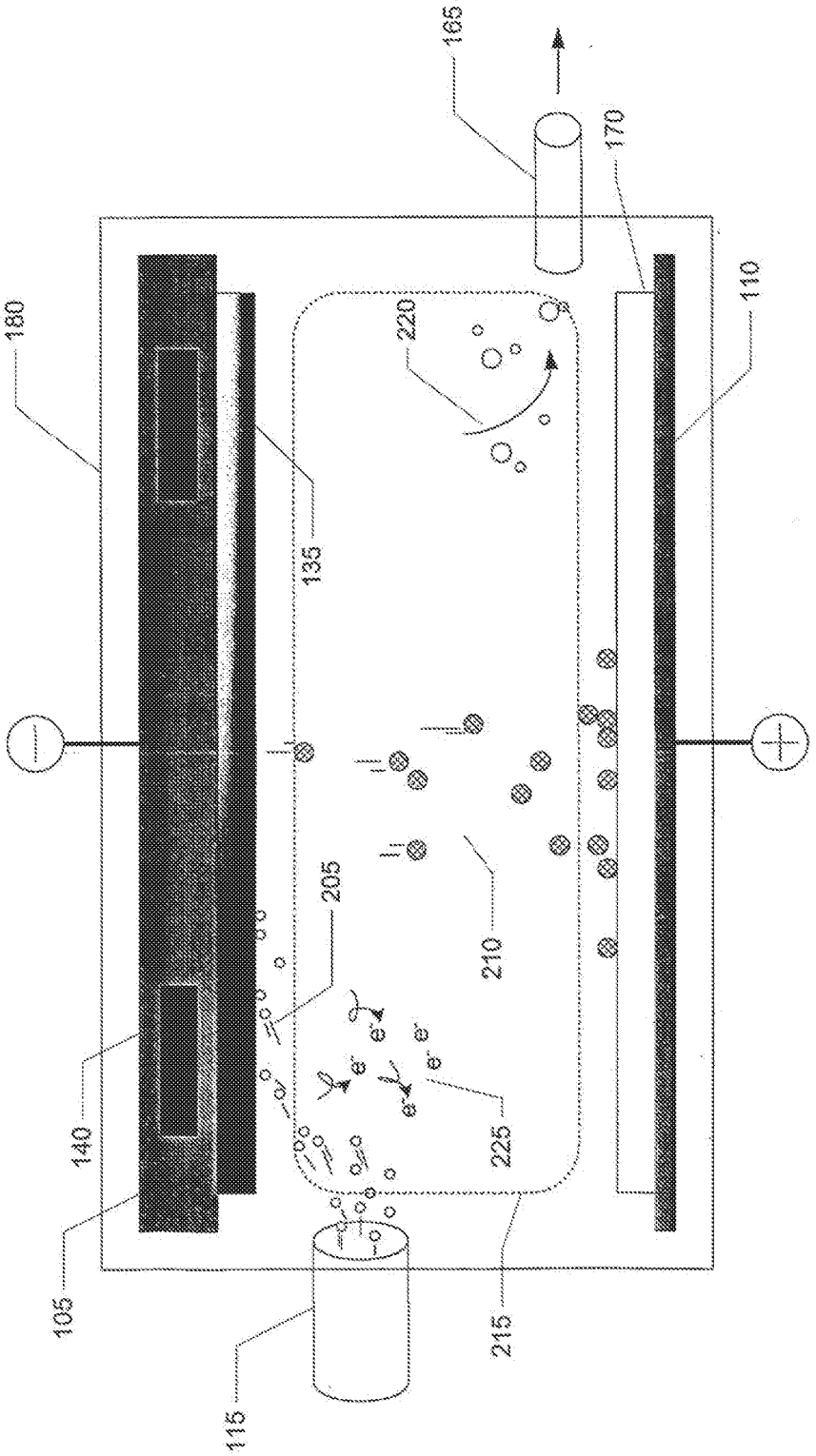


Figure 2

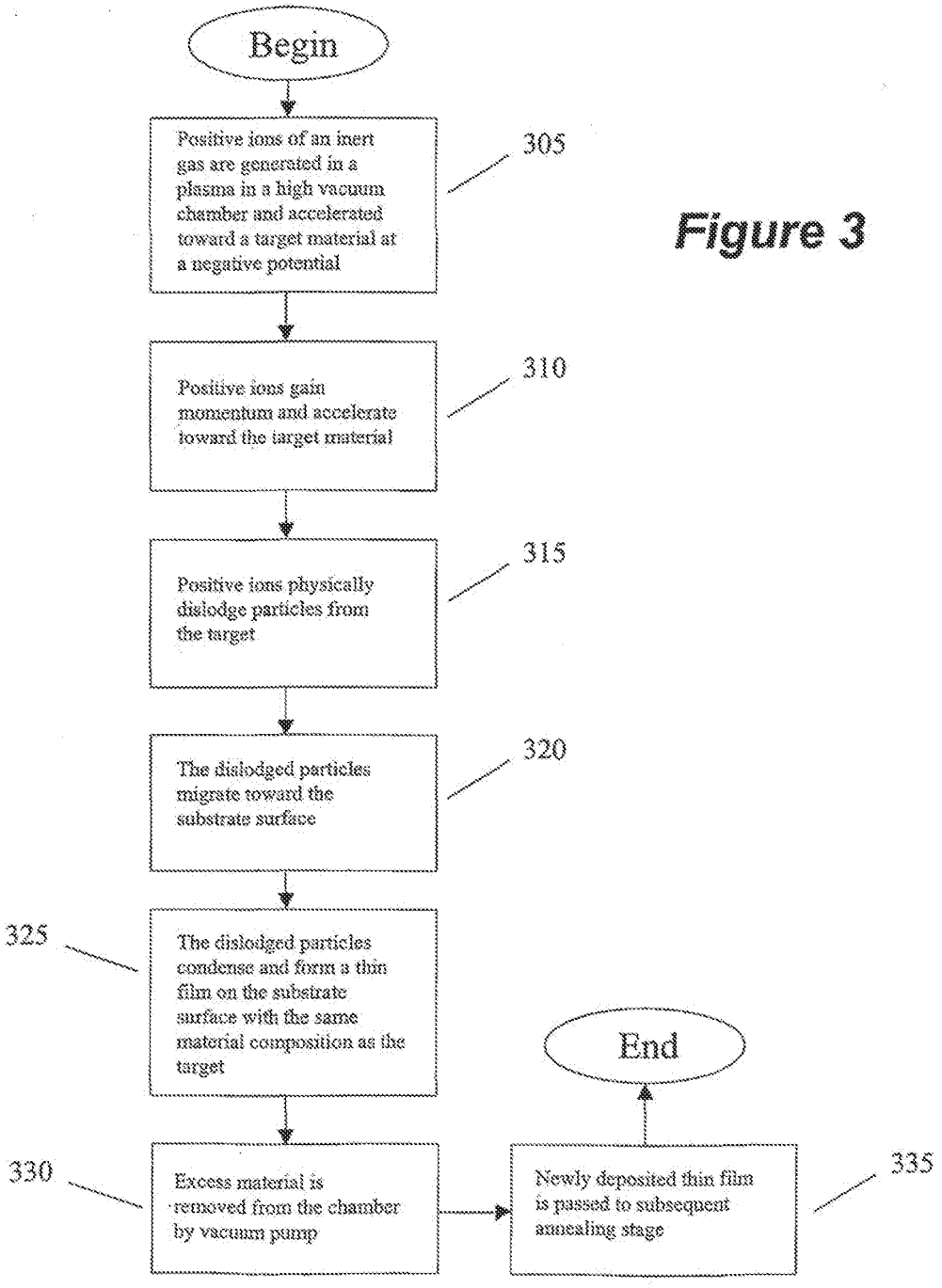


Figure 3

SAMSUNG EX. 1002 - 2205/4148

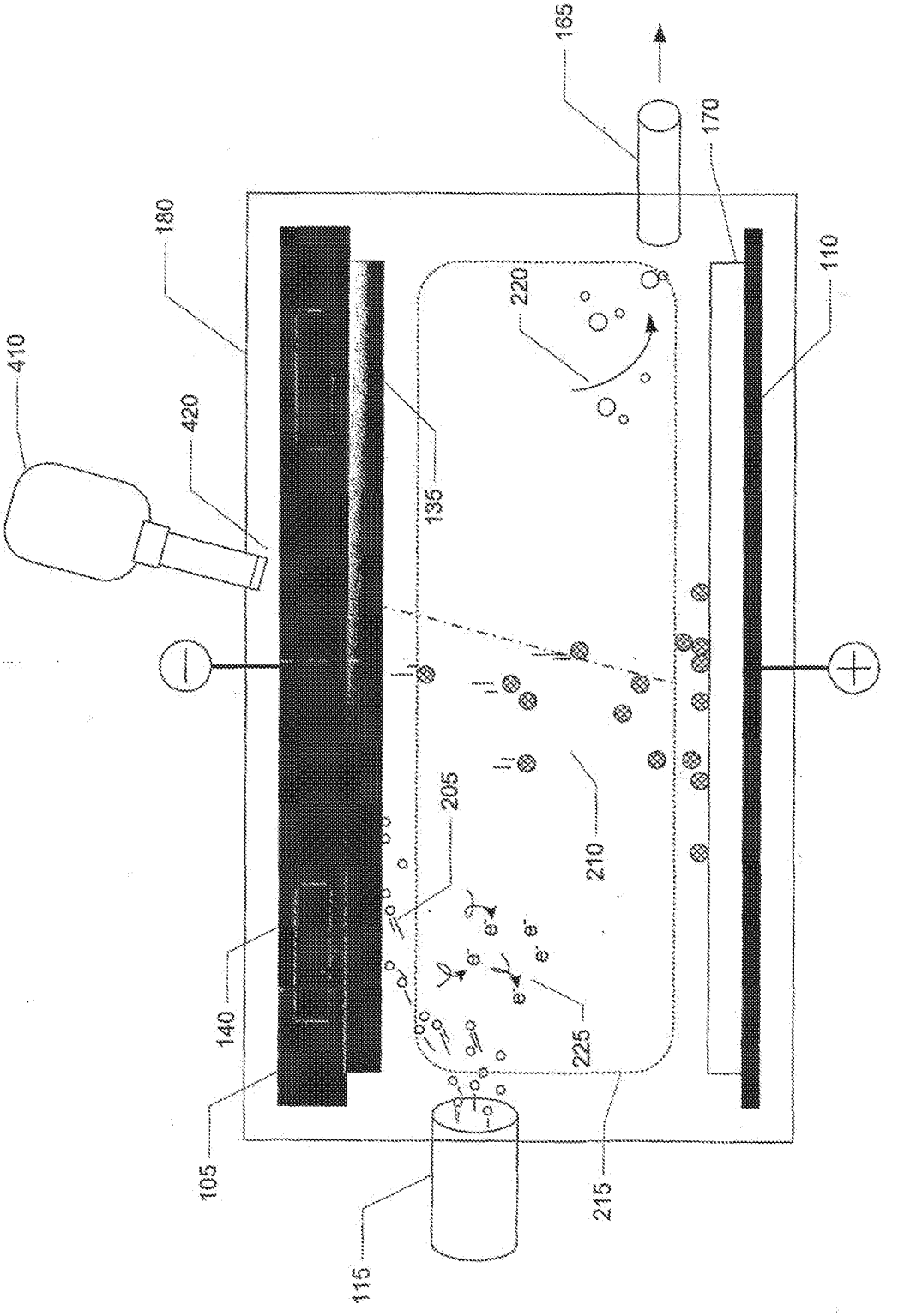


Figure 4

SAMSUNG EX. 1002 - 2206/4148

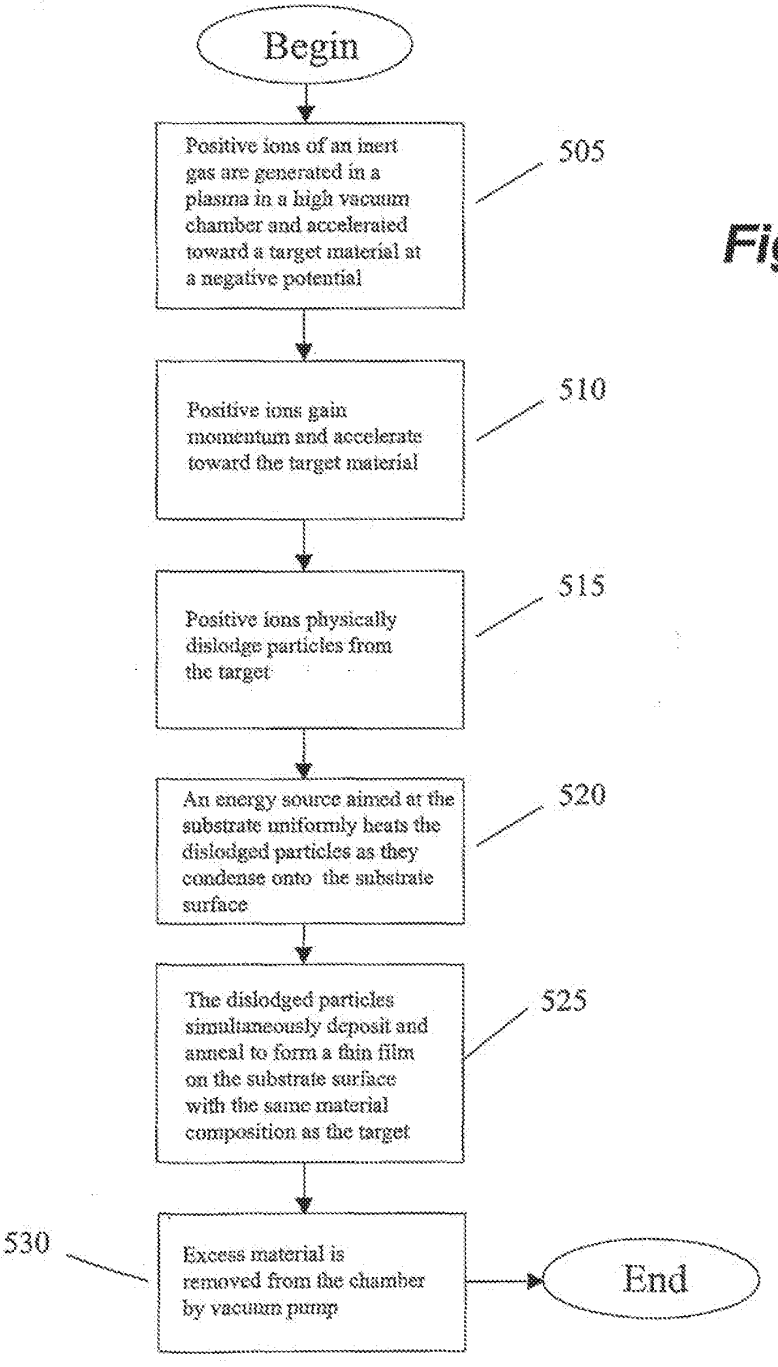


Figure 5

SAMSUNG EX. 1002 - 2207/4148

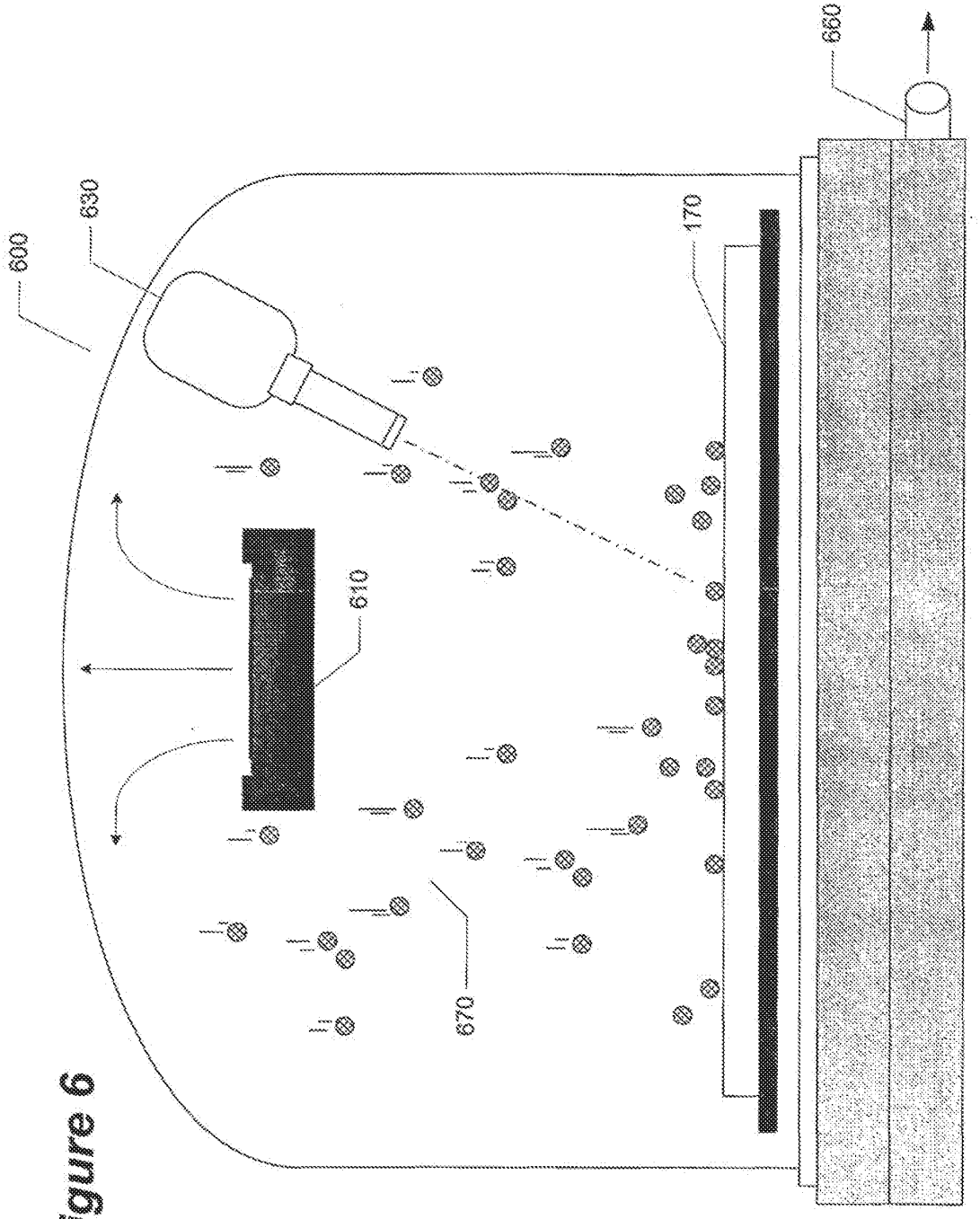


Figure 6

SAMSUNG EX. 1002 - 2208/4148

(12) INTERNATIONAL APPLICATION PUBLISHED UNDER THE PATENT COOPERATION TREATY (PCT)

(19) World Intellectual Property Organization
International Bureau

(43) International Publication Date
24 July 2003 (24.07.2003)

PCT

(10) International Publication Number
WO 03/059390 A1

(51) International Patent Classification[7]: A61K 47/30

(21) International Application Number: PCT/KR03/00084

(22) International Filing Date: 15 January 2003 (15.01.2003)

(25) Filing Language: Korean

(26) Publication Language: English

(30) Priority Data:
10-2002-0002577 16 January 2002 (16.01.2002) KR

(71) Applicant *(for all designated States except US)*: **DONG WHA PHARM. IND. CO., LTD.** [KR/KR]; 5, Soonwha-dong, Joong-gu, Seoul 100-130 (KR).

(72) Inventors; and

(75) Inventors/Applicants *(for US only)*: **CHUNG, Yong-Ho** [KR/KR]; 301-204, Semmaul Apt. Hogae-dong, Dongan-gu, Anyang-si, Kyonggi-do 431-080 (KR). **RYU, Jei-Man** [KR/KR]; 207-101, Eunhasu Apt. Bubeung-dong, Dongan-gu, Anyang-si, Kyonggi-do 431-054 (KR). **JUNG, Jae-Hee** [KR/KR]; 10-503, Namsantown Apt. Sindang-dong, Joong-gu, Seoul 100-754 (KR). **KIM, Yu-Eun** [KR/KR]; 1104, Will Town, #402-3, Sang 1-dong, Wonmi-gu, Bucheon-si, Kyonggi-do 420-814 (KR). **CHO, Chong-Su** [KR/KR]; 211-501, Hangaram Apt. Ichon 1-dong, Yongsan-gu, Seoul 140-728 (KR). **CHOI, Hoo-Kyun** [KR/KR]; 3-1408, Pyeonghwa Mansion, #768, Hak-dong, Dong-gu, Gwangju 501-847 (KR). **CHUN, Myung-Kwan** [KR/KR]; 529-29, Bangnim 1-dong, Nam-gu, Gwangju 503-051 (KR). **AHN, Jae-Soon** [KR/KR]; 105-1404, Donga Apt, Hupyeong-dong, Chuncheon-si, Gangwon-do 200-160 (KR). **KIM, Tae-Hee** [KR/KR]; 123-404, Mugunghwa Apt, Geumjeong-dong, Gunpo-si, Kyonggi-do 435-050 (KR).

(74) Agent: **LEE, Byung-Hyun**; #705, New Seoul Bldg., 828-8, Yeoksam-dong, Kangnam-gu, Seoul 135-080 (KR).

(81) Designated States *(national)*: AE, AG, AL, AM, AT, AU, AZ, BA, BB, BG, BR, BY, BZ, CA, CH, CN, CO, CR, CU, CZ, DE, DK, DM, DZ, EC, EE, ES, FI, GB, GD, GE, GH, GM, HR, HU, ID, IL, IN, IS, JP, KE, KG, KP, KZ, LC, LK, LR, LS, LT, LU, LV, MA, MD, MG, MK, MN, MW, MX, MZ, NO, NZ, OM, PH, PL, PT, RO, RU, SC, SD, SE, SG, SK, SL, TJ, TM, TN, TR, TT, TZ, UA, UG, US, UZ, VC, VN, YU, ZA, ZM, ZW.

(84) Designated States *(regional)*: ARIPO patent (GH, GM, KE, LS, MW, MZ, SD, SL, SZ, TZ, UG, ZM, ZW), Eurasian patent (AM, AZ, BY, KG, KZ, MD, RU, TJ, TM), European patent (AT, BE, BG, CH, CY, CZ, DE, DK, EE, ES, FI, FR, GB, GR, HU, IE, IT, LU, MC, NL, PT, SE, SI, SK, TR), OAPI patent (BF, BJ, CF, CG, CI, CM, GA, GN, GQ, GW, ML, MR, NE, SN, TD, TG).

Published:
— *with international search report*

For two-letter codes and other abbreviations, refer to the "Guidance Notes on Codes and Abbreviations" appearing at the beginning of each regular issue of the PCT Gazette.

(54) Title: ORAL MUCOADHESIVE FILM

(57) Abstract: The present invention relates to a new oral mucoadhesive film containing mucoadhesive polymers. The film, consisting of two layers of an adhesive layer containing drugs and a protective layer functioning as a protector and supporter, adheres to oral mucous membranes so that the drugs may be absorbed steadily through the oral mucous membranes.

WO 03/059390 A1

SIONYX1403000023.0051

SAMSUNG EX. 1002 - 2209/4148

ORAL MUCOADHESIVE FILM

Technical Field

The present invention relates to a new oral mucoadhesive film, which consists of two layers of an adhesive layer containing a drug, a polyacrylic acid polymer, a cellulose derivative, poloxamer and a plasticizer and a protective layer containing a water-insoluble and water-impermeable polymer and a plasticizer, and a method of preparing the same.

Background Art

Contrary to skin, most of mucous membranes placed in gastrointestinal tract and oral cavity, etc. easily absorb active substances of large molecular weight such as peptides so that they are of great value for essential administration route of such active substances. Especially, drugs absorbed through oral mucous membrane or gum are not influenced by gastrointestinal effect and hepatic first-pass metabolism, and therefore, they are effectively used in oral diseases as well as other diseases requiring systemic effect.

Gels, one of drug administration preparations using oral mucous membrane, are usually used in treating ulcerative stomatitis, herpes simplex, etc. However, gels are easily mixed with saliva and swell to lose the gel form quickly so that the amount of drugs absorbed in oral mucous membrane is less than that swallowed per os. Tablets, even though having the advantage of elongated time of maintaining the form, give a feeling of foreign substances to users due to their bulkiness and thickness as well as have the possibility to be swallowed with food during a mealtime. On the other hand, films are suitable to be oral mucoadhesive preparations since they are easy to use with little feeling of foreign substances, maintain the adhesiveness during the attached time for drug administration, and provide protection to the treatment time.

In order to administrate drug through oral mucous membrane, the form of preparation containing the drug should be maintained within a certain period of time. Most of mucoadhesive polymers used in conventional oral mucoadhesive films are quickly swelled or dissolved when contacted with water so that they remain on the oral mucous membrane only for a short time, which prevents

SAMSUNG EX. 1002 - 2210/4148

sustained release of drugs. Further, with the swelling of polymers, the diffusion of drugs varies and then its delivery rate cannot be estimated.

Among the polymers, polyacrylic acid and cellulose derivatives have excellent mucoadhesiveness (*J. Pharm. Sci.*, 89(7), 850-866, 2000). However, the polymers cannot maintain their form in oral cavity for a long time due to the high swelling or solubility in saliva (U.S. Patent Nos. 4,292,299 and 4,740,365, and European Patent No. 654,261). In the preparations having an adhesive layer containing sodium carboxymethyl cellulose, polyacrylic acid and hydroxyethyl cellulose (U.S. Patent No. 6,159,498), the shape maintenance time of preparations is only less than 1 hour and the preparations are changed to gel form after being attached, so that drugs in the preparations cannot be delivered effectively. Further, in case of the preparations containing hydroxypropylmethyl cellulose (U.S. Patent No. 5,948,430), the polymer has too high solubility in water to be used in the preparations which need to be attached for a long time.

Considering the above, the introduction of new mucoadhesive polymers which maintain their forms and adhesiveness during the release of drugs is required in the development of oral mucoadhesive preparations. Oral mucoadhesive preparations need to be convenient for use, to give minimum feeling of foreign substances after being attached so as to enhance the compliance of patients, to maintain the adhesiveness without changing their forms for a certain period of time in order to deliver drugs effectively, and to have ease and effectiveness of preparing.

There is disclosed a method of preparing a mucoadhesive preparation containing three or four layers of adhesive layer, impermeable layer, drug reservoir layer and controlled release layer. The method comprises making each layer to be dried to a fixed weight, binding each layer with one another, and then completely drying the combined layers (U.S. Patent Nos. 5,196,202 and 4,900,552). However, the preparing processes are complicated and have low effectiveness due to the difficulty in adjusting dry weight and binding these layers. The hydration speed differs in each layer, which results in twist and curling of the preparation and also loss of drugs. Further, the film also has the defect that it has the thickness of about 800 μm, which is thicker than those of conventional oral mucoadhesive films, and gives the feeling of foreign substances when attached.

In case of a single layer film, the residence time of the preparation is affected as the mucoadhesive layer is exposed to water in oral cavity, which limits the use of the film only to delivery of rapid-acting drugs (U.S. Patent No. 5,948,430).

SAMSUNG EX. 1002 - 2211/4148

Also disclosed is a film consisting of two layers of a protective layer and an adhesive layer, which lengthens the residence time of the preparation and increases the efficiency of drug absorption in mucous membrane, thereby somewhat solving the problem of single- or multiple-layered films. However, the double-layered film consisting of an adhesive layer containing vinyl acetate, polyacrylic acid, etc. and a protective layer containing polyethylene, aluminum, etc. (U.S. Patent No. 5,137,729) has some defects that the two layers are separated each other and that a feeling of foreign substances is given to users when attached. Further, the film having a protective layer containing water-insoluble materials such as ethyl cellulose (EC), hydroxypropyl cellulose phthalate (HPC-P) and cellulose acetate phthalate (CA-P) (U.S. Patent No. 4,876,092) has decreased affinity between protective layer and adhesive layer, and also has different rate of hydration by saliva after being attached, which results in the possibility of separation of the two layer. Accordingly, the type of mucoadhesive polymers used in protective layer and adhesive layer and the affinity between the layers should be considered preferentially for maintaining the form of preparations.

Disclosed is a method to add a plasticizer such as polyalcohols in an adhesive layer and a protective layer for increasing the affinity between the two layers. However, this method has a defect that it is difficult to maintain the preparations for a long time due to the high solubility and swelling of the mucoadhesive polymers used in the adhesive layer (Korean Laid-open Publication No. 2000-31828). Further disclosed is a method to add a water-insoluble carbonated titanium and talc in an adhesive layer for maintaining the form of preparations. This method also has a defect that the affinity between layers decreases due to the low flexibility of the adhesive layer, thereby resulting in the separation of layers (Korean Laid-open Publication No. 1997-9794).

Considering the above-mentioned problems of oral mucoadhesive films, the present inventors have been able to prepare a new oral mucoadhesive film on the base of the revelation that when polyacrylic acid polymers and cellulose derivatives, which cannot maintain the adhesiveness for a long time due to the swelling and solubility in saliva despite of the excellent mucoadhesiveness, are added with poloxamer, the swelling and solubility in saliva can be adjusted.

Disclosure of the Invention

The present invention relates to an oral mucoadhesive film for an effective drug delivery through oral mucous membrane, which has a long lasting adhesiveness

SIONYX1403000023.0054

SAMSUNG EX. 1002 - 2212/4148

and a good flexibility, does not give a feeling of foreign substances to users, and is prepared with ease and efficiency, and a method of preparing the same.

In accordance with one aspect of the present invention, it is provided an oral mucoadhesive film which contains an adhesive layer consisting essentially of a polyacrylic acid polymer, poloxamer, a cellulose derivative, a drug which can be absorbed through mucous membrane and a plasticizer, and a protective layer consisting essentially of a water-insoluble and water-impermeable polymer and a plasticizer,

wherein each of the polyacrylic acid polymer and the cellulose derivative is in an amount of 5 to 80 % by weight and the poloxamer is in an amount of 5 to 70 % by weight, based on the weight of the polymers in the adhesive layer, and a mixture of the polymers is in an amount of 5 to 20 % by weight, the drug is in an amount of 0.05 to 20 % by weight, and the plasticizer in the adhesive layer is in an amount of 0.1 to 10 % by weight, based on the weight of the adhesive layer;

the water-insoluble and water-impermeable polymer is in an amount of 5 to 50 % by weight and the plasticizer in the protective layer is in an amount of 0.1 to 10 % by weight, based on the weight of the protective layer; and

the film has a thickness ranging from 30 to 500 μm.

The oral mucoadhesive film of the present invention consists of an adhesive layer containing a drug and a protective layer. The protective layer consists of a water-insoluble and water-impermeable polymer such as ethyl cellulose (EC), polyurethane (PU), polyethylene (PE), and polyester, and a plasticizer. Further, the adhesive layer consists of a cellulose derivative such as hydroxypropyl cellulose (HPC), hydroxymethyl cellulose (HMC), hydroxyethyl cellulose (HEC), hydroxypropylethyl cellulose (HPEC) and hydroxypropylmethyl cellulose (HPMC), a polyacrylic acid polymer such as carbomer and polycarbophil, poloxamer and a plasticizer. The adhesive layer is a drug-containing layer and can adhere to oral mucous membrane to deliver the drug, and the protective layer prevents the drug-containing adhesive layer from being lost or detached from the mucous membrane due to rapid swelling .

Examples of polyacrylic acid polymers contained in the adhesive layer are carbomer, polycarbophil, and mixtures thereof. Polycarbophil is a cross-linked acrylic acid polymer with divinyl glycol and carbomer is polymerized by allyl sucrose or allyl pentaerythritol. Examples of carbomer are carbopol series 980, 934, 940, 941, 934P, 971P, 974P, 981, 1342, 1382, 2984 and 5984EP sold on the market by the trade name "Carbopol" and Noveon series AA-1, CA-1 and CA-2 sold on the market by the trade name "Noveon", preferably carbopol 934P and

SIONYX1403000023.0055

SAMSUNG EX. 1002 - 2213/4148

carbopol 971P.

Cellulose derivatives have an excellent film-forming ability and are used as a binder and film-coating agent for tablets. Examples of cellulose derivatives are hydroxypropyl cellulose, hydroxymethyl cellulose, hydroxyethyl cellulose, hydroxypropylethyl cellulose and hydroxypropylmethyl cellulose, preferably hydroxypropylethyl cellulose and hydroxypropylmethyl cellulose.

Poloxamer, a copolymer of polyethylene glycol and polypropylene glycol, used as an emulsifier and a supplementary solubilizer, is characterized by a variety of gel formation according to the type, concentration and mixing ratio. Examples are poloxamer series 124, 188, 338 and 407, preferably poloxamer 188 and poloxamer 407.

Examples of the plasticizer used in the adhesive layer are castor oil and polyethylene glycol (PEG), preferably polyethylene glycol.

Drugs which are added in the adhesive layer include all drugs that can be absorbed through mucous membranes. Examples of the drugs are those for oral diseases such as triamcinolone acetonide and glycyrrhetinic acid; anti-inflammatory agents such as ketoprofen and piroxicam; anti-histamines such as diphenhydramine and chlorpheniramine; hormones such as estradiol and testosterone; antihypertensive agents such as clonidine and propranolol; bronchodilators such as theophylline and terbutaline; and anesthetics such as lidocaine and dibucaine. Preferably used are such drugs as have high bioavailability enough to be administered in a small amount, as are easily metabolized when administered orally, and as have a gastro-intestinal adverse effect.

Examples of the water-insoluble and water-impermeable polymers are polyester, polyurethane, polyethylene and ethyl cellulose, preferably polyurethane and ethyl cellulose. Ethyl cellulose is used as a water-insoluble coating agent for tablets or granules for the purpose of controlled release, masking of taste, and improvement of stability, etc.

Examples of the plasticizer used in the protective layer are triethyl citrate (TEC), castor oil and polyethylene glycol (PEG), preferably polyethylene glycol and triethyl citrate.

The film according to the present invention consists of two layers of an adhesive layer and a protective layer, as illustrated in Fig. 1.

In the preparing process of an adhesive layer with excellent film-forming ability and mucoadhesiveness, films are manufactured by preparing a solution mixed with cross-linked polyacrylic acid polymer and cellulose derivative, which have an excellent mucoadhesiveness. Even though the film prepared from the

SIONYX1403000023.0056

SAMSUNG EX. 1002 - 2214/4148

solution is homogeneous, it has high swelling and solubility in saliva to decrease the delivery of drugs through mucous membranes, and also it has too high viscosity for large-scale production of the high concentrated solution. Further, it has low flexibility to give a feeling of foreign substances when attached to mucous membranes.

Considering the above problems, the present inventors have prepared a film by adding poloxamer into the polymer solution to prepare an adhesive layer, in which the solution can be prepared at a low temperature, the viscosity of the mixed solution is so low as to make it easy to prepare the film, and the film has low swelling and solubility in saliva, thereby enabling the film to be attached to mucous membranes for a long time.

The result of measuring the change of water contents in films prepared by adding poloxamer shows that the water contents decrease in films with an increase of poloxamer in the composition, thereby increasing the shape maintenance time in an aqueous solution (see Experiment 2). It is suggested that poloxamer and carbopol or hydroxypropylmethyl cellulose form a hydrogen bond, thereby forming a dense third-dimensional network structure.

The formation of hydrogen bond due to the addition of poloxamer can be confirmed by infrared spectrophotometer (IR), and the change of film flexibility can be identified by dynamic mechanical thermal analyzer (DMTA). It is confirmed that the characteristic peaks of poloxamer due to hydrogen bonds in IR change to short wave number with an increase of poloxamer in the composition. It is considered that the decrease of glass transition temperature, which shows the movement of molecules, compared to that of the mixture of hydroxypropylmethyl cellulose and carbopol, indicates the increase of film flexibility (see Experiment 3).

An adhesive layer is required to have a mucoadhesiveness as well as an ability to control the release of drug into mucous membranes. A proper combination of the above-mentioned polymers is important for the requirements. Each of the polyacrylic acid polymer and cellulose derivative is added in an amount of 5 to 80 % by weight, preferably 20 to 50 % by weight, based on the weight of the polymers in the adhesive layer. If the amount of each polymer is less than 5 % by weight, it is impossible to prepare the film with constant thickness because of low viscosity of polymer solution, thereby also decreasing the adhesiveness of film. While if the amount of each polymer is more than 80 % by weight, it is difficult to prepare the polymer solution.

Poloxamer is added in an amount of 5 to 70 % by weight, preferably 20 to 50 % by weight, based on the weight of the polymers in the adhesive layer. If the

SIONYX1403000023.0057

SAMSUNG EX. 1002 - 2215/4148

amount is less than 5 % by weight, the solubility and swelling of film increase so that it is difficult to maintain the form of film. Further, in case the poloxamer is added in an amount of more than 70 % by weight, it is difficult to prepare the polymer solution of high concentration.

The mixed solution of the above three polymers is prepared so that the concentration of the polymers is 5 to 20 % based on the weight of the adhesive layer, in which the preferred weight ratios of poloxamer/cross-linked polyacrylic acid and poloxamer/hydroxypropylmethyl cellulose range from 1:1 to 1:1.5, respectively. Within the above range of concentration, it is easy to adjust the film thickness and drying time at the time of preparing the film.

Drugs are added in an amount of 0.05 to 20 % by weight based on the weight of the adhesive layer. If the drug is added in an amount of more than 20 % by weight, it has an adverse effect on the viscosity of the solution of adhesive layer and makes the preparing of film difficult.

In the protective layer which protects the adhesive layer from saliva, the water-insoluble and water-impermeable polymer is added in an amount of 5 to 50 % by weight, preferably 10 to 30 % by weight, based on the weight of the protective layer. If the amount is less than 5 % by weight, the fluidity of solution containing the polymer is too high to make film. Further, in case the polymer is added in an amount of more than 50 % by weight, it is difficult to prepare film having a constant thickness.

In order to maintain the form of oral mucoadhesive film consisting of a mucoadhesive layer and a water-insoluble and water-impermeable protective layer until an active substance is released, coherence between the two layers is required for a long time.

According to the present invention, a proper plasticizer for each layer is selected in consideration of the mucoadhesiveness of adhesive layer and the affinity between the two layers. Examples of the plasticizer used in the adhesive layer of the present film are castor oil and polyethylene glycol (PEG). Examples of the plasticizer used in the protective layer of the present film are triethyl citrate (TEC), castor oil and polyethylene glycol (PEG).

When triethyl citrate is used in the adhesive layer, it is impossible to form a film. Castor oil and polyethylene glycol added in the adhesive layer have a good effect on the film formation and flexibility. In the adhesive layer, polyethylene glycol is better to be added than castor oil for a good adhesiveness.

Most preferred is the film having polyethylene glycol added in the adhesive layer and triethyl citrate added in the protective layer, which has the most

SIONYX1403000023.0058

SAMSUNG EX. 1002 - 2216/4148

superior mucoadhesiveness, flexibility and high affinity between layers to provide a long residence time of the preparation in oral cavity.

The amount of plasticizer added in the adhesive layer or protective layer is 0.1 to 10 % by weight, preferably 2 to 8 % by weight, based on the respective weight of the adhesive layer or protective layer. If the amount is more than 10 % by weight, it affects adversely the film formation and drying process of adhesive layer and protective layer and makes it difficult to prepare the film.

The method of preparing the mucoadhesive film of the present invention are described as follows:

5 to 80 % by weight of a polyacrylic acid polymer, 5 to 70 % by weight of poloxamer and 5 to 80 % by weight of a cellulose derivative, based on the total weight of the polymers in the adhesive layer, are dissolved in a mixed solvent of water and ethanol to make a solution in which the concentration of the polymers is 5 to 20 % by weight based on the total weight of the adhesive layer. 0.05 to 20 % by weight of a drug and 0.1 to 10 % by weight of a plasticizer for adhesive layer, based on the total weight of the adhesive layer, are added to the solution in turn to make a homogeneous coating solution for adhesive layer.

Separately, 5 to 50 % by weight of a water-insoluble and water-permeable polymer and 0.1 to 10 % by weight of a plasticizer for protective layer, based on the total weight of the protective layer, are dissolved in ethanol to make a homogeneous coating solution.

After being defoamed, the coating solution for adhesive layer is coated on a release liner with a coater (Laboratory Drawdown Coater LC-100, Chem Instruments) and then dried to make an adhesive layer.

After being defoamed, the coating solution for protective layer is also coated on the adhesive layer with a coater and then dried to make an oral mucoadhesive film consisting of an adhesive layer and a protective layer.

The oral mucoadhesive film of the present invention has a thickness ranging from 30 to 500 μm, preferably from 50 to 300 μm, when being dried, in which each thickness of an adhesive layer and a protective layer is 20 to 300 μm and 10 to 200 μm, respectively. The film with the thickness of less than 30 μm has difficulty in maintaining the form of film and adversely affects favorable release of drug. Further, the film with the thickness of more than 500 μm gives a feeling of foreign substances to users.

The oral mucoadhesive film of the present invention may be prepared with the addition of the conventional lubricants, disintegrating agents, coloring agents, etc. according to the type of preparations.

SIONYX1403000023.0059

SAMSUNG EX. 1002 - 2217/4148

Brief Description of the Drawings

The above and other objects, features and other advantages of the present invention will be more clearly understood from the following detailed description taken in conjunction with the accompanying drawings, in which:

Fig. 1 is a schematic cross-sectional view of the oral mucoadhesive film consisting of an adhesive layer containing a drug and a protective layer.

Fig. 2 is a graph showing the dissolution rate of drug in Examples 1 and 2, Comparative Example 1 and Aftach tablet.

Fig. 3 is a graph showing the change of concentration of drug in the surface of tongue when the films of Example 1 and Control group 2 are attached to the tongue of rat.

Fig. 4 is a graph showing the change of concentration of drug absorbed into the tissue of tongue when the films of Example 1 and Control group 2 are attached to the tongue of rat.

Best Mode for Carrying Out the Invention

Hereinafter, the present invention will be described in detail, in conjunction with various examples. These examples are provided only for illustrative purposes, and the present invention is not to be construed as being limited to these examples.

Examples 1 to 19

Each of the solutions for adhesive layer and protective layer was prepared according to the compositions shown in the following Tables 1 and 2.

A polyacrylic acid polymer, poloxamer and a cellulose derivative were dissolved in a mixed solvent of water and ethanol to make a homogeneous solution, to which a drug and a plasticizer for adhesive layer were added and dissolved to obtain a homogeneous coating solution for adhesive layer.

Separately, a water-insoluble and water-impermeable polymer and a plasticizer for protective layer were dissolved in ethanol to make a homogeneous coating solution.

After being defoamed, the solution for adhesive layer was coated on a release liner with a coater (Laboratory Drawdown Coater LC-100, Chem Instruments) and dried to obtain an adhesive layer.

After removing bubbles, the solution for protective layer was also coated on

SIONYX1403000023.0060

SAMSUNG EX. 1002 - 2218/4148

the adhesive layer with a coater and then dried to prepare an oral mucoadhesive film consisting of an adhesive layer and a protective layer and containing 25 μg of triamcinolone acetonide per one sheet of film. The film has the thickness of 60 to 100 μm.

Comparative Examples 1 to 12

The procedures of Examples were repeated using the following composition as shown in Table 3 to obtain a film consisting of an adhesive layer and a protective layer.

Comparative Examples 13 to 22

The procedures of Examples 1 to 10 were repeated except the type of plasticizer as shown in the following composition of Table 4 to obtain a film consisting of an adhesive layer and a protective layer.

Table 1

Comp. \ Examples		1	2	3	4	5	6	7	8	9	10
AL	TAA	0.1	0.1	0.1	0.1	0.1	0.1	0.1	0.1	0.1	0.1
	P407	3.0	4.0	4.0	3.0	3.0					
	P188						4.5	4.0	2.2	2.5	2.4
	CP971P	3.5	4.5	4.5			5.0	4.5			
	CP934P				4.2	3.5			2.8	3.5	3.0
	HPMC	3.5	4.5	5.0	3.7	4.5	5.5	4.5	3.1	3.1	2.6
	PEG	3.9	3.9	4.0	6.6	1.9	2.3	3.5	4.0	7.2	3.9
	Water	43.0	41.5	41.2	41.2	43.5	41.3	41.7	43.9	41.8	44.0
	EtOH	43.0	41.5	41.2	41.2	43.5	41.3	41.7	43.9	41.8	44.0
	Total(g)	100	100	100	100	100	100	100	100	100	100
PL	EC	15	12	17	22	13	20	12	17	21	16
	TEC	4.0	3.5	4.2	4.0	3.2	2.9	3.3	4.2	4.3	3.5
	EtOH	81	84.5	78.8	74.0	83.8	77.1	84.7	78.8	74.7	80.5
	Total(g)	100	100	100	100	100	100	100	100	100	100

Table 2

Comp. \ Examples	11	12	13	14	15	16	17	18	19

AL	TAA	0.1	0.1	0.1	0.1	0.1	0.1	0.1	0.1	0.1
	P407	1.5	1.5	1.5	1.5	1.5	1.5	1.5	1.5	1.5
	P188									
	CP971P	1.75	1.75	1.75	1.75	1.75	1.75			
	CP934P							1.75		
	CP940								1.75	
	CP974P									1.75
	HPMC	1.75	1.75	1.75	1.75	1.75	1.75	1.75	1.75	1.75
	PEG	1.9	0.9	0.9	2.9	1.9	1.9	1.9	1.9	1.9
	Water	46.5	47.0	47.0	46.0	46.5	46.5	46.5	46.5	46.5
	EtOH	46.5	47.0	47.0	46.0	46.5	46.5	46.5	46.5	46.5
	Total(g)	100	100	100	100	100	100	100	100	100
PL	PU	15	12	17	22	13	20	12	17	21
	TEC	4.0	3.5	4.2	4.0	3.2	2.9	3.3	4.2	4.3
	EtOH	81	84.5	78.8	74.0	83.8	77.1	84.7	78.8	74.7
	Total(g)	100	100	100	100	100	100	100	100	100

Table 3

Comp. \ C. E.		1	2	3	4	5	6	7	8	9	10	11	12
A	TAA	0.1	0.1	0.1	0.1	0.1	0.1	0.1	0.1	0.1	0.1	0.1	0.1
L	P407		8.4		12.5			10				2	2
	P188						9.0			7.4	7.9		
	CP971P	3.5	2.5									1.5	1
	CP934P				2.0	3.5			2.5				
	HPMC			3.5		9.9	7.4		3.0	5.0		1.0	1
	PEG	4.0	4.0	4.0	6.6	1.9	2.3	3.5	4.0	7.3	4.0	4.0	3.9
	CO												
	TEC												
	Water	46.2	42.5	46.2	39.4	42.3	40.6	43.2	45.2	40.1	44.0	45.7	46.0
	EtOH	46.2	42.5	46.2	39.4	42.3	40.6	43.2	45.2	40.1	44.0	45.7	46.0
	Total(g)	100	100	100	100	100	100	100	100	100	100	100	100
P	EC	18	18	13	21	17	23	14	12	18	23	18	18
L	CO												
	PEG												
	TEC	4.0	3.5	4.2	4.0	3.2	2.9	3.3	4.2	4.3	3.5	4.0	4.0

	EtOH	78.0	78.5	82.8	75.0	79.8	74.1	82.7	83.8	77.7	73.5	78	78
	Total(g)	100	100	100	100	100	100	100	100	100	100	100	100

Table 4

Comp. \ C.E.		13	14	15	16	17	18	19	20	21	22
AL	TAA	0.1	0.1	0.1	0.1	0.1	0.1	0.1	0.1	0.1	0.1
	P407	3.0	4.0	4.5	3.0	3.0					
	P188						4.7	4.0	2.2	2.5	2.4
	CP971P	3.5	4.4	5.9			5.2	4.5			
	CP934P				4.1	3.5			2.8	3.5	3.0
	HPMC	3.5	4.5	5.7	3.7	4.5	4.9	4.5	3.1	3.1	2.6
	PEG		4.0						4.0	7.2	
	CO	3.9		4.0	6.7		2.3	3.5			3.9
	TEC					1.9					
	Water	43.0	41.5	39.9	41.2	43.5	41.4	41.7	43.9	41.8	44.0
	EtOH	43.0	41.5	39.9	41.2	43.5	41.4	41.7	43.9	41.8	44.0
	Total(g)	100	100	100	100	100	100	100	100	100	100
PL	EC	15	12	17	22	13	20	12	17	21	16
	CO		3.5		4.0	3.2	2.9			4.3	3.5
	PEG			4.2				3.3	4.2		
	TEC	4.0									
	EtOH	81.0	84.5	78.8	74.0	83.8	77.1	84.7	78.8	74.7	80.5
	Total(g)	100	100	100	100	100	100	100	100	100	100

In Tables 1 to 4, the abbreviations have the following meanings:

AL: Adhesive layer

PL: Protective layer

C.E.: Comparative Examples

Comp.: Component

TAA: Triamcinolone acetonide

P407: Poloxamer 407

P188: Poloxamer 188

CP971P: Carbopol 971P

CP934P: Carbopol 934P

CP940: Carbopol 940

SIONYX1403000023.0063

SAMSUNG EX. 1002 - 2221/4148

CP974P: Carbopol 974P
HPMC: Hydroxypropylmethyl cellulose
PEG: Polyethylene glycol
EtOH: Ethanol
EC: Ethyl cellulose
TEC: Triethyl citrate
PU: Polyurethane
CO: Castor oil

Control group 1

Among the products on the market, Aftach tablet (Dong Wha Pharm. Ind. Co., Ltd.), an oral mucoadhesive film which contains triamcinolone acetonide, hydroxypropyl cellulose and carboxyvinyl polymer in an adhesive layer and hydroxypropyl cellulose and calcium carboxymethyl cellulose in a protective layer, was selected as control group 1.

Control group 2

Among the products on the market, Innert plaster (Sudo Pharm. Ind. Co., Ltd.), an oral mucoadhesive film which contains triamcinolone acetonide as a main component, was selected as control group 2.

Control group 3

Among the products on the market, Stomatitis patch Taisho A (Japan Taisho Pharm. Ind. Co., Ltd.), an oral mucoadhesive film which contains extract of Lithospermi Radix and enoxolone as main components, was selected as control group 3.

Experiment 1: measurement of adhesiveness and mechanical strength

Each of the film samples prepared in Examples and Comparative Examples was attached to a polypropylene plate, and then the strength required to detach each film from the polypropylene plate was measured using Instron (AGS-5000D, Shimadzu). Table 5 shows the adhesiveness and mechanical strength of each film.

Table 5

Films	Adhesiveness (N)	Mechanical Strength (N)	Concentration of Polymer (%)

SIONYX1403000023.0064

SAMSUNG EX. 1002 - 2222/4148

Example 10	6.5	1.92	8
Comparative Example 10	2.8	-	7.9
Comparative Example 22	3.3	-	8
Example 1	7.8	2.01	10
Comparative Example 2	4.0	-	10.9
Comparative Example 13	4.7	-	10
Example 5	8.0	2.07	11
Comparative Example 4	4.3	-	14.5
Comparative Example 17	-	-	11
Example 6	8.5	2.13	15
Comparative Example 5	6.3	-	13.4
Comparative Example 18	5.6	-	14.8

As the concentration of mucoadhesive polymers in adhesive layer increases from 8 to 10 %, the adhesiveness of film also increases. When the concentration increases over 10 %, however, the adhesiveness shows a little increase. Even in case of similar concentration of polymers, the films prepared from the compositions consisting of three polymers of poloxamer, carbopol and hydroxypropylmethyl cellulose (Examples 10, 1, 5 and 6) show more increased adhesiveness than those prepared from the composition consisting of one or two polymers (Comparative Examples 10, 2, 4 and 5). Further, the films prepared from the composition containing polyethylene glycol in adhesive layer and triethyl citrate in protective layer as a plasticizer (Examples 10, 1, 5 and 6) show superior adhesiveness to those prepared from the composition containing castor oil and triethyl citrate in adhesive layer and protective layer (Comparative Examples 13, 18 and 22). Meanwhile, the composition containing triethyl citrate in adhesive layer may not be used to prepare a film (Comparative Example 17).

As a result, the films containing polyethylene glycol in adhesive layer and triethyl citrate in protective layer as a plasticizer show the most superior affinity between layers. Such result is considered to be caused by the fact that polyethylene glycol is similar to poloxamer contained in adhesive layer in structure, and triethyl citrate to ethyl cellulose contained in protective layer.

Mechanical strength shows no great change in proportion to the concentration of polymers in adhesive layer. Further, it is impossible to measure mechanical strength of other films except those containing polyethylene glycol and triethyl citrate in adhesive layer and protective layer, respectively, as a plasticizer (Examples 10, 1, 5 and 6),

Experiment 2: measurement of water content and shape maintenance time of film

Water content and shape maintenance time of each film were measured in phosphate buffer (pH 6.8). Table 6 shows the results.

Water content of film is calculated by the following formula:

Water content (% by weight)=[(the weight of swollen film-the weight of dried film)/the weight of swollen film]x100

As the proportion of poloxamer increases in composition, water content decreases but shape maintenance time of film increases.

Table 6

Films	Water content (% by weight)	shape maintenance time (hr)	Poloxamer (%)
Comparative Example 8	89	6.2	-
Comparative Example 11	78	8.2	2
Example 1	45	>24	3
Comparative Example 12	75	9.1	2
Control group 1	84	7.8	-
Control group 2	96	4.5	-

Control group 1: Aftach tablet

Control group 2: Innert plaster

Experiment 3: infrared spectrophotometer (IR) and dynamic mechanical thermal analyzer (DMTA)

FT-IR (M. Series, Midac Corporation, USA) was used for IR of films and DMTA was used to measure glass transition temperature (Tg) in the temperature ranging from room temperature to 300 °C at the rate of 5 °C/min. Table 7 shows the results.

As the proportion of poloxamer increases in composition, the IR peak derived from the hydrogen bond of poloxamer and carboxyl group of carbopol shifts from 1110 to 1107 cm^{-1} and the Tg shown in the mixture of carbopol and hydroxypropylmethyl cellulose decreases from 190 to 170 °C.

Table 7

Films	Wave number (cm^{-1})	Tg (°C)	Poloxamer (%)
Comparative Example 8	1110	190	-

SIONYX1403000023.0066

SAMSUNG EX. 1002 - 2224/4148

Comparative Example 11	-	180	2
Comparative Example 12	-	180	2
Example 1	1107	170	3

Experiment 4: measurement of bioadhesiveness

Rectal mucous membrane of rabbit was attached to both vials of the apparatus for measurement of bioadhesiveness, and then films were attached therebetween. Putting counterweights in turn on the opposite site, the counterweight was weighed as bioadhesiveness when the vial was dropped (H. G. Choi, J. H. Jung, J. M. Ryu, S. J. Yoon, Y. K. Oh and C. K. Kim, Development of in situ-gelling and mucoadhesive acetaminophen liquid suppository, *Int. J. Pharm., 165*, 33-44, 1998). Table 8 shows the bioadhesiveness measured as above.

Table 8

Films	Bioadhesiveness (dyne/cm^2)x10^2	Remark	
		Polymer (% by weight)	Plasticizer (adhesive layer, protective layer)
Example 16	6.27	5	PEG, TEC
Example 10	8.57	8	PEG, TEC
Example 1	10.33	10	PEG, TEC
Example 3	11.02	13.5	PEG, TEC
Comparative Example 14	8.0	12.9	PEG, CO
Comparative Example 13	6.67	10	CO, TEC
Comparative Example 15	6.93	16.1	CO, PEG
Comparative Example 19	6.14	13	CO, PEG
Comparative Example 16	4.87	10.8	CO, CO

PEG: polyethylene glycol
TEC: triethyl citrate
CO: castor oil

As shown in Examples of Table 8, when polyethylene glycol and triethyl citrate are added in adhesive layer and protective layer, respectively, as a plasticizer, the bioadhesiveness increases from 6.27 to 11.02 according to the increase of the concentration of polymer contained in adhesive layer. Meanwhile, the film containing polyethylene glycol and castor oil as a plasticizer (Comparative Example 14), that containing castor oil and triethyl citrate (Comparative Example

SIONYX1403000023.0067

SAMSUNG EX. 1002 - 2225/4148

13), those containing castor oil and polyethylene glycol (comparative Examples 15 and 19), and that containing castor oil and castor oil (Comparative Example 16) show lower adhesiveness than those containing polyethylene glycol and triethyl citrate in adhesive layer and protective layer, respectively. Further, these films show no great change in adhesiveness to living body according to the increase of polymers.

Experiment 5: measurement of attached time

The films prepared in Examples and Comparative Examples were cut and attached to glass wall of dissolution test vessel at a height of 5, 7.5 and 10 cm each. Detachment of each sample was observed in 900 ml of phosphate buffer (pH 6.8) at 37± 0.5 °C with the rotation of paddle at 100 rpm by applying method 2 of dissolution test. The attached time of control group was measured in the same manner. Table 9 shows the film thickness and attached time measured as above.

Table 9

Films	Film thickness (μm)	Attached time (hr)
Example 1	75.3	>24
Example 9	77.2	>24
Comparative Example 20	72.6	13.7
Comparative Example 16	69.7	6.0
Comparative Example 14	71.4	15.2
Comparative Example 19	74.8	14.7
Comparative Example 1	65.3	6.07
Comparative Example 2	70.7	13.4
Comparative Example 5	69.3	12.0
Control group 1	1,100	7.8
Control group 2	100	4.5

The films containing polyethylene glycol and triethyl citrate as a plasticizer show long attached time above 24 hours when they contain all three type of polymers in adhesive layer (Examples 1 and 9), which is longer than that of the films containing single or two polymers in adhesive layer (Comparative Examples 1, 2 and 5). The attached time varies from 6.0 to 24 hours in accordance with the type of plasticizer, which corresponds to the results from the adhesive force and bioadhesiveness.

Experiment 6: drug dissolution test

Each oral mucoadhesive film was attached to cellulose membrane and then dissolution test was carried out using diffusion cell. Dissolution solvent was mixture of phosphate buffer (pH 6.8) and ethanol (3:2, v/v). Sample solution was collected at regular intervals and the amount of released drug was analyzed by HPLC.

Comparing the drug dissolution of the film of the present invention with that of control group 1 shows that the films of the present invention has more favorable drug dissolution than those on the market. Fig. 2 is a graph showing the dissolution rate of drug in Examples 1 and 2, Comparative Example 1 and Aftach tablet.

Experiment 7: evaluation of adhesiveness to oral mucous membrane

In order to evaluate the adhesiveness to actual oral mucous membrane, each film was attached to the inside of lower lip of applicant and time required to be detached was measured. Further, feeling of use was evaluated when applied to oral mucous membrane and indicated by the following four stages:

1: little feeling;

2: a little feeling of foreign substances;

3: discomfort resulting from feeling of foreign substances; and

4: others (feeling of irritation, pain, etc.)

Table 10 shows the attached time and feeling of use as measured above.

Table 10

Films	Adhesion time (hr)	Feeling of use
Example 1	3.8	1.4
Example 3	4.2	1.7
Example 8	3.0	1.8
Comparative Example 1	1.2	1.5
Comparative Example 13	1.7	1.6
Comparative Example 22	1.4	1.9
Control group 1	3.2	2.8
Control group 2	1.5	2.7
Control group 3	3.5	2.1

The film of Example 3 shows the longest adhesion time of 4.2 hours, and those of Examples 1 and 8 show the adhesion time of 3.8 and 3.0 hours,

respectively, all of them show over 3 hours. The film containing carbopol only as a mucoadhesive polymer (Comparative Example 1) and that containing castor oil and triethyl citrate as a plasticizer for adhesive layer and protective layer, respectively (Comparative Example 13), have the adhesion time ranging from 1.2 to 1.7 hours, which are shorter than those of the above Examples. Further, control group 1 (Aftach tablet) shows 3.2 hours of attached time, control group 2 (Innert plaster) shows 1.5 hours and control group 3 (Stomatitis patch Taisho A) shows 3.5 hours.

While the control groups give a feeling of foreign substances when attached to oral mucous membrane, the films prepared in Examples and Comparative Examples give no feeling of foreign substances.

The films according to the present invention have superior initial adhesion to oral mucous membrane, show no swelling or detachment of polymers, and leave no remnants on oral mucous membrane during their adhesion and after being detached. Meanwhile, the films of control groups 1 and 2 show increase of swelling in polymers within several minutes after their adhesion to oral mucous membrane, which gives a notable feeling of foreign substances to users. Especially, the film of control group 2 has a good initial adhesion, but the polymer layer in the film swells to be detached from the protective film, which augments the feeling of foreign substances and displeasure and also gives a bitter taste. Further, a portion of the detached polymer layer remains in oral cavity to make some problems.

Experiment 8: animal experiment (in vivo)

Each oral mucoadhesive film of Example 1 and control group 2 was attached to the tongue of rats, and then each amount of drug remained in the surface of tongue and that absorbed into the tissue of tongue was assayed. SPF male wister rats (Charles River, Japan, weigh 260 to 350 g) were used and five rats were placed in a group.

After being anesthetized, each rat was provided with the films, and then was left freely. After a certain period of time, each tissue of tongue was removed and then analyzed. Each of the amount of drug remained in the surface of tongue and that absorbed into the tissue of tongue was determined by HPLC and LC/MS. As shown in Fig. 3, the film of Example 1 is superior to that of control group 2 in the maintenance of drug in the surface of tongue. Further, according to Fig. 4, the film of Example 1 shows a slowly increase of drug absorbed into the tissue of tongue with the lapse of time, and produces a superior result to that of Control group 2 in 2 hours.

SIONYX1403000023.0070

SAMSUNG EX. 1002 - 2228/4148

Industrial Applicability

The oral mucoadhesive film of the present invention is superior in physicochemical aspects such as adhesiveness, mechanical strength and attached time as well as bioadhesiveness. Further, the film shows sustained-release of drugs and gives long attached time and little feeling of foreign substances when attached to users. Moreover, the preparing process of the present invention is convenient for adjusting the film thickness and drying time.

What is Claimed is:

1. An oral mucoadhesive film which contains an adhesive layer consisting essentially of a polyacrylic acid polymer, poloxamer, a cellulose derivative, a drug which can be absorbed through mucous membrane and a plasticizer, and a protective layer consisting essentially of a water-insoluble and water-impermeable polymer and a plasticizer,

wherein each of the polyacrylic acid polymer and the cellulose derivative is in an amount of 5 to 80 % by weight and the poloxamer is in an amount of 5 to 70 % by weight, based on the weight of the polymers in the adhesive layer, and a mixture of the polymers is in an amount of 5 to 20 % by weight, the drug is in an amount of 0.05 to 20 % by weight, and the plasticizer in the adhesive layer is in an amount of 0.1 to 10 % by weight, based on the weight of the adhesive layer;

the water-insoluble and water-impermeable polymer is in an amount of 5 to 50 % by weight and the plasticizer in the protective layer is in an amount of 0.1 to 10 % by weight, based on the weight of the protective layer; and

the film has a thickness ranging from 30 to 500 μm.

2. The oral mucoadhesive film according to claim 1,

wherein the polyacrylic acid polymer is one or more selected from the group consisting of carbopol series 980, 934, 940, 941, 934P, 971P, 974P, 981, 1342, 1382, 2984 and 5984EP, and Noveon series AA-1, CA-1 and CA-2;

the poloxamer is one or more selected from the group consisting of poloxamer series 124, 188, 338 and 407;

the cellulose derivative is one or more selected from the group consisting of hydroxypropyl cellulose, hydroxymethyl cellulose, hydroxyethyl cellulose, hydroxypropylethyl cellulose and hydroxypropylmethyl cellulose;

the drug is one or more selected from the group consisting of medicines for oral diseases, anti-inflammatory agents, anti-histamines, hormones, antihypertensive agents, bronchodilators and anesthetics;

the plasticizer in the adhesive layer is polyethylene glycol;

the water-insoluble and water-impermeable polymer is one or more selected from the group consisting of polyester, polyurethane, polyethylene and ethyl cellulose; and

the plasticizer in the protective layer is triethyl citrate.

SIONYX1403000023.0072

SAMSUNG EX. 1002 - 2230/4148

3. The oral mucoadhesive film according to claim 2,

wherein the polyacrylic acid polymer is one or more selected from the group consisting of carbopol series 934P and 971P;

the poloxamer is one or more selected from the group consisting of poloxamer series 188 and 407;

the cellulose derivative is one or more selected from the group consisting of hydroxypropylethyl cellulose and hydroxypropylmethyl cellulose;

the drug is medicines for oral diseases; and

the water-insoluble and water-impermeable polymer is one or more selected from the group consisting of polyurethane and ethyl cellulose.

4. The oral mucoadhesive film according to one of claims 1 to 3,

wherein the weight ratios of poloxamer/polyacrylic acid polymer and poloxamer/cellulose derivative range from 1:1 to 1:1.5, respectively;

the water-insoluble and water-impermeable polymer is in an amount of 10 to 30 % by weight based on the weight of the protective layer; and

the film has a thickness ranging from 50 to 300 μm.

5. A method of preparing an oral mucoadhesive film containing an adhesive layer and a protective layer, which comprises:

(1) dissolving 5 to 80 % by weight of a polyacrylic acid polymer, 5 to 70 % by weight of poloxamer and 5 to 80 % by weight of a cellulose derivative, based on the total weight of the polymers in the adhesive layer, in a mixed solvent of water and ethanol to make a solution in which the concentration of the polymers is 5 to 20 % by weight based on the total weight of the adhesive layer, and then adding 0.05 to 20 % by weight of a drug and 0.1 to 10 % by weight of a plasticizer for the adhesive layer, based on the total weight of the adhesive layer, to the solution to make a homogeneous coating solution for the adhesive layer;

(2) dissolving 5 to 50 % by weight of a water-insoluble and water-impermeable polymer and 0.1 to 10 % by weight of a plasticizer for the protective layer, based on the total weight of the protective layer, in ethanol to make a homogeneous coating solution for the protective layer;

(3) defoaming the coating solution for the adhesive layer prepared by (1), coating the solution on a release liner with a coater, and then drying the coated layer to make the adhesive layer; and

SIONYX1403000023.0073

SAMSUNG EX. 1002 - 2231/4148

(4) defoaming the coating solution for the protective layer prepared by (2), coating the solution on the adhesive layer prepared by (3) with a coater, and then drying the coated layer to make the oral mucoadhesive film.

6. The method according to claim 5,

wherein the weight ratios of poloxamer/polyacrylic acid polymer and poloxamer/cellulose derivative range of from 1:1 to 1:1.5, respectively;

the water-insoluble and water-impermeable polymer is added in an amount of 10 to 30 % by weight based on the weight of the protective layer; and

the film has a thickness ranging from 50 to 300 μm.

FIG. 1

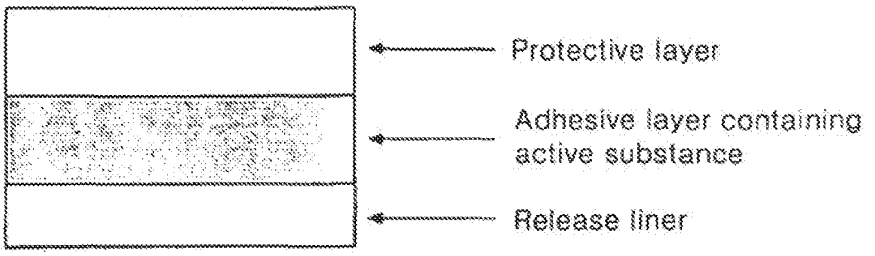
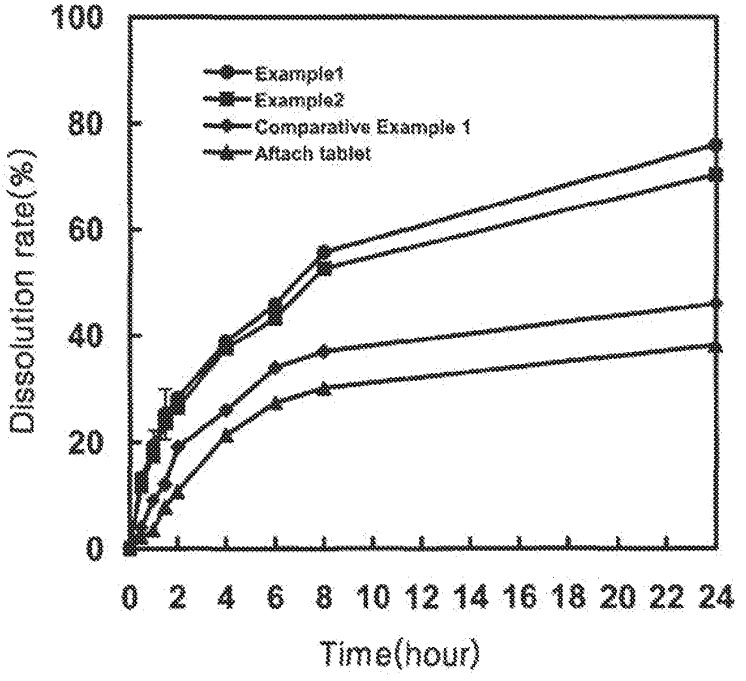
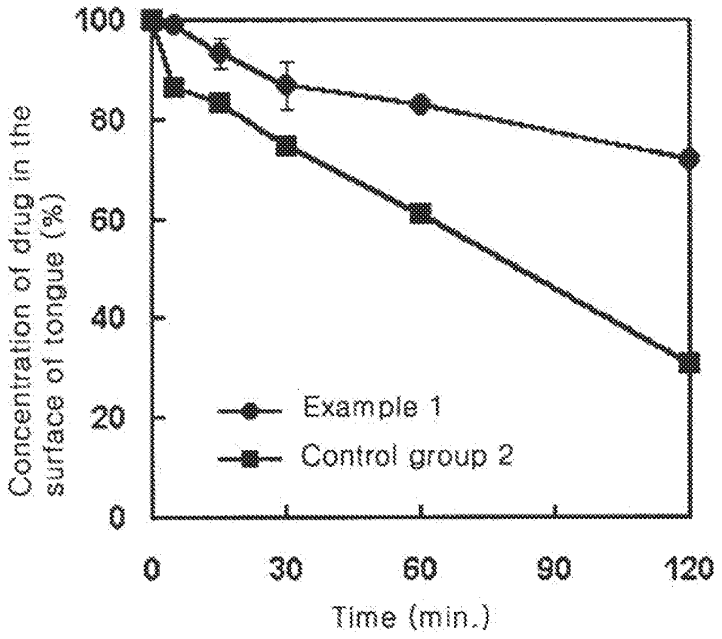


FIG. 2



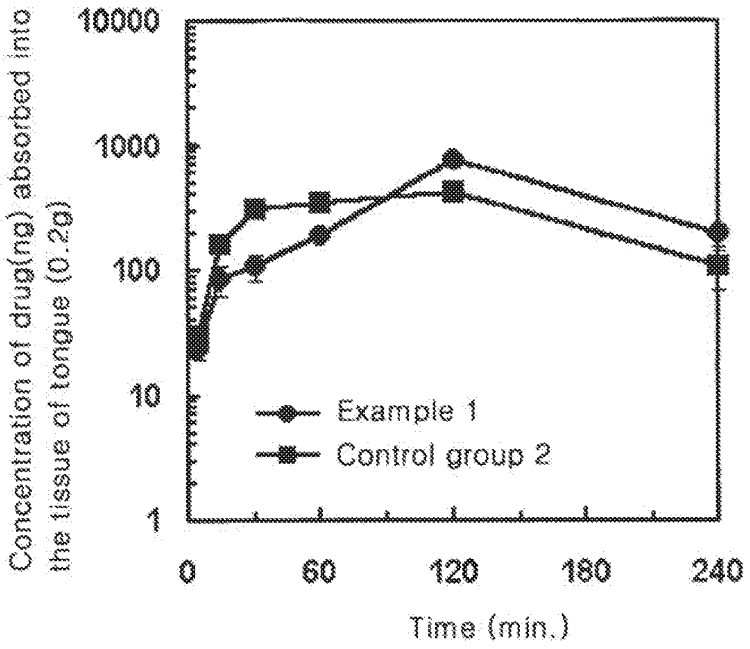
SAMSUNG EX. 1002 - 2233/4148

FIG. 3



SAMSUNG EX. 1002 - 2234/4148

FIG. 4



SAMSUNG EX. 1002 - 2235/4148

INTERNATIONAL SEARCH REPORT

International application No.
PCT/KR03/00084

A. CLASSIFICATION OF SUBJECT MATTER

IPC7 A61K 47/30

According to International Patent Classification (IPC) or to both national classification and IPC

B. FIELDS SEARCHED

Minimum documentation searched (classification system followed by classification symbols)
IPC:A61K

Documentation searched other than minimum documentation to the extent that such documents are included in the fields searched
Korean patents and applications for inventions since 1975

Electronic data base consulted during the international search (name of data base and, where practicable, search terms used)
CAPLUS(STN), SCISEARCH(STN), PASCAL(STN), IFA(STN), BIOTECHNO(STN), PROMT(STN)

C. DOCUMENTS CONSIDERED TO BE RELEVANT

Category*	Citation of document, with indication, where appropriate, of the relevant passages	Relevant to claim No.
A	WO 01/70224 A2 (PIERRE FABRE MEDICAMENT) 27 SEP 2001 see the whole document	1-6
A	"Mucoadhesive and physicochemical characterization of carbopol-poloxamer gels containing triamcinolone acetonide", Drug Development and Industrial Pharmacy, USA, 2000, Vol.26, No.3, pp.307-312	1-6
A	"Poloxamer/poly(acrylic acid) interpolymer complex for transmucosal drug delivery", Proceedings of the International Symposium on Controlled Release of Bioactive Materials, USA, 1998, 25th, pp.800-801	1-6
A	US 6177096 B1 (LTS Lohmann Therapie-systems GmbH) 23 JAN 2001 see the whole document	1-6
A	US 5,047,244 (Watson Laboratories, Inc.,) 10 SEP 1991 see the whole document	1-6

☐ Further documents are listed in the continuation of Box C. ☒ See patent family annex.

* Special categories of cited documents:
"A" document defining the general state of the art which is not considered to be of particular relevance
"E" earlier application or patent but published on or after the international filing date
"L" document which may throw doubts on priority claim(s) or which is cited to establish the publication date of citation or other special reason (as specified)
"O" document referring to an oral disclosure, use, exhibition or other means
"P" document published prior to the international filing date but later than the priority date claimed
"T" later document published after the international filing date or priority date and not in conflict with the application but cited to understand the principle or theory underlying the invention
"X" document of particular relevance; the claimed invention cannot be considered novel or cannot be considered to involve an inventive step when the document is taken alone
"Y" document of particular relevance; the claimed invention cannot be considered to involve an inventive step when the document is combined with one or more other such documents,such combination being obvious to a person skilled in the art
"&" document member of the same patent family

Date of the actual completion of the international search	Date of mailing of the international search report
31 MARCH 2003 (31.03.2003)	31 MARCH 2003 (31.03.2003)

Name and mailing address of the ISA/KR	Authorized officer
Korean Intellectual Property Office 920 Dunsan-dong, Seo-gu, Daejeon 302-701, Republic of Korea Facsimile No. 82-42-472-7140	CHANG, Jin Ah Telephone No. 82-42-481-5602

Form PCT/ISA/210 (second sheet) (July 1998)

INTERNATIONAL SEARCH REPORT

Information on patent family members

International application No.
PCT/KR03/00084

Patent document cited in search report	Publication date	Patent family member(s)	Publication date
WO 0170224 A2	27.09.2001	FR 2806625 B1	30.08.2002
		FR 2806625 A1	28.09.2001
		AU 0146622 A5	03.10.2001
US 6177096 B1	23.01.2001	WO 9820862 A1	22.05.1998
		KR 0053184 A	25.08.2000
		JP 1504106 T2	27.03.2001
		EP 936905 A1	25.08.1999
		AU 4868297 A1	03.06.1998
		AU 0739698 B2	18.10.2001
US 5047244 A	10.09.1991	None	

SIONYX1403000023.0079

SAMSUNG EX. 1002 - 2237/4148

(12) INTERNATIONAL APPLICATION PUBLISHED UNDER THE PATENT COOPERATION TREATY (PCT)

(19) World Intellectual Property Organization
International Bureau

(43) International Publication Date
17 August 2006 (17.08.2006)

PCT

(10) International Publication Number
WO 2006/086014 A2

(51) International Patent Classification:
H01L 31/0236 (2006.01) *H01L 31/18* (2006.01)

(21) International Application Number:
PCT/US2005/034180

(22) International Filing Date:
23 September 2005 (23.09.2005)

(25) Filing Language: English

(26) Publication Language: English

(30) Priority Data:
10/950,230 24 September 2004 (24.09.2004) US
10/950,248 24 September 2004 (24.09.2004) US

(71) Applicant *(for all designated States except US)*: **PRESIDENT AND FELLOWS OF HARVARD COLLEGE** [US/US]; 17 Quincy Street, Cambridge, MA (US).

(72) Inventors; and
(75) Inventors/Applicants *(for US only)*: **MAZUR, Eric** [NL/US]; 57 Lowell Road, Concord, MA 01742 (US). **CAREY, James, Edward, III** [US/US]; 8 Brock Street, Apt. 1, Brighton, MA 02135 (US).

(74) Agents: **ENGELLENNER, Thomas J.** et al.; Nutter McClennen & Fish LLP, World Trade Center West, 155 Seaport Boulevard, Boston, MA 02210-2604 (US).

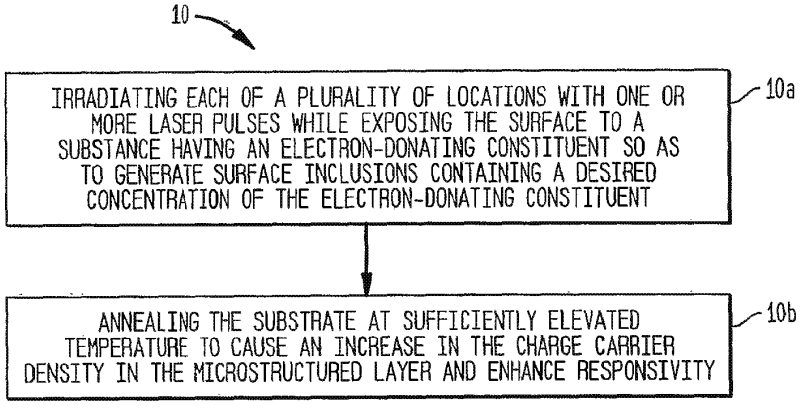
(81) Designated States *(unless otherwise indicated, for every kind of national protection available)*: AE, AG, AL, AM, AT, AU, AZ, BA, BB, BG, BR, BW, BY, BZ, CA, CH, CN, CO, CR, CU, CZ, DE, DK, DM, DZ, EC, EE, EG, ES, FI, GB, GD, GE, GH, GM, HR, HU, ID, IL, IN, IS, JP, KE, KG, KM, KP, KR, KZ, LC, LK, LR, LS, LT, LU, LV, LY, MA, MD, MG, MK, MN, MW, MX, MZ, NA, NG, NI, NO, NZ, OM, PG, PH, PL, PT, RO, RU, SC, SD, SE, SG, SK, SL, SM, SY, TJ, TM, TN, TR, TT, TZ, UA, UG, US, UZ, VC, VN, YU, ZA, ZM, ZW.

(84) Designated States *(unless otherwise indicated, for every kind of regional protection available)*: ARIPO (BW, GH, GM, KE, LS, MW, MZ, NA, SD, SL, SZ, TZ, UG, ZM, ZW), Eurasian (AM, AZ, BY, KG, KZ, MD, RU, TJ, TM), European (AT, BE, BG, CH, CY, CZ, DE, DK, EE, ES, FI, FR, GB, GR, HU, IE, IS, IT, LT, LU, LV, MC, NL, PL, PT, RO, SE, SI, SK, TR), OAPI (BF, BJ, CF, CG, CI, CM, GA, GN, GQ, GW, ML, MR, NE, SN, TD, TG).

Published:
— *without international search report and to be republished upon receipt of that report*

[Continued on next page]

(54) Title: MANUFACTURE OF SILICON-BASED DEVICES HAVING DISORDERED SULFUR-DOPED SURFACE LAYERS



(57) Abstract: The present invention provides methods of fabricating a radiation-absorbing semiconductor wafer by irradiating at least one surface location of a silicon substrate, e.g., an n-doped crystalline silicon, by a plurality of temporally short laser pulses, e.g., femtosecond pulses, while exposing that location to a substance, e.g., SF_6, having an electron-donating constituent so as to generate a substantially disordered surface layer (i.e., a microstructure layer) that incorporates a concentration of that electron -donating constituent e.g., sulfur. The substrate is also annealed at an elevated temperature and for a duration selected to enhance the charge carrier density in the surface layer. For example, the substrate can be annealed at a temperature in a range of about 700 K to about 900 K.

WO 2006/086014 A2

SAMSUNG EX. 1002 - 2238/4148

For two-letter codes and other abbreviations, refer to the "Guidance Notes on Codes and Abbreviations" appearing at the beginning of each regular issue of the PCT Gazette.

MANUFACTURE OF SILICON-BASED DEVICES HAVING DISORDERED SULFUR-DOPED SURFACE LAYERS

Federally Sponsored Research

The invention was made with Government support under contract DE-FC36-016011051 awarded by Department of Energy (DOE). The Government has certain rights in the invention.

Related Applications

The present application is a continuation-in-part (CIP) of co-pending patent application entitled "Systems and Methods for Light Absorption and Field Emission Using Microstructured Silicon," filed on May 24, 2002, and having a Serial No. 10/155,429, which is herein incorporated by reference in its entirety.

Background of the Invention

The present invention relates generally to methods for fabricating radiation-absorbing semiconductor wafers, and more particularly, to methods for fabricating silicon wafers that can absorb radiation and exhibit diodic current-voltage characteristics.

Modern semiconductor circuits are predominantly based on silicon, which can be readily procured at a lower cost than any other semiconductor and can be easily oxidized. Further, a band gap of 1.05 eV renders silicon suitable for detection of visible light and conversion of sunlight into electricity. Silicon, however, has several shortcomings. For example, it is an indirect band-gap material, and hence it is a relatively poor light emitter. In addition, silicon is not particularly suitable for use in detecting radiation having long wavelengths, such as, infrared radiation employed for telecommunications. Although other semiconductor materials are available that can detect long wavelength radiation better than silicon, they are generally more costly and cannot be readily integrated in optoelectronic circuits that are primarily silicon-based.

Hence, there is a need for silicon-based semiconductor structures and wafers with enhanced radiation-absorbing properties, particularly in wavelengths beyond the band-gap of crystalline silicon. There is also a need for such wafers that can be utilized

SAMSUNG EX. 1002 - 2240/4148

in fabricating photodetectors that exhibit enhanced responsivity in detecting radiation over a wide wavelength range. Further, there is a need for methods of manufacturing such silicon-based wafers.

Summary of the Invention

In one aspect, the present invention provides a method of fabricating a radiation-absorbing semiconductor wafer by irradiating at least one surface location of a silicon substrate, e.g., a crystalline silicon, with a plurality of temporally short laser pulses while exposing that location to a substance having an electron-donating constituent so as to generate a substantially disordered surface layer that incorporates a desired concentration of the electron-donating constituent, e.g., a concentration in a range of about 0.5 atom percent to about 5 atom percent, or from about 0.5 atom percent to about 1 atom percent. The substrate is preferably annealed at an elevated temperature and for a duration selected to enhance charge carrier density, e.g., electron carrier density, in the disordered surface layer.

In a related aspect, an annealing temperature and duration can be selected to cause re-arrangement of atomic bonds in the surface layer so as to increase the concentration of free electrons in the surface layer. Further, the annealing temperature and duration can be selected to cause the surface layer to form a diode junction, e.g., a p-n junction, with the underlying silicon substrate. The term "diode junction" is known in the art and generally refers to a junction that can exhibit current rectification (e.g., a junction that exhibits drastically different conductivities in one bias direction relative to the other). Moreover, the annealing temperature and duration can be selected such that the annealed substrate would exhibit a responsivity in a range of about 1 Ampere/Watt (A/W) to about 200 A/W, or preferably in a range of about 10 A/W to about 200 A/W, upon exposure of the surface layer to visible radiation having wavelengths in a range of about 250 nm to about 1050 nm and application of a reverse bias in a range of about 0.1 V to about 15 V, or about 0.5 to about 15 V, to the substrate. Further, the annealing temperature and duration can be selected such that the annealed substrate will exhibit a responsivity in a range of about 0.1 Ampere/Watt (A/W) to about 100 A/W upon exposure of the surface layer to visible radiation having at least a wavelength in a range

SAMSUNG EX. 1002 - 2241/4148

of about 1050 nm to about 3500 nm and application of a reverse bias in a range of about 0.1 V to about 15 V to the substrate.

In a related aspect, the laser pulses irradiating the substrate's surface have pulse widths in a range of about a few nanoseconds to about 10 femtoseconds, and more preferably in a range of about 50 to about 500 femtoseconds. The laser pulse fluences can range from about 1 kJ/m^2 to about 30 kJ/m^2, or from about 3 kJ/m^2 to about 15 kJ/m^2, or from about 3 to about 8 kJ/m^2. The annealing temperature can be in a range of about 500 K to about 1100 K, preferably in a range of about 500 K to about 900 K, and more preferably in a range of about 700 K to about 900 K, and the annealing duration can be from about a few seconds to about a few hours.

In another aspect, the substance containing an electron-donating constituent can be a gas, a fluid or a solid. Some examples of such substances include, without limitation, SF_6, H_2S, Cl_2, and N_2. For example, when SF_6 is utilized, the exposure of the silicon surface to the laser pulses generates sulfur inclusions in a surface layer of the substrate. The silicon substrate is preferably n-doped, but it can also be p-doped. The substrate's bulk doping level can be in a range of about 10^{11} to about 10^{18} cm^{-3}.

In another aspect, the present invention provides a method of fabricating a radiation-absorbing semiconductor structure that calls for irradiating each of a plurality of locations on a surface of a silicon substrate with one or more femtosecond laser pulses while exposing the surface to a sulfur-containing substance so as to generate a plurality of sulfur inclusions in a surface layer of the substrate. The substrate is annealed at a temperature in a range of about 500 K to about 1100 K for a time duration in a range of about a few seconds to about a few hours. The annealing step can be performed subsequent to, or simultaneously, with irradiation of the substrate's surface with laser pulses. Further, the annealing step can be performed in an inert atmosphere or in vacuum (i.e., a low-pressure atmosphere).

In a related aspect, the light emitted in each laser pulse can have a narrow spectrum and a central wavelength in a range of about 200 nm to about 1200 nm (e.g., 800 nm or 1064 nm), fluences in a range of about 1 kJ/m^2 to about 30 kJ/m^2, and more preferably in a range of about 1 kJ/m^2 to about 10 kJ/m^2 ,and a repetition rate in a range of about 1 kHz to about 50 MHz, or in a range of about 1 kHz to about 1 MHz.

In another aspect, the invention provides a method of fabricating a semiconductor wafer by irradiating a plurality of locations on a surface of a silicon substrate with one or more laser pulses having pulse widths in a range of about 50 to about 500 femtoseconds while exposing the surface to a substance having an electron-donating constituent so as to generate a microstructured surface comprising inclusions that incorporate the electron-donating constituent. The laser pulses can be directed at the substrate in a direction forming a selected angle relative to the substrate's surface, e.g., normal to the surface. The substrate is annealed at an elevated temperature in range of about 500 K to about 1100 K for a selected time duration, e.g., in a range of about a few seconds to about a few hours. In certain applications, the annealing temperature can be between about 500 K and 1000 K, and more preferably between 575 K and 875 K.

In another aspect, the invention provides a method of fabricating a semiconductor wafer by irradiating at least one location on a surface of a silicon substrate with temporally short laser pulses, e.g., femtosecond pulses, while exposing the surface to a substance having an electron-donating constituent so as to generate a microstructured surface layer having inclusions containing the electron-donating constituent. The substrate can be annealed, either following the laser irradiation or simultaneous therewith, at a temperature and for a duration selected to enhance the responsivity of the microstructured substrate to electromagnetic radiation having at least one wavelength in a range of about 250 nm to about 1100 nm by a factor of about 10, or preferably about 20, or more preferably about 100, relative to a similarly microstructed substrate but without annealing. The responsivity can be measured upon application of a reverse bias voltage in a range of about 0.5 V to about 15 V to the substrate. A suitable annealing temperature for effecting such enhancement of the wafer's responsivity lies in a range of about 600 K to about 900 K, and more preferably in a range of about 700 K to about 900 K, and a suitable annealing duration lies in a range of about a few seconds to about a few hours.

In another aspect, the present invention provides a photodetector that includes a silicon substrate having a surface layer, configured for exposure to external radiation, that is doped with sulfur inclusions with an average concentration in a range of about 0.5 atom percent to about 5 atom percent so as to exhibit a diodic current-voltage characteristic. The photodetector further includes a plurality of electric contacts, e.g., in

the form of metallic coatings, that are disposed on selected portions of the substrate for applying a selected reverse bias voltage, e.g., in a range of about 0.1 to about 15 volts, to the surface layer for facilitating generation of an electrical signal, e.g., a photocurrent, in response to exposure of the surface layer to electromagnetic radiation. The surface layer is configured such that an electrical signal in response to an incident radiation having at least a wavelength in a range of about 250 nm to about 1050 nm can be generated at a responisivity greater than about 1 A/W. Preferably, the responsivity over the entire range of about 250 nm to about 1050 nm is greater than about 1 A/W. For example, the responsivity to at least one wavelength in this wavelength span, and preferably to all wavelengths in this span, can be in a range of about 1 A/W to about 100 A/W, or in a range of about 10 A/W to about 100 A/W, or in a range of about 10 A/W to about 200 A/W.

In another aspect, the photodetector can exhibit an average responsivity (i.e., responsivity averaged over a wavelength range) to wavelengths in a range of about 250 nm to about 1050 nm that is greater than about 1 A/W, e.g., an average responsivity in a range of about 1 A/W to about 100 A/W, or an average responsivity in a range of about 10 A/W to about 200 A/W.

In another aspect, the photodetector can exhibit a responsivity greater than about 1 A/W (e.g., in a range of about 1 A/W to about 100 A/W) for wavelengths in a range of about 250 nm to about 600 nm, as well as in a range of about 600 nm to about 1050 nm. In a related aspect, the photodetector can exhibit a responsivity greater than about 0.1 A/W for incident radiation having at least one wavelength in a range of about 1050 nm to about 2000 nm, and preferably in a range of about 1050 nm to about 3500 nm. Preferably, the photodetector's responsivity to all wavelengths in this range (about 1050 nm to about 3500 nm) is greater than about 0.1 A/W. For example, the detector's responsivity in this wavelength span can be in a range of about 0.1 A/W to about 100 A/W.

In another aspect, the photodetector can exhibit an average responsivity greater than about 0.1 A/W (e.g., a responsivity in a range of about 0.1 A/W to about 100 A/W) for radiation having wavelengths in a range of about 1050 nm to about 2000 nm, and preferably in a range of about 1050 nm to about 3500 nm.

SAMSUNG EX. 1002 - 2244/4148

Photodetectors according to the teachings of the invention, such as those described above, provide a marked improvement over conventional silicon photodiodes where responsivities greater than 1 A/W for wavelengths in a range of about 250 nm to about 1050 nm are unknown. Further, responsivities of conventional silicon photodiodes degrade drastically for wavelengths beyond 1050 nm, and are significantly less than those that can be achieved by photodetectors of the present invention.

In another aspect, the surface layer can have a thickness in a range of about 10 nanometers to about 1 micron, and a microstructured morphology. For example, the microstructured layer can be formed by a plurality of conical microstructures, each of which can be composed of a core silicon portion forming a junction with a surface portion that is doped with sulfur. A term "conical structure or microstructure" as used herein refers to a generally cone-like or columnar protrusion above the silicon surface that can have vertical walls, or slanted walls that taper in the vertical direction. The microstructures can have a height in a range of about 0.5 micron to about 30 microns protruding from a base portion on the surface of the silicon substrate to a tip portion having a radius of curvature of about a few hundred nanometers. The gradient of sulfur concentration across the junction is substantially abrupt, although in some cases it can be gradual with the core portion having some sulfur dopants. The sulfur-doped surface layer can comprise silicon nanocrystals having diameters in a range of about 10 about 50 nanometers.

In another aspect, the invention provides a photodetector that includes a silicon substrate having a microstructured layer incorporating inclusions containing an electron-donating constituent. The microstructured layer is adjacent an underlying bulk silicon portion and forms a diode junction therewith. The term "diode junction" is known in the art and generally refers to a junction that can exhibit current rectification (e.g., a junction that exhibits drastically different conductivities in one bias direction relative to the other). A well-known example of a diode junction is a p-n junction. An electrical contact is disposed on a surface portion of the microstructured layer such that at least another surface portion of that layer remains available for receiving incident electromagnetic radiation. The photodetector can further include another electrical contact disposed on a surface of the bulk silicon portion opposed to the microstructured layer. The electrical contact layers allow application of a reverse bias voltage to the

SAMSUNG EX. 1002 - 2245/4148

substrate to facilitate generation of an electrical signal, e.g., a photocurrent, in response to exposure of the microstructured layer to incident radiation having wavelengths in range of about 250 nm to about 1050 nm at a responsivity in a range of about 1 A/W to about 200 A/W.

In a related aspect, the substrate can generate a photocurrent in response to irradiation of the microstructured layer with radiation having wavelengths in a range of about 1050 nm to about 3500 nm at a responsivity in a range of about 0.1 A/W to about 100 A/W.

In another aspect, the electron-donating constituent can be, for example, sulfur, chlorine or nitrogen, and can be present in the microstructured layer at a concentration in a range of about 0.5 to about 5 atom percent, or in a range of about 0.5 to about 1.5 atom percent, or in a range of about 0.5 to about 1 atom percent.

In another aspect, the present invention provides a photodetector for use in the visible and the infrared regions of the electromagnetic spectrum that includes a crystalline silicon substrate having a microstructured surface layer characterized by a plurality of substantially conical microstructures. The microstructured layer includes a doped layer having a plurality of silicon nanocrystals that contain an electron-donating dopant, such as sulfur, chlorine or nitrogen, with an average concentration in a range of about 0.5 to about 1.5 atom percent. The microstructured layer exhibits a diodic current-voltage curve and is configured to receive an external radiation. A plurality of electrical contacts are disposed on selected portions of the substrate for applying a reverse bias voltage to the microstructured layer in order to facilitate generation of an electrical signal in response to irradiation of at least a portion of that layer. The photodetector exhibits a responsivity greater that about 1 amperes/watt (A/W) for radiation wavelengths in a range of about 250 nm to about 1050 nm and a responsivity greater than about 0.1 amperes/watt for radiation wavelengths in a range of about 1050 nm to about 3500 nm.

Further understanding of the invention can be obtained by reference to the following detailed description in conjunction with the associated drawings, which are briefly described below.

Brief Description of the Drawings

FIGURE 1 is a flow chart depicting various steps in an exemplary embodiment for generating a microstructured silicon wafer suitable for absorbing radiation,

FIGURE 2 is a schematic diagram of an exemplary apparatus for microstructuring silicon wafers in accordance with one aspect of the invention,

FIGURE 3 is a scanning electron micrograph of a silicon surface, obtained at a 45-degree angle relative to the surface, after irradiation of the surface with 100 fsec pulses having a central wavelength of 800 nm and a fluence of about 5 kJ/m^2,

FIGURE 4 schematically illustrates an experimental set-up for performing resistivity and Hall effect measurements on a silicon sample microstructured in accordance with the teachings of the invention,

FIGURE 5 presents a plurality of graphs depicting wavelength absorptance of prototype microstructured silicon wafers as a function of an average number of 100 laser shots (8 kJ/m^2) per location employed for microstructuring the wafers in the presence of SF_6,

FIGURE 6 presents a plurality of graphs depicting wavelength dependence of absorptance of a plurality of prototype silicon wafers annealed at different temperatures subsequent to their microstructuring by a plurality of femtosecond laser pulses (the room temperature (300 K) data corresponds to a wafer that was not annealed),

FIGURE 7 presents graphs depicting wavelength dependence of absorptance for exemplary femtosecond-laser-formed and nanosecond-laser-formed microstuctured silicon wafers, before and after thermal annealing at 875 K for about 30 minutes (the absorptance of an unstructured silicon substrate as a function of wavelength is also shown for comparative purposes),

SAMSUNG EX. 1002 - 2247/4148

FIGURE 8A presents graphs depicting absorptance as a function of wavelength for a plurality of prototype silicon wafers microstructured by exposure to 500 laser shots of femtosecond pulses (fluence of 8 kJ/m^2) in the presence of different gases in the absence of annealing (the graph designated vacuum relates to wafer microstructured in a vacuum chamber at a base pressure less than about 10^{-6} bar),

FIGURE 8B presents absorptance data as a function of wavelength for a plurality of prototype silicon wafers microstructured by exposure to 500 shots of 100 femtosecond laser pulses (fluence of 8 kJ/m^2 in the presence of sulfur-bearing and non-sulfur-bearing gases) indicating the positive effects of sulfur incorporation in enhancing below band-gap absorptance,

FIGURE 9 presents graphs depicting wavelength dependence of absorptance for a plurality of prototype silicon wafers microstructured by femtosecond laser pulses in the presence of SF_6 at different partial pressures,

FIGURE 10 schematically illustrates a p-n junction in thermal equilibrium,

FIGURE 11A is a perspective view of a photodetector formed in accordance with one embodiment of the invention,

FIGURE 11B is a side view of the photodetector depicted in FIGURE 11A,

FIGURE 12 presents graphs depicting current-voltage characteristics of a plurality of exemplary silicon wafer microstructured by exposure to femtosecond laser pulses in the absence of annealing as well as in the presence of annealing at different annealing temperatures,

SAMSUNG EX. 1002 - 2248/4148

FIGURE 13 presents graphs depicting responsivity of a plurality of silicon wafers microstructured by exposure to femtosecond laser pulses in the presence of SF_6 (with no annealing and with annealing at different temperatures) as a function of wavelength in comparison with that of a commercial photodiode illustrating that a significantly enhanced responsivity can be obtained by judicious annealing of wafers subjected to laser microstructuring,

FIGURE 14 present graphs depicting current-voltage characteristics of a plurality of exemplary prototype silicon wafers microstructured by femtosecond laser pulses at different laser fluences and each annealed at 825 K,

FIGURE 15A presents comparative responsivity measurements for prototype silicon wafers microstructured by femtosecond laser pulses at different fluences and each annealed at 825 K for about 30 minutes,

FIGURE 15B presents comparative responsivity measurements for prototype silicon wafers microstructured by femtosecond laser pulses at different fluences and each annealed at 1075 K for about 30 minutes,

FIGURE 16A presents current-voltage characteristics for n-doped and p-doped silicon substrates microstructured by exposure to femtosecond laser pulses at a fluence of 6 kJ/m^2 followed by annealing at 825 K for about 30 minutes,

FIGURE 16B presents current-voltage characteristics for n-doped and p-doped silicon substrates microstructured by exposure to femtosecond laser pluses at a fluence of 4 kJ/m^2 followed by annealing at 1075 K for about 30 minutes,

FIGURE 17A presents responsivity measurements for prototype exemplary n-doped and p-doped silicon substrates microstructured at two different laser fluences (4 kJ/m^2 and 6 kJ/m^2) and annealed at 825 K for about 30 minutes,

SAMSUNG EX. 1002 - 2249/4148

FIGURE 17B presents responsivity measurements for prototype exemplary n-doped and p-doped silicon substrates microstructured by femtosecond laser pulses at a fluence of 4 kJ/m^2 and annealed at 1075 K for about 30 minutes,

FIGURE 18 presents a graph depicting responsivity as a function of back bias for an n-doped silicon substrate microstructured via irradiation by femtosecond laser pulses at a fluence of 4 kJ/m^2 and annealed at 825 K for about 30 minutes (the measurement was performed by employing a white light source with an approximate power of 50 microwatts),

FIGURE 19A presents graphs depicting current-voltage characteristics of an n-doped silicon sample microstructuured by femtosecond laser pulses at a fluence of 4 kJ/m^2 and annealed at 825 K as a function of operating temperature,

FIGURE 19B presents a graph depicting the responsivity of a microstructured silicon wafer to incident radiation having a wavelength of 1064 nm as a function of operating temperature,

FIGURE 20 illustrates current-voltage characteristics for a high resistivity (resistivity greater than 1 Ohm-m) microstructured silicon wafer that can be utilized as a solar cell, with and without one sun illumination,

FIGURE 21 illustrates current-voltage characteristics for a low resistivity (e.g., a resistivity in a range of about 0.01 to about 0.1 Ohm-m) microstructured silicon wafer that can be utilized as solar, with and without one sun illumination,

FIGURE 22 schematically depicts an exemplary experimental set-up for measuring field emission of a silicon substrate microstructured in accordance with the teachings of the invention, and

FIGURE 23 shows a graph depicting field emission current generated by a silicon wafer microstructured by exposure to femtosecond laser pulses in the presence of SF_6 as a function of a potential difference applied thereto.

Detailed Description

With reference to a flow chart 10 of FIGURE 1, in one aspect, the present invention provides a method of fabricating a radiation-absorbing semiconductor structure in which, in an initial step 10a, each of a plurality of locations on a surface of a silicon substrate is irradiated with one or more laser pulses while exposing the surface to a substance having an electron-donating constituent so as to generate surface inclusions containing a concentration of the electron-donating constituent. The laser pulses can have a central wavelength in a range of about 200 nm to about 1200 nm, and a pulse width in a range of about tens of femtoseconds to about hundreds of nanometers. Preferably, the laser pulse widths are in a range of about 50 femtoseconds to about 50 picoseconds. More preferably, the laser pulse widths are in the range of about 50 to 500 femtoseconds. The number of laser pulses irradiating the silicon surface can be in a range of about 2 to about 2000, and more preferably, in a range of about 20 to about 500. Further, the repetition rate of the pulses can be selected to be in a range of about 1 kHz to about 50 MHz, or in a range of about 1 kHz to about 1 MHz. Moreover, the fluence of each laser pulse can be in a range of about 1 kJ/m^2 to about 12 kJ/m^2, and more preferably in a range of about 3 kJ/m^2 to about 8 kJ/m^2.

While in some embodiments, the electron donating constituent is a fluid (gas or liquid), in other embodiments it can be a solid deposited over the silicon surface exposed to laser pulses. By way of example, in some embodiments, the silicon surface can be exposed to a sulfur-containing gas (e.g., SF_6 or H_2S) while irradiated with the laser pulses. In some other embodiments, Cl_2 or N_2 is employed as the electron-donating substance with which the silicon surface is in contact during laser irradiation. In yet other embodiments, selenium or tellurium can be employed. Without any loss of generality, in the following discussion, it is assumed that SF_6 is employed as the substance containing an electron-donating constituent, and that the irradiating pulses have femtosecond pulse widths, unless otherwise indicated. However, it should be clear to those having ordinary skill in the art that various embodiments of the invention

described below can also be practiced with other fluids or solids and laser pulses having other pulse widths, such as those listed above.

In some embodiments, the silicon substrate is p-doped (e.g., doped with Boron) with a doping level in a range of about 10^{11} to about 10^{18}. In other embodiments, the silicon substrate is slightly n-doped (e.g., doped with Phosphorus) with a doping level in a range of about 10^{11} to about 10^{18}, and preferably in a range of about 10^{12} to about 10^{15}. The substrate thickness is not typically a critical parameter, and can be in a range of about 2 microns to about 1000 microns. The substrate can have an electrical resistivity in a range of about 0.001 ohm-m to about 10 ohm-m.

FIGURE 2 schematically depicts an exemplary apparatus 12 that can be utilized for irradiating a silicon sample with a plurality of femtosecond pulses. The apparatus 12 includes a sample processing chamber 14 that comprises a stainless steel cube 16 with Conflat flange connections on each of its six sides. A three-axis, precision motion controller 18 is attached to the back side of the cube. This controller contains two orthogonal micrometer precision axes driven by computer controlled motors. The third axis is hand-controlled with about 1 mil precision. The controller can translate a one-inch diameter stainless steel rod 20 that supports a 2-inch diameter mounting magnet 22 in the center of the cube to which a magnetizable sample holder can be mounted. A two-stage roughing pump 24 is coupled to the cube to evacuate the chamber to a base pressure of approximately 10^{-3} torr. Two pressure gauges 26 and 28 are employed to monitor the chamber's pressure. A leak valve 30 and a gas-handling manifold (not shown) allow introduction of gases of interest into the chamber. An optical grade, 4.5 inch quartz window 32 is attached to the front of the chamber for providing laser access. Further, a quick-access viewport door 34 allows rapid loading and removal of samples as well as safe viewing of the sample during microstructuring.

In this exemplary apparatus, a regeneratively amplified, femtosecond Ti:Sapphire laser system (not shown) provides approximately 100 fs laser pulses having a central wavelength of 800 nm at a repetition rate of 1 kHz. The laser pulses are focused by a anti-reflection coated, plano-convex lens 36 (e.g., having a focal length of about 250-nm) through the quartz window onto the sample surface. In this exemplary embodiment, the lens is mounted on a single axis linear translation stage and positioned such that its focal point is behind the sample. By moving the lens, and hence its focal

point, the laser spot size can be varied at the sample surface (e.g., from a diameter of about 30 microns to 250 microns). In order to measure the laser spot size, a CCD (charge coupled device) camera 38 can be placed at the same distance as the sample surface from the lens. A flipper mounted mirror 40 can redirect the laser beam onto the camera to determine its spot size on the sample surface. A second CCD camera 42 can measure reflections of light generated by a white light fiber lamp 44 from the sample surface to monitor progress during microstructuring.

In one exemplary mode of operation, samples attached to a magnetizable sample holder can be loaded through the access door and attached to the mounting magnet. Samples can be then positioned in the center of the magnet to allow for maximum translation. The chamber can be evacuated to a base pressure of 10^{-3} torr and then filled to the desired pressure with an ambient gas (e.g., 0.67 bar of sulfur hexafluoride). The sample can then be irradiated with a 1-kHz train of 100-femtosecond 800-nm laser pulses. The fluence of each pulse can be set by selecting a spot size (e.g., 150 microns) and employing a waveplate/polarizing cube combination to vary the pulse energy. Either a single spot can be irradiated, or more typically the sample can be translated by utilizing the motion controller relative to the laser beam. For example, the sample can be translated in a raster scan pattern. An average number of pulses irradiating a given spot on the sample can be controlled by utilizing a shutter and varying the horizontal translation speed.

The irradiation of the silicon surface with the laser pulses in the presence of SF_6 at a selected partial pressure, for example, a partial pressure in a range of about 0.005 bar to about 1 bar, can cause formation of a sulfur-rich layer having a sulfur concentration in a range of about 0.1 atom percent to about 5 atom percent, and more preferably, in a range of about 0.5 atom percent to about 1 atom percent. This sulfur-rich layer exhibits an undulating surface morphology (topography) with micron-sized surface height variations. Such a textured surface obtained by irradiating a silicon surface with a plurality of temporally short laser pulses in the presence SF_6 (or other substances having an electron-donating constituent) is herein referred to as a micro-structured surface. By way of example, FIGURE 3 shows a scanning electron micrograph (SEM) of a such a micro-structured silicon surface (obtained in a direction forming a 45 degree angle relative to the surface) after irradiation of the silicon surface

with an average of 5 shots of femtosecond laser pluses (100 femtoseconds) at a wavelength of 800 nm and having a fluence of 8 kJ/m2 in 0.67 bar of SF_6.

The sulfur-rich layer can be a substantially disordered layer that is several hundred nanometers thick and made up of nanocrystallites (e.g., about 10 – 50 nm in diameter) and nanopores. Selected area diffraction (SAD) measurements indicate that the surface layer retains a substantial crystalline order with a strong possibility that amorphous-like material is present between the nanocrystalline grains. Further, SAD measurements performed on silicon substrates exposed to either 10 or 500 pulses per location indicate that the substrate below the disordered layer comprises substantially undisturbed crystalline silicon (when a crystalline silicon substrate is utilized). Further, Rutherford backscattering spectroscopy (RBS) and energy dispersive X-ray (EDX) emission spectroscopy performed on such exemplary substrates show a large concentration of sulfur is present in the disordered layer (about 1 atom percent). Further, RBS spectra obtained from silicon samples exposed to different femtosecond (100 femtoseconds) laser shots per irradiation location show that the concentration of sulfur increases with increasing laser pulse numbers up to about 50 pulses. In particular, the measured sulfur concentration increases from about 0.2 atom percent for a sample exposed to 2 pulses per location to about 0.7 atom percent for a sample exposed to 50 laser pulses per location with the sulfur concentration exhibiting a plateau for laser pulses higher than about 50. It should be, however, understood that the above experimental results are provided simply for further elucidation of salient features of the invention, and not as limiting the scope of the invention. For example, higher sulfur concentrations in the disordered layer than those described above can also be obtained, and higher laser shots per location can be utilized.

A number of factors can affect the morphology of the microstructured surface. For example, samples microstructured by irradiating a portion thereof with laser pulses, without moving them relative to the laser beam (i.e., single spot irradiation), exhibit a subtle difference in their morphology relative to samples microstructured by irradiating a plurality of their surface locations via translation relative to the laser beam. With the rest of the experimental parameters left the same, there are two visible differences between translated and stationary samples. The microstructures in the stationary samples have a micrometer-sized sphere at the tip while the translated samples are

SAMSUNG EX. 1002 - 2254/4148

sharper and lack the spheres. Further, the translated samples have a larger amount of nanoscale particles spread across the microstructured surface.

In addition, the wavelength of the irradiating laser pulses, their fluence, and pulsewidths can also affect the morphology of the microstructured surface. For example, in a number of prototype samples microstructured by femtosecond pulses, with increasing the fluence (at constant shot number) the morphology showed a transition from laser-induced periodic surface structures, to a coarsened surface, to sharp microstructures, such as those depicted in the above FIGURE 3. As the laser pulse fluence increases, there is typically an increase in both the microstructure height and distance between the microstructures. In general, the fluence is preferably selected to be above a threshold fluence that would cause melting (e.g., 1.5 kJ/m^2). At very high fluences (e.g., greater than 12 kJ/m^2), material removal can become extreme and gaussian-shaped holes, rather than conical structures, can be formed in the surface.

Although in many embodiments described herein, femtosecond laser pulses are employed, in other embodiments, the microstructuring of the surface can also be achieved by employing picosecond or nanosecond pulses. For example, a number of silicon samples were microstructured by utilizing a train of 248-nm, 30-ns laser pulses with a flat-top spatial profile and a fluence of 30 kJ/m^2 generated by a KrF+ excimer laser in the presence of 1 bar of SF_6 (an average of 1500 pulses per spot were employed). The nanosecond-laser-formed microstructures showed some similarities and some differences relative to the femtosecond-laser-formed microstructures. In both cases, the microstructures were roughly conical, but the structures formed with the femtosecond laser pulses were smaller and more densely packed. For example, the femtosecond structures were roughly 8 microns tall and separated by about 4 microns while the nanosecond-formed structures were roughly 40 microns tall and separated by about 20 microns. Further, the femtosecond-formed structures were covered with nanoparticles 10 – 50 nm in diameter while the surface of the nanosecond-formed structures were much smoother.

Sample silicon wafers exposed to picosecond pulses (e.g., 10 picosecond) in the presence of SF_6 also showed a microstructured surface. The average separation between the microstructures exhibited a decrease from about 100 femtosecond pulse widths to

about 5 picosecond pulse widths but then showed an increase for pulse widths longer than about 5 picoseconds.

The laser wavelength can also affect the final morphology of the microstructures. By way of example, a prototype silicon sample microstructured with a train of 400 nm pulses exhibited a higher density of microstructures (but smaller) than those generated by 800 nm pulses at a similar fluence.

Other factors that can affect the microstructures' morphology include laser polarization and laser propagation direction relative to the irradiated silicon surface. For example, the direction of microstructure growth is parallel to the direction of incident light, and appears to be independent of the substrate's crystallographic planes. The base of microstructure can have an elliptical shape with the long axis perpendicular to the polarization of the irradiating laser light. Without being limited to any theory, this elliptical shape can be understood as being due to a higher absorption of p-polarized light relative to s-polarized light. For circularly polarized light, there is no preferential ablation, and the base of the microstructures can be substantially circular.

The fluid or solid in contact with the silicon surface during its microstructuring can also affect the resultant surface morphology. For example, utilizing SF_6 or Cl_2 as the ambient gas can lead to sharp-tipped conical structures with a radius of curvature of about 500 nm. In contrast, structures made in air, N_2 or vacuum are much more rounded (the radius of curvature of their tips is approximately 2 – 3 microns) than those made in these halogen-containing gases. In a number of exemplary samples microstructured in the presence of different gases, those made in SF_6 exhibited the greatest density of microstructures followed by those made in Cl_2. The microstruture densities produced in the presence of N_2 were approximately equal to those made in air, but approximately a factor of two less than the densities obtained by employing SF_6.

In some embodiments, the laser microstructuring of a silicon wafer is performed in the presence of a mixture of two or more substances. For example, samples microstructured in the presence of a mixture of SF_6 and Cl_2 exhibited an increase in the microstructure density at higher partial pressure of SF_6.

The sulfur-rich mircrostructured layer has unique optical and electrical properties. For example, it can exhibit a sheet charge carrier density in a range of about 10^{12} cm^{-2} to about 10^{14} cm^{-2}. By way of example and only for illustrative purposes, the

SAMSUNG EX. 1002 - 2256/4148

results of some resistivity and Hall effect measurements performed on a number of exemplary microstructured samples, each formed in an n-doped silicon substrate in accordance with the teachings of the invention, such as those described above, are presented below. For resistivity and Hall effect measurements, the van der Pauw technique, well-known to those having ordinary skill in the art, was employed. Briefly, four ohmic electrical contacts were formed on the disordered microstructured layer. The electrical contacts were formed by initially dipping a microstructured sample in a 5% HF solution for 5 minutes to remove any native oxide layer. Subsequently, with a mask covering all but the very corners of a selected microstructured surface area (e.g., a 10 x 10 mm^2 surface area), chromium/gold (Cr/gold) was evaporated onto the surface to form metal contacts at the exposed corners. A dicing saw was then used to cut slivers (e.g., 0.25 mm slivers) from each side. Cutting the sample edges ensures that the contacts are only connected to the surface layer and not the substrate layer. Finally, a wire bonder is utilized to connect the contacts on the corners of the sample to four Cr/Au contact pads evaporated onto a glass slide. It should be understood that this experimental arrangement, shown schematically in FIGURE 4, is sensitive primarily to the electronic properties of the microstructured layer, and not that of the substrate.

With continued reference to FIGURE 4, the resistivity measurements can be performed by applying a small DC current (e.g., 10 microamperers) from corner 2 to corner 1 while measuring a voltage from corner 3 to corner 4. Hall effect measurements can be performed by placing the sample in a strong magnetic field (e.g., a field of several thousand gauss) with the magnetic field perpendicular to the silicon surface. In one experiment, a small AC current (about 1-2 microamperes) was then applied from contact 1 to contact 3 while measuring an induced voltage across contacts 2 and 4. Control measurements were also performed on an n-doped (resistivity = 8 – 12 ohm-m) unstructured silicon wafer. Table 1 below lists the results of these measurements for microstructured layers formed in an n-doped silicon wafer having a resistivity in a range of about 8 – 12 ohm-m at a number of different laser pulse fluences.

Original doping	Average fluence (kJ/m^2)	Doping after structuring	Sheet resistance Rs (Ohm)	Sheet carrier density n_s (cm^{-2})	Hall mobility μ ($cm^2V^{-1}s^{-1}$)
n	unstructured	-	31931	$1.78x10^{11}$	1101
n	4.0	n	4865	$7.37x10^{12}$	174
n	6.0	n	4992	$7.15x10^{12}$	175
n	8.0	n	6253	$4.52x10^{12}$	221
n	10.0	n	4554	$8.83x10^{12}$	155

This data shows that microstructured layer exhibits a higher sheet carrier density than the original substrate, but a lower carrier mobility – presumably as a result of the disorder in the microstructured layer.

Referring again to the flow chart 10 of FIGURE 1, subsequent to irradiation of the silicon surface with a plurality of laser pulses (step 10a), the substrate can annealed (step 10b) at a sufficiently elevated temperature for a selected time duration so as to cause an increase in the charge carrier density in the microstructured layer, e.g., by a factor in a range of about 10 percent to about 200 percent. For example, the substrate can be annealed at a temperature in a range of about 500 K to about 1100 K, and more preferably, in a range of about 500 K to about 900 K, for a selected time duration, e.g., a time duration in a range of about a few minutes to about a few hours (e.g., one-half hour).

The annealing step can be performed by employing a variety of different techniques. For example, the substrate can be placed in a thermal oven to be exposed to an elevated temperature for a selected duration. Alternatively, the substrate can be exposed to laser radiation, e.g., radiation having a wavelength in a range of about 200 to about 1200 nm, to cause its heating to a desired temperature. Further, the annealing step can be performed, for example, in an inert atmosphere (e.g., an argon atmosphere) or in a vacuum (a low-pressure environment). Alternatively, the annealing step can be applied simultaneously with the irradiation step. That is, the irradiation of the silicon substrate with the laser pulses can be performed while the substrate is maintained at an elevated temperature.

SAMSUNG EX. 1002 - 2258/4148

Without being limited to any theory, the annealing step is designed to cause a rearrangement of the atomic bonds within the metastable microstructured layer to enhance the density of charge carriers – electrons – within that layer. The term "charge carrier density" is known to those having ordinary skill in the art. To the extent that any further explanation may be required, it refers to density of those charged particles, e.g., electrons, that are primarily responsible for current conduction, e.g., electrons in the conduction band states or in shallow impurity states below the conduction band. Such charged carriers are also herein referred to as free electrons or holes.

In other words, the annealing temperature and duration are selected to cause structural changes in the microstructured layer that result in increasing the carrier density in that layer while substantially maintaining responsivity of the layer for generating an electrical current when exposed to radiation within a selected wavelength range at a given applied back bias voltage, as discussed in more detail below. The structural changes caused in the microstructured sulfur-rich layer by an annealing step according to the teachings of the invention can be appreciated by considering that in many embodiments in which a p-doped silicon substrate is exposed to a plurality of laser pulses to generate a microstructured surface layer thercin, holes, rather than electrons, constitute the dominant charge carriers even after incorporation of about 1 atom percent sulfur having two possible donor electrons per atom. However, after annealing, electrons can constitute the dominant charge carriers in the microstructured layer. Without being limited to any particular theory, such observations suggest that sulfur in the microstructured layer, before annealing, is incorporated in silicon such that its donor electrons do not substantially contribute to conduction (the donor electrons are likely locked up in a trap, or perhaps the coordination number of the implanted sulfur is larger than four). An annealing step according to the teachings of the invention causes atomic bond rearrangements in the microstructured layer so as to free up donor electrons for contributing to electrical conduction. In fact, in case of p-doped silicon substrates, the number of donor electrons released during annealing can be sufficiently large to eliminate the holes as the dominant charge carriers and turn the microstructured layer into an n-doped layer having a sheet carrier concentration on the order of about 10^{14} cm^{-2}.

SAMSUNG EX. 1002 - 2259/4148

A microstructured silicon wafer formed in accordance with the teachings of the invention exhibits absorption of incident electromagnetic radiation, particularly radiation having wavelengths in a range of about 250 nm to about 2500 nm. By way of example, FIGURE 5 presents absorption data for a microstructured silicon wafer (an n-Si (111) wafer having a thickness of about 260 microns and a resistivity in a range of about 8 – 12 ohm-m), each of which was generated by exposing its surface to 100 femtosecond laser pulses (2 to 500 shots per location) having a central wavelength of 800 nm and a fluence of about 8 kJ/m^2. This exemplary absorption data was recorded in a manner known in the art, prior to annealing the wafer, by employing an spectrophotometer equipped with an integrating sphere. The absorption data for an unstructured silicon wafer is also provided for comparative purposes.

This exemplary data indicates that the microstructured wafers exhibit an enhanced absorption of incident electromagnetic radiation, relative to unstructured silicon, across the entire recorded wavelength range, and particularly for wavelengths above about 1050 nm, which corresponds to the band-gap energy of crystalline silicon (1.05 eV). In the unstructured silicon, light photons having wavelengths longer than a wavelength corresponding to the band-gap energy do not contain sufficient energy to promote an electron from the valence band to the conduction band, leading to a drastic drop in absorption.

In contrast, the silicon wafers microstructured in accordance with the teachings of the invention exhibit significant absorption not only for wavelengths below the band-gap but also for those above it. In fact, the exemplary data of FIGURE 5 shows that silicon wafers structured by exposure to 20 pulses per location or higher (e.g., 500 pulses in this exemplary data set) exhibit near-unity, featureless absorption of wavelengths from about 0.4 micron to about 1 micron, a small decrease in absorption for wavelengths around about 1.05 micron (a wavelength corresponding to the band edge of unstructured silicon), and strong featureless absorption from about 1.05 microns to about 2.5 microns. It should be understood that this data is presented only for illustrative purposes, and is not necessarily intended to present the optimal absorption of a silicon wafer structured in accordance with the teachings of the invention.

As noted above, in many embodiments of the invention, a microstructured wafer is annealed at a temperature and for a duration designed to enhance the charge carrier concentration in its microstructured layer. Such annealing can be performed at a variety of different temperatures. By way of example, FIGURE 6 schematically illustrates electromagnetic radiation absorptance data for a plurality of microstructured silicon wafers generated by utilizing 500 laser pulses per surface location (100 fs pulses at a central wavelength of 800 nm and a fluence of 8 kJ/m2) in the presence of 0.67 bar of SF_6 relative to that of unstructured silicon. Each structured wafer was annealed at a selected temperature in a range of about 575 K to about 875 K for about 30 minutes. This exemplary data shows that annealing at temperatures below about 575 K has little effect on the observed absorptance. On the other hand, such annealing performed at a temperature between about 575 K and 875 K does not substantially affect absorptance above the bandgap, but lowers the below band-gap absoptance – the higher the annealing temperature, the greater is the reduction in absorptance. It should, however, be understood that this data is only exemplary, and different results may be obtained for microstructured wafers generated by employing different parameters (e.g., difference fluence or laser shot numbers).

A microstructured silicon wafer according to the teachings of the invention can be generated not only by utilizing femtosecond pulses, but also other pulse widths (e.g., nanosecond and picosecond pulse widths). By way of example and only for illustrative purposes, FIGURE 7 illustrates exemplary absorptance graphs as a function of incident radiation wavelength for femtosecond-laser-formed and nanosecond-laser-formed microstructured silicon surfaces, before and after annealing at about 875 K for about 30 minutes, as well as that of an unstructured silicon wafer. The femtosecond-formed mircrostructures were generated by employing 100 fs laser pulses (500 shots per location) having a central wavelength of about 800 nm and a fluence of about 8 kJ/m^2. The nanosecond-formed microstructures were generated by employing 30 ns laser pulses (about 1500 shots per location) having a central wavelength of 248 nm and a fluence of about 30 kJ/m^2. It should be understood that this data is presented only for illustrative purposes and is not intended to necessarily indicate absorptance exhibited by a microstructured silicon formed in accordance with the teachings of the invention under all circumstances.

In some embodiments of the invention, microstructuring of a silicon wafer can be accomplished in the presence of a background fluid rather than SF_6. For example, H_2S, Cl_2, N_2 or air can be utilized. By way of example, FIGURE 8A and 8B compare absorptance of some exemplary prototype microstructured silicon wafers generated by employing femtosecond laser pulses (100 fs, 800 nm, 8 kJ/m^2 and 500 shots per location) in the presence of various fluids – without an annealing step – with that of unstructured silicon. The vacuum data corresponds to microstructuring the wafer in a chamber evacuated to a base pressure that is less than about 10^{-6} bar. While all microstructured samples exhibit an enhanced absorption relative to unstructured silicon, this exemplary data shows the microstructuring in SF_6 and H_2S brings about the most dramatic change in absorptance relative to unstructured silicon. In particular, samples structured with SF_6 exhibit near-unity, substantially featureless absorptance across the entire measured spectrum.

A variety of background fluid pressures can be employed in many embodiments of the invention for generating microstructured silicon wafers. By way of example, FIGURE 9 shows absorptance data for a number of exemplary prototype microstructured silicon wafers generated in SF_6 (100 fs pulses, 800 nm, 500 shots per location) at different ambient pressures, as well as a wafer microstructured in vacuum (e.g., a pressure of less than 10^{-6}). The greatest rate of increase is observed at low pressures. In this exemplary data set, at pressures above about 27 mbar, the below band-gap absorptance does not show much variation with wavelength, while at lower pressures, it decreases with increasing wavelength.

The microstructured silicon wafers generated in accordance with the teachings of the invention, particularly those subjected to an annealing step at an elevated temperature in a range of about 500 K to about 900 K, not only exhibit enhanced absorption of electromagnetic radiation over a wide range (e.g., from ultraviolet wavelengths to near infrared), but they also exhibit voltage-versus-current profiles that are characteristic of diodes. As discussed in more detail below, these properties allow the use of such microstructured silicon wafers in fabricating photodetectors that exhibit enhanced responsivity relative to conventional silicon photodetectors.

More specifically, a microstructured silicon layer formed in accordance with the teachings of the invention, particularly one formed by exposure of a wafer surface to laser pulses followed by, or simultaneous with, an annealing step designed to release electrons in the layer structured by the pulses, forms a diode junction, e.g., a p-n junction, with the underlying silicon substrate. It should be understood that a diode junction as used herein can also refer a junction formed between two n-doped portions having different free electron densities. As shown schematically in FIGURE 10, a p-n junction can be formed by bringing a semiconductor material having acceptor impurity atoms (p-doped) into contact with a semiconductor material having donor impurity atoms (n-doped). The difference in charge carrier concentration between the p-doped and the n-doped portions generates a diffusion potential across the junction – electrons and holes begin to diffuse across the junction to portions having a respective lower concentration. As they cross to the other side of the junction, they recombine with their oppositely charged electrical counterparts in a region very close to the junction. This migration of charge carries across the junction causes formation of space charges (immobile ions) with opposite polarities on the two sides of junction. As the number of space charges increases (positively charged for the n-type side and negatively changed for the p-type side), a potential difference builds up across the junction, which results in an electric field in a direction opposite that of the diffusion potential.

Upon reaching thermal equilibrium, a thin insulating layer is present near the junction in which charge carriers have been depleted by recombination (depletion region). A strong electric field is present in the depletion region and a large electric potential exists across this region. The junction can be reverse-biased by applying an electric field across it that reinforces this internal electric field. Such a reverse-bias voltage expands the insulating depletion region and enhances both the internal electric field and the potential difference across the junction. The junction can also be forward-biased by applying an electric field that is opposite to the internal field across it. Such a forward-bias voltage shrinks the depletion region, thereby diminishing the internal electric field and the potential difference across the junction. When forward-biased, a current flows across the junction with electrons injected into the n-doped portion and leaving from the p-doped portion. In other words, the p-n junction can act as a rectifier

by allowing current flow in only one direction. This behavior gives rise to a current-voltage (I-V) curve characteristic of a diode.

As discussed above, a silicon wafer in which a microstructured layer is formed according to the teachings of the invention can exhibit an I-V curve characteristic of that obtained by a diode junction. Without being limited to any theory, such a current-voltage behavior can be understood by considering that the wafer includes two adjacent, yet distinct, layers: a surface layer in which a concentration of an electron-donating constituent is incorporated and an underlying substantially undisturbed silicon substrate layer. These two layers exhibit different crystalline structures, chemical compositions, and charge carrier doping concentrations. In addition, the microstructured layer has unique optical properties including high absorptance of incident electromagnetic radiation from the near ultraviolet into the near-infrared wavelengths. In one aspect, the invention employs such microstructured silicon wafers for fabricating photodiodes, as discussed in more detail below.

By way of example, FIGURE 11A schematically illustrates a photodetector 46 according to one embodiment of the invention that includes a microstructured silicon wafer 48 having a microstructured surface layer 50 that is formed in a silicon substrate 51 by irradiating a plurality of locations on a substrate's surface with short laser pulses (e.g., pulse widths in a range of about tens of femtoseconds to tens of nanoseconds) while exposing the surface to a substance having an electron-donating consitutent (e.g., SF_6). The laser-irradiated wafer is then annealed under conditions (e.g., at an elevated temperature and for a selected duration) designed to enhance concentration of electrons in the microstructured surface layer (e.g., annealing at a temperature in a range of about 500 K to about 900 K for a duration of a few minutes to a few hours).

The exemplary photodetector 46, functioning as a photodiode, also includes a plurality of metallic electrical contacts 52, which have a finger grid geometry, that are disposed on the microstructured surface layer. In addition, an electrical contact 54, in the form of a metallic coating layer, is disposed on the back surface of the silicon substrate (i.e., the undisturbed silicon surface opposite the microstructured surface) that substantially covers the entire surface. In this exemplary embodiment, a chromium/gold alloy (Cr/Au) is employed for fabricating the electrical contact. However, those having

ordinary skill in the art will appreciate that the contacts can be formed of other metals, as well.

The metallic contacts 52 and 54 allow applying a bias voltage, e.g., a reverse bias voltage, across the wafer by employing, for example, a voltage source 56. The reverse bias voltage can reinforce the internal electrical field in the depletion layer of a diode junction formed between the microstructured layer 50 and the underlying silicon substrate 51. As discussed in detail below, the photodetector 46 can operate with small bias voltages, e.g., voltages in a range of about 0.1 V to about 15 V, with a responsivity (i.e., photocurrent generated per unit of power of incident light (amperes/watts)) that is considerably better than that typically exhibited by a conventional silicon photodetector. These attributes allow incorporating silicon photodetectors formed according to the teachings of the invention, such as the exemplary photodetector 46, into integrated silicon photo-electronic circuits as high sensitivity detectors.

In operation, radiation (i.e., photons) incident on the microstructured surface layer of the photodiode's silicon wafer is absorbed (when the radiation wavelength is in the operating range of the photodetector), e.g., by valence electrons, in the microstructured layer. The absorption of the incident radiation causes generation of electron-hole pairs. The electric field within the depletion region causes separation of the generated electron-hole pairs, especially those created at or in proximity of the diode junction, which is formed between the microstructured silicon layer and the underlying silicon substrate. The separated electron-hole pairs provide a photocurrent that is proportional to the number of incident photons (those skilled in the art appreciate that such a photocurrent is added to a generation current and a recombination current that can be inherently present in a diode junction). Hence, incident radiation can be detected, and quantified, by measuring the induced photocurrent.

A photodetector formed according to the teachings of the invention not only exhibits absorptance across a wide range of wavelengths (the absoptance is generally commensurate with that exhibited by the photodetector's microstructured silicon wafer), but it also exhibits a diodic I-V behavior. By way of example and further elucidation of the salient features of a photodetector of the invention, FIGURE 12 illustrates a plurality of graphs, each representing current as a function of bias voltage for a plurality of microstructured silicon samples prepared under different conditions in an n-doped

silicon substrate for use as the active component of photodetectors. All samples were irradiated with a plurality of femtosecond laser pulses (800 nm, 100 fs, fluence of 4 kJ/m^2) in the presence of SF_6, but were subjected to different annealing conditions. The graph A represents the current-voltage curve associated with a microstructured sample that was not annealed. This curve is substantially linear, indicating that the junction between the microstructured layer and the underlying silicon substrate in this sample is not diodic, but is merely resistive. In other words, such a wafer is not optimal for fabricating a photodetector.

In contrast, graphs B, C, and D illustrate current-versus-voltage behavior of those microstructured silicon samples that were subjected to annealing at different temperatures (the annealing duration was about 30 minutes in all cases). This exemplary data indicates that with an increase in the annealing temperature, the measured I-V curve approaches one expected from a diode. For example, at an annealing temperature of about 825 K, the I-V curve is diodic, characterized by an exponentially increasing current for a forward bias and a smaller, less rapidly increasing current for a reverse bias. The I-V curve corresponding to an annealing temperature of about 1075 K is also diodic. However, annealing a microstructured silicon wafer for a significant duration at a very elevated temperature can lead to a degradation of the below-band gap absorptance, and hence a degradation in the performance of a photodetector utilizing such a microstructured wafer in the near-infrared. In this exemplary data set, the substrate annealed at 825 K exhibit an optimal I-V characteristic. It should, however, be understood that such very elevated annealing temperatures may be employed so long as the annealing duration is sufficiently short. In general, the annealing of a microstructured silicon wafer to be employed in a photodetector of the invention should be carefully designed (i.e., annealing temperature and duration) to cause release of electrons in the microstructured surface layer without significantly degrading the wafer's absorptance of and responsivity to incident radiation.

A photodetector of the invention, such as the above exemplary photodetector 46, exhibits a responsivity that can be superior across a wavelength range of about 250 nm to about 10 microns to that of a conventional silicon photodiode. By way of example and only for illustration and corroboration purposes, FIGURE 13 presents experimental graphs representing responsivity of exemplary photodetectors formed in accordance with

the teachings of the invention, over a selected wavelength range, in comparison with a conventional photodiode and those fabricated by employing microstructured silicon, but with no annealing or annealing at too high a temperature. In particular, graphs A and B show that photodetecotors of the invention that employ silicon wafers microstructured by femtosecond laser pulses in the presence of SF_6 (100 fs, 800 nm central wavelength and a fluence of 4 kJ/m^2) followed by annealing at 825 K or 725 K, exhibit a significantly enhanced responsivity relative to that of a conventional commercially available silicon photodiode. In particular, these photodetectors exhibit a responsivity that is more than an order of magnitude greater that that of the conventional photodiode in a wavelength range of about 250 nm to about 1050 nm. Although the responsivity shows a decrease for wavelengths longer than the band-gap edge (i.e., wavelengths longer than about 1050 nm), nonetheless, it remains significantly higher than that exhibited by a conventional silicon detector. In fact, conventional silicon detectors typically do not operate at useful levels of responsivity at wavelengths that are longer than the band-gap edge. For example, in this exemplary illustration, the responsivity of the commercial photodiode drops steeply to about 10^{-6} A/W for wavelengths longer than about 1050 nm

Further, the responsitivy data for wafers formed according to the teachings of the invention (e.g., graphs A and B) were obtained by applying small bias voltages (e.g., a bias voltage of about –0.5 volts in this exemplary embodiment). In contrast, conventional silicon photodetectors exhibit much lower responsivities, or require much higher bias voltages (e.g., 100 to 1000 volts) and/or have more complex structures. This indicates that while photodetectors formed in accordance with the teachings of the invention can be readily incorporated in integrated silicon circuitry, the incorporation of conventional silicon detectors, which require large bias voltages, into integrated silicon circuits can be impractical.

The data depicted in FIGURE 13 also shows that proper annealing of a silicon wafer irradiated by a plurality of short laser pulses, as described above, can considerably enhance the responsivity of a photodetector that employs that wafer. In particular, a photodetector fabricated by utilizing a wafer that, though exposed to laser pulses, was not annealed, exhibits a much degraded responsivity relative to those that were subjected to an annealing step at appropriate temperatures, e.g., at 725 K or 825 K. This

exemplary data also shows that a photodetector that incorporates a microstructured wafer annealed, subsequent to irradiation by laser pulses, at a temperature of 1075 for thirty minutes exhibits a much degraded responsitivy relative to those annealed at 725 K or 825 K.

Hence, one aspect of the invention relates to annealing a silicon wafer, subsequent to – or simultaneous with – its irradiation by a plurality of short pulses in the presence of a substance having an electron-donating constituent, under conditions that would release electrons in the microstructured layer while preserving the responsivity of the wafer for detecting electromagnetic radiation. For example, in some embodiments of the invention, the annealing temperature is selected to be in range of about 500 K to about 1100 K, and more preferably in a range of about 700 K to about 900 K, and the annealing duration is selected to be in a range of about 1 minute to about several hours, and more preferably in a range of about 5 minutes to about 30 minutes. Alternatively, higher annealing temperatures can be employed so long as the annealing duration is properly selected to avoid degrading the responsivity of the resultant annealed wafer. For example, although the above data indicates that annealing the wafer at temperature of about 1075 K for about 30 minutes may not be desirable, this annealing temperature with a lower annealing duration can be suitable for practicing the invention in certain applications. To certain extent, annealing temperature and duration are inter-related. For example, shorter annealing time at a higher temperature can be employed in certain applications.

In other words, it is not simply annealing at an elevated temperature that is required. Rather, the annealing temperature and its duration need to be properly selected to ensure that a photodetector exhibiting enhanced responsivity over a wide wavelength range can be fabricated by utilizing the annealed wafer. It has been discovered that annealing a silicon wafer subsequent to, or simultaneous with, its exposure to short laser pulses in presence of a substance having an electron-donating constituent at a temperature that is too low can lead to noisy photodiode and annealing at too high a temperature and duration can lower the wafer's response to both visible and infrared wavelengths. More specifically, the annealing temperature and duration are preferably selected to enhance the concentration of carrier electrons in the microstructured layer – formed by laser irradiation in presence of a substance having an electron-donating

SAMSUNG EX. 1002 - 2268/4148

constituent – by a factor in a range of about 10% to about 200% while ensuring that the resultant annealed wafer exhibits a responsivity greater than about 20 A/W at least at one wavelength, and preferably over the entire span, of a wavelength range of about 250 nm to about 1050 nm, and a responsivity greater than about 0.1 A/W at least at one wavelength, and preferably over the entire span, of a wavelength range of about 1050 nm to about 3500 nm. By way of example, in some embodiments of the invention, the annealing temperature is preferably selected to be in a range of about 700 to about 900 K.

The choice of the fluence of laser pulses irradiating a silicon wafer to generate a microstructured layer therein can also affect the performance characteristics of a photodetector that incorporates the microstructured wafer for detecting radiation. By way of example, FIGURE 14 presents exemplary data corresponding to current-voltage characteristics of a plurality of silicon wafers irradiated with a plurality of femtosecond laser pulses (100 fs, 800 nm central wavelength, 200 pulses per location) in the presence of SF_6 followed by annealing at 825 K for about 30 minutes. The laser pulse fluences, however, differed from one wafer to another. More particularly, the following laser fluences were employed: 4 kJ/m^2, 6 kJ/m^2, 8 kJ/m^2, and 10 kJ/m^2. This exemplary data indicates that increasing the fluence decreases the dark current for a given reverse bias voltage.

FIGURE 15A illustrates the responsivity of a plurality of photodetectors incorporating the above silicon wafers that were microstructured with different laser pulse flunces (the wafers were annealed at 825 K for 30 minutes). This exemplary responsivity data indicates that, in this sample set, the photodetector's responsivity decreases, and the wavelength of peak response shifts to longer wavelengths, with increasing fluence (the sample made with a fluence of 4 kJ/m^2 exhibits the highest response). By way of further illustration, FIGURE 15B presents responsivity data for photodetectors made with microstructured silicon wafers that were generated through irradiation with femtosecond pulses (100 fs, 800 nm central wavelength, 200 pulses per location) in the presence of SF_6 followed by annealing at 1075 K for about 30 minutes. The laser pulse fluences, however, varied from one sample to the next (4 kJ/m^2, 6 kJ/m^2, 8 kJ/m^2, and 10 kJ/m^2). A comparison of this data with the data presented in FIGURE 15A shows that the responsivity exhibited by the samples subjected to the higher

annealing temperature of 1075 is much lower that that of the samples annealed at 825 K. However, the samples annealed at the higher temperature exhibit much less variation in responsivity as a function of fluence. Further, the samples annealed at 1075 K – though exhibiting a lower responsivity – are less noisy and have a higher quantum efficiency.

It should be understood that the above data is presented only for illustration purposes, and is not intended to necessarily indicate an optimal fluence under all conditions. For example, the above exemplary samples were made with an average laser shot number of about 200 pulses, and may exhibit improved characteristics with a greater shot number. In general, in various embodiments of the invention, the laser pulse fluence is selected to be greater than about 3 kJ/m^2. More preferably, the fluence is chosen to be in a range of about 3 kJ/m^2 to about 10 kJ/m^2, or a range of about 3 kJ/m^2 to about 8 kJ/m^2.

In many embodiments of the invention an n-doped silicon substrate is employed for forming a microstructured wafer, as described above. Alternatively, a p-doped silicon wafer can be utilized. By way of example, FIGURE 16A presents graphs comparing the diodic characteristics of a microstructured wafer generated according to the teachings of the invention, such as those described above, employing a p-doped silicon substrate (p-Si(100), 350 micron thick, resistivity (ρ) greater than 1 ohm-cm) with one fabricated utilizing an n-doped silicon substrate. In both cases, a laser pulse fluence of about 6 kJ/m^2, an annealing temperature of about 825 K, and an annealing duration of about 30 minutes were utilized. Similar data is presented in FIGURE 16B for p-dopend and n-doped samples annealed at 1075 K for about 30 minutes.

This exemplary data shows that the p-doped samples annealed at 825 K exhibit a higher forward bias current than equivalently generated n-doped samples. The dark current for back biases also increases more rapidly for p-doped samples. Upon annealing at 1075 K, the p-doped samples exhibit very good diodic properties with the back bias decreasing to substantially the same level as that in equivalently generated n-doped samples. Further, the forward bias current increases more rapidly, resulting in good rectification ratios. As noted above, annealing at higher temperatures can increase donor concentration from sulfur doping. Such increase in the donor concentration can lead p-doped samples annealed at higher temperature to exhibit better rectification.

SAMSUNG EX. 1002 - 2270/4148

A silicon substrate's doping can also affect the responsivity of a silicon wafer formed by microstructuring that substrate in accordance with the teachings of the invention. By way of example, FIGURE 17A shows measured responsivity data for two n-doped microstructured wafers and two p-doped microstructured wafers, both of which were annealed at 825 K for about 30 minutes. This exemplary data indicates that the responsivity of n-doped substrates is higher over the measured spectral range. However, FIGURE 17B shows that the responsivities of microsturctured wafers formed in p-doped and n-doped substrates, via laser irradiation and annealing at a higher temperature of about 1075 K, are nearly identical.

In general, the above illustrative data indicates that microstructured p-doped samples have a lower response but exhibit a better quantum efficiency. It should be understood that the above data is presented only for illustrative purposes and is not intended to limit the scope of the invention. In general, both p-doped and n-doped substrates can be employed in the practice of the invention, and the resultant diodic characteristics and responsivity of microstuctured wafers generated by utilizing such substrates can be different than those depicted above based on selection of other parameters, such as laser fluence, number of pulses, etc.

In addition to responsivity, another parameter of interest associated with performance of a photodetector can be its quantum efficiency. The term 'quantum efficiency' is known in the art, and is generally defined as the number of electron-hole pairs generated per incident photon at a zero applied voltage. In some cases, a microstructured sample that exhibits a high level of responsivity may not show a correspondingly high level of quantum efficiency. For example, in the above exemplary prototype microstructured silicon wafers, samples fabricated by employing n-doped substrates, laser pulses having a fluence of 4 kJ/m^2, and an annealing temperature of about 825 K exhibit the highest responsivity, but not the highest quantum efficiency. In fact, samples fabricated by employing similar conditions but a higher annealing temperature of 1075 K show higher quantum efficiencies, though lower responsivities. Similarly, the measured responsivities of samples made on p-doped substrates and annealed at 825 K or 1075 K are lower, but their quantum efficiencies are higher. Such variations of responsivity and quantum efficiency are preferably considered when

selecting various parameters in practicing the teachings of the invention for fabricating a silicon photodetector.

The responsivity of a photodetector fabricated in accordance with the teachings of the invention can also vary as a function of a back bias applied thereto. Typically, the responsivity increases as the applied back bias increases. By of example, FIGURE 18 exhibits the responsivity of a silicon wafer microstructured in accordance with the teachings of the invention through irradiation by a plurality of femtosecond pulses at a fluence of $4kJ/m^2$ followed by annealing at 825 K for about 30 minutes, as a function of an applied back bias voltage. The sample was illuminated with a white light source with an approximate power of 50 microwatts. The responsivity, and hence gain, increases quickly up to a bias voltage of –5 volts and more slowly up to –15 volts. At voltages beyond –15 volts, the responsivity begins to fall. In some cases, the responsivity of a photodetector that exhibits a large gain may not be sufficiently linear for certain applications. Hence, in selecting a proper back voltage, in addition to responsivity, other factors, such as the linearity of the response should be considered. In addition, in applications in which the photodetectors are incorporated in an integrated silicon circuit, the bias voltage should be compatible with the requirements of that circuit.

A photodetector formed according to the teachings of the invention can operate within a wide range of temperatures. In some cases, it may be advantageous to cool the photodetector to decrease its average noise level. By way of example, FIGURE 19A presents current-voltage curves corresponding to an n-doped microstructured silicon sample made with femtosecond pulses at a fluence of about 4 kJ/m^2 and annealed at 825 K at different operating temperatures. The measured current in both the back bias and forward bias conditions decreases with decreasing the temperature. At very low temperatures (below 100 K), conduction becomes very low for both forward and back biases. FIGURE 19B shows the responsivity of such a microstructured wafer to incident radiation having a wavelength of 1064 nm (a wavelength close to the band gap of silicon at room temperature) at a back bias of –0.5 V as a function of operating temperature. The measured responsivity drops with temperature. This behavior may be, however, different if the wavelength of the illuminating light is far from the silicon band gap. A graph of the dark current at a bias voltage of –0.5 V as a function of temperature, however, shows that the noise decreases much more rapidly that the responsivity.

In sum, photodiodes formed according to the teachings of the invention can exhibit responsivities in a wide region of the electromagnetic spectrum (e.g., wavelengths in a range of about 250 nm to about 1100 nm) that are nearly two orders of magnitude higher than those exhibited by conventional commercial silicon photodiodes. Further, responsivities at longer wavelengths, e.g., as long as 1600 nm, can be nearly five orders of magnitude greater than those exhibited by conventional silicon photodiodes in this range. In some of the above prototype samples fabricated according to the teachings of the invention for illustration purposes, the carrier mobility in the surface layer was measured to be about 101 $cm^2V^{-1}s^{-1}$; the response times included a rise time of about 10 ns and a fall time of about 30 ns; and a diode capacitance of about 63.9 nF at a back bias of –0.5 V was measured. A photodiode of the invention can exhibit a large gain at very small applied bias voltages, e.g., a gain greater than 1000 for an applied bias voltage of – 0.5 V.

A silicon photodetector according to the teachings of the invention, such as the above exemplary photodetector 46 (FIGURE 11A), can be fabricated by employing a variety of techniques. By way of example, in one exemplary method of fabricating such a photodetector, a selected portion of a silicon wafer, e.g., a 5 x 5 mm^2 area, is microstructured via exposure to short laser pulses in the presence of a suitable material, e.g., SF_6, in a manner described above. The wafer is then dipped in a solution of HF (e.g., a 5% solution) in order to remove any native oxide layer before forming electric contacts with the microstructured layer. Subsequently, a mask is deposited over the surface of the microstructued layer having exposed portions which correspond to a desired pattern of a conductive electrode to be formed on that surface. A selected metal, e.g., a Cr/Au alloy, is then evaporated over the masked surface, and the mask is removed to leave behind a patterned conductive layer, such as the conductive layer 52 shown in FIGURE 11A, and uncoated portions suitable for receiving radiation. Further, a conductive layer can be formed on a back surface of the wafer, an unstructured surface opposed to the microstructured layer, such as the layer 54 shown in FIGURE 11A. In many embodiments, the entire back surface is coated with the metal. The wafer can be then be coupled to a voltage source, such as the source 56 shown in FIGURE 11A, that can apply a bias voltage thereto and optionally other electronic elements, e.g.,

capacitors, in a manner known in the art. Further, a the wafer and its associated circuitry can be placed in an appropriate housing by employing techniques known in the art.

The applications of microstructured silicon wafers formed according to the teachings of the invention, such as those discussed above, are not limited to photodetectors. For example, such silicon wafers can be employed in fabricating solar cells. In some cases, the optimal values of various parameters, such as substrate doping, associated with the microstructured wafer utilized in generating solar cells can be different than those in fabricating silicon photodetectors. A solar cell can be considered a p-n junction photodiode with high quantum efficiency. The conversion of photons into photocarriers is the physical mechanism by which light is converted in a solar cell into electricity. However, there is a fundamental difference between a photodetector and a solar cell. A photodetector is generally operated in a "photoconductive" mode: a back bias is applied thereto and a current is measured. In contrast, a solar cell is operated in a "photovoltaic" mode: it is operated in an open circuit mode or attached to a load without application of a bias voltage.

In one embodiment, a microstructured layer is formed in a p-doped crystalline silicon substrate by initially irradiating a plurality of locations on a surface thereof with femtosecond (e.g., 100 fs, and a central wavelength of 800 nm) laser pulses having a fluence of about 4 kJ/m^2 followed by annealing at 1075 K for about one hour. The wafer can then be utilized in fabricating a solar cell. More specifically, metal contacts, e.g., Cr/Au contacts, can be evaporated on the microstructure layer's surface so as to coat selected portions thereof while leaving at least a portion of the surface uncovered for receiving radiation, e.g., a finger grid metallic pattern can be disposed on the surface. In addition, the back surface of the substrate, the unstructured surface opposing the structured surface, can be coated, e.g., via evaporation, with a metallic coating. A load can be attached the wafer via electrical coupling to the metallic layers on the both sides of the wafer.

FIGURE 20 presents data comparing current-voltage (*I-V*) behavior of such a wafer, formed in a high resistivity (resistivity greater than about 1 ohm-m) silicon substrate, that can be utilized as a solar cell in the presence and in the absence of illumination. And FIGURE 21 presents a similar comparative data for a wafer formed in low resistivity silicon substrate (resistivity in a range of about 0.01 – 0.1 ohm-m). The

solar cell fabricated by employing the high resistivity substrate has an open circuit voltage of 0.4 volts and a short circuit current of 13.4 mA while the solar cell fabricated by utilizing the low resistivity substrate has an open circuit voltage of 0.31 volts and a short circuit current of 13.45 mA. It should be understood that this data is presented only for illustration purposes, and to show the possibility of utilizing a wafer microstructured in accordance with the teachings of the invention in forming a solar cell. However, this data is not intended to indicate optimal performance of a solar cell generated in accordance with the teachings of the invention. For example, the deposition of electrical contacts on the substrate can be optimized to obtain better performance than that described above.

In another application, a silicon wafer microstructured in accordance with the teachings of the invention can be utilized as a field emitter. In other words, an electric field can be applied to the microstructured surface to cause emission of electrons therefrom. To show the possibility of utilizing a microstructured wafer for generating field emission current, a number of prototype exemplary microstructured wafers were fabricated and field emission currents generated by them were measured. The experimental step-up for performing these measurements is shown schematically in FIGURE 22. A microstructured silicon sample 58 with a gold coating 60 evaporated on a back surface is mounted to a silicon wafer 62 having a gold coating 64, which functions as an anode, and is separated therefrom by a pair of mica spacers 66 and 68. The mounted sample is placed in a vacuum chamber, which is evacuated to a pressure of about 10^{-6} torr. A potential difference can be applied between the microstructured sample 58 and the gold-coated anode. And emission current can be measured at each applied voltage, e.g., via a picoammeter 70, a resistive elements 72 placed in series with the ammeter to protect it from unexpected surges in current.

FIGURE 23 shows exemplary results of field emission currents measured for silicon samples microstructured in SF_6. The typical figures of merit for a field emitting surface are turn-on-field, defined as the electric field (bias voltage divided by the tip-to-anode spacing) for which a current density of 0.01 microampere/mm^2 is observed, and threshold field, defined as the field at which a current density of 0.1 microamperes/mm^2 is produced. The turn-on field for a plurality of exemplary prototype substrates microstructured in SF_6 was measured as 1.3 V/micrometer, and the threshold field was

measured as 2.15 V/micrometer – excellent values that are on par with those exhibited by nanotubes.

Those having ordinary skill in the art will appreciate that various modifications can be made to the above embodiments without departing from the scope of the invention. It should also be understood that various exemplary data presented above are intended only for illustrating salient features of various aspects of the invention, and is not intended to limit the scope of the invention.

What is claimed is:

1. A method of fabricating a radiation-absorbing semiconductor structure, comprising:

irradiating each of a plurality of locations on a surface of a silicon substrate with one or more femtosecond laser pulses while exposing said surface to a sulfur-containing substance so as to generate a plurality of sulfur inclusions in a surface layer of said substrate, and

annealing said substrate at a temperature in a range of about 500 K to about 1100 K for a time duration in a range of about a few seconds to about a few hours.

2. The method of claim 1, further comprising selecting a duration of each laser pulse to be in a range of about 50 femtoseconds to about 500 femtoseconds.

3. The method of claim 1, further comprising selecting a fluence of each pulse to be in a range of about 1 kJ/m^2 to about 15 kJ/m^2.

4. The method of claim 1, further comprising selecting a central wavelength of said laser pulses to be in a range of about 200 nm to about 800 nm.

5. The method of claim 1, wherein said irradiating step comprises exposing each location to a number of laser pulses ranging from 2 to about 500.

6. The method of claim 1, further comprising subjecting each of said surface locations to successive laser pulses separated from one another by a time interval in a range of about 1 microsecond to about 1 millisecond.

7. The method of claim 1, further comprising performing said annealing step in any of an inert atmosphere or a low-pressure atmosphere.

8. The method of claim 1, further comprising selecting said sulfur-containing substance to be any of SF_6 and H_2S.

9. The method of claim 1, wherein said semiconductor structure absorbs radiation having wavelength components in a range of about 0.25 to about 10 microns.

10. The method of claim 1, wherein said semiconductor structure absorbs radiation having wavelength components in a range of about 0.35 to about 2.5 microns.

11. The method of claim 1, wherein said semiconductor structure exhibits a substantially uniform absorption for wavelength components in a range of about 1.2 to about 2.5 microns.

12. A method of fabricating a photodetector, comprising:

forming a semiconductor structure absorbing radiation in a wavelength range of about 0.25 to about 3.5 microns and exhibiting a diodic current-voltage characteristic in said wavelength range, said forming step comprising:

irradiating a surface of a silicon substrate at one or more locations thereof with one or more laser pulses having short pulse widths while exposing said surface to a sulfur-containing gas to generate a micro-structured layer having sulfur inclusions,

annealing said substrate at a temperature in a range of about 500 K to about 1000 K for a time duration in a range of about a few seconds to about a few hours, and

depositing a plurality of metallic contacts on selected portions of said semiconductor structure to allow applying a reverse bias voltage thereto.

13. The method of claim 12, wherein said pulse widths are selected to be in a range of about tens of femtoseconds to about tens of nanoseconds.

14. The method of claim 12, further comprising selecting said sulfur-containing substance to be any of SF_6 and H_2S.

15. The method of claim 12, further comprising performing said annealing step in an inert atmosphere.

16. The method of claim 12, wherein said depositing step comprises thermally evaporating one or more selected metals on said selected portions of the semiconductor structure.

17. The method of claim 12, further comprising selecting a thickness of said metal contacts to be in a range of about 5 nm to about 100 nm.

18. The method of claim 16, wherein said depositing step comprises thermally evaporating a chromium layer followed by thermally evaporating a gold layer on a selected portion of said semiconductor structure to generate at least one of said metal contacts.

19. The method of claim 18, further comprising selecting a thickness of said chromium layer to be in a range of about 1 nm to about 5 nm.

20. The method of claim 19, further comprising selecting a thickness of said gold layer to be in a range of about 4 nm to about 100 nm.

21. The method of claim 12, further comprising configuring said metal contacts so as to ensure that at least a portion of said micro-structured layer remains capable of receiving an external radiation.

22. A method of fabricating a semiconductor structure, comprising

irradiating a plurality of locations on a surface of a silicon substrate with one or more laser pulses having pulse widths in a range of about 50 to about 500 femtoseconds while exposing said surface to a substance having an electron-donating constituent so as to generate a micro-structured surface layer comprising inclusions incorporating said electron-donating constituent, and

annealing said substrate at an elevated temperature in a range of about 500 K to about 1100 K for a selected time period.

23. The method of claim 22, further comprising selecting said electron-donating constituent to be any of chlorine (Cl_2), nitrogen (N_2) and air.

24. The method of claim 22, wherein said irradiating step further comprises directing said laser pulses at said surface along a direction substantially perpendicular to said surface.

25. The method of claim 22, wherein said selected annealing period is in a range of about a few seconds to about a few hours.

26. The method of claim 22, wherein said annealing step is performed in an inert atmosphere.

27. A method of fabricating a radiation-absorbing semiconductor wafer, comprising:

irradiating at least one surface location of a silicon substrate with a plurality of temporally short laser pulses while exposing said location to a substance having an electron-donating constituent so as to generate a substantially disordered surface layer incorporating a concentration of said electron-donating constituent, and

annealing said substrate at an elevated temperature and for a duration selected to enhance charge carrier density in said substantially disordered surface layer.

28. The method of claim 27, wherein said elevated temperature and duration are selected to cause re-arrangement of atomic bonds in said surface layer so as to increase concentration of carrier electrons in surface layer.

29. The method of claim 27, wherein said elevated temperature and duration are selected to enhance electron carrier density in the surface layer by a factor of about 10% to about 200% relative to a pre-annealing level.

30. The method of claim 27, wherein said elevated temperature and duration are selected to cause said surface layer to form a diode junction with underlying silicon substrate.

31. The method of claim 27, wherein said elevated temperature and duration are selected such that said annealed substrate exhibits a responsivity in a range of about 1 A/W to about 200 A/W upon exposure of said surface layer to radiation having wavelengths in a range of about 250 nm to about 1100 nm and application of a reverse bias in a range of about 0.1 V to about 15 V to said wafer.

32. The method of claim 27, wherein said elevated temperature is selected to be in a range of about 500 K to about 1100 K.

33. The method of claim 33, wherein said duration is selected to be in a range of about a few seconds to about few hours.

34. The method of claim 27, further comprising selecting said short laser pulses to have pulse widths in a range of about tens of femtoseconds to about tens of nanoseconds.

35. The method of claim 27, further comprising selecting a fluence of said pulses and a partial pressure of said substance having an electron-donating constituent such that the concentration of said electron-donating constituent incorporated in said surface layer ranges from about 0.5 to about 5 atom percent.

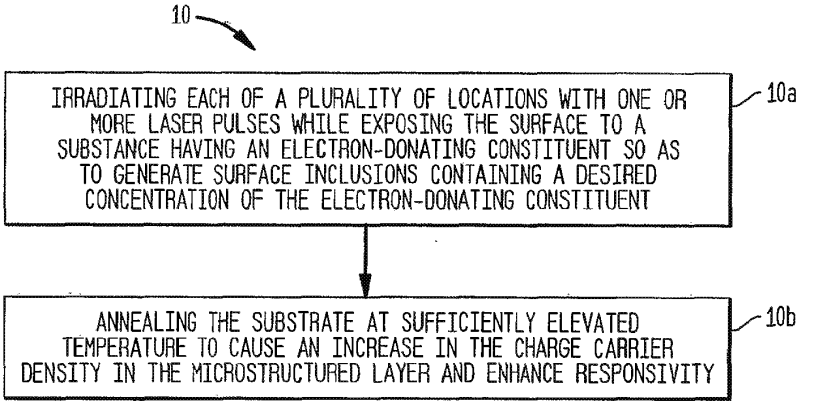
36. A method of fabricating a radiation-absorbing semiconductor wafer, comprising

irradiating at least one surface location of a silicon substrate with temporally short laser pulses while exposing the substrate to a substance having an electron-donating constituent so as to generate a microstructured surface layer having inclusions containing the electron-donating constituent, and

annealing the substrate at an elevated temperature and for a duration selected to enhance a responsivity of the microstructured substrate to radiation having at least one wavelength in a range of about 250 nm to about 1100 nm incident on the microstructured surface layer by at least a factor of about 10.

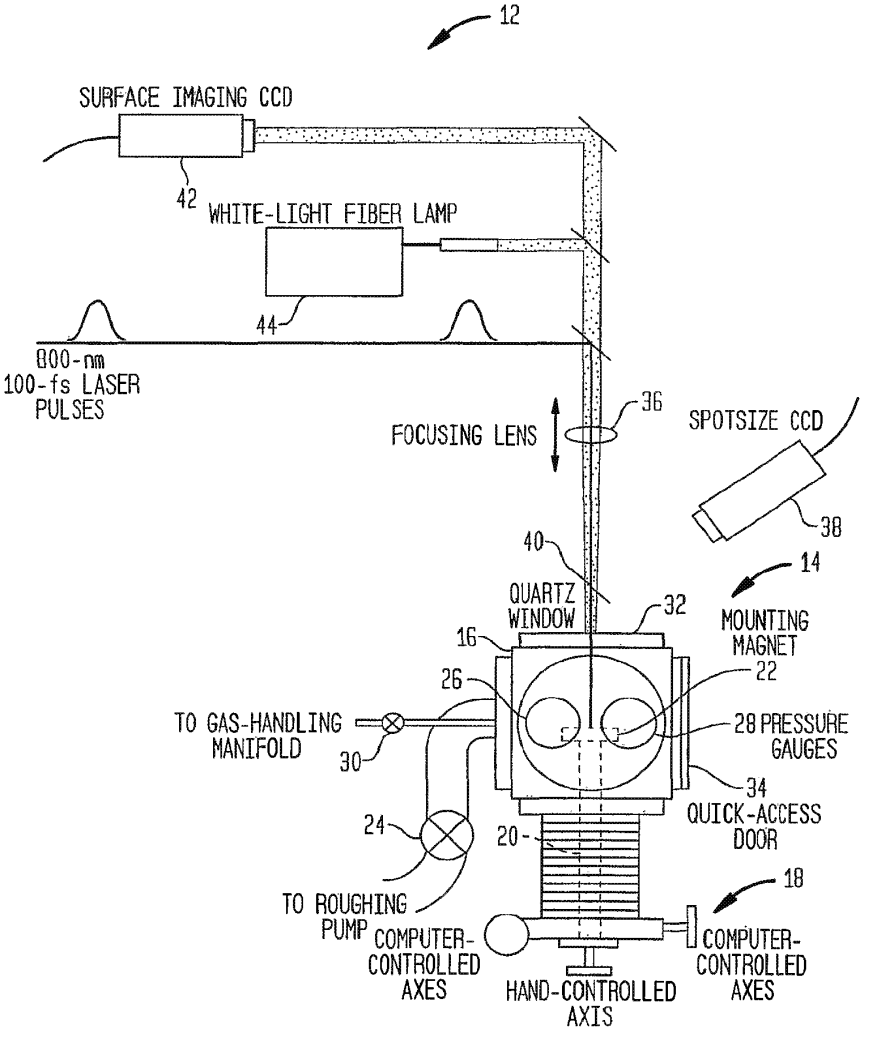
37. The method of claim 37, wherein the annealing temperature lies in a range of about 700 K to about 900 K.

FIG. 1



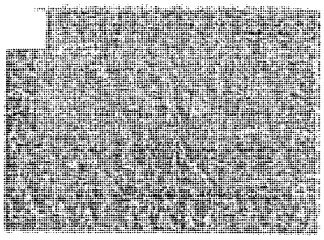
SAMSUNG EX. 1002 - 2283/4148

FIG. 2



SAMSUNG EX. 1002 - 2284/4148

FIG. 3



SAMSUNG EX. 1002 - 2285/4148

FIG. 4

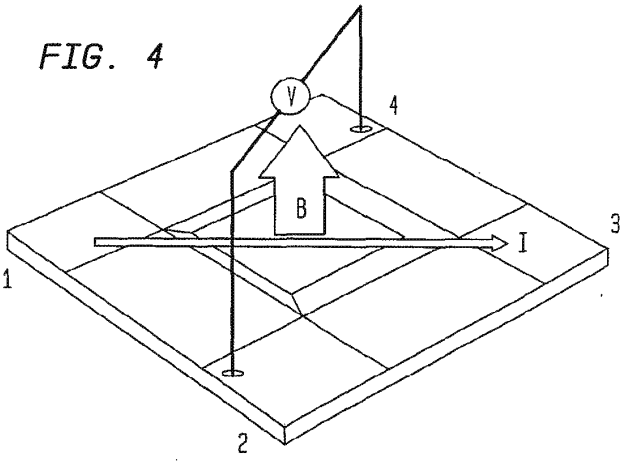
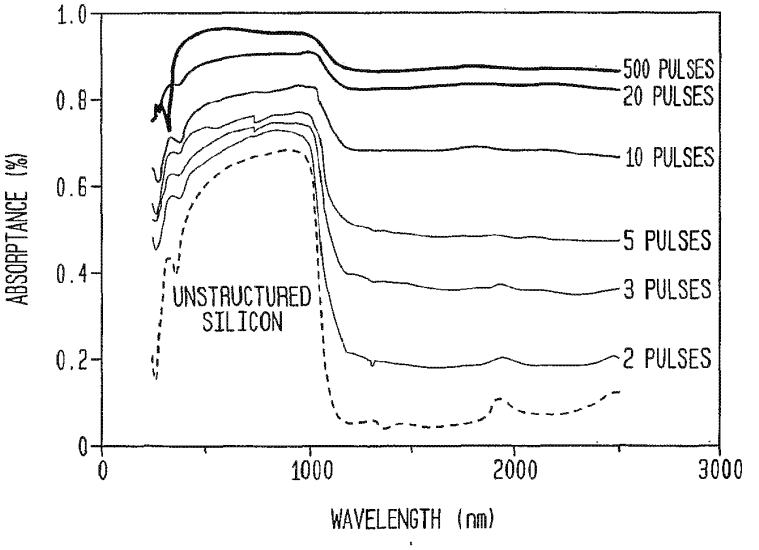


FIG. 5



SAMSUNG EX. 1002 - 2286/4148

FIG. 6

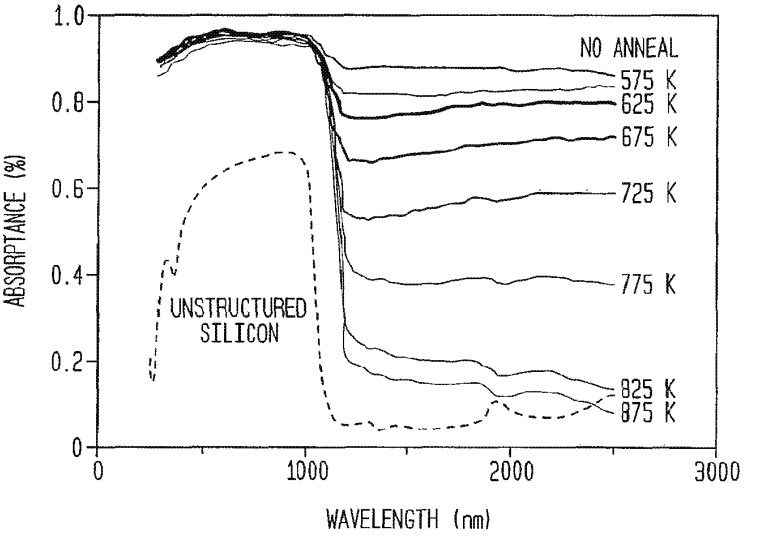
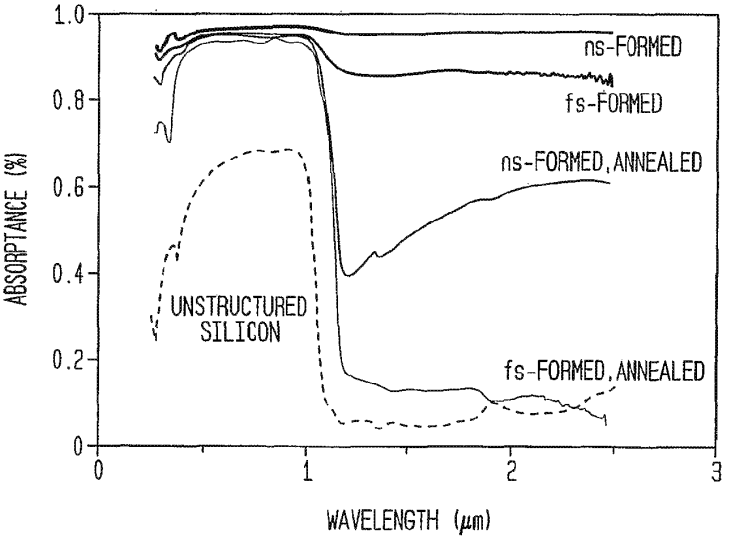


FIG. 7



SAMSUNG EX. 1002 - 2287/4148

FIG. 8A

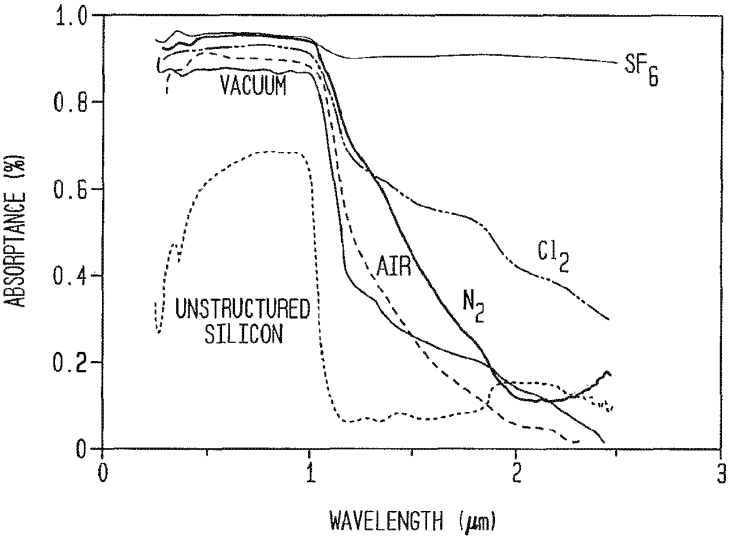
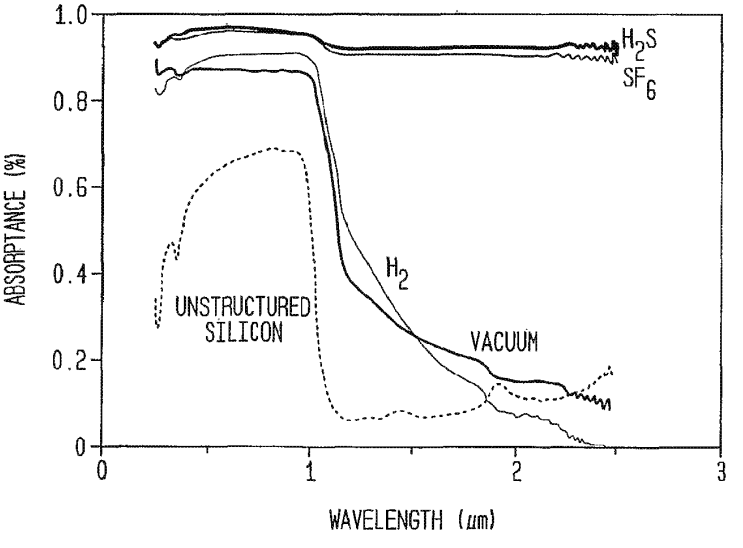


FIG. 8B



SAMSUNG EX. 1002 - 2288/4148

FIG. 9

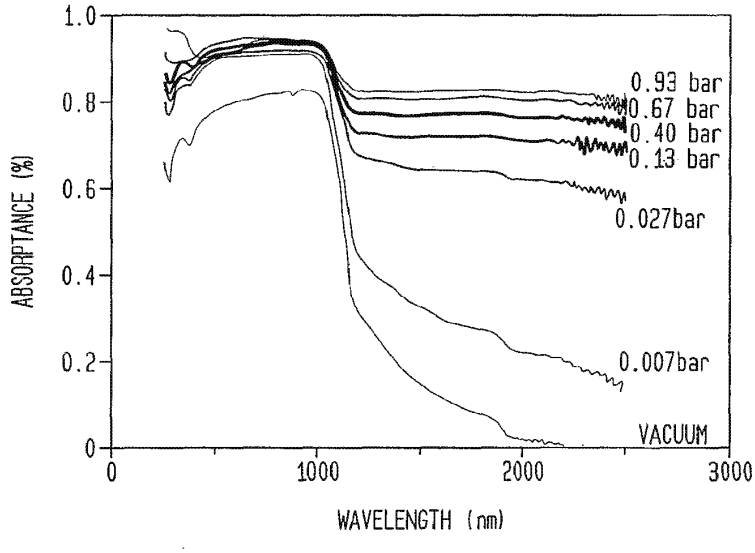
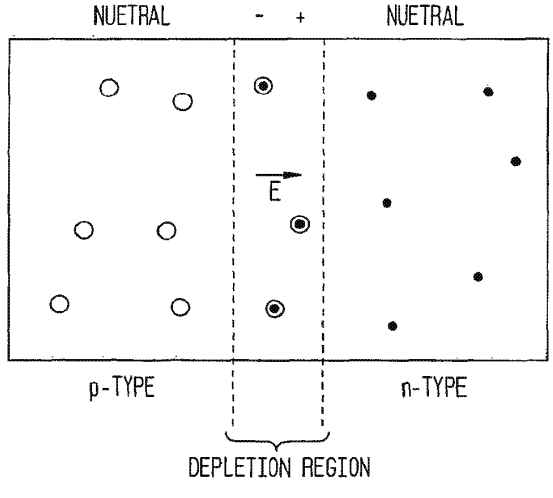


FIG. 10



SAMSUNG EX. 1002 - 2289/4148

FIG. 11A

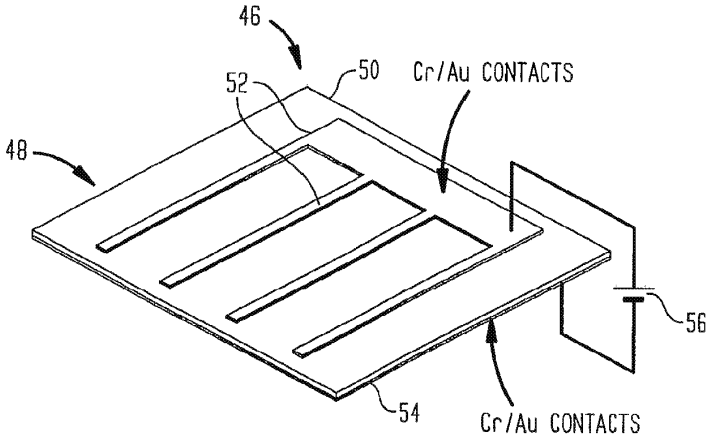
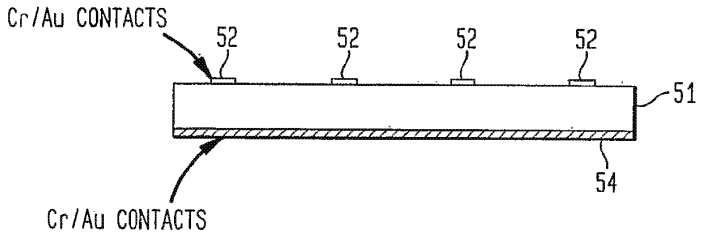


FIG. 11B



SAMSUNG EX. 1002 - 2290/4148

FIG. 12

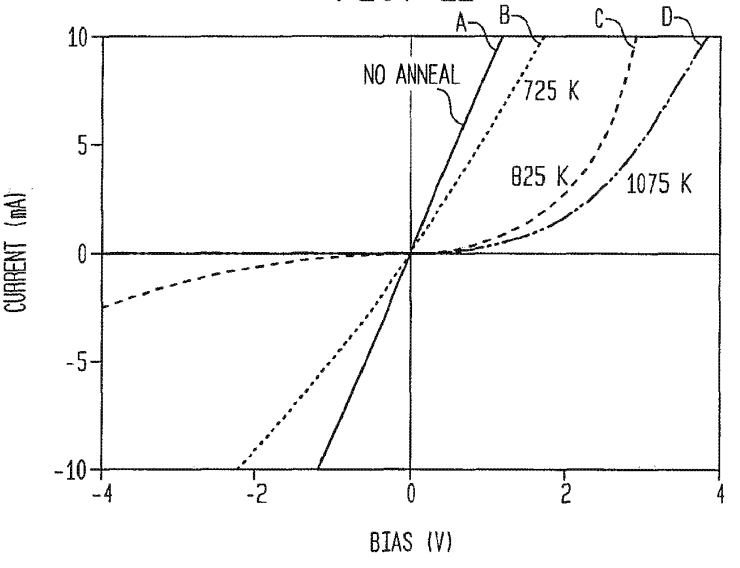
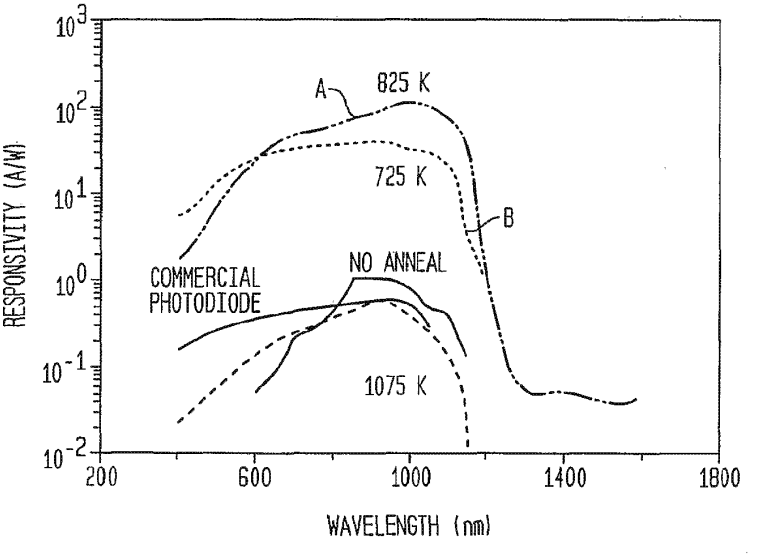


FIG. 13



SAMSUNG EX. 1002 - 2291/4148

FIG. 14

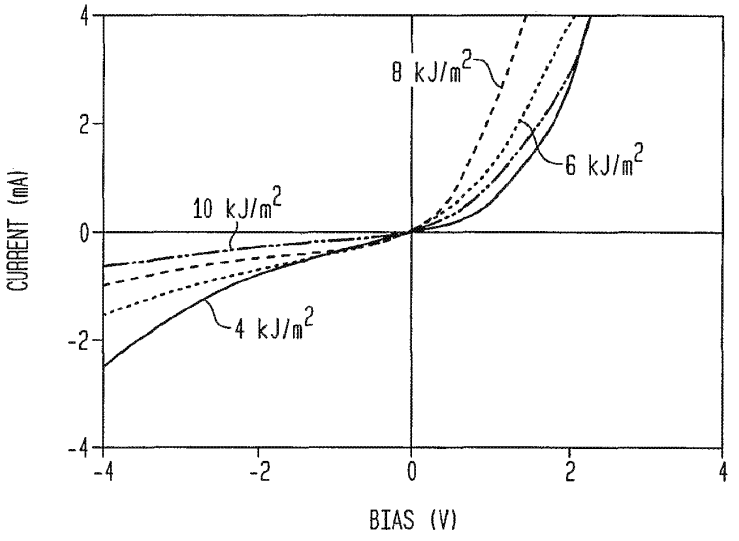
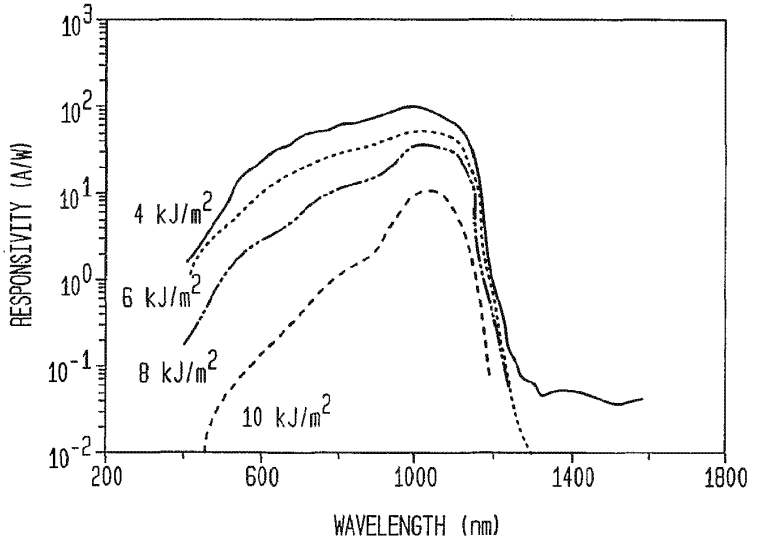


FIG. 15A



SAMSUNG EX. 1002 - 2292/4148

FIG. 15B

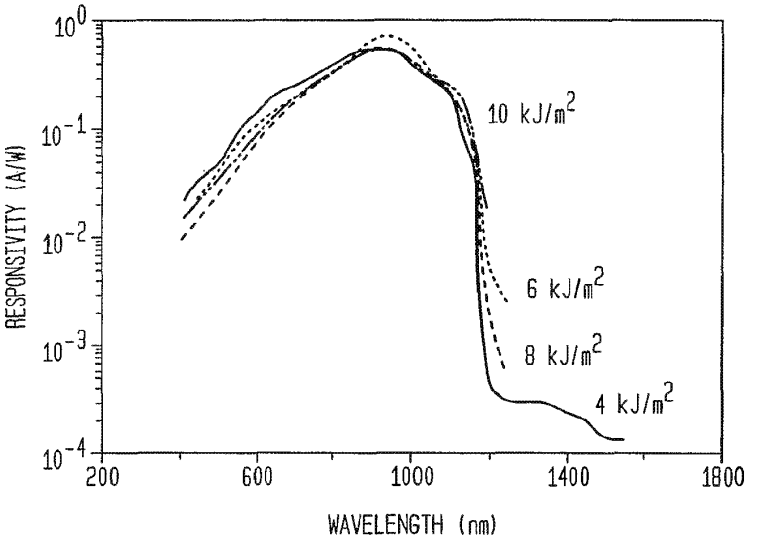
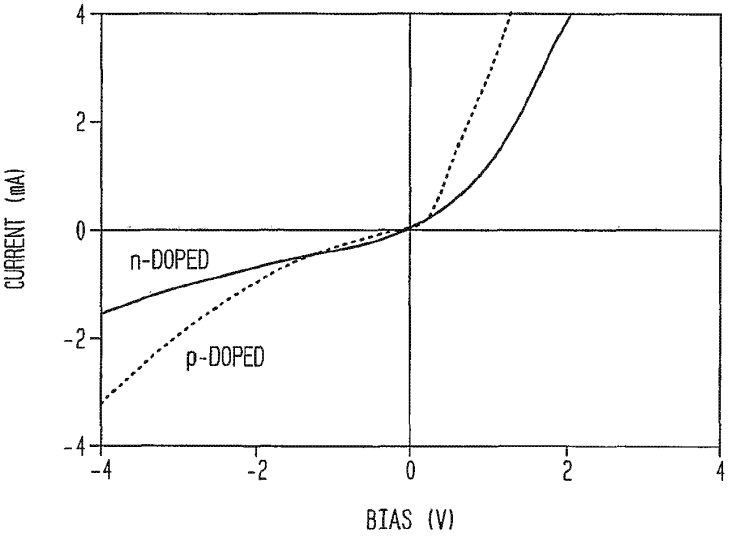


FIG. 16A



SAMSUNG EX. 1002 - 2293/4148

FIG. 16B

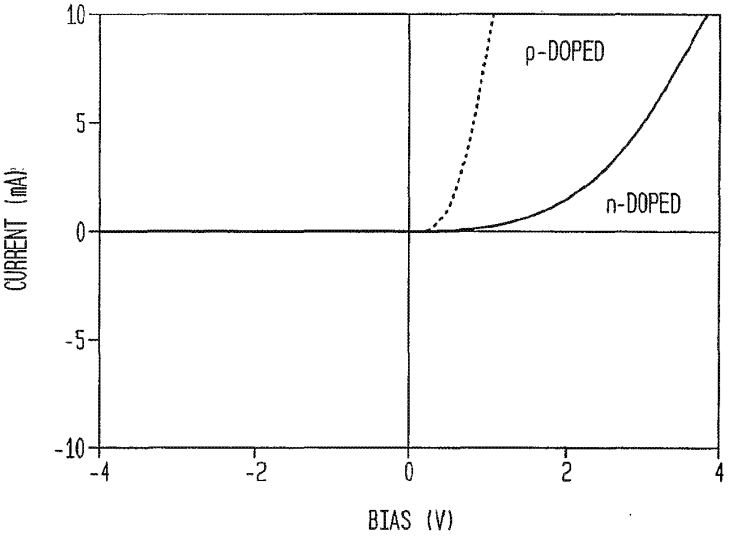
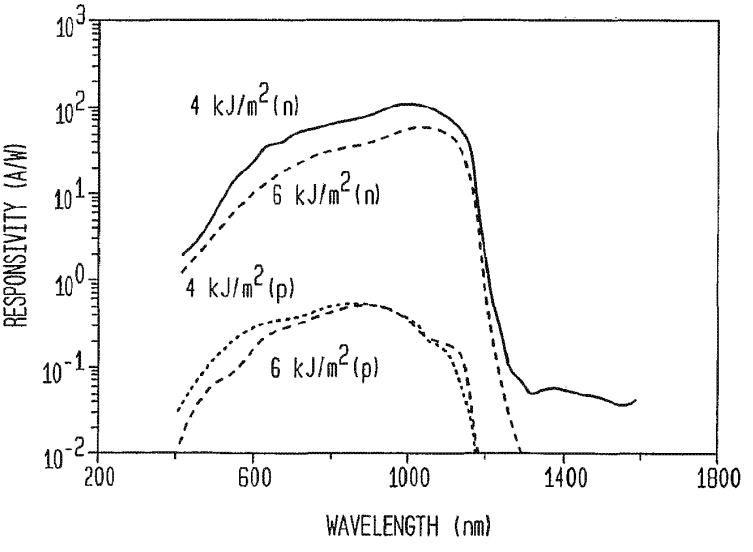


FIG. 17A



SAMSUNG EX. 1002 - 2294/4148

FIG. 17B

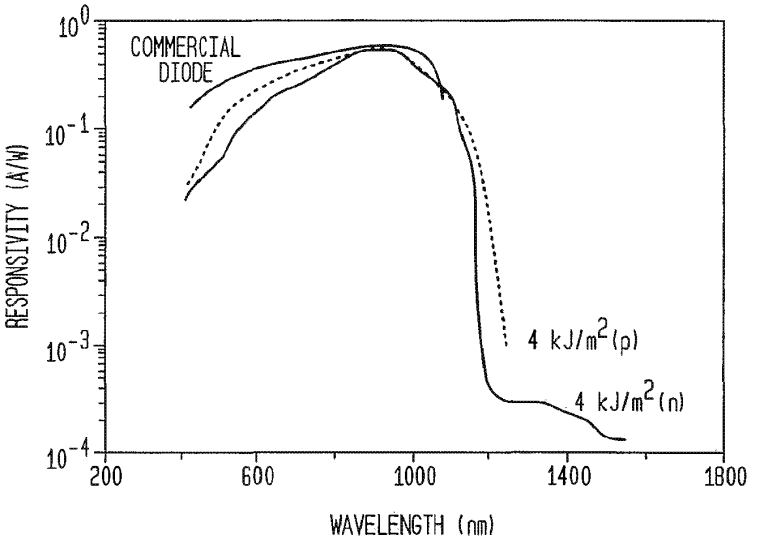
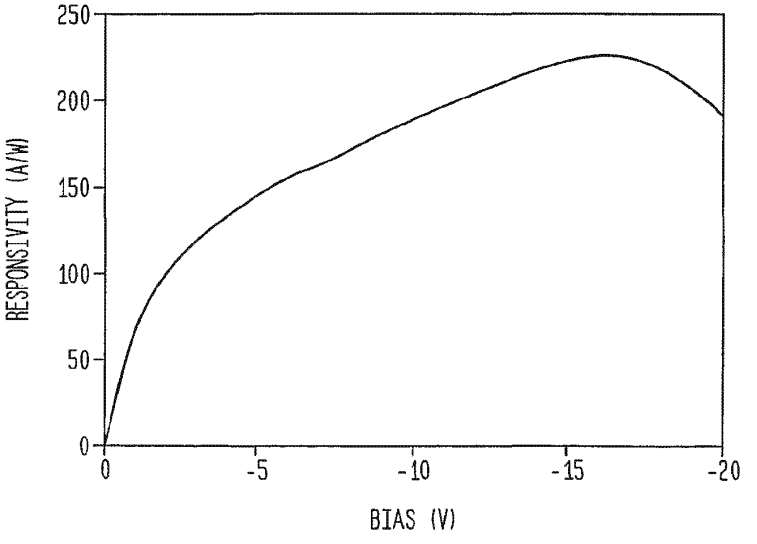


FIG. 18



SAMSUNG EX. 1002 - 2295/4148

FIG. 19A

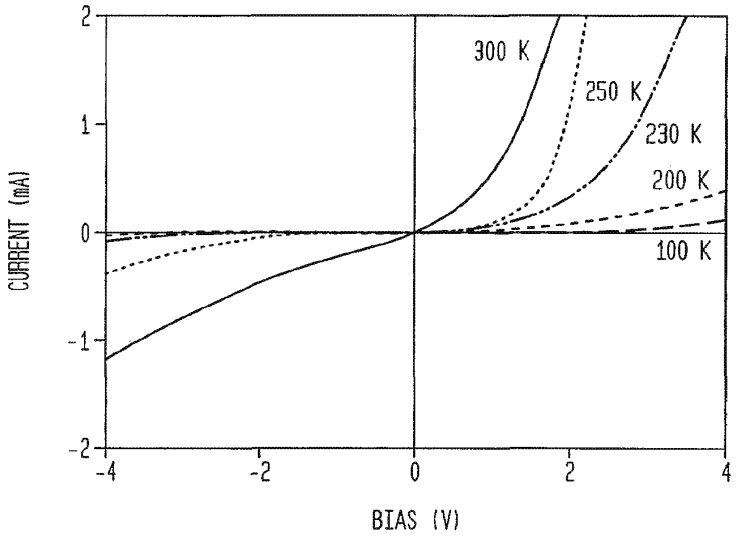


FIG. 19B

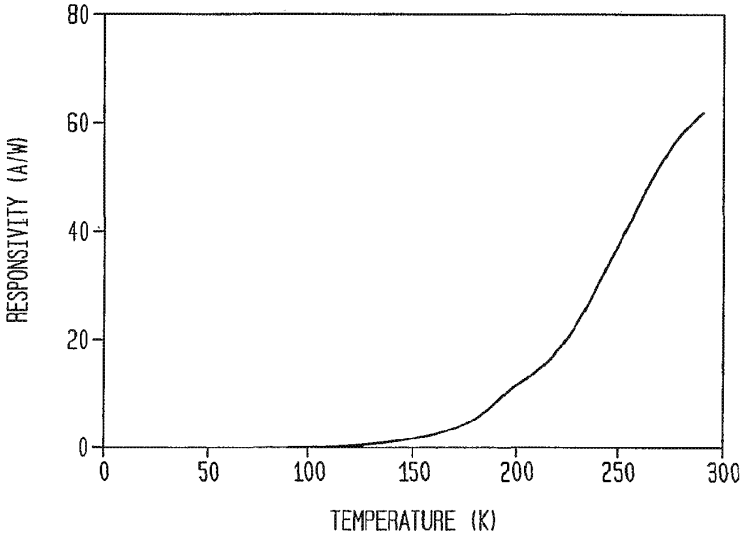


FIG. 20

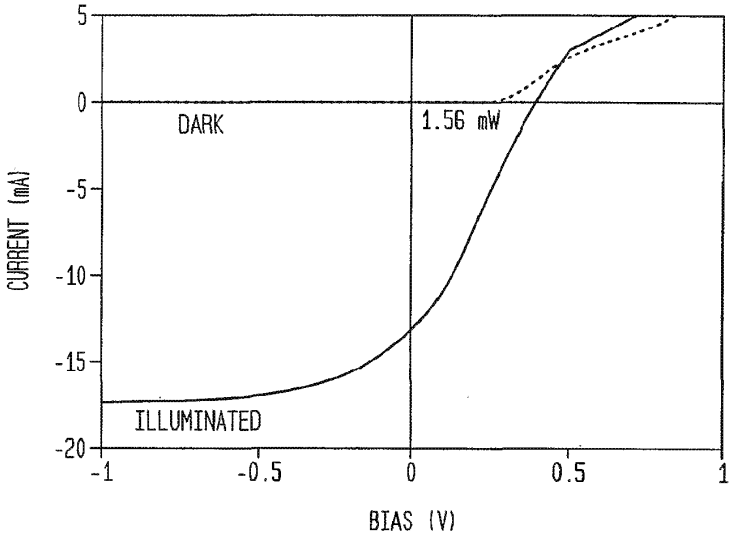
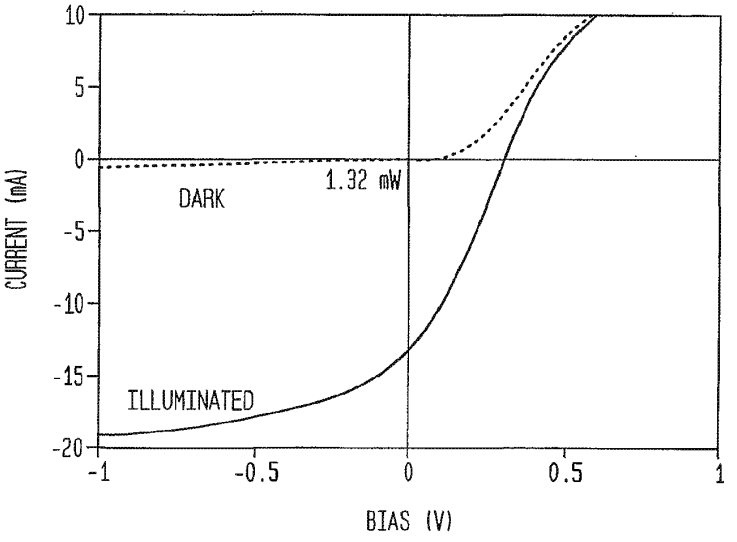


FIG. 21



SAMSUNG EX. 1002 - 2297/4148

FIG. 22

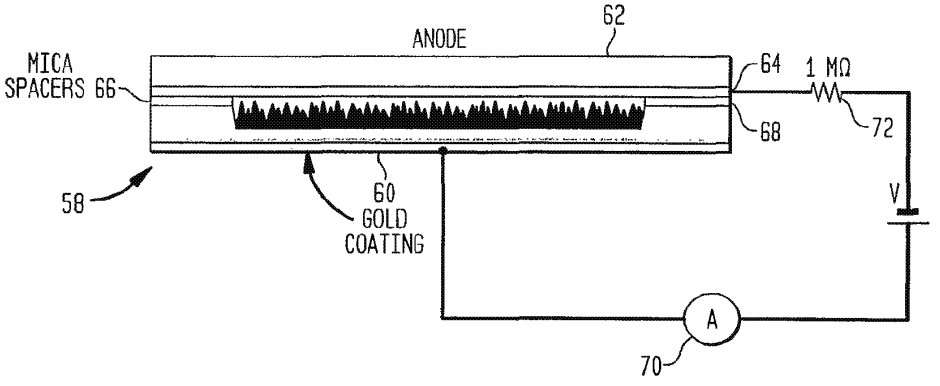
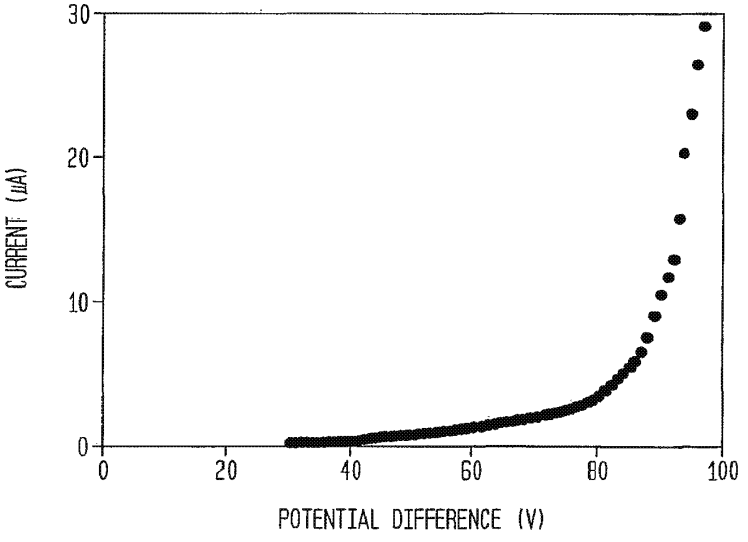


FIG. 23



SAMSUNG EX. 1002 - 2298/4148

(12) INTERNATIONAL APPLICATION PUBLISHED UNDER THE PATENT COOPERATION TREATY (PCT)

(19) World Intellectual Property Organization
International Bureau

(43) International Publication Date
31 July 2008 (31.07.2008)

PCT

(10) International Publication Number
WO 2008/091242 A2

(51) International Patent Classification:
B32B 38/04 (2006.01)

(21) International Application Number:
PCT/US2006/049065

(22) International Filing Date:
21 December 2006 (21.12.2006)

(25) Filing Language: English

(26) Publication Language: English

(30) Priority Data:

60/752,545	21 December 2005 (21.12.2005)	US
60/843,874	12 September 2006 (12.09.2006)	US
60/860,735	22 November 2006 (22.11.2006)	US

(71) Applicant *(for all designated States except US)*: **UVA PATENT FOUNDATION** [US/US]; 250 West Main Street, Suite 300, Charlottesville, VA 22902 (US).

(72) Inventors; and

(75) Inventors/Applicants *(for US only)*: **GUPTA, Mool, C.** [US/US]; 104 Birkdale Court, Yorktown, VA 23693 (US). **NAYAK, Baruda, K.** [IN/US]; 86 University Gardens, Apt #7, Charlottesville, VA 22903 (US).

(74) Agents: **DECKER, Robert, J.** et al.; University of Virginia Patent Foundation, 250 West Main Street, Suite 300, Charlottesville, VA 22902 (US).

(81) Designated States *(unless otherwise indicated, for every kind of national protection available)*: AE, AG, AL, AM, AT, AU, AZ, BA, BB, BG, BR, BW, BY, BZ, CA, CH, CN, CO, CR, CU, CZ, DE, DK, DM, DZ, EC, EE, EG, ES, FI, GB, GD, GE, GH, GM, GT, HN, HR, HU, ID, IL, IN, IS, JP, KE, KG, KM, KN, KP, KR, KZ, LA, LC, LK, LR, LS, LT, LU, LV, LY, MA, MD, ME, MG, MK, MN, MW, MX, MY, MZ, NA, NG, NI, NO, NZ, OM, PG, PH, PL, PT, RO, RS, RU, SC, SD, SE, SG, SK, SL, SM, SV, SY, TJ, TM, TN, TR, TT, TZ, UA, UG, US, UZ, VC, VN, ZA, ZM, ZW.

(84) Designated States *(unless otherwise indicated, for every kind of regional protection available)*: ARIPO (BW, GH, GM, KE, LS, MW, MZ, NA, SD, SL, SZ, TZ, UG, ZM, ZW), Eurasian (AM, AZ, BY, KG, KZ, MD, RU, TJ, TM), European (AT, BE, BG, CH, CY, CZ, DE, DK, EE, ES, FI, FR, GB, GR, HU, IE, IS, IT, LT, LU, LV, MC, NL, PL, PT, RO, SE, SI, SK, TR), OAPI (BF, BJ, CF, CG, CI, CM, GA, GN, GQ, GW, ML, MR, NE, SN, TD, TG).

Published:
— *without international search report and to be republished upon receipt of that report*

(54) Title: SYSTEMS AND METHODS OF LASER TEXTURING AND CRYSTALLIZATION OF MATERIAL SURFACES

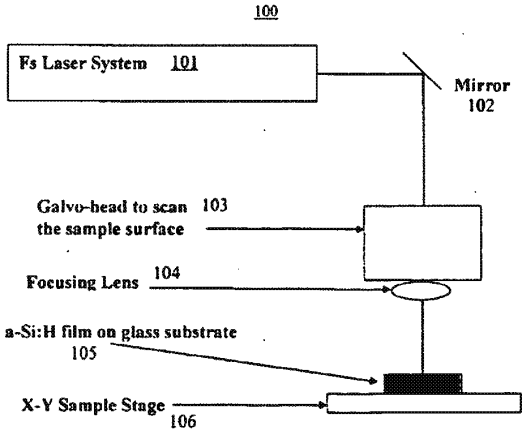


FIG. 1

(57) Abstract: The surface of a material is textured and crystallized in a single step by exposing the surface to pulses from an ultrafast laser. The laser treatment causes pillars to form on the treated surface. These pillars provide for greater light absorption. The crystallization of the material provides for higher electric conductivity and changes in optical properties of the material. The method may be performed in a gaseous environment, so that laser assisted chemical etching will aid in the texturing of the surface. This method may be used on various material surfaces, such as semiconductors, metals, ceramics, polymers, and glasses.

WO 2008/091242 A2

SAMSUNG EX. 1002 - 2299/4148

SYSTEMS AND METHODS OF LASER TEXTURING AND CRYSTALLIZATION OF MATERIAL SURFACES

CROSS-REFERENCE TO RELATED APPLICATIONS

[0001] This application claims priority from U.S. Provisional Patent Application No. 60/752,545, filed on December 21, 2005; U.S. Provisional Patent Application No. 60/843,874, filed on September 12, 2006; and U.S. Provisional Patent Application No. 60/860,735, filed on November 22, 2006. The full disclosures of these provisional applications are incorporated herein by reference.

STATEMENT OF GOVERNMENT INTEREST

[0002] The present invention was developed under National Science Foundation Grant No. GA10507-31335 427250. The government has certain rights in the invention.

FIELD OF THE INVENTION

[0003] Apparatuses and methods consistent with the present invention relate to modifying surfaces, and more particularly, to modifying surfaces of thin films in order to alter their thermal, structural, optical, and electrical properties.

BACKGROUND OF THE INVENTION

[0004] Laser processing provides a unique method of modifying materials by depositing large amounts of energy onto the surface of a material in an extremely controlled manner. Laser processing enables the precisely localized treatment of a material. Laser processing is particularly useful after thin-film deposition of amorphous materials, which usually involves low temperature processing, and allows for the use of flexible and low melting temperature

SAMSUNG EX. 1002 - 2300/4148

substrates for large area device fabrication. However, these devices lack better performance, usually due to poor electrical, optical, and/or structural properties. Laser processing of these devices with ultra-short laser pulses has been found to improve the properties of the devices, because the high peak intensities of the laser pulses rapidly texture the surface, and a subsequent quenching process induces crystallization in the material. The texturing of the surface leads to more light absorption in the material, and the subsequent crystallization improves the electronic properties of the material.

[0005] For example, thin film amorphous silicon (a-Si) based devices are inexpensive compared to their crystalline counterparts because of low temperature processing, which is suitable for deposition on large substrates, such as glass, plastic, and steel foils. However, solar cell devices fabricated using a-Si thin-films lack efficiency, have a high reflectivity across the electromagnetic spectrum, possess a larger band gap (~ 1.7 eV), and have limited carrier mobility. In order to improve the efficiency and sensitivity of a-Si based devices, post-deposition laser processing is usually recommended. This includes texturing and subsequent crystallization of the surface. Pulsed laser crystallization of thin a-Si films on various substrates has potential applications in the fabrication of thin film transistors for active matrix liquid crystal displays and efficient solar cells. Typically, nanosecond or microsecond lasers are utilized to crystallize such films through a rapid melting and solidification process. Methods of using a laser to crystallize a material surface are also disclosed by U.S. Patent No. 6,169,014 to McCulloch, U.S. Patent No. 6,451,631 to Grigoropoluos et al., U.S. Patent No. 6,489,188 to Jung, and U.S. Patent No. 6,635,932 to Grigoropoluos et al.

[0006] Methods of using an ultrafast laser to texture the surface of crystalline bulk silicon are disclosed in U.S. Patent Application No. 10/155,429 to Mazur. Mazur discloses a method of texturing the surface of a silicon substrate by irradiating the surface with ultra-short laser

SAMSUNG EX. 1002 - 2301/4148

pulses in the presence of a background gas, such as SF_6. After texturing, the silicon surface in Mazur contains cone-like microstructures that are up to 50 μm high, and have widths of about 0.8 μm near the tip and up to 10 μm near the base. Also, Mills and Kolasinski disclose nanospikes formed atop silicon pillars when the sample is exposed to SF_6 gas diluted with helium (17 Nanotechnology 2471, 2006). Further, Vorobyev and Guo disclose the formation of nanoprotrusions with spherical tips on copper, gold, and platinum surfaces by using a femtosecond laser ablation technique (14 Optics Express 2164, 2006).

[0007] While the prior art discussed above provides important advantages, it suffers from a number of drawbacks. The prior art fails to disclose a method of producing periodic arrays of pillar structures on a surface of a material by texturing the surface. Further, the prior art does not teach a method of texturing and crystallizing a surface in one step. Also, the prior art does not teach a method of forming pillar structures on metal surfaces. In addition, the prior art fails to disclose a method of utilizing laser texturing and crystallization in many novel applications.

SUMMARY OF THE INVENTION

[0008] Exemplary embodiments of the present invention overcome the above disadvantages and other disadvantages not described above. Also, the present invention is not required to overcome the disadvantages described above, and an exemplary embodiment of the present invention may not overcome any of the problems described above.

[0009] The present invention provides a method for texturing a surface of a semiconductor material, including providing an etching gas in an area around the surface of the material, irradiating a portion of the surface with short laser pulses, and translating at least one of the surface and a laser beam to allow the short laser pulses to impact another portion

SAMSUNG EX. 1002 - 2302/4148

of the surface. This method produces a periodic array of pillar structures on the surface, resulting in changes in properties of the surface.

[0010] According to an aspect of the present invention, the method additionally produces nanospikes atop the pillar structures.

[0011] Also, the present invention provides a method for texturing a surface of a semiconductor material, including providing an etching gas in an area around the surface of the material; irradiating a portion of the surface with short laser pulses while simultaneously crystallizing the portion of the surface; and translating at least one of the surface and a laser beam to allow the short laser pulses to impact another portion of the surface. This method produces pillar structures on the surface, resulting in changes in properties of the surface.

[0012] In addition, the present invention provides a method for texturing a metallic surface, including irradiating a portion of the metallic surface with short laser pulses, and translating at least one of the surface and a laser beam to allow the short laser pulses to impact another portion of the surface. This method produces pillar structures on the surface, resulting in changes in properties of the surface.

SAMSUNG EX. 1002 - 2303/4148

BRIEF DESCRIPTION OF THE DRAWINGS

[0013] The above and other aspects of the present invention will be better understood from a consideration of the following detailed description of exemplary embodiments of the present invention, and the accompanying drawings, in which:

[0014] **FIG. 1** illustrates the components in a surface modification system, according to an exemplary embodiment of the present invention;

[0015] **FIG. 2** illustrates an example of a sample material to which surface modification is performed, according to an exemplary embodiment of the present invention;

[0016] **FIG. 3** is a photograph of a hydrogenated amorphous silicon (a-Si:H) surface, with **FIG. 3(a)** illustrating a non-modified portion, and **FIG. 3(b)** illustrating a modified portion, according to an exemplary embodiment of the present invention;

[0017] **FIG. 4** illustrates scanning electron microscopy (SEM) images of an a-Si:H surface, with **FIG. 4(a)** illustrating a non-modified portion, and **FIG. 4(b)** illustrating a modified portion, according to an exemplary embodiment of the present invention;

[0018] **FIG. 5** illustrates graphical results of absorption versus wavelength for an a-Si:H surface, with **FIG. 5(a)** illustrating the absorption for an untreated sample, and **FIG. 5(b)** illustrating the absorption for a treated sample, according to an exemplary embodiment of the present invention;

[0019] **FIG. 6** illustrates graphical results of an X-ray diffraction pattern for an a-Si:H surface, with **FIG. 6(a)** illustrating the results for an untreated sample, and **FIG. 6(b)** illustrating the results for a treated sample, according to an exemplary embodiment of the present invention;

[0020] **FIG. 7** illustrates graphical results of current versus voltage for an a-Si:H surface with varying light levels, with **FIG. 7(a)** illustrating the results for an untreated control sample,

SAMSUNG EX. 1002 - 2304/4148

and **FIG. 7(b)** illustrating the results for a treated sample, according to an exemplary embodiment of the present invention;

[0021] FIG. 8 illustrates an atomic force microscope image of an a-Si:H surface that has been treated according to an exemplary embodiment of the present invention;

[0022] FIG. 9 is a graph illustrating the average roughness of laser treated a-Si:H surfaces at different laser fluences, according to an exemplary embodiment of the present invention;

[0023] FIG. 10 illustrates results of X-ray photoelectron spectroscopy (XPS) measurements of a-Si:H surfaces, with **FIG. 10(a)** illustrating the XPS measurement of untreated control surfaces, **FIG. 10(b)** illustrating the XPS measurement of treated surfaces, and **FIG. 10(c)** illustrating depth profiles of oxygen concentration for untreated control and treated surfaces, according to an exemplary embodiment of the present invention;

[0024] FIG. 11 is a graph illustrating the reflectivity of surfaces of polished silicon, unpolished silicon, and treated a-Si:H surfaces, according to an exemplary embodiment of the present invention;

[0025] FIG. 12 is a graph illustrating the transmission of samples of unpolished silicon and treated a-Si:H surfaces, according to an exemplary embodiment of the present invention;

[0026] FIG. 13 illustrates SEM images of germanium surfaces, with **FIG. 13(a)** illustrating an SEM image viewed at 45° from the surface normal, **FIG. 13(b)** illustrating a higher magnification SEM image showing nanospikes formed on each germanium pillar, **FIG. 13(c)** illustrating a single nanospike of a treated sample, and **FIG. 13(d)** illustrating a nanotip formed after brief chemical etching, according to exemplary embodiments of the present invention;

[0027] FIG. 14 shows a comparison of SEM images viewed at 45° from the surface normal of Ge (100) surfaces irradiated at different laser power levels, with **FIG. 14(a)** showing a surface irradiated with a laser power of 0.66 J/cm^2, **FIG. 14(b)** showing a surface irradiated

SAMSUNG EX. 1002 - 2305/4148

with a laser power of 0.56 J/cm^2, **FIG. 14(c)** showing a surface irradiated with a laser power of 0.3 J/cm^2, and **FIG. 14(d)** showing a surface irradiated with a laser power of 0.2 J/cm^2, according to embodiments of the present invention;

[0028] FIG. 15 is graphical representation of an X-ray diffraction pattern of a laser treated germanium surface having nanospikes, according to an exemplary embodiment of the present invention;

[0029] FIG. 16 illustrates SEM images of treated surfaces, with **FIG. 16(a)** illustrating an image taken towards the edge of the scanned line for a Ge (100) surface, **FIG. 16(b)** indicating ball formation instead of spikes for a Ge (100) surface, and **FIG. 16(c)** illustrating an image taken in the middle of the scanned line for a Si (100) surface, according to exemplary embodiments of the present invention;

[0030] FIG. 17 illustrates SEM images of pillars, viewed at 45° from the surface normal, formed on a silicon surface, with **FIG. 17(a)** illustrating an SF_6 gaseous environment, and **FIG. 17(b)** illustrating an HCl gaseous environment, according to exemplary embodiments of the present invention;

[0031] FIG. 18 illustrates SEM images of pillars, viewed 45° from the surface normal, formed on a germanium surface, with **FIG. 18(a)** illustrating an SF_6 gaseous environment, and **FIG. 18(b)** illustrating an HCl gaseous environment, according to exemplary embodiments of the present invention;

[0032] FIG. 19 illustrates SEM images periodic structures formed on a silicon surface, with **FIG. 19(a)** illustrating a one-dimensional periodic structure, and **FIG. 19(b)** illustrating a two-dimensional periodic structure, according to embodiments of the present invention;

[0033] FIG. 20 illustrates SEM images of titanium surfaces, with **FIG. 20(a)** illustrating a titanium surface treated in air, **FIG. 20(b)** illustrating a titanium surface treated in vacuum, **FIG. 20(c)** illustrating a titanium surface treated in helium, and **FIG. 20(d)** illustrating a

SAMSUNG EX. 1002 - 2306/4148

titanium surface treated in SF_6, according to exemplary embodiments of the present invention;

[0034] FIG. 21 illustrates SEM images of stainless steel surfaces, with **FIG. 21(a)** illustrating a stainless steel surface treated in air, **FIG. 21(b)** illustrating a stainless steel surface treated in vacuum, **FIG. 21(c)** illustrating a stainless steel surface treated in helium, and **FIG. 21(d)** illustrating a stainless steel surface treated in SF_6, according to exemplary embodiments of the present invention;

[0035] FIG. 22 illustrates SEM images viewed at 45° from the surface normal, with **FIG. 22(a)** illustrating a treated SiC surface, **FIG. 22(b)** illustrating a treated GaAs surface, **FIG. 22(c)** illustrating a treated titanium surface, and **FIG. 22(d)** illustrating a treated stainless steel surface, according to exemplary embodiments of the present invention;

[0036] FIG. 23 is a schematic representation of field emission from the treated surface, according to exemplary embodiments of the present invention;

[0037] FIG. 24 is a schematic representation of reflectivity and absorption of the treated surface, according to exemplary embodiments of the present invention;

[0038] FIG. 25 is a schematic representation of the effect on external flow by the treated surface, according to exemplary embodiments of the present invention;

[0039] FIG. 26 is a schematic representation of photovoltaic and photodetection applications using the treated surface, according to exemplary embodiments of the present invention;

[0040] FIG. 27 is a schematic representation of heat dissipation using the treated surface, according to exemplary embodiments of the present invention;

[0041] FIG. 28 is a schematic representation of surface marking created by surface alternations, according to exemplary embodiments of the present invention; and

SAMSUNG EX. 1002 - 2307/4148

[0042] FIG. 29 is a schematic representation of the placement of chemical or biochemical materials at the tips on the treated surface, according to exemplary embodiments of the present invention.

DETAILED DESCRIPTION OF EXEMPLARY EMBODIMENTS OF THE INVENTION

[0043] In describing an exemplary embodiment of the present invention illustrated in the drawings, certain specific terminology will be used for the sake of clarity. However, the invention is not intended to be limited to that specific terminology, and it is to be understood that the terminology includes all technical equivalents that operate in a similar manner to accomplish the same or a similar result.

[0044] Apparatuses and methods consistent with the present invention texture and crystallize the surface of a material in one step by exposing the surface of the material to an ultrafast laser. In order to expose an area of the surface that is larger than the beam spot size, the material may be translated relative to the laser. The texturing causes pillars to form on the surface of the material, increasing the light absorption of the treated material. Pillars are height variations over a surface, including valleys and hills. Pillars can be formed in a variety of shapes, including conical, arrowhead, pyramid, and spheroid structures. The top of the pillar has a narrower diameter than the bottom of the pillar. Additionally, crystallization increases the electrical conductivity of the treated material. Texturing and crystallizing the surface of the material in a single step allows for faster manufacturing and lower costs than performing these steps separately.

[0045] The texturing and crystallization may be performed under atmospheric conditions, or while the material to be treated is in a non-atmospheric gaseous environment. In such a gaseous environment, additional surface texturing will occur through chemical etching. Sulfur hexafluoride and hydrogen chloride gases have been examined, and have been shown

SAMSUNG EX. 1002 - 2308/4148

to be suitable gases in which to perform the surface texturing. Hydrogen chloride is advantageous over sulfur hexafluoride, because when sodium hexafluoride is used, impurities in the material may result. In contrast, when hydrogen chloride is used, no impurities are created, and the material remains in its pure form. It is to be understood that other gases may also be used. Surface texturing and crystallization have also been achieved in a helium gas environment and in a vacuum.

[0046] The materials that have undergone surface texturing and crystallization are also within the scope of the present invention. For amorphous materials, the surface will become textured and the material will become crystallized. Hydrogenated amorphous silicon has been examined using the method of the invention, and has been shown to be well-suited to benefit from this method. Thin-film, poly-crystalline, and single crystal materials may also be used. These materials will benefit from the surface texturing methods of the present invention. Silicon and germanium have been studied, and have been shown to be suitable materials to undergo the laser treatment method in the presence of sodium hexafluoride gas and hydrogen chloride gas. Metals, dielectrics, and polymers have also been shown to be suited to be textured using the method of the present invention. However, it is to be appreciated that other materials are suited to undergo the laser treatment methods of the present invention.

[0047] Additionally, the use of materials that have undergone the treatment methods of the present invention is within the scope of the present invention. The present invention has many useful applications. The methods described herein will provide for a material with a higher light absorption capacity and a higher electrical conductivity than an untreated material. These two properties are desirable in photovoltaic applications. Enhanced light trapping capabilities are also useful in photo-sensing applications. Photodetectors utilizing

SAMSUNG EX. 1002 - 2309/4148

the present invention will be more sensitive to light, and will be able to detect a broader spectrum of electromagnetic waves.

[0048] The surface texturing greatly enhances the heat transfer capability of a given material. A material that has been textured can dissipate more heat through convection because of the increased surface area of the material that is exposed to a fluid flowing over the material. Additionally, the texturing will ensure a turbulent flow of the fluid, which is advantageous in convection heat transfer. For radiation heat transfer, the increased surface area will allow for more heat dissipation.

[0049] In an exemplary embodiment of the present invention, the surface alteration process was performed on hydrogenated amorphous silicon (a-Si:H), in particular a-Si:H thin films. Thin films with thicknesses from 1.5 to 2 μm were deposited on glass substrates, using a low temperature Plasma Enhanced Chemical Vapor Deposition (PECVD) technique. The a-Si:H films were deposited at a rate of around 1 Å/s in a hydrogen diluted silane environment at about 200°C. The samples were then treated using a femtosecond Ti:Sapphire laser system (Spectra-Physics Spitfire). The laser system delivered pulses at a repetition rate of 1 kHz, with a pulse energy that could vary from 0-1.2 mJ, and a wavelength of 800 nm. The wavelength of the laser can also be frequency doubled or halved to achieve wavelengths from 200 to 1600 nm. The temporal profile of the pulses was measured to be 110 fs using a background free, scanning second-order auto-correlator. The sample was placed on a stationary stage, and the laser beam was deflected by a Scanlab galvo-head to scan the sample surface. The beam spot on the sample surface was circular, with a beam diameter of 0.5 mm. The beam scanning speed was around 12.5 cm/sec. Scanning electron micrographs of treated and untreated surfaces of the a-Si:H films were taken using a Cambridge Instruments high resolution electron microscope for a surface texture study.

SAMSUNG EX. 1002 - 2310/4148

Surface roughness and formation of spikes in the treated films were also examined with an atomic force microscope (Digital Instruments Nanoscope III).

[0050] The optical transmission and reflection of a 20 mm × 30 mm laser treated area of the sample was measured using a PERKIN-ELMER LAMBDA 9 spectrophotometer. The reflectance and transmittance percentages were then used to obtain the absorption percentage in the material: $A = 100 - R - T$. Light from a He-Ne laser source was incident on the treated sample at different angles, and the scattered light was measured by a silicon sensor with an active region of around 4 cm^2 to estimate the scattering of light due to texturing. It was observed from the measurements that scattering might contribute to a 5-10% variation in the reflection measured by the spectrophotometer. In addition to the optical properties, X-ray diffraction (XRD) was performed on the untreated and laser treated samples to study the structural modification induced by the laser treatment. The Rigaku Miniflex 2005 X-ray diffractometer with a Cu target (CuK_α-line) was used for the XRD measurements. The grain size of the treated films was estimated from the X-ray data. Also, the oxygen incorporation into silicon films during this ultrafast laser treatment was studied using a Physical Electronics Inc. 560 XPS/SAM spectrophotometer with a dual source anode (Mg/Al) radiating 1253.6 eV X-ray photons.

[0051] FIG. 1 shows an exemplary system 100 that can be used to provide surface modifications. The femtosecond laser system 101 provides a laser pulse incident on the a-Si:H sample 105, which is supported by an X-Y sample stage 106. The system 100 uses a mirror 102 to direct the laser pulse to a galvo-head unit 103, which scans the sample surface. A focusing lens 104 is used to focus the pulses on the surface. An exemplary a-Si:H sample 200 is illustrated in FIG. 2, with a glass slide 205, an intervening layer 204, and amorphous silicon layers 201-203.

SAMSUNG EX. 1002 - 2311/4148

[0052] FIG. 3 illustrates that the change in the surface of the a-Si:H film deposited on the glass substrate can be observed optically. FIG. 3(a) shows a photograph of the untreated surface, and FIG. 3(b) shows a photograph of the treated surface. After treatment, the a-Si:H films turned completely dark, in contrast with their original shiny reddish gray color. FIG. 4(a) shows an SEM image of the untreated surface, and FIG. 4(b) shows an SEM image of the treated surface. FIG. 4(b) shows that microstructures and small spikes have been spontaneously formed upon laser treatment.

[0053] In order to study the optical characteristics, the reflectance and transmittance of a treated 20 × 30 mm^2 area were measured using a spectrophotometer. FIG. 5 shows the absorptance of treated and untreated a-Si:H films. FIG. 5(b) that there is a significant enhancement in the optical absorption below a-Si:H band gap (1.7 eV) for treated films, when compared to the untreated films in FIG. 5(a). Since the experiments were carried out under atmospheric conditions, XPS spectra of a treated sample (FIG. 10(b)) and an untreated control sample (FIG. 10(a)) were also obtained. SiO_x formation was observed in the treated sample. The oxygen concentration was estimated by taking XPS measurements at different depths of the sample. Depth profiles of the oxygen concentration in the treated and untreated control samples are shown in FIG. 10(c). Traces of oxygen were observed up to a depth of around 50 nm in treated samples, compared to a depth of 10 nm in the untreated control sample. The samples appeared to be pitch black after treatment, and it is suggested that the below-band edge absorption might be due to trapping the light, which is caused by multiple reflections from the textured surface. Also, structural defects induced during the micro-structuring process most likely produce bands of defect and impurity states in the bandgap, and further enhance the overall absorption.

[0054] FIG. 6(a) shows the X-ray diffraction pattern for an untreated a-Si:H sample, and FIG. 6(b) shows an X-ray diffraction pattern for a treated a-Si:H sample. Peaks around 2θ =

SAMSUNG EX. 1002 - 2312/4148

30° and 56° are observed for the treated sample. These peaks are absent in the untreated control sample, indicating a structural change after laser treatment. The X-ray wavelength used for these measurements was the CuK_{α} line at 1.54 Å. The observed peaks are due to the (111) and (311) orientations of crystalline silicon. Regardless of the fluence conditions, the (111) orientation dominated in the crystallized films, as the (111) plane has least surface energy. Dominant (111) and (311) peak formation is typically observed in nanosecond laser crystallization. The (111) peak was fitted with a Gaussian curve and the full width at half-maximum (FWHM) was determined. The particle size was determined to be around 85 nm using the Scherrer's formula: $L = k^*\lambda / \Gamma \cos\theta$; where λ is the X-ray wavelength for measurement; Γ is the X-ray line width (FWHM) (measured in radians); θ is the Bragg angle of diffracted rays (measured in degrees); and k is a constant equal to 0.9.

[0055] The current-voltage characteristics of the treated and untreated a-Si:H samples were also examined, as shown in FIG. 7. FIG. 7(a) shows a graph of the current density as a function of voltage for several light levels for the untreated sample. As illustrated in FIG. 7(b), the current-voltage characteristics change considerably, due to the surface modification and changes in the properties of the material. The transmission and reflectivity of the treated and untreated surfaces were also examined. The reflectivity of polished silicon, unpolished silicon, and treated silicon with pillars is shown in FIG. 11. Similarly, the transmission of the treated silicon versus the rough silicon surface is presented in FIG. 12. The changes in the optical properties shown in FIG. 3 are further substantiated by the changes in reflectivity and transmission as functions of wavelength. These results impact the use of silicon in many applications, as discussed below.

[0056] In order to measure the roughness and spike distribution, atomic force microscopy (AFM) images of the treated a-Si:H samples were obtained. FIG. 8 shows that spikes of a height of about 300 nm were formed, with a spacing between the tips of around 1 μm. The

SAMSUNG EX. 1002 - 2313/4148

heights of these spikes were found to increase with laser fluence. The average height of the microstructures was 150 nm at a laser fluence of 0.3 J/cm^2, and the height increased nearly linearly with the laser fluence. Microstructures with a height of around 350 nm were observed at a fluence of 0.5 J/cm^2. Beyond 0.5 J/cm^2, the films became very rough, and material ablation deteriorated the texturing. Also, the average roughness of the surface correlates with the laser fluence, as illustrated in the graph in FIG. 9. FIG. 9 shows that the surface roughness increases approximately linearly with the laser fluence.

[0057] Increasing the efficiency of a-Si:H thin film solar cells requires more light absorption and a reduction in carrier recombination. A thick i-layer increases the light absorption, but recombination deteriorates the performance. On the other hand, for sufficiently thin film solar cells, the light absorption becomes an issue. Keeping a thin micro or nano crystalline phase with surface texturing could both reduce recombination and improve light trapping. The treated surface had a silicon oxide formation layer of about 50 nm, and was found to be semiconducting. This layer could be used as an n-layer in a p-i-n type solar cell, and an active layer for other optoelectronic devices. The simultaneous formation of light trapping structures and crystallization might find applications in devices such as thin film solar cells, large area sensors, and display devices.

[0058] As discussed previously, the femtosecond laser treatment results in the enhancement of optical absorption in a-Si:H thin films. The high absorption of the film is suggested to be due to the light trapping occurring in the silicon spikes formed at the surface after laser treatment, and the structural defects induced during micro structuring process most likely producing bands of defect and impurity states in the band gap. Also, crystallization in the film after femtosecond laser treatment is attributed to a non-thermal ultrafast phase transition and subsequent surface-initiated crystallization. By performing the surface

SAMSUNG EX. 1002 - 2314/4148

texturing and crystallization as a one-step laser process, optoelectronic devices can be fabricated efficiently.

[0059] Exemplary embodiments of the present invention also form nanospiked, nearly periodic microstructures, by exposing a germanium surface to femtosecond laser pulses in a gaseous sulfur hexafluoride (SF_6) environment. The microstructures that are formed in germanium have a different aspect ratio than the microstructures formed on silicon. Because reducing light reflection and increasing absorption are key issues in improving optoelectronic device performance, this type of microstructure formation in germanium could lead to the fabrication of highly responsive infrared photodetectors and solar cells. In addition, these textured surfaces might find potential applications in the fabrication of biomedical devices and sensors.

[0060] The surface modification of germanium can occur according to the following process. Undoped Ge (100) wafers are cleaved into small chips and ultrasonically cleaned with acetone and methanol. One or more chips are put on a stage inside a vacuum chamber with a base pressure of around 1 mTorr, which is mounted on a high-precision computer-controlled X-Y stage. The chamber is rinsed with SF_6 at least twice, and then backfilled with SF_6 at 400 mbar. The samples are exposed to 1.4 mJ pulses of light with a wavelength of 800 nm, a pulse duration of 130 fs, and a repetition rate of 1 kHz from a regeneratively amplified Spectra-Physics Ti-sapphire laser system. The wavelength of the laser can be frequency doubled or halved to achieve wavelengths from 200 to 1600 nm. Short laser pulse widths can also be used, including 1 fs to 1 μs pulses. Ultrafast laser pulses are a subcategory of short pulses, and can range from 1 femtosecond to hundreds of picoseconds. The laser beam is focused along the surface normal onto the sample surface by a coated lens with a focal length of 1 m, and the laser fluence is adjusted with a Glan laser calcite polarizer.

SAMSUNG EX. 1002 - 2315/4148

[0061] The spatial profile of the laser pulse is nearly Gaussian, but is elongated in one axis, creating an elliptical profile. The fluence is calculated by using the laser spot size, which is determined by exposing a point on the sample surface to thousands of shots. In order to scan an area that is bigger than the laser spot size, the samples are translated using a motorized X-Y stage. Scanning also assists in making the surface structure more uniform by smoothing out any shot-to-shot irregularities in the beam profile. By varying the scanning speed of the X-Y stage, the number of laser pulses impinging on the sample surface at a particular location is controlled. The spot size is 0.3 mm along the minor axis and 0.6 mm along the major axis. Scanning is performed parallel to the minor axis.

[0062] Samples are produced with isolated single line scans, or with large areas created by overlapping several line scans. The step size between the scan lines is chosen to be sufficiently small (generally 0.38 mm), so that successive lines overlap substantially. This further improves layer homogeneity. Homogeneity is further enhanced by performing two overlapping scans in orthogonal directions, rather than one overlapping scan with an exposure of the same total number of shots. After laser processing, the samples are analyzed with a scanning electron microscope (Zeiss SUPRA 40).

[0063] FIG. 13 shows an SEM image at increasing levels of magnification, viewed at 45° from the surface normal line of a germanium surface after exposing the surface to femtosecond laser pulses. Sharp conical structures with nanospikes are formed when the sample is under a pressure of 400 mbar SF_6, and is scanned by a laser beam with a fluence of about 0.6 J/cm^2. FIG. 13 shows that these structures are almost regular in position, are 10 to 15 μm tall, and have a base diameter around 5 μm, which tapers down to around 100 nm near the tip. The areal density of pillars in FIG. 13(a) is 0.027 μm^{-2}, which corresponds to a mean spacing of roughly 6 μm between pillars. The sizes of the microstructures vary across the scanned line, indicating a response to the spatial profile of the laser pulse. In the region of

SAMSUNG EX. 1002 - 2316/4148

low fluence towards the edge of the irradiated line, the structures have a smaller height and are more densely packed than in the center.

[0064] FIG. 13(b) shows that the microstructures have two distinct features: (a) a conical shape (b) that is crowned with a very sharp spike, which has a radius of about 400 nm (about 100 nm at the tip), and is up to about 2 μm long (see FIG.13(c)). The tips can be sharpened further by a brief chemical etching with 100 ml H_2O_2 (10 vol %), 8g NaOH for 10 seconds at room temperature. Alternatively, the tips can be sharpened further by ion etching, including etching with an Argon ion beam. Nanoclusters, which are formed during laser ablation and deposited on the surface, are also evident from FIG. 13(b).

[0065] The SEM images of FIG. 14 show the effect of laser fluence on the surface texturing of germanium. In this figure, the average number of laser shots at each point on the sample surface is 400. The germanium surface in FIG. 14(a) was irradiated with laser pulses with a fluence of 0.66 J/cm^2, and the germanium surface in FIG. 14(b) was irradiated with laser pulses with a fluence of 0.56 J/cm^2. In contrast, the germanium surface in FIG. 14(c) was irradiated with laser pulses with a fluence of 0.3 J/cm^2, and the germanium surface in FIG. 14(d) was irradiated with laser pulses with a fluence of 0.2 J/cm^2. FIG. 14(d) shows that texturing is observed at fluences as low as 0.2 J/cm^2, resulting in features are smaller in width and height, less regular, less smooth, and densely populated, with very tiny or no spike formation. However, for higher fluence conditions, such as those in Figs. 14(a) and 14(b), the structures are more well-developed, sharper, and more conical, and spike-formation takes place atop the pillars. Also, increasing the number of laser shots from 400 to 600 and keeping the fluence almost the same wipes out all the spikes.

[0066] Germanium expands upon freezing. When a shell of germanium material starts freezing and expanding, it exerts pressure on the liquid trapped inside, causing the liquid to shoot upward and solidify to form nanospikes. As Mills and Kolasinski disclose, in order to

SAMSUNG EX. 1002 - 2317/4148

obtain nanospikes in silicon, it is necessary to dilute the SF_6 with He. This reduces the chemical etching that results from the interaction of fluoride with the silicon surface. If the etching is too aggressive, it can remove the nanospikes. In contrast, it is unnecessary to dilute the SF_6 in order to obtain nanospikes on a germanium sample, probably because of differences in the chemistry of etching in the F/Ge system compared to the F/Si system. Another possible reason why germanium appears to be more conducive for nanospike formation might be that the thermal conductivity of undoped germanium is less than half of the thermal conductivity of undoped silicon. Therefore, the heat dissipation to the pillar in germanium is slower, and the liquid bulb remains in a molten state for a longer time, as compared to silicon.

[0067] In order to investigate the properties of the textured germanium surfaces, an X-ray diffraction study was conducted. FIG. 15 shows an X-ray diffraction spectrum of a laser textured germanium surface. The sharp high-intensity peak corresponds to the (400) plane, because the starting material is Ge (100). However, two relatively weak peaks at (111) and (220) are also observed. This indicates that the textured pillars and the nanospikes remain predominantly crystalline.

[0068] The SEM images of FIGs. 16(a) and 16(b) show the structural formations in germanium, and FIG. 16(c) compares the structural formations in silicon, after laser treatment under similar conditions. For all three samples the laser fluence was around 0.56 J/cm^2, the number of laser shots was around 600, the sample was in a gaseous SF_6 environment at 400 mbar, and an orthogonal scanning mode was used. The SEM image in FIG. 16(a) was taken toward the edge of the scanned line, while the SEM image in FIG. 16(b) was taken in the middle of the scanned line. FIG. 16 shows that the germanium pillars are not as smooth as the silicon pillars. Also, the aspect ratio, defined as the ratio of the tip height to the tip width, is higher in silicon than germanium for a given laser condition. For example, at a fluence of

SAMSUNG EX. 1002 - 2318/4148

0.5 J/cm^2, silicon has an aspect ratio of around 200, whereas germanium has an aspect ratio of around 100. Also, as mentioned previously, spikes were not formed on germanium under higher laser shot conditions. However, pillars formed under higher laser shot conditions are taller than pillars formed under fewer shots, as shown in FIGs. 13 and 14. In contrast, silicon shows a well-developed smooth structure under a greater variety of shot conditions.

[0069] FIG. 16(a) shows that toward the edge of the laser scanned line on the germanium surface, pyramidal structures were formed, which tend to form a small spherical cap at the top, instead of the nanospikes formed in FIG. 16(b). This spherical cap formation is typical of silicon. The spherical shape of the cap suggests that a liquid germanium drop resolidified before it could spill over the pillar. The lack of nanospikes in FIG. 16(a) might be due to three possible reasons: (a) the fluence is low to achieve the high melting condition necessary for nanospike formation; (b) the higher number of laser shots destroyed nanospikes that were already formed; or (c) an insufficient density of nanostructures was formed. With further regard to (c), deposition of nanoclusters has been implicated in the formation of nanospikes. A sufficient nanoclusters deposition rate is required, and because fewer nanoclusters are formed at a lower fluence, there may be a critical fluence for the formation of nanospikes, not only because a sufficient melt must be formed, but also because a sufficient density of nanoclusters must be created.

[0070] FIG. 17 shows SEM images viewed at 45° from the surface normal of sharp conical pillars formed on the surface of B-doped Si (100) wafers. The pillars were produced with 240 shots of 130-fs laser pulses at a fluence of 0.6 J/cm^2. FIG. 17(a) shows the results for a sample in 400 mbar of SF_6, and FIG. 17(b) shows the results for a sample in 400 mbar of HCl. The pillar size varies across the scanned laser line, indicating the intensity variation of the laser fluence across the spatial profile of the laser pulse. The scan lines were

SAMSUNG EX. 1002 - 2319/4148

overlapped to minimize height variation over a large area on the sample surface. The spikes that are obtained in SF_6 are around 15 μm tall and have a base diameter of around 5 μm.

[0071] On the other hand, the structures formed under similar laser conditions in the presence of HCl are composed of taller and wider pillars, with a height of around 20 μm and a base diameter of around 7 μm. FIGs. 17(a) and 17(b) show that the pillars formed in SF_6 are narrower towards the tips, compared to the pillars formed in HCl. Although the pillar density is comparable in both cases, the pillars formed in HCl look stronger and are relatively blunt towards the tip, indicating that differences in the etch chemistry of the F/Si system and the Cl/Si system are responsible for significant structural differences.

[0072] The role of chemistry in structure formation is not well understood, and it is a significant result that regular conical pillars are formed during femtosecond irradiation in SF_6 as well as HCl. Regular conical pillars can be formed during nanosecond irradiation of silicon in the presence of SF_6, but they are not formed for nanosecond irradiation of silicon in the presence of HCl. Nanosecond irradiation of silicon in HCl produces significantly blunter tips, the pillars are much taller, with a height greater than 50 μm, and the pillars are porous, instead of having a solid core. This is a further indication that the mechanisms of pillar formation are different for the femtosecond and nanosecond irradiation regimes. This result is also significant because chemical impurities, namely sulfur, incorporated during laser processing have been implicated in changing the optical and electronic properties of the textured surfaces.

[0073] FIG. 18 shows SEM images taken for germanium samples treated under similar laser and gaseous conditions as described above for silicon. A very different surface texturing was created for germanium. FIG. 18(a) shows that for germanium processed in SF_6, there were two distinct features that were not observed for silicon treated under similar conditions: (a) conical pillar formation with a higher cone angle up to a neck; and (b) very

SAMSUNG EX. 1002 - 2320/4148

sharp spikes, up to about 2 μm in length with a tip radius of about 100 nm, formed atop the pillars. Nanoclusters formed during laser ablation are more abundant in germanium than silicon under similar laser conditions, which might be due to the lower melting temperature of germanium. On the other hand, FIG. 18(b) shows that the germanium structures formed in the presence of HCl are less densely populated, shorter, have a higher cone angle and a wider base, and exhibit greater variations in pillar height than the silicon structures shown in FIG. 17(b). Gas phase silicon etching is anisotropic in HCl, and the etch rate is around 20 μm min^{-1} for the (100) plane at temperatures in the range of 1050–1250°C, whereas in germanium the etch rate is around 3 μm min^{-1}, the etch rate is independent of temperature beyond 800°C, and etching leads to the development of square pits for the (100) orientation. The differences in etch chemistry are involved in determining the different structure formation dynamics, which result in more regular spike formation in HCl for silicon than for germanium.

[0074] Laser induced surface texturing that produces regular structures on materials in the presence of reactive species is a complex process involving: (1) interactions between the plume and the process gas, and the plume and the surface, such as decomposition of the reactive gas, chemical etching enhanced by laser heating of the material and the formation of radicals, and deposition out of the plume; (2) laser ablation of the material; and (3) optical phenomena that initiate the formation of regular structures. The laser parameters, gaseous environment, and nature of the substrate all play a role in the final outcome of the surface morphology. Structure formation is ultimately a convoluted dynamical process involving all three factors. The dimensions and character of the pillars formed in silicon have been shown to depend critically on the temporal pulse width of the laser beam. While pillar production with pulse durations in the range of 100 fs to 20 ns has been demonstrated, with much smaller pillars being formed in the case of femtosecond irradiation, pillars were not producible with a

SAMSUNG EX. 1002 - 2321/4148

300 ns Nd:VO_4 laser. It appears that laser pulses significantly shorter than the melt lifetime of about 250 ns are required for sharp pillar formation.

[0075] FIG. 19(a) illustrates an SEM image of a one-dimensional periodic structure made on a silicon substrate, according to exemplary embodiments of the present invention. FIG. 19(b) illustrates an SEM image of a two-dimensional periodic structure made on a silicon substrate, according to exemplary embodiments of the present invention. Periodic structures can be produced by controlling the laser intensity distribution on the surface of the sample. The laser intensity distribution can be controlled by using interference and diffraction. For example, interference fringes are created by placing a metal wire in a portion of the laser beam. The light diffracted by the wire interferes to produce an intensity distribution on the sample surface that results in a periodic structure of pillars. Alternatively, the incident laser beam is split into two components, and then recombined at various angles to control the periodicity. It is also possible to place several pinholes in the path of the laser beam to create a periodic circular pattern of pillars on the surface. By using laser beams with different wavelengths and controlling the interference patterns, the periodicity of the pillars can be adjusted from tens of nanometers to tens of micrometers.

[0076] In an exemplary embodiment of the present invention, copper or tungsten wires with diameters from 100 to 250 μm are used to create interference fringes. The sample is exposed to 1.4 mJ pulses of light with a wavelength of 800 nm, a pulse duration of 130 fs, and a repetition rate of 1 kHz. The laser scan speed is 0.1 in/sec, and scanning is performed after placing the sample inside a vacuum chamber filled with SF_6 at a pressure of 400 mbar. In order to create a two-dimensional array of pillars, the metal wires are crossed orthogonally and placed in the path of the laser beam. Also, the spacing between adjacent pillars can be controlled by changing the wavelength of the laser pulses. For example, when the laser wavelength is decreased, the spacing between adjacent pillars also decreases.

SAMSUNG EX. 1002 - 2322/4148

[0077] In another exemplary embodiment of the present invention, the laser texturing method was performed on various metallic surfaces. A metal is defined as an electrically conducting material. For example, titanium and stainless steel sheets are cut into small square-inch sized chips and cleaned with acetone and methanol. One such chip is put on a stage inside a vacuum chamber with a base pressure of around 1 mTorr, which is mounted on a high-precision computer-controlled X-Y stage. The chamber is rinsed and then backfilled with air at atmospheric pressure, SF_6 in a pressure range from 75 to 800 mbar, or helium in a pressure range from 75 to 800 mbar. The laser texturing method can also be conducted with a mixture of gases in different proportions and at different pressures, or in vacuum, with a chamber pressure of around 1 mbar. The samples are exposed to ultrafast laser pulses with a pulse energy of 0.95 mJ, a wavelength of 800 nm, a pulse width of 130 fs, and a repetition rate of 1 kHz from a regeneratively amplified Spectra-Physics Ti-sapphire laser system. Short laser pulse widths can also be used, including 1 fs to 1 μs pulses. Ultrafast laser pulses are a subcategory of short pulses, and can range from 1 femtosecond to hundreds of picoseconds. The laser beam is focused onto the sample surface by a coated lens with a focal length of 1 m, and the laser fluence is adjusted by using a Glan calcite polarizer.

[0078] The spatial profile of the laser pulse is Gaussian, and the fluence is calculated by using the laser spot size, which is determined by exposing a point on the sample surface to thousands of shots. In order to scan an area that is bigger than the laser spot size, the samples are translated using a motorized X-Y stage. Scanning also assists in making the surface structure more uniform by smoothing out any shot-to-shot irregularities in the beam profile. By varying the scanning speed of the X-Y stage, the number of laser pulses impinging on the sample surface at a particular spot is controlled. The spot size is about 0.3 mm.

[0079] Samples are produced with isolated single line scans, or with large areas created by overlapping several line scans. The step size between scan lines is chosen to be

SAMSUNG EX. 1002 - 2323/4148

sufficiently small (less than 0.38 mm), so that successive lines overlap substantially. This further improves layer homogeneity. Homogeneity is further enhanced by performing two overlapping scans in orthogonal directions, rather than one overlapping scan with an exposure of the same total number of shots. After laser processing, the samples are analyzed with a scanning electron microscope (Zeiss SUPRA 40).

[0080] FIG. 20 shows SEM images of titanium surfaces treated with the laser texturing method for different background gas conditions. FIG. 20(a) shows an SEM image of a titanium surface treated in air, and FIG. 20(b) shows an SEM image of a titanium surface treated in vacuum. FIG. 20(c) shows an SEM image of a titanium surface treated in helium at a pressure less than 200 mbar, and FIG. 20(d) shows an SEM image of a titanium surface treated in SF_6 at a pressure greater than 400 mbar. As these figures show, pillar formation occurs in titanium that is treated with a laser fluence from 0.6 to 1.0 J/cm^2, and in vacuum or gas at low pressures less than 200 mbar. In order to create a well-developed pillar on titanium, it is necessary to irradiate the sample with around 1000 shots. However, increasing the number of shots or the laser fluence destroys the pillars.

[0081] FIG. 21 shows SEM images of stainless steel surfaces treated with the laser texturing method for different background gas conditions. FIG. 21(a) shows an SEM image of a stainless steel surface treated in air, and FIG. 21(b) shows an SEM image of a stainless steel surface treated in vacuum. FIG. 21(c) shows an SEM image of a stainless steel surface treated in helium at a pressure less than 200 mbar, and FIG. 21(d) shows an SEM image of a stainless steel surface treated in SF_6 at a pressure greater than 400 mbar. As shown in the figures, laser texturing forms pillars on stainless steel surfaces in air, vacuum, helium, and SF_6. However, in order to create a well-developed pillar on stainless steel, it is necessary to irradiate the sample with around 2000 shots. Both the stainless steel samples and the titanium

SAMSUNG EX. 1002 - 2324/4148

samples turn pitch black after laser treatment. However, unlike titanium, pillar formation occurs on stainless steel in air.

[0082] FIG. 22 shows a series of SEM images viewed at 45° from the surface normal, which compares the results of the laser texturing method for various semiconductors and metals. In each case the surface of the material is treated with ultrafast laser pulses with a pulse width of 130 fs. FIG. 22(a) shows an SEM image of SiC treated with 260 shots at a laser fluence of around 1 J/cm^2 in 400 mbar of SF_6. FIG. 22(b) shows an SEM image of GaAs treated with 260 shots at a laser fluence of around 0.5 J/cm^2 in 400 mbar of SF_6. FIG. 22(c) shows an SEM image of titanium treated with 2000 shots at a laser fluence of around 0.3 J/cm^2 in 400 mbar of SF_6. FIG. 22(d) shows an SEM image of stainless steel treated with 2500 shots at a laser fluence of around 4.5 J/cm^2 in 400 mbar of SF_6. These figures show that the laser texturing method can form pillars on various semiconductors and metals.

[0083] In addition, the laser texturing method is likely to form pillars on ceramics, polymers, and alloys. By controlling the processing conditions of the laser texturing method for each material, the thermal, structural, optical, and electronic properties of the material can be tailored. Further, the formation of pillars can be controlled by changing the polarization state of the laser beam. A polarizer can change the output from the laser to be linearly, circularly, elliptically, or randomly polarized. The laser texturing method can be performed on surfaces of any geometrical shape, and is not limited to planar surfaces.

[0084] Similarly, the laser texturing method could also be used to process transparent materials, such as glass. The incident light could be absorbed by a two-photon process, or an appropriate wavelength could be selected for absorption by the transparent material. The altered surfaces formed by this method could be used in magnetic disk drives, because the disk drive and the head are spaced very closely together for data writing and reading.

SAMSUNG EX. 1002 - 2325/4148

[0085] The altered surfaces formed by the apparatuses and methods of the present invention can have great utility in photovoltaic technologies, as schematically illustrated in FIG. 26. The increased light trapping and the control of photogenerated charges can provide improved efficiency. In particular, the altered surfaces would be beneficial in photodetectors, because the surfaces allow for the development of more sensitive detectors with a high responsivity, and extend the spectral range into the infrared region of the spectrum. This could also enable the building of infrared sensors for various applications.

[0086] The altered surfaces would also be beneficial in heat dissipation, as schematically illustrated in FIG. 27. A large surface area is created by texturing, which allows gas molecules to exchange energy with the surface, and increases heat dissipation. Such a high-efficiency heat sink could be very important for microelectronics, power electronics, optoelectronics, and other devices that require efficient heat dissipation.

[0087] The altered surfaces can also be used in field emission, as schematically illustrated in FIG. 23. Due to the sharp geometry of pillars formed by the laser texturing process, very high electric fields can be generated at relatively low voltages. These high electric fields can be used for electron emission from surfaces, providing an efficient source of electrons for various electronic and optoelectronic device applications, such as field emission displays, sensors, and instruments.

[0088] The altered surfaces would also be beneficial in surface property control, as schematically illustrated in FIG. 25. Laser textured surfaces can be made hydrophobic or hydrophilic by controlling the texture and surface coating. This can affect the air or fluid flow across the surface of the material.

[0089] The altered surfaces would also be beneficial in micro fluidic applications. There is an increasing number of micro fluidic applications for chemical and biomedical applications of chips. As schematically illustrated in FIG. 25, textured surfaces in micro

SAMSUNG EX. 1002 - 2326/4148

channels can provide a good method of controlling the fluid flow, which can impact DNA sequencing and other applications. The altered surfaces would also be beneficial in turbulence control for aerodynamic applications. The flow of gases can be controlled by inserting a textured surface into the flow path. Also, turbulence can be generated by using of textured surfaces. This effect can be used in aerospace applications.

[0090] The altered surfaces would also be beneficial in an optical beam block, as schematically illustrated in FIG. 24. The laser textured surface has an extremely low reflectance and transmittance in the visible to the far infrared region, allowing the surface to be an efficient beam block for various optical and manufacturing applications. The altered surfaces would also be beneficial in controlling the visual appearance of products, including the surface color. The laser texturing process provides a completely black surface, hence it can be used to control the color of the surface without using any paints, dyes, or pigments.

[0091] The altered surfaces would also be beneficial in catalytic activity, as schematically illustrated in FIG. 29. The large surface area created by texturing provides many sites for enhanced chemical activity, such as catalytic activity. These catalytic activities would be useful in fuel cell technology, chemical plants, and biomedical applications, including conversion of carbon monoxide to carbon dioxide. The large surface area can also be used for enhanced tissue growth and control. The altered surfaces would also be beneficial in bond strength improvement. The large surface area created by texturing allows more sites for bonding and interlocking, and improves the overall bond strength.

[0092] The altered surfaces would also be beneficial in thin film or fibrous whisker growth. Due to the formation of nanospikes or microspikes, it is possible to utilize a large number of tips for growth of other materials atop these tips, as schematically illustrated in FIG. 29. Also, because a small voltage can provide a high electric field, the growth can be controlled by the electric field.

SAMSUNG EX. 1002 - 2327/4148

[0093] The altered surfaces would also be beneficial in the production of nano or micro tips, as schematically illustrated in FIG. 29. Because the texturing process produces a large array of two-dimensional structures, micro or nano ordered tips can be fabricated. The nanospikes can be solid or hollow. These tips can be used in atomic force microscopy, optical data storage, and fluid control for automobiles and drug delivery.

[0094] The altered surfaces would also be beneficial in surface-enhanced Raman scattering. The Raman scattering method can be used to detect chemical or biochemical species. Usually Raman scattering signals are relatively low, but a Raman signal can be enhanced by many orders of magnitude by surface-enhanced Raman scattering. Laser textured surfaces coated with metals could provide an ideal template for surface-enhanced Raman scattering for sensor applications, such as single molecule detection. The altered surfaces would also be beneficial in biosensor applications. As schematically illustrated in FIG. 29, specific molecules can be attached atop the tips, and can be used for chemical or biochemical detection, by using methods such as fluorescence and phosphorescence.

[0095] The altered surfaces would also be beneficial in manufacturing optical elements. As schematically illustrated in FIGs. 24 and 28, various optical elements, such as diffraction gratings, low scattering surfaces, and antireflection surfaces can be prepared by texturing the optical element surface. Also, light absorption properties can be tailored by adjusting the laser parameters and thermal annealing conditions.

[0096] The altered surfaces would also be beneficial in photonic crystals. Photonic crystals are increasingly used for optoelectronic applications, such as wavelength selection and fabrication of negative refractive index materials. Periodic textured surfaces fabricated by laser texturing would be useful in these photonic crystals. The altered surfaces would also be beneficial in producing masters for replication. A textured surface can be used as template for transferring a pattern to a softer material by using mechanical pressure, with or without

SAMSUNG EX. 1002 - 2328/4148

heat. This can provide a very low cost process for pattering surfaces such as compact discs. This process can also be used for transferring patterns to polymerics and biomaterials.

[0097] The altered surfaces would also be beneficial in fabricating mask-less periodic structures. By using an optical interference technique, periodic textured surfaces can be fabricated with a sub-micron period, without any mask fabrication. The altered surfaces would also be beneficial in pixelated devices. Some optoelectronic and microelectronic devices, such as CCD cameras, diode lasers, and light emitting diodes, require a two-dimensional geometry. Two-dimensional textured surfaces can be easily fabricated for optoelectronic and microelectronic applications. The altered surfaces would also be beneficial in producing substrates for single crystal film or nanoparticle growth.

[0098] The altered surfaces would also be beneficial in nano or micro pores. Textured surfaces can be further processed with chemical etching to provide a large number of nano or micro pores, which can be used for filtration or fluid flow control. Pores can be made by the laser texturing process if thin substrates are used, or if longer processing times are used. The altered surfaces would also be beneficial in controlling surface emissivity. By adjusting the surface texture, the surface emissivity and spectral properties can be controlled. This can provide camouflage objects, because such objects are harder to detect if they emit a low radiation signal.

[0099] The altered surfaces would also be beneficial in art and photography applications. As schematically illustrated in FIG. 28, laser texturing of surfaces can be used to write text and images on surfaces by controlling the light reflectivity of the surface. This technique can be used to produce name plates, part identification, hidden logos, trademarks, logos, and images. The texturing provides a black color, which produces a very high contrast between the written and unwritten areas. The process of the present invention can also be used to control the gray level in forming high definition images.

SAMSUNG EX. 1002 - 2329/4148

[00100] The altered surfaces would also be beneficial in radiation shielding. Laser textured surfaces provide a very good method for controlling radiation scattering, reflection, absorption, and transmission over a broad spectral range, including visible, infrared, microwave, terahertz, and radio waves.

[00101] The altered surfaces would also be beneficial in plasma applications. Sharp tips can provide a very high electric field, and hence can be used for localized or large area generation of plasma sources. These plasma sources can be used to purify water, kill germs, and destroy bio-chemical agents.

[00102] The altered surfaces would also be beneficial in protecting substrates from corrosion, and improving adhesion, such as epoxy adhesion to a metal surface. They can also be used to improve the adhesion of thin films to a surface, such as a TiN coating on drill bits, which would extend the lifetime of the drill bits.

[00103] The altered surfaces would also be beneficial in bone grafting applications. Body implants can become detached from the host tissue, due to inadequate biocompatibility and poor osteointegration. Using laser texturing to change the surface chemistry and physical texture of the implants can improve the biocompatibility and adhesion.

[00104] The altered surfaces would also be beneficial in controlling the tribological properties of materials, such as friction, wear resistance, load-bearing properties, and lubrication. The textured surface can act as a micro-hydrodynamic bearing, a micro-reservoir for a lubricant, or a trap for debris particles generated during a sliding or other motion. This could result in significant friction reduction in piston rings. Similarly, laser texturing of cylinder liners in the interior of an engine compartment could reduce wear, friction, oil consumption, and gas emissions.

[00105] Instead of performing the laser texturing method in chemical gases, the method could be performed in the presence of gaseous plasma. Because charged species in gaseous

SAMSUNG EX. 1002 - 2330/4148

plasma can be very reactive, laser irradiation in the presence of gaseous plasma will provide a much faster speed for texture formation, and further enable control of surface properties. Plasma sources can be created by various methods, such as excitation with a radio frequency (RF) source, direct current (DC), alternating current (AC), or a laser system. This approach provides a method for multi-energy processing technology, where electrical energy for plasma or discharge creation, laser irradiation for melting and ablation, and chemical energy by the gaseous environment are utilized to enhance the process and the control of the surface properties. Also, the sample can be kept at elevated temperatures, or the sample surface can be irradiated by an infrared lamp to raise the surface temperature, in order to enhance the chemical reactions or reduce the laser energy. In addition, plasma or ion etching methods are commonly used for semiconductor chip fabrication and preparation of samples for transmission electron microscopy. The addition of ultrafast pulsed laser energy could be used to further enhance this process.

[00106] Combining the laser texturing method with various other processes would also be beneficial. For example, a one-step process for doping, texturing, and crystallization would be advantageous from a manufacturing standpoint. Also, laser texturing and laser surface cleaning could be combined to provide a one-step process. In addition, laser texturing and surface passivation could be performed as a one-step process. The chemical gas used in laser texturing could provide the surface passivation by sulfur or phosphorous diffusion. Finally, laser texturing could be performed in a one-step process with surface hardening. For example, the surface of steel can be textured, and if a reactive gas such as ammonia or nitrogen plasma is used, surface nitridation can be achieved. This provides improved surface properties, such as wear, wetting characteristics, and chemical interactions.

[00107] The foregoing description and drawings should be considered as only illustrative of the principles of the present invention. The present invention may be configured and

SAMSUNG EX. 1002 - 2331/4148

performed in a variety of ways, and is not intended to be limited by the exemplary embodiments discussed herein. Numerous applications of the present invention will readily occur to those skilled in the art who consider the foregoing description. Therefore, the present invention is not to be limited to the specific examples disclosed, or the construction and operation shown and described. Rather, all suitable modifications and equivalents are within the scope of the present invention, as defined in the appended claims.

SAMSUNG EX. 1002 - 2332/4148

WHAT IS CLAIMED IS:

1. A method for texturing a surface of a semiconductor material, comprising:

providing an etching gas in an area around the surface of the material;

irradiating a portion of the surface with short laser pulses; and

translating at least one of the surface and a laser beam to allow the short laser pulses to irradiate another portion of the surface;

wherein the method produces a periodic array of pillars on the surface, resulting in changes in properties of the surface.

2. The method of claim 1, wherein the method additionally produces nanospikes atop the pillars.

3. The method of claim 2, further comprising sharpening the nanospikes by at least one of chemical etching and ion etching after irradiating the surface.

4. The method of claim 1, wherein the laser pulses have a duration of between one femtosecond and one microsecond.

5. The method of claim 4, wherein the laser pulses have a duration of between one femtosecond and hundreds of picoseconds.

6. The method of claim 1, wherein the laser pulses have a laser pulse energy density of between 0.1 J/cm^2 and 1.4 J/cm^2.

SAMSUNG EX. 1002 - 2333/4148

7. The method of claim 1, wherein the laser pulses have a wavelength of between 200 and 1600 nm.

8. The method of claim 1, wherein irradiating the surface further comprises scanning the surface in a plurality of directions.

9. The method of claim 1, wherein irradiating the surface further comprises scanning the surface in a single direction a plurality of times.

10. The method of claim 1, further comprising controlling a surface texture by controlling a polarization state of the laser pulses.

11. The method of claim 1, further comprising controlling an electrical conductivity of the material by controlling texturing parameters.

12. The method of claim 1, wherein irradiating the surface comprises at least partially crystallizing the irradiated surface.

13. The method of claim 1, further comprising controlling a spacing between adjacent pillars by controlling a wavelength of the laser pulses, a laser pulse energy density, and a number of laser pulses.

14. The method of claim 1, wherein the etching gas comprises at least one of sulfur hexafluoride gas, hydrogen chloride gas, helium gas, and argon gas.

SAMSUNG EX. 1002 - 2334/4148

15. The method of claim 1, wherein the etching gas has a pressure of no more than 0.1 atmospheres.

16. The method of claim 1, wherein the etching gas comprises a gaseous plasma.

17. A method for texturing a surface of a semiconductor material, comprising:

providing an etching gas in an area around the surface of the material;

irradiating a portion of the surface with short laser pulses while simultaneously crystallizing the portion of the surface; and

translating at least one of the surface and a laser beam to allow the short laser pulses to irradiate another portion of the surface while simultaneously crystallizing the other portion of the surface;

wherein the method produces pillars on the surface, resulting in changes in properties of the surface.

18. A method for texturing a metallic surface, comprising:

irradiating a portion of the metallic surface with short laser pulses; and

translating at least one of the surface and a laser beam to allow the short laser pulses to irradiate another portion of the surface;

wherein the method produces pillars on the surface, resulting in changes in properties of the surface.

19. The method of claim 18, wherein the pillars are produced in a periodic array.

SAMSUNG EX. 1002 - 2335/4148

20. The method of claim 18, further comprising providing an etching gas in an area around the surface.

21. The method of claim 20, wherein the etching gas comprises at least one of sulfur hexafluoride gas, hydrogen chloride gas, helium gas, and argon gas.

22. The method of claim 20, wherein the etching gas has a pressure of no more than 0.1 atmospheres.

23. The method of claim 20, wherein the etching gas comprises a gaseous plasma.

24. The method of claim 18, wherein the surface is in air at atmospheric pressure.

25. The method of claim 18, wherein the laser pulses have a duration of between one femtosecond and one microsecond.

26. The method of claim 25, wherein the laser pulses have a duration of between one femtosecond and hundreds of picoseconds.

27. The method of claim 18, wherein the laser pulses have a laser pulse energy density of between 0.1 J/cm^2 and 1.4 J/cm^2.

28. The method of claim 18, wherein the laser pulses have a wavelength of between 200 and 1600 nm.

SAMSUNG EX. 1002 - 2336/4148

29. The method of claim 18, wherein irradiating the surface further comprises scanning the surface in a plurality of directions.

30. The method of claim 18, further comprising controlling a surface texture by controlling a polarization state of the laser pulses.

31. The method of claim 18, further comprising controlling an electrical conductivity of the material by controlling texturing parameters.

32. A semiconductor surface, comprising a portion on which pillars are formed with nanospikes atop the pillars by irradiating the surface with short laser pulses while a substantially pure sulfur hexafluoride gas is provided around the surface.

33. A metallic surface, comprising a portion on which pillars are formed by irradiating the surface with short laser pulses.

34. A method of using the textured surface of claim 1 to provide a photovoltaic device.

35. A method of using the textured surface of claim 1 to provide a photodetector.

36. A method of using the textured surface of claim 1 or 18 to provide a high-efficiency heat sink for an electronic device.

SAMSUNG EX. 1002 - 2337/4148

37. A method of using the textured surface of claim 1 or 18 to provide a very high electric field for electron emission.

38. A method of using the textured surface of claim 1 or 18 to generate catalytic activity.

39. A method of using the textured surface of claim 1 or 18 to perform osteointegration of a body implant.

40. A method of using the textured surface of claim 1 or 18 to control the flow of air or fluid over the surface.

41. A method of using the textured surface of claim 1 or 18 to create a two-dimensional array of micro or nano dimensioned ordered tips.

42. A method of using the textured surface of claim 1 or 18 to manufacture an optical beam block which absorbs substantially all light from the visible to the far-infrared.

43. A method of using the textured surface of claim 1 or 18 in micro fluidic applications.

44. The method of claim 1 or 18, further comprising controlling a color of the surface.

SAMSUNG EX. 1002 - 2338/4148

45. A method of using the textured surface of claim 1 or 18 to produce a master for replication.

46. The method of claim 1 or 18, further comprising processing the surface with chemical etching to provide nano or micro pores on the surface.

47. The method of claim 1 or 18, further comprising controlling an emissivity of the surface.

48. The method of claim 1 or 18, further comprising writing text or images on the surface by controlling a light reflectivity.

49. A method of using the textured surface of claim 1 or 18 to provide a radiation shield which operates in a broad spectral range.

50. A method of using the textured surface of claim 1 or 18 to provide an infrared sensor.

51. A method of using the textured surface of claim 18 to prevent corrosion and provide adhesion.

52. The method of claim 1, wherein the changed properties are at least one of optical properties, thermal properties, and electrical properties.

SAMSUNG EX. 1002 - 2339/4148

53. The method of claim 18, wherein the changed properties are at least one of optical properties, thermal properties, and electrical properties.

SAMSUNG EX. 1002 - 2340/4148

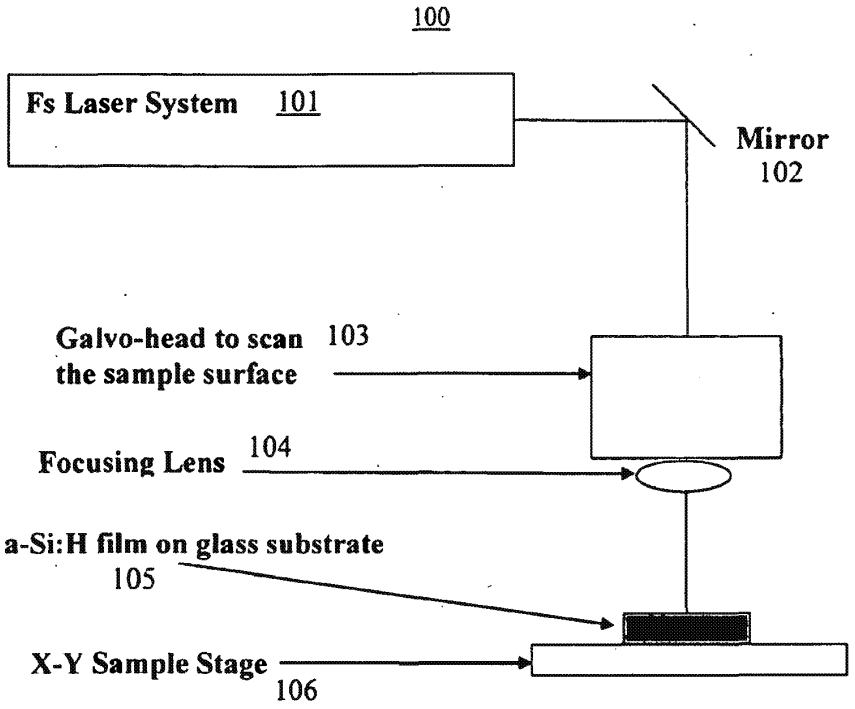


FIG. 1

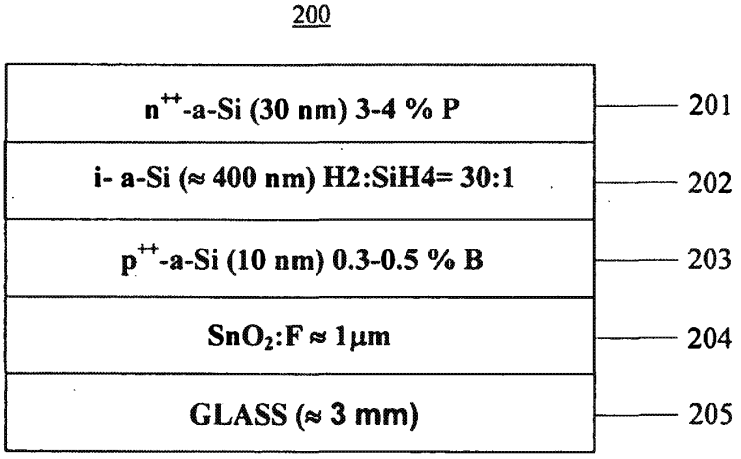


FIG. 2

SAMSUNG EX. 1002 - 2341/4148

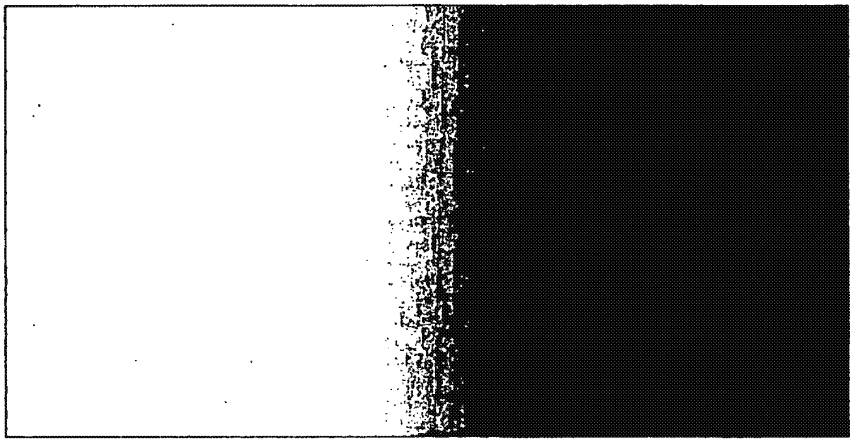


FIG. 3(a) FIG. 3(b)

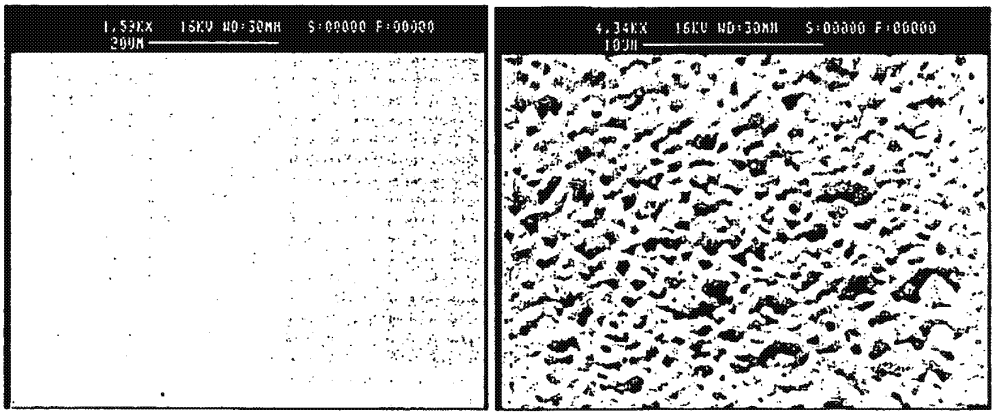


FIG. 4(a) FIG. 4(b)

SAMSUNG EX. 1002 - 2342/4148

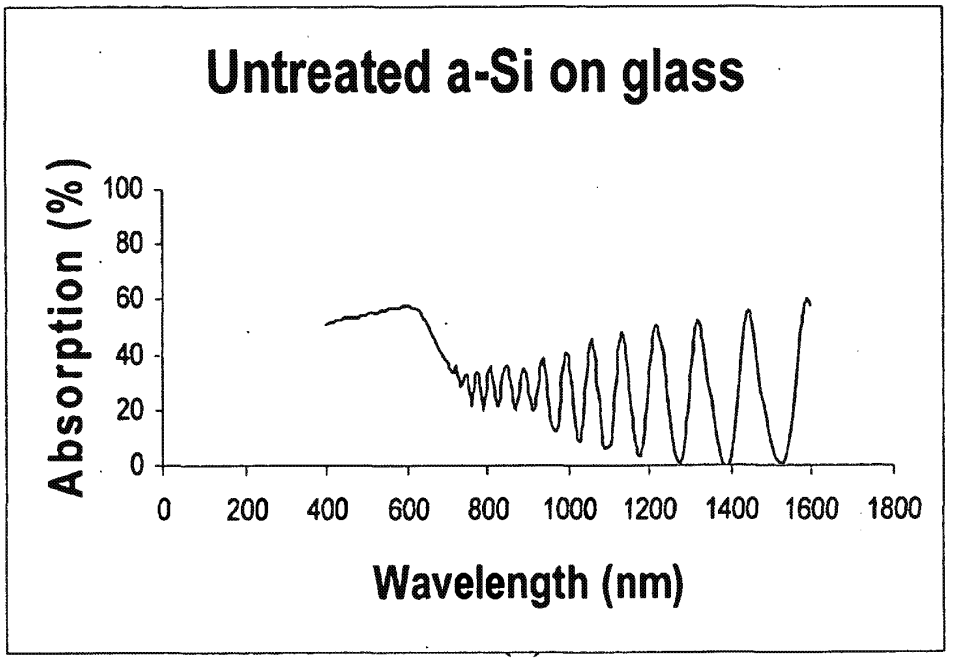


FIG. 5(a)

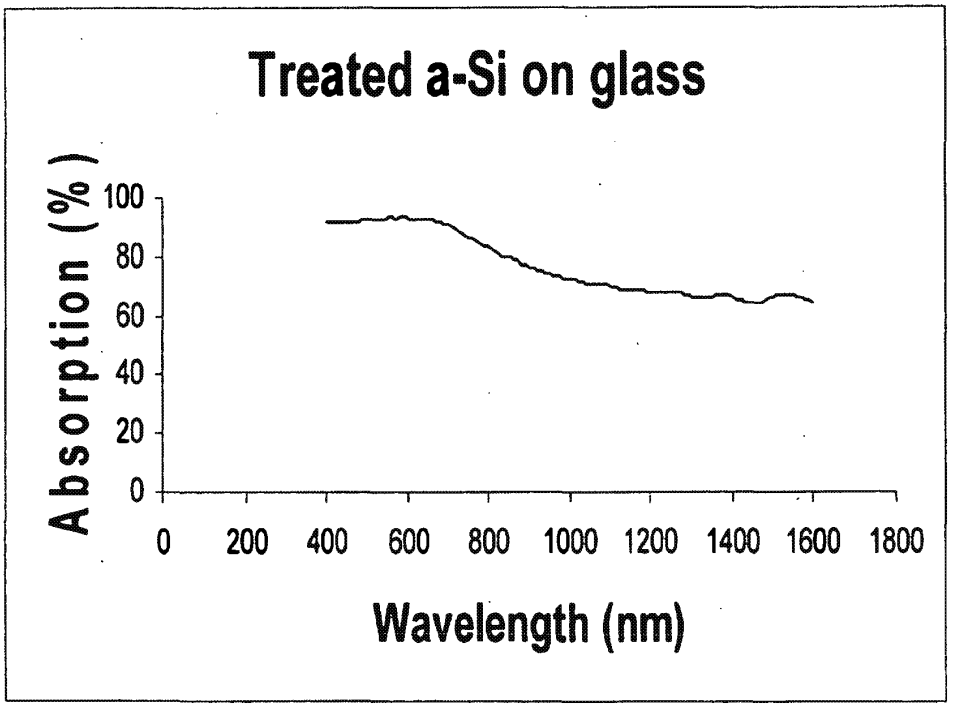


FIG. 5(b)

SAMSUNG EX. 1002 - 2343/4148

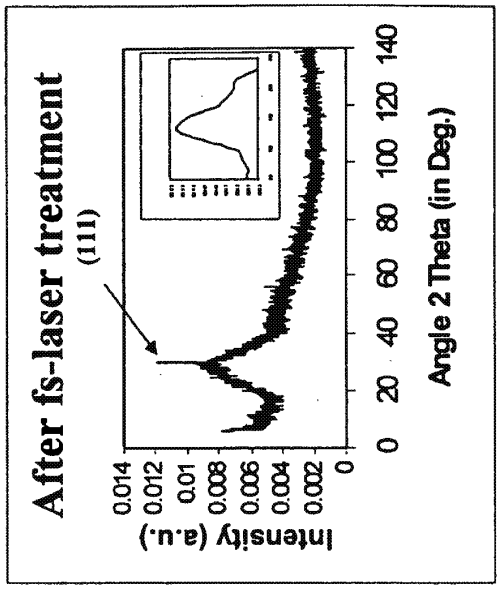


FIG. 6(b)

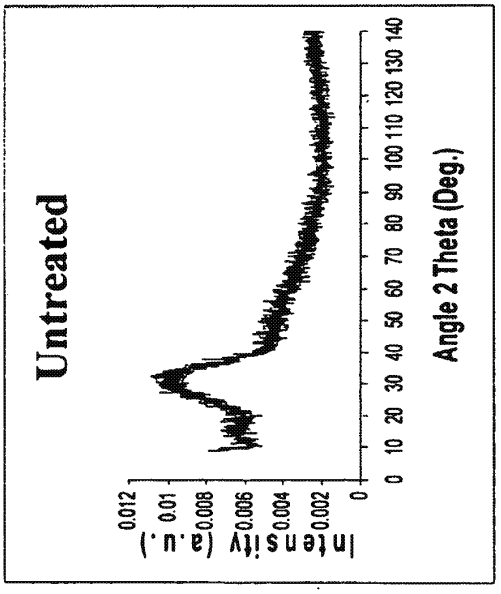


FIG. 6(a)

SAMSUNG EX. 1002 - 2344/4148

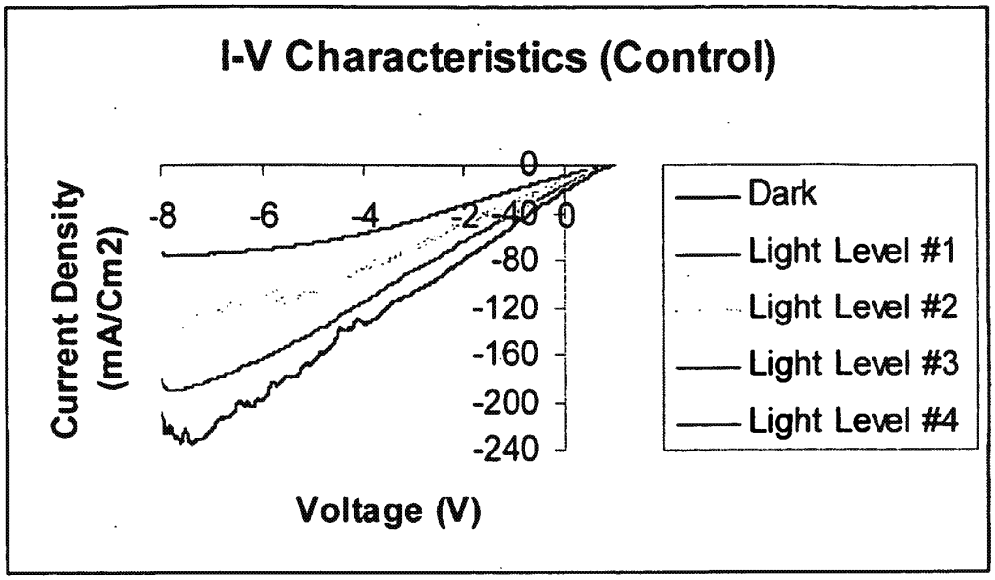


FIG. 7(a)

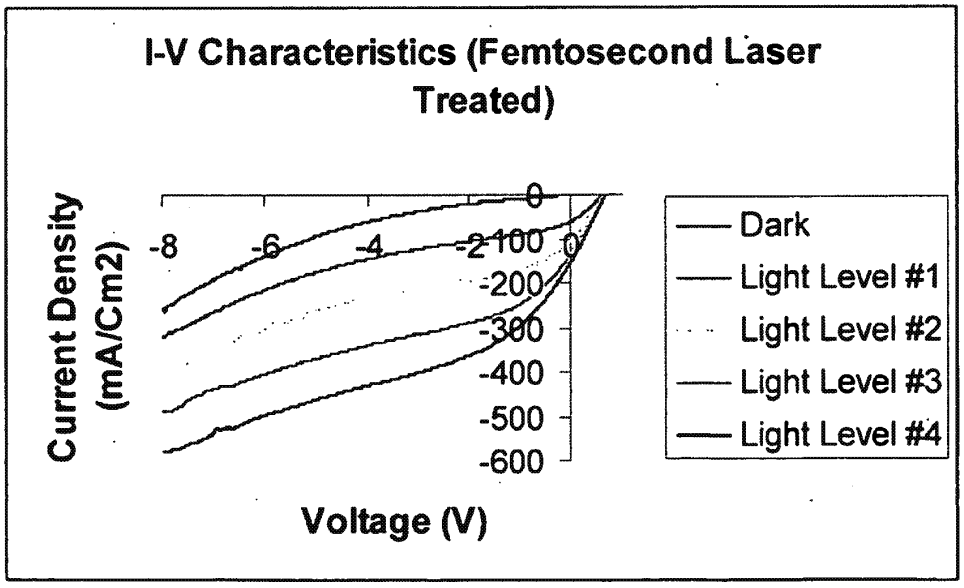


FIG. 7(b)

SAMSUNG EX. 1002 - 2345/4148

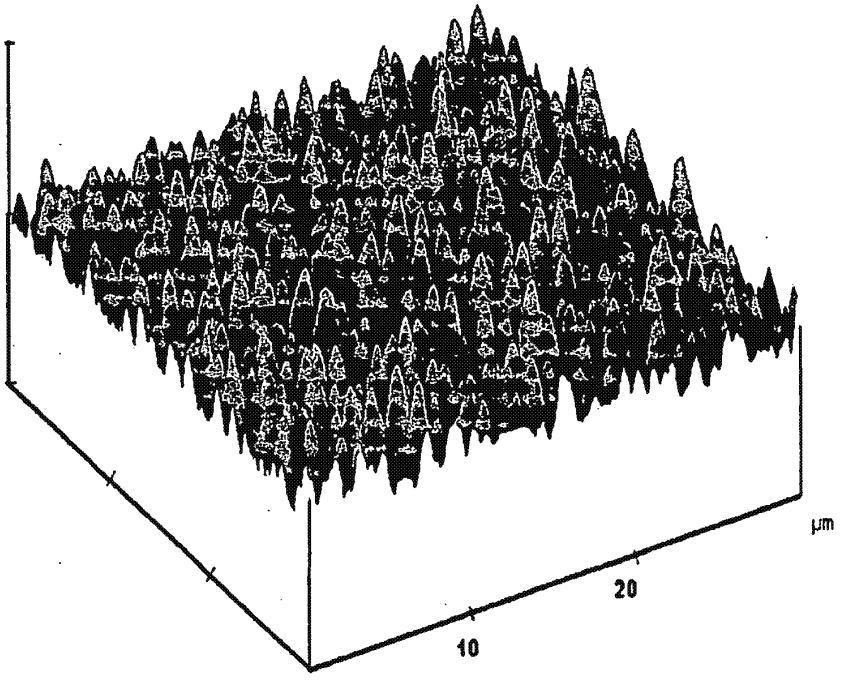


FIG. 8

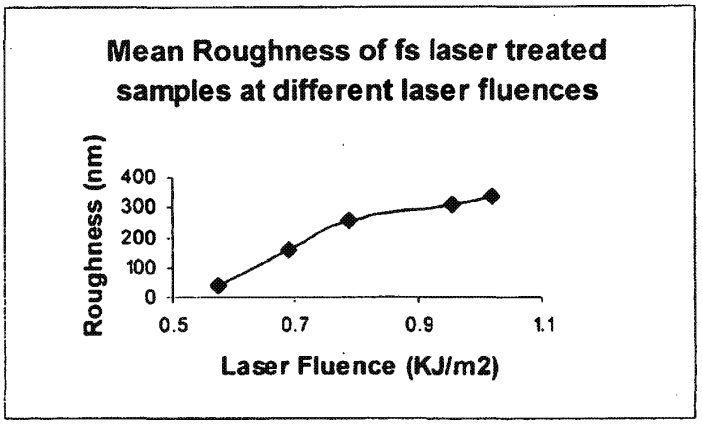


FIG. 9

SAMSUNG EX. 1002 - 2346/4148

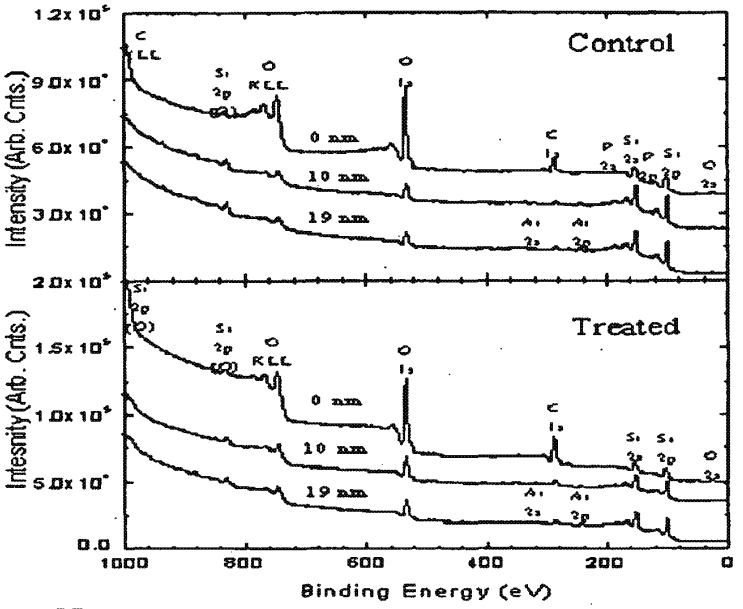


FIG. 10(a)

FIG. 10(b)

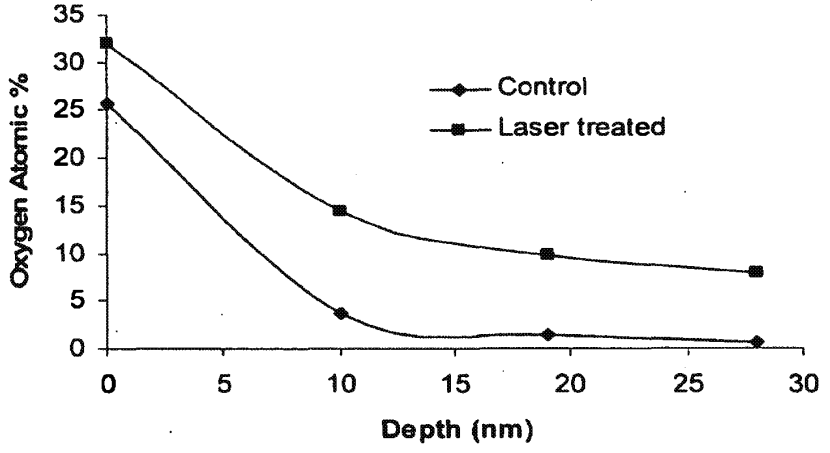


FIG. 10(c)

SAMSUNG EX. 1002 - 2347/4148

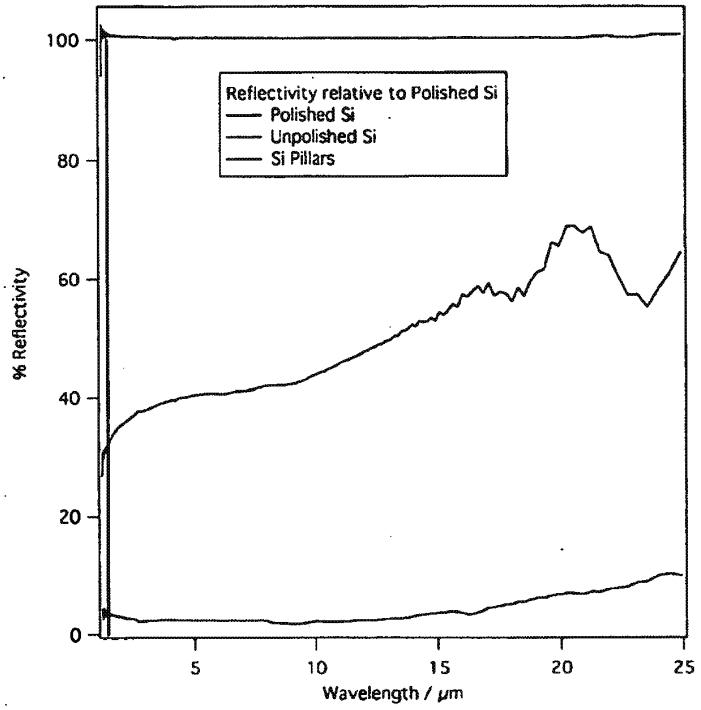


FIG. 11

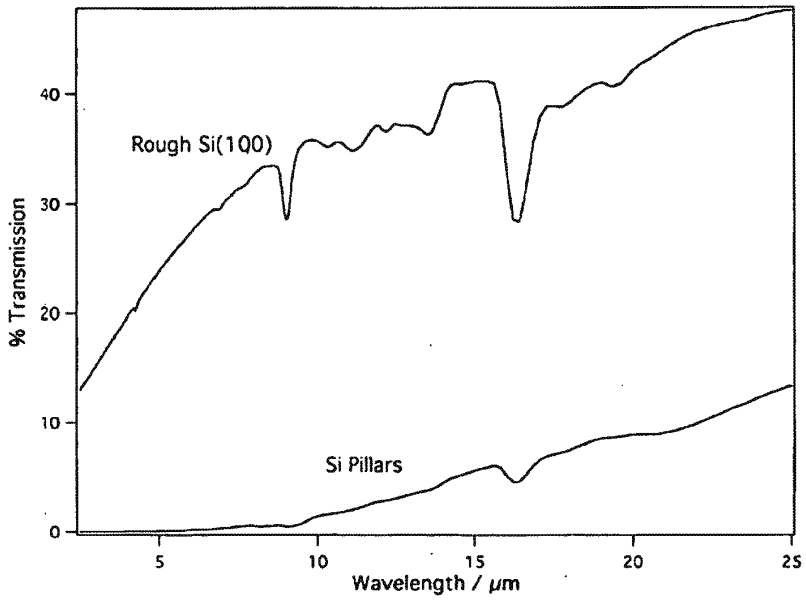


FIG. 12

SAMSUNG EX. 1002 - 2348/4148

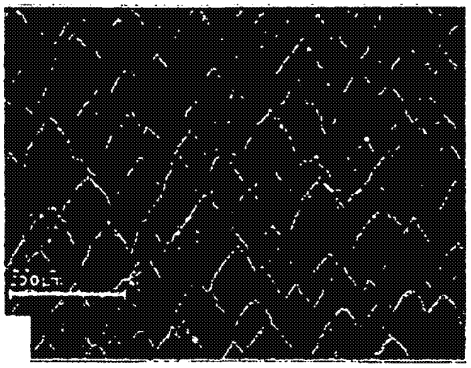


FIG. 13(a)

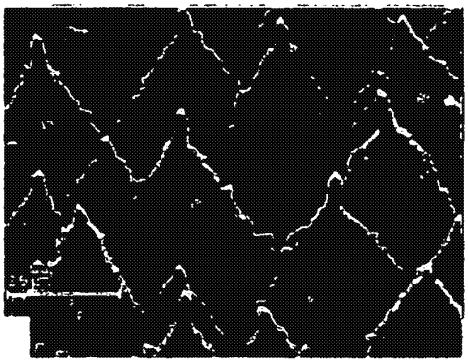


FIG. 13(b)

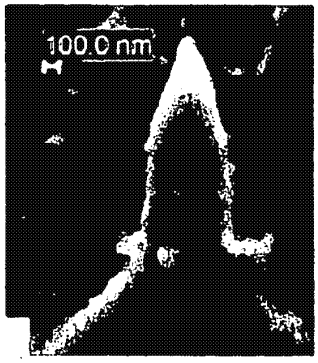


FIG. 13(c)

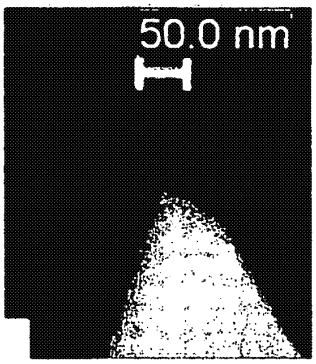


FIG. 13(d)

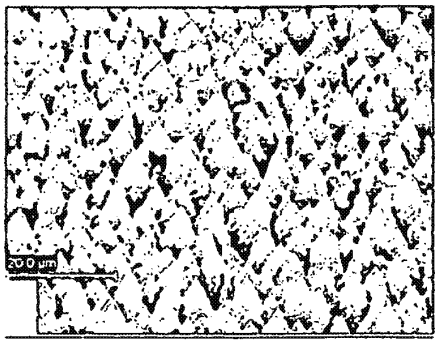


FIG. 14(a)

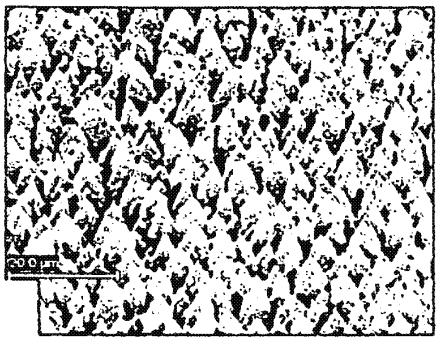


FIG. 14(b)

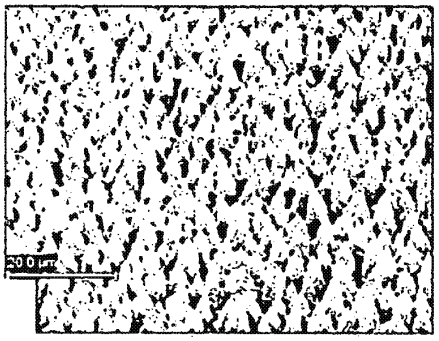


FIG. 14(c)

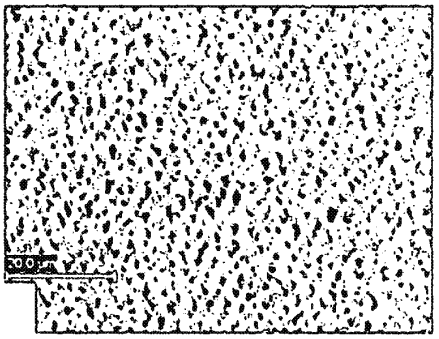


FIG. 14(d)

SAMSUNG EX. 1002 - 2350/4148

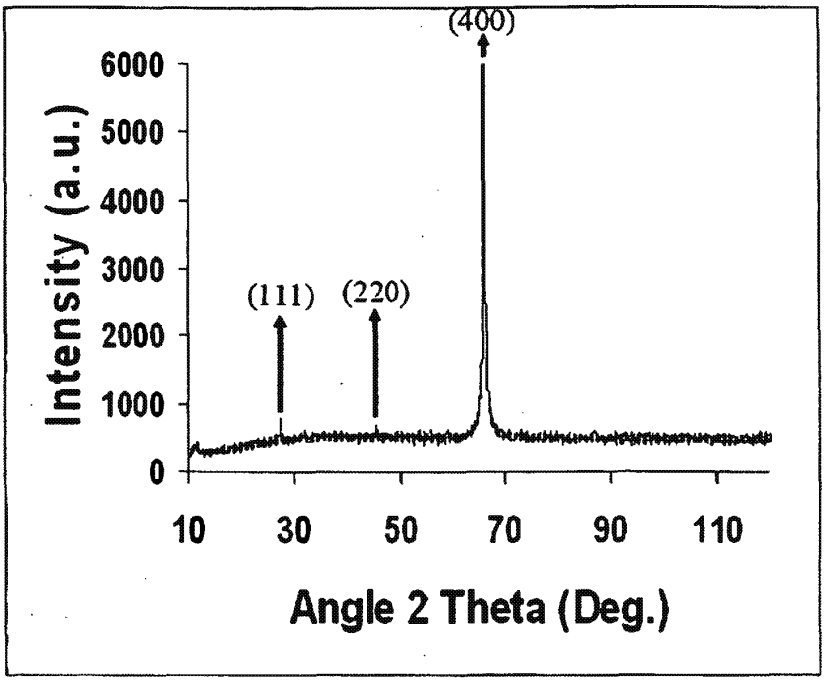


FIG. 15

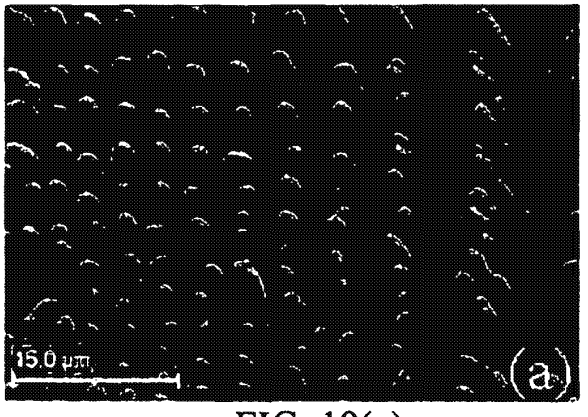


FIG. 19(a)

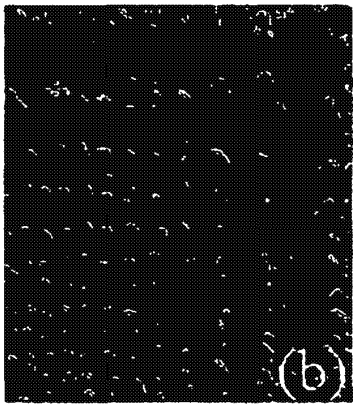


FIG. 19(b)

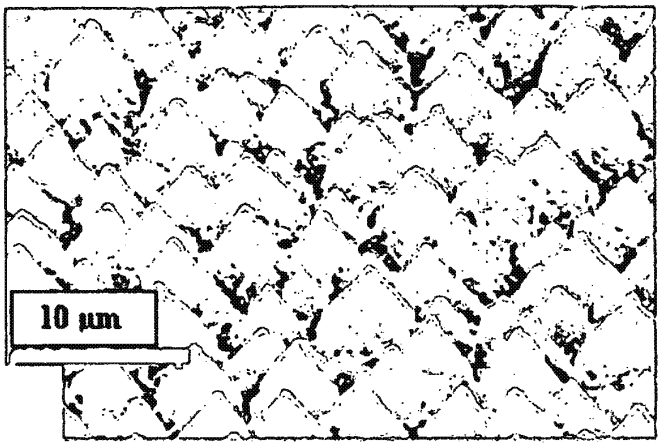


FIG. 16(a)

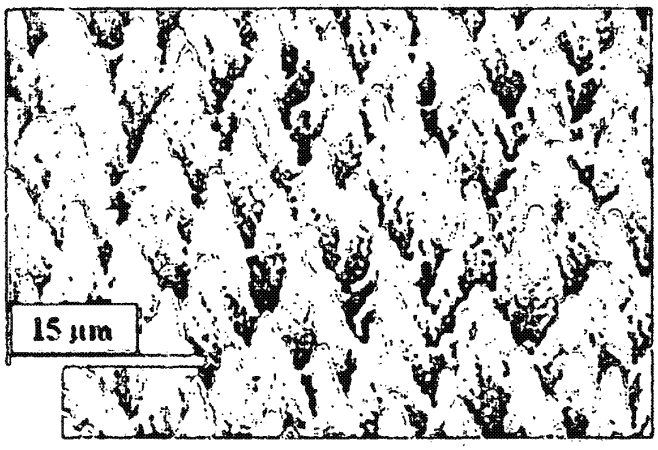


FIG. 16(b)

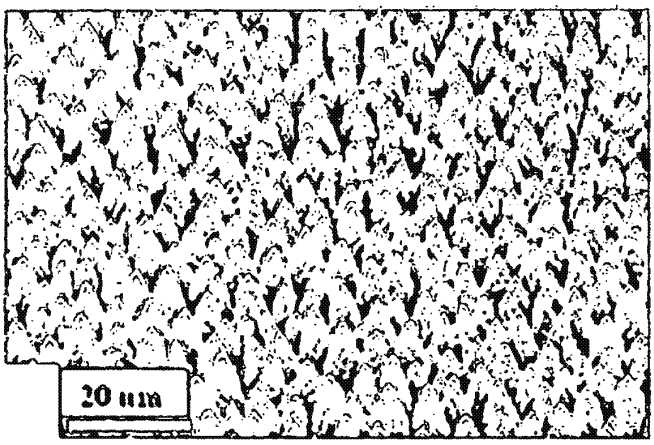


FIG. 16(c)

13 / 17

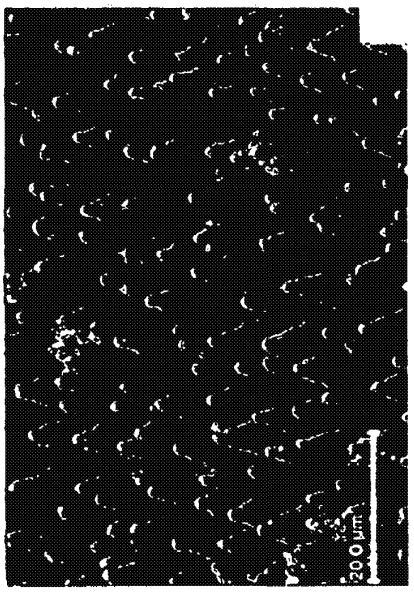


FIG. 17(b)

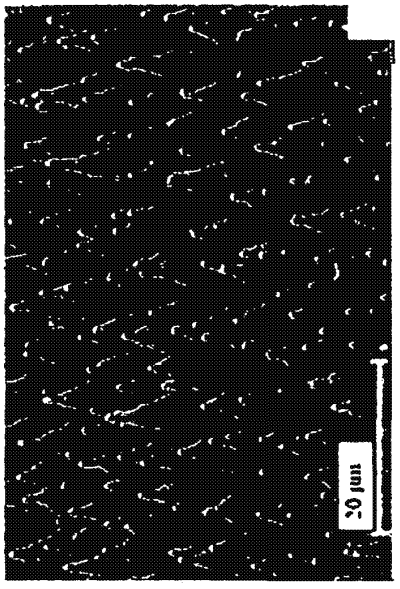


FIG. 17(a)

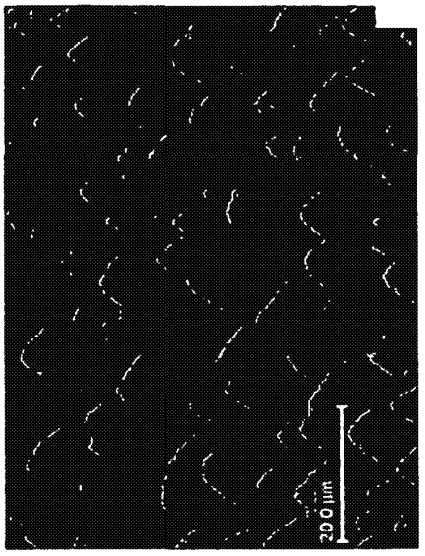


FIG. 18(b)

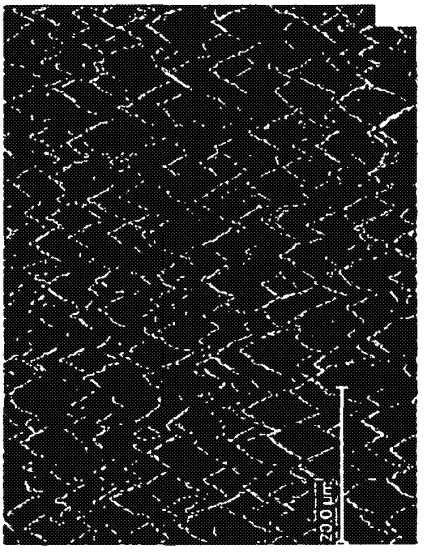


FIG. 18(a)

SAMSUNG EX. 1002 - 2353/4148

FIG. 20(a)

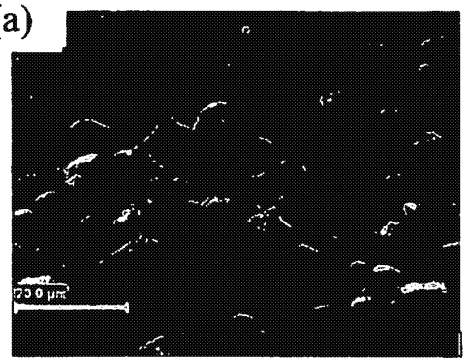


FIG. 20(b)

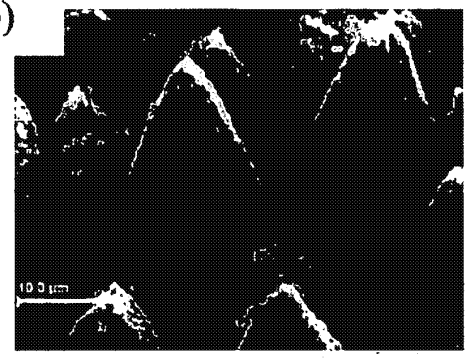


FIG. 20(c)

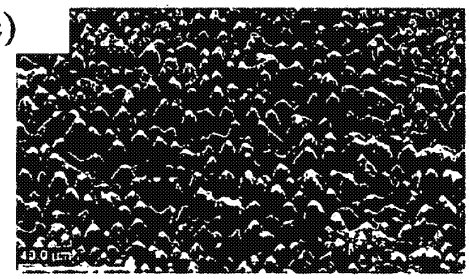
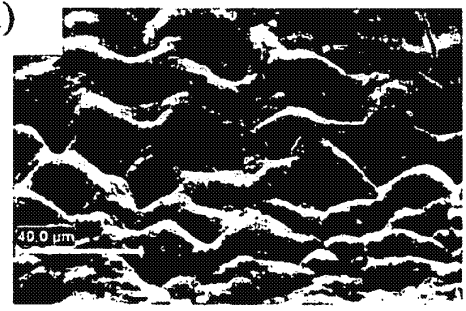


FIG. 20(d)



SAMSUNG EX. 1002 - 2354/4148

FIG. 21(a)

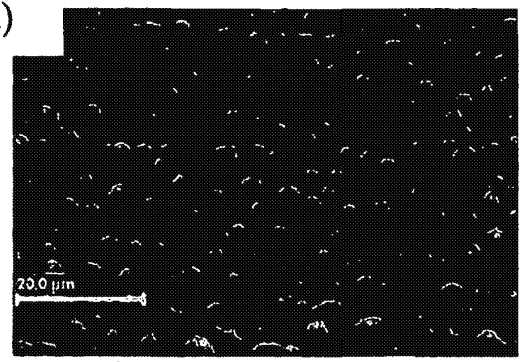


FIG. 21(b)

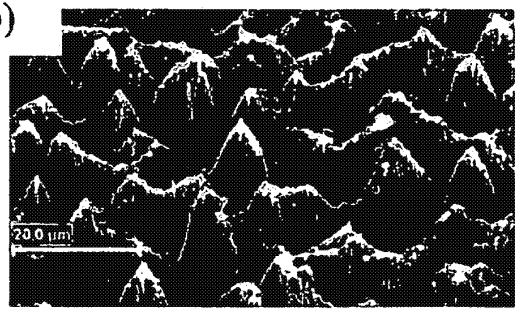


FIG. 21(c)

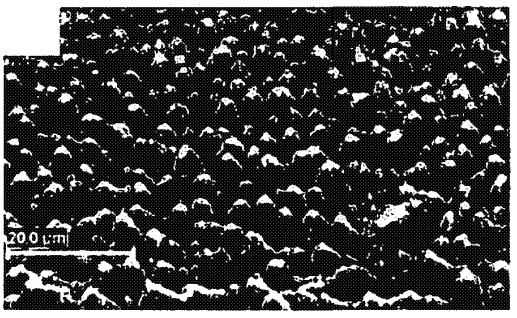
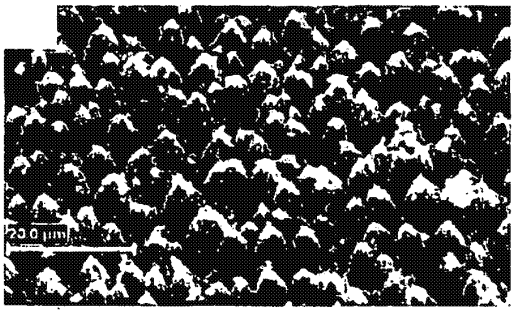


FIG. 21(d)



SAMSUNG EX. 1002 - 2355/4148

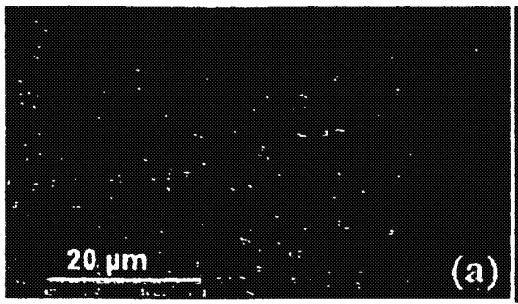


FIG. 22(a)

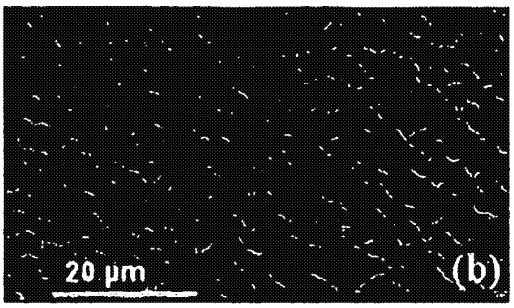


FIG. 22(b)

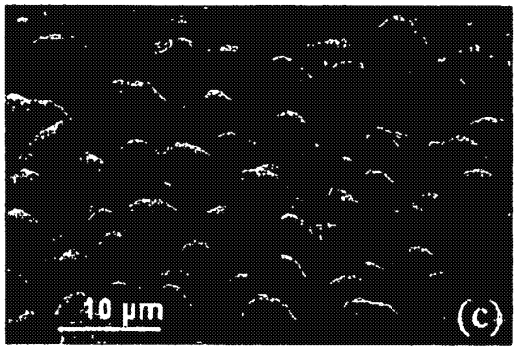


FIG. 22(c)

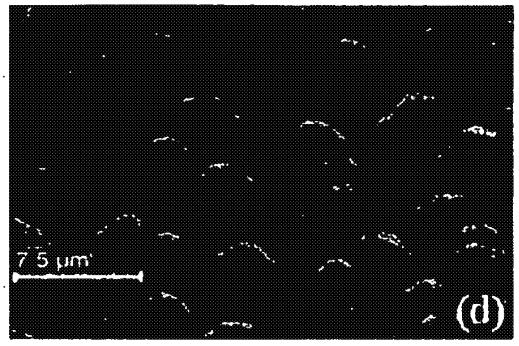


FIG. 22(d)

SAMSUNG EX. 1002 - 2356/4148

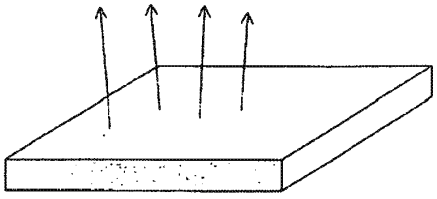


FIG. 23

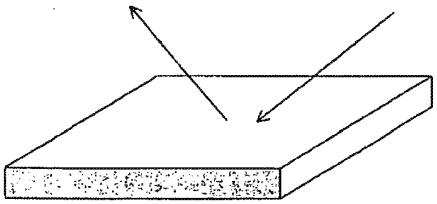


FIG. 24

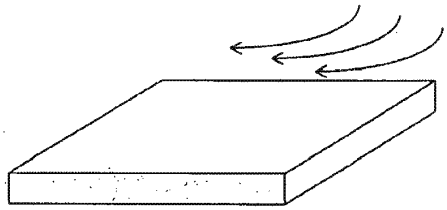


FIG. 25

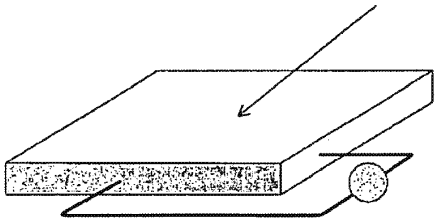


FIG. 26

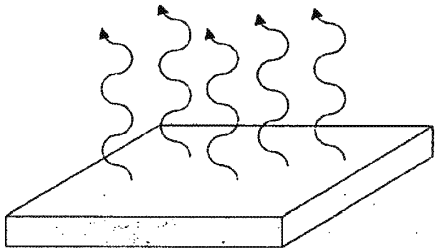


FIG. 27

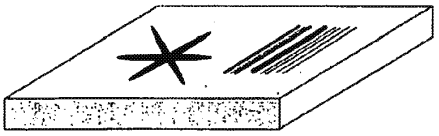


FIG. 28

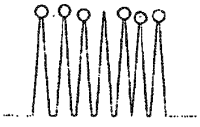


FIG. 29

(12) NACH DEM VERTRAG ÜBER DIE INTERNATIONALE ZUSAMMENARBEIT AUF DEM GEBIET DES PATENTWESENS (PCT) VERÖFFENTLICHTE INTERNATIONALE ANMELDUNG

(19) Weltorganisation für geistiges Eigentum
Internationales Büro

PCT

(43) Internationales Veröffentlichungsdatum
4. Dezember 2008 (04.12.2008)

(10) Internationale Veröffentlichungsnummer
WO 2008/145097 A2

(51) Internationale Patentklassifikation:
H01L 31/04 (2006.01) *H01L 31/0352* (2006.01)

(21) Internationales Aktenzeichen: PCT/DE2008/000870

(22) Internationales Anmeldedatum:
21. Mai 2008 (21.05.2008)

(25) Einreichungssprache: Deutsch

(26) Veröffentlichungssprache: Deutsch

(30) Angaben zur Priorität:
10 2007 024 478.0 25. Mai 2007 (25.05.2007) DE

(71) Anmelder *(für alle Bestimmungsstaaten mit Ausnahme von US)*: **FRAUNHOFER-GESELLSCHAFT ZUR FÖRDERUNG DER ANGEWANDTEN FORSCHUNG E.V.** [DE/DE]; Hansastrasse 27 c, 80686 München (DE). **FRIEDRICH-SCHILLER-UNIVERSITÄT JENA** [DE/DE]; Fürstengraben 1, 07743 Jena (DE).

(72) Erfinder; und

(75) Erfinder/Anmelder *(nur für US)*: **FÜCHSEL, Kevin** [DE/DE]; Werner-Seelenbinder-Strasse 35, 07747 Jena (DE). **TÜNNERMANN, Andreas** [DE/DE]; Wilhelm-Wagenfeldstrasse 16, 99425 Weimar (DE). **KLEY, Ernst-Bernhard** [DE/DE]; Reichardtsteg 7, 07743 Jena (DE).

(74) Anwalt: **EPPING HERMANN FISCHER PATENTANWALTSGESELLSCHAFT MBH**; Ridlerstrasse 55, 80339 München (DE).

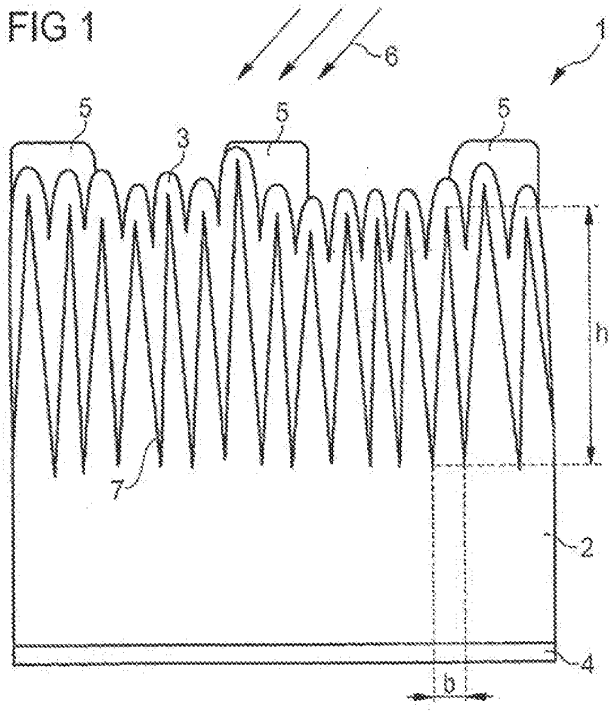
(81) Bestimmungsstaaten *(soweit nicht anders angegeben, für jede verfügbare nationale Schutzrechtsart)*: AE, AG, AL,

[Fortsetzung auf der nächsten Seite]

(54) Title: PHOTOSENSITIVE SEMICONDUCTOR COMPONENT

(54) Bezeichnung: FOTOEMPFINDLICHES HALBLEITERBAUELEMENT

FIG 1



(57) Abstract: The invention relates to a semiconductor component (1) comprising a photosensitive doped semiconductor layer (2), in which electric charge carriers are released during the absorption of electromagnetic radiation (6). The photosensitive semiconductor layer (2) has a structured boundary layer (7). The structured boundary layer (7) is positioned after at least one layer (3) that generates an electric field for separating the released charge carriers, said electric field extending over the structured boundary surface (7). The photosensitive semiconductor component (1) is characterised by a highly efficient charge carrier separation, in particular for generating an electric current.

(57) Zusammenfassung: Bei einem Halbleiterbauelement (1) mit einer fotoempfindlichen dotierten Halbleiterschicht (2), in der bei Absorption elektromagnetischer Strahlung (6) elektrische Ladungsträger freigesetzt werden, weist die fotoempfindliche Halbleiterschicht (2) eine strukturierte Grenzfläche (7) auf. Der strukturierten Grenzfläche (7) ist mindestens eine Schicht (3) nachgeordnet, die ein elektrisches Feld zur Trennung der freigesetzten Ladungsträger erzeugt, wobei sich das elektrische Feld über die strukturierte Grenzfläche (7) erstreckt. Das photoempfindliche Halbleiterbauelement (1) zeichnet sich durch eine hohe Effizienz der Ladungsträgertrennung, insbesondere zur Erzeugung eines elektrischen Stroms, aus.

WO 2008/145097 A2

SIONYX1403000024.0047

SAMSUNG EX. 1002 - 2358/4148

AM, AO, AT, AU, AZ, BA, BB, BG, BH, BR, BW, BY, BZ, CA, CH, CN, CO, CR, CU, CZ, DK, DM, DO, DZ, EC, EE, EG, ES, FI, GB, GD, GE, GH, GM, GT, HN, HR, HU, ID, IL, IN, IS, JP, KE, KG, KM, KN, KP, KR, KZ, LA, LC, LK, LR, LS, LT, LU, LY, MA, MD, ME, MG, MK, MN, MW, MX, MY, MZ, NA, NG, NI, NO, NZ, OM, PG, PH, PL, PT, RO, RS, RU, SC, SD, SE, SG, SK, SL, SM, SV, SY, TJ, TM, TN, TR, TT, TZ, UA, UG, US, UZ, VC, VN, ZA, ZM, ZW.

(84) **Bestimmungsstaaten** *(soweit nicht anders angegeben, für jede verfügbare regionale Schutzrechtsart)*: ARIPO (BW, GH, GM, KE, LS, MW, MZ, NA, SD, SL, SZ, TZ, UG, ZM, ZW), eurasisches (AM, AZ, BY, KG, KZ, MD, RU, TJ, TM), europäisches (AT, BE, BG, CH, CY, CZ, DE, DK, EE, ES, FI, FR, GB, GR, HR, HU, IE, IS, IT, LT, LU, LV, MC, MT, NL, NO, PL, PT, RO, SE, SI, SK, TR), OAPI (BF, BJ, CF, CG, CI, CM, GA, GN, GQ, GW, ML, MR, NE, SN, TD, TG).

Veröffentlicht:

— *ohne internationalen Recherchenbericht und erneut zu veröffentlichen nach Erhalt des Berichts*

Beschreibung

Fotoempfindliches Halbleiterbauelement

Die Erfindung betrifft ein fotoempfindliches Halbleiterbauelement gemäß dem Oberbegriff des Patentanspruchs 1.

Diese Patentanmeldung beansprucht die Priorität der deutschen Patentanmeldung 102007024478.0, deren Offenbarungsgehalt hiermit durch Rückbezug aufgenommen wird.

Ein fotoempfindliches Halbleiterbauelement in Form einer Solarzelle ist zum Beispiel aus der Druckschrift US 4,177,093 bekannt. Die darin beschriebene Solarzelle umfasst ein dotiertes Halbleitersubstrat, eine darauf aufgebrachte Schicht aus Indiumzinnoxid (ITO) sowie elektrische Kontakte, die auf der Rückseite des Substrats und auf der Oberfläche der ITO-Schicht aufgebracht sind. Die ITO-Schicht wirkt mit dem Substrat derart zusammen, dass ähnlich wie bei einem pn-Übergang die im Substrat durch Absorption elektromagnetischer Strahlung freigesetzten elektrischen Ladungsträger zur Erzeugung eines elektrischen Stroms getrennt werden.

Eine weitere Solarzelle ist aus der Druckschrift US 5,949,123 bekannt. Diese Solarzelle basiert auf einem p-dotierten Siliziumsubstrat, in das ein n-Dotierstoff zur Erzeugung eines vergrabenen pn-Übergangs implantiert ist. Um die Reflexion der Oberfläche des Siliziumsubstrats zu vermindern, ist die Oberfläche des Siliziumsubstrats strukturiert. Auf diese Weise wird erreicht, dass ein höherer Lichtanteil in das Siliziumsubstrat eindringen kann.

In der Druckschrift WO 02/13279 A2 wird beschrieben, die

SAMSUNG EX. 1002 - 2360/4148

Oberfläche einer Solarzelle mittels eines Ätzverfahrens zu strukturieren, um die Reflexion der Oberfläche zu vermindern.

Aus der Druckschrift M. Stubenrauch, M. Fischer, C. Kremin, S. Stoebenau, A. Albrecht, O. Nagel, „Black Silicon - New Functionalities in Microsystems", J. Michromech. Microeng. 16 (2006), S. 82-86, ist ein Plasmaätzverfahren zur Herstellung von nadelartigen Strukturen in Siliziumschichten bekannt. Weiterhin beschreibt auch die Druckschrift H. Jansen, M. De Boer, R. Legtenberg, M. Elwenspoek, „The black silicon method: a universal method for determining the parameter setting of a fluorine-based reactive ion etcher in deep silicon trench etching with profile control", J. Michromech. Microeng. 5 (1995), S. 115-120, ein Verfahren zur Herstellung von nadelartigen Strukturen in Silizium.

Der Erfindung liegt die Aufgabe zugrunde, ein verbessertes fotoempfindliches Halbleiterbauelement anzugeben, das sich insbesondere durch eine effizientere Ladungsträgertrennung der in einem fotoempfindlichen Halbleitermaterial erzeugten Ladungsträger auszeichnet.

Diese Aufgabe wird durch den Gegenstand des Patentanspruchs 1 gelöst. Vorteilhafte Ausgestaltungen und Weiterbildungen der Erfindung sind Gegenstand der abhängigen Ansprüche.

Bei einem erfindungsgemäßen Halbleiterbauelement mit einer fotoempfindlichen dotierten Halbleiterschicht, in der bei Absorption elektromagnetischer Strahlung elektrische Ladungsträger freigesetzt werden, weist die fotoempfindliche Halbleiterschicht eine strukturierte Grenzfläche auf. Der strukturierten Grenzfläche ist mindestens eine Schicht nachgeordnet, die ein elektrisches Feld zur Trennung der freigesetzten

SAMSUNG EX. 1002 - 2361/4148

Ladungsträger erzeugt, wobei sich das elektrische Feld über die strukturierte Grenzfläche erstreckt.

Die der fotoempfindlichen Halbleiterschicht nachgeordnete Schicht kann unmittelbar auf die strukturierte Grenzfläche aufgebracht sein oder durch eine oder mehrere Zwischenschichten von der fotoempfindlichen Halbleiterschicht beabstandet sein. Dadurch, dass die zur Erzeugung eines elektrischen Feldes geeignete Schicht der fotoempfindlichen Halbleiterschicht nachgeordnet ist, wird erreicht, dass sich das elektrische Feld über die strukturierte Grenzfläche der fotoempfindlichen Schicht erstreckt. Somit ist der aktive Bereich, in dem eine Ladungsträgertrennung stattfindet, aufgrund der Strukturierung der photoempfindlichen Schicht wesentlich größer als bei herkömmlichen Bauelementen, bei denen der aktive Bereich beispielsweise aus einer ebenen Grenzfläche zwischen einem Siliziumsubstrat und einer ITO-Schicht oder aus einem innerhalb des Substrats ausgebildeten pn-Übergang gebildet ist. Durch die Strukturierung der fotoempfindlichen Schicht wird also nicht nur die Reflexion der Grenzfläche vermindert, sondern auch der aktive Bereich, in dem Ladungsträgertrennung stattfindet, vergrößert.

Die dem Substrat nachgeordnete Schicht enthält insbesondere ein transparentes elektrisch leitfähiges Material. Vorzugsweise ist das transparente elektrisch leitfähige Material ein transparentes leitfähiges Oxid, insbesondere Indiumzinnoxid (ITO), Indiumzinkoxid (IZO), Zinkoxid (ZnO) oder Cadmium-Stannat (CTO, Cd_2SnO_4).

Weiterhin kann das transparente elektrisch leitfähige Material auch ein transparentes leitfähiges Polymer sein.

SAMSUNG EX. 1002 - 2362/4148

Bei einer weiteren bevorzugten Ausführungsform ist die der fotoempfindlichen Halbleiterschicht nachgeordnete Schicht eine Halbleiterschicht, die sich in ihren Dotierungstyp und/oder ihrer Dotierstoffkonzentration von der fotoempfindlichen Halbleiterschicht unterscheidet.

Insbesondere kann die der dotierten fotoempfindlichen Halbleiterschicht nachgeordnete Schicht den entgegengesetzten Dotierungstyp aufweisen, so dass zum Beispiel die fotoempfindliche Halbleiterschicht p-dotiert ist und die nachgeordnete Schicht n-dotiert ist oder umgekehrt. Auf diese Weise wird an der Grenzfläche der strukturierten fotoempfindlichen Halbleiterschicht ein pn-Übergang ausgebildet, wobei der pn-Übergang aufgrund der Strukturierung vorteilhaft größer ist als bei einer ebenen Grenzfläche zwischen den Halbleiterschichten entgegengesetzten Dotierungstyps.

Zwischen der fotoempfindlichen Schicht und der ihr nachgeordneten Schicht kann mindestens eine Zwischenschicht angeordnet sein. Insbesondere kann es sich bei der Zwischenschicht um eine Silizium oxidschicht handeln, die sich beispielsweise auf der fotoempfindlichen Halbleiterschicht ausbilden kann, bevor die transparente leitfähige Schicht aufgebracht wird. Weiterhin kann es sich bei der Zwischenschicht auch um eine Schicht aus einem intrinsischen Halbleitermaterial handeln, insbesondere wenn es sich bei der fotoempfindlichen Halbleiterschicht und der nachgeordneten Schicht um zwei Halbleiterschichten mit verschiedenem Dotierungstyp handelt.

Die strukturierte Grenzfläche der fotoempfindlichen Halbleiterschicht ist vorzugsweise derart strukturiert, dass sie Strukturen mit einer Breite von weniger als 100 nm aufweist.

SAMSUNG EX. 1002 - 2363/4148

Bevorzugt weist die strukturierte Grenzfläche Strukturen auf, die eine Breite zwischen 10 nm und 100 nm aufweisen.

Aufgrund der strukturierten Grenzfläche ist zwischen der fotoempfindlichen Schicht und der nachfolgenden Schicht ein Brechungsindexgradient ausgebildet, so dass die Grenzfläche zwischen den Schichten als effektives Medium wirkt.

Weiterhin ist es vorteilhaft, wenn die an der Grenzfläche der fotoempfindlichen Halbleiterschicht erzeugten Strukturen eine Höhe von mehr als 100 nm aufweisen. Insbesondere kann die Höhe der an der strukturierten Grenzfläche erzeugten Strukturen zwischen 1,5 µm und 10 µm betragen.

Die an der Grenzfläche der fotoempfindlichen Halbleiterschicht erzeugten Strukturen zeichnen sich insbesondere durch ein hohes Aspektverhältnis aus. Dies hat den Vorteil, dass die Grenzfläche im Vergleich zu einer nahezu glatten Grenzfläche erheblich vergrößert wird. Bevorzugt beträgt die Höhe der Strukturen im Mittel mindestens das 10-fache der Breite, besonders bevorzugt sogar mindestens das 50-fache der Breite.

Bei einer vorteilhaften Ausgestaltung weist die strukturierte Grenzfläche der fotoempfindlichen Halbleiterschicht Strukturen auf, die überwiegend, also mehr als zur Hälfte, eine Flankensteilheit von mehr als 45° aufweisen. Beispielsweise können die Flanken der Strukturen Winkel im Bereich von 80° bis 85° mit einer Hauptebene der photoempfindlichen Halbleiterschicht einschließen. Insbesondere kann es sich bei den Strukturen um nadelförmige Strukturen handeln.

Die strukturierte Grenzfläche kann insbesondere eine stochastische Struktur aufweisen, also eine Struktur, bei der

SAMSUNG EX. 1002 - 2364/4148

die Strukturhöhen und Strukturbreiten im Gegensatz zu deterministischen Strukturen, die beispielsweise mit lithografischen Techniken erzeugt werden, eine statistische Verteilung aufweisen.

Bevorzugt ist die strukturierte Grenzfläche mittels eines Ätzverfahrens strukturiert. Dazu wird vorzugsweise ein Plasmaätzverfahren eingesetzt, wie insbesondere ein ICP-Ätzverfahren (inductively coupled plasma). Alternativ können aber auch andere Verfahren der physikalischen Abtragung wie beispielsweise Laserstrukturierung eingesetzt werden.

Die Anwendung eines Ätzverfahrens zur Erzeugung einer stochastischen Struktur ist im Vergleich zu lithographischen Strukturierungsverfahren vorteilhaft, weil der Herstellungsaufwand vergleichsweise gering ist.

Alternativ ist es aber auch möglich, dass die Grenzfläche der fotoempfindlichen Halbleiterschicht eine deterministische, also vorbestimmte Struktur aufweist, die beispielsweise lithografisch, insbesondere unter Verwendung einer Ätzmaske, hergestellt ist.

Die Erfindung wird im Folgenden anhand von Ausführungsbeispielen näher erläutert.

Es zeigen:

Figur 1 eine schematische Darstellung eines Halbleiterbauelements gemäß einem ersten Ausführungsbeispiel der Erfindung,

SAMSUNG EX. 1002 - 2365/4148

Figur 2 eine grafische Darstellung der Reflexion einer strukturierten Siliziumschicht im Vergleich zu einer unstrukturierten Siliziumschicht und

Figur 3 eine schematische Darstellung eines Halbleiterbauelements gemäß einem zweiten Ausführungsbeispiel der Erfindung.

Gleiche oder gleich wirkende Elemente sind in den Figuren mit den gleichen Bezugszeichen versehen. Die Figuren sind nicht als maßstabsgerecht anzusehen, vielmehr können einzelne Elemente zur Verdeutlichung übertrieben groß dargestellt sein.

Das in Figur 1 dargestellte Halbleiterbauelement 1 gemäß einem ersten Ausführungsbeispiel der Erfindung ist eine Solarzelle, die eine fotoempfindliche Halbleiterschicht 2, zum Beispiel eine p-dotierte Siliziumschicht, enthält. Die Halbleiterschicht 2 kann insbesondere ein Silizium-Wafer sein, der typischerweise eine Dicke von mehr als 100 µm aufweist. Alternativ kann die Halbleiterschicht 2 aber auch eine auf ein Substrat aufgebrachte Halbleiterschicht sein, zum Beispiel eine auf einen metallischen Reflektor (nicht dargestellt) aufgebrachte Halbleiterschicht.

In der fotoempfindlichen Halbleiterschicht 2 werden beim Auftreffen elektromagnetischer Strahlung, die durch die Pfeile 6 angedeutet ist, elektrische Ladungsträger freigesetzt. Insbesondere kann es sich bei dem Halbleiterbauelement 1 um eine Solarzelle handeln, bei der durch Absorption von Sonnenlicht in der fotoempfindlichen Halbleiterschicht 2 Elektron-Loch-Paare als freie Ladungsträger erzeugt werden.

SIONYX1403000024.0055

SAMSUNG EX. 1002 - 2366/4148

Auf die fotoempfindliche Halbleiterschicht 2 ist eine Schicht 3 aufgebracht, mittels der ein elektrisches Feld zur Trennung der freigesetzten Ladungsträger erzeugt wird. Auf diese Weise kann insbesondere ein elektrischer Strom aus den freigesetzten Ladungsträgern erzeugt werden. Um den elektrischen Strom aus dem Halbleiterbauelement 1 abzuführen, kann ein erster elektrischer Kontakt 4 an einer von der Schicht 3 abgewandten Rückseite der Halbleiterschicht 2 und ein weiterer elektrischer Kontakt 5 auf der Schicht 3 angeordnet sein. Der zweite elektrische Kontakt 5 kann beispielsweise streifenförmig über die Grenzfläche der Schicht 3 geführt sein.

Die fotoempfindliche Halbleiterschicht 2 weist eine strukturierte Grenzfläche 7 auf. Die strukturierte Grenzfläche 7 kann beispielsweise mit einem Plasmaätzverfahren, insbesondere durch induktiv gekoppeltes Plasmaätzen (ICP) erzeugt werden. Dabei werden beispielsweise SF_6 und O_2 als Ätzgase verwendet. Die Form der erzeugten Strukturen kann dabei durch die Wahl der Ätzparameter, insbesondere der Zusammensetzung der Ätzgase, gezielt eingestellt werden. Geeignete Plasmaätzverfahren, insbesondere zur Erzeugung nadelförmiger Strukturen, sind an sich aus den in der Einleitung zitierten Druckschriften bekannt und werden daher nicht näher erläutert.

Bevorzugt werden mit dem Ätzverfahren an der Grenzfläche 7 Strukturen erzeugt, die ein hohes Aspektverhältnis aufweisen. Die Grenzflächenstrukturen weisen bevorzugt eine Höhe h auf, die größer als ihre Breite b ist. Bevorzugt beträgt die Höhe der Strukturen h im Mittel mindestens das 10-fache der Breite b, besonders bevorzugt sogar mindestens das 50-fache der Breite b. Insbesondere zeichnen sich die Strukturen vorteilhaft durch eine hohe Flankensteilheit auf. Bevorzugt weisen

SAMSUNG EX. 1002 - 2367/4148

die Strukturen überwiegend, das heißt mindestens zur Hälfte, eine Flankensteilheit von mehr als 45° auf.

Die Breite b der Strukturen beträgt bevorzugt weniger als 100 nm, insbesondere zwischen einschließlich 10 nm und einschließlich 100 nm. Die Höhe h der Strukturen der Grenzfläche 7 beträgt vorzugsweise zwischen einschließlich 1,5 µm und einschließlich 5 µm.

Die Strukturierung der Grenzfläche 7 der Halbleiterschicht 2 wirkt sich in zweifacher Hinsicht positiv auf die Effizienz des Halbleiterbauelements 1 aus. Zum einen wird die Reflexion der Grenzfläche der Halbleiterschicht 2 durch die Strukturierung vermindert. Aufgrund der Strukturierung der fotoempfindlichen Halbleiterschicht 2 vermindert sich auch die Reflexion der Oberfläche des Halbleiterbauelements, wenn die mindestens eine der Halbleiterschicht nachfolgende Schicht 3 derart dünn ist, dass auch ihre Oberfläche die Strukturierung aufweist. Die Verminderung der Reflexion der Grenzfläche 7 der Halbleiterschicht 2 wird in Figur 2 verdeutlicht, in der die Reflexion einer Siliziumschicht vor und nach der Strukturierung in Abhängigkeit von der Wellenlänge dargestellt ist. Die Kurve 9 stellt die Reflexion der Siliziumschicht vor der Strukturierung und die Kurve 10 die Reflexion der Siliziumschicht nach der Strukturierung dar. Da die strukturierte Schicht eine wesentliche geringere Reflexion als eine unstrukturierte Schicht aufweist, kann ein größerer Anteil der auftreffenden Strahlung in die photoempfindliche Schicht eindringen, wodurch die Effizienz des photoempfindlichen Halbleiterbauelements verbessert wird.

Ein weiterer Vorteil der Strukturierung der Halbleiterschicht 2 ergibt sich daraus, dass die Schicht 3, mittels der ein

SIONYX1403000024.0057

SAMSUNG EX. 1002 - 2368/4148

elektrisches Feld zur Trennung der in der fotoempfindlichen Halbleiterschicht 2 freigesetzten Ladungsträger erzeugt wird, der Halbleiterschicht 2 nachgeordnet ist, d.h. auf oder über der photoempfindlichen Halbleiterschicht 2 angeordnet ist. Auf diese Weise wird erreicht, dass sich das elektrische Feld, mit dem die freigesetzten Ladungsträger getrennt werden, über die strukturierte Grenzfläche 7 der Halbleiterschicht 2 erstreckt. Der Bereich, in dem die Ladungsträgertrennung stattfindet, ist daher größer als im Fall einer unstrukturierten Grenzfläche zwischen einer Halbleiterschicht 2 und der ihr nachgeordneten Schicht 3. Beispielsweise kann durch die Strukturierung die Grenzfläche 7 der fotoempfindlichen Halbleiterschicht um einen Faktor 10 oder mehr vergrößert werden.

Die der strukturierten Halbleiterschicht 2 nachgeordnete Schicht 3 enthält vorzugsweise ein transparentes elektrisch leitfähiges Material, insbesondere ein transparentes leitfähiges Oxid oder ein transparentes leitfähiges Polymer. Die Schicht 3 kann zum Beispiel eine Dicke von etwa 1 µm aufweisen.

Geeignete transparente leitfähige Oxide sind insbesondere Indiumzinnoxid (ITO) und Indiumzinkoxid (IZO). Weiterhin sind Zinkoxid (ZnO), das insbesondere mit Al dotiert sein kann, oder Cadmium-Stannat (Cd_2SnO_4) geeignet.

Alternativ ist es auch möglich, dass die Schicht 3 ein Halbleitermaterial aufweist, das einen zu der Halbleiterschicht 2 entgegengesetzten Dotierungstyp aufweist. Beispielsweise kann die Halbleiterschicht 2 p-dotiert und die Schicht 3 n-dotiert sein. In diesem Fall ist zwischen der Halbleiterschicht 2 und der Schicht 3 ein pn-Übergang ausgebildet, der sich über die

SAMSUNG EX. 1002 - 2369/4148

strukturierte Grenzfläche 7 der Halbleiterschicht 2 erstreckt. Der Bereich des pn-Übergangs ist aufgrund der Strukturierung vorteilhaft wesentlich größer als im Fall einer ebenen Grenzfläche zwischen einer p-dotierten Halbleiterschicht und einer n-dotierten Halbleiterschicht. Bei den Schichten 2, 3 kann es sich beispielsweise um Siliziumschichten mit unterschiedlicher Dotierung handeln. Alternativ können aber auch andere Halbleitermaterialien eingesetzt werden, beispielsweise III-V-Halbleitermaterialien wie insbesondere GaAs oder InAs.

Das in Figur 3 dargestellte Ausführungsbeispiel eines Halbleiterbauelements unterscheidet sich von dem in Figur 1 dargestellten dadurch, dass zwischen der fotoempfindlichen Halbleiterschicht 2 und der ihr nachgeordneten Schicht 3, mittels der das elektrische Feld zur Ladungsträgertrennung erzeugt wird, eine Zwischenschicht 8 angeordnet ist. Insbesondere kann die fotoempfindliche Halbleiterschicht 2 eine Siliziumschicht und die Zwischenschicht 8 eine Siliziumoxidschicht sein. Die Siliziumoxidschicht 8 kann insbesondere eine natürliche Oxidschicht sein, die sich auf der Siliziumschicht 2 ausbildet, wenn die Halbleiterschicht 2 vor dem Aufbringen der Schicht 3 in Kontakt mit Luft gerät.

Weiterhin kann es sich bei der Zwischenschicht 8 auch um eine Schicht aus einem intrinsischen Halbleitermaterial handeln, die beispielsweise zwischen zwei entgegengesetzten dotierten Halbleiterschichten eingefügt ist, um die Rekombination der Ladungsträger zu vermindern.

Die Erfindung ist nicht durch die Beschreibung anhand der Ausführungsbeispiele beschränkt. Vielmehr umfasst die Erfindung jedes neue Merkmal sowie jede Kombination von Merkmalen,

SAMSUNG EX. 1002 - 2370/4148

was insbesondere jede Kombination von Merkmalen in den Patentansprüchen beinhaltet, auch wenn dieses Merkmal oder diese Kombination selbst nicht explizit in den Patentansprüchen oder Ausführungsbeispielen angegeben ist.

SAMSUNG EX. 1002 - 2371/4148

Patentansprüche

1. Halbleiterbauelement (1) mit einer fotoempfindlichen dotierten Halbleiterschicht (2), in der bei Absorption elektromagnetischer Strahlung (6) elektrische Ladungsträger freigesetzt werden, wobei die fotoempfindliche Halbleiterschicht (2) eine strukturierte Grenzfläche (7) aufweist,
dadurch gekennzeichnet, dass
der strukturierten Grenzfläche (7) mindestens eine Schicht (3) nachgeordnet ist, die ein elektrisches Feld zur Trennung der freigesetzten Ladungsträger erzeugt, wobei sich das elektrische Feld über die strukturierte Grenzfläche (7) erstreckt.

2. Halbleiterbauelement nach Anspruch 1,
dadurch gekennzeichnet, dass
die der fotoempfindlichen Halbleiterschicht (2) nachgeordnete Schicht (3) ein transparentes elektrisch leitfähiges Material enthält.

3. Halbleiterbauelement nach Anspruch 2,
dadurch gekennzeichnet, dass
das transparente elektrisch leitfähige Material ein transparentes leitfähiges Oxid ist.

4. Halbleiterbauelement nach Anspruch 3,
dadurch gekennzeichnet, dass
das transparente leitfähige Oxid Indiumzinnoxid, Indiumzinkoxid, Zinkoxid oder Cadmium-Stannat ist.

5. Halbleiterbauelement nach Anspruch 2,
dadurch gekennzeichnet, dass

SIONYX1403000024.0061

SAMSUNG EX. 1002 - 2372/4148

das transparente elektrisch leitfähige Material ein transparentes leitfähiges Polymer ist.

6. Halbleiterbauelement nach Anspruch 2, dadurch gekennzeichnet, dass die der fotoempfindlichen Halbleiterschicht (2) nachgeordnete Schicht (3) eine Halbleiterschicht ist, die sich in ihrem Dotierungstyp und/oder ihrer Dotierstoffkonzentration von der fotoempfindlichen Halbleiterschicht (2) unterscheidet.

7. Halbleiterbauelement nach einem der vorhergehenden Ansprüche, dadurch gekennzeichnet, dass zwischen der fotoempfindlichen Schicht (2) und der ihr nachgeordneten Schicht (3) mindestens eine Zwischenschicht (8) angeordnet ist.

8. Halbleiterbauelement nach Anspruch 7, dadurch gekennzeichnet, dass die Zwischenschicht (8) ein Siliziumoxid oder ein intrinsisches Halbleitermaterial enthält.

9. Halbleiterbauelement nach einem der vorhergehenden Ansprüche, dadurch gekennzeichnet, dass die strukturierte Grenzfläche (7) der fotoempfindlichen Halbleiterschicht (3) Strukturen mit einer Breite (b) von weniger als 100 nm aufweist.

10. Halbleiterbauelement nach einem der vorhergehenden Ansprüche, dadurch gekennzeichnet, dass

SAMSUNG EX. 1002 - 2373/4148

die strukturierte Grenzfläche (7) der fotoempfindlichen Halbleiterschicht (2) Strukturen mit einer Höhe (h) von mehr als 100 nm aufweist.

11. Halbleiterbauelement nach Anspruch 10, dadurch gekennzeichnet, dass die strukturierte Grenzfläche (7) der fotoempfindlichen Halbleiterschicht (2) Strukturen mit einer Höhe (h) zwischen 1,5 µm und 10 µm aufweist.

12. Halbleiterbauelement nach einem der vorhergehenden Ansprüche, dadurch gekennzeichnet, dass die strukturierte Grenzfläche (7) der fotoempfindlichen Halbleiterschicht (2) Strukturen aufweist, deren Höhe mindestens das 50-fache der Breite beträgt.

13. Halbleiterbauelement nach einem der vorhergehenden Ansprüche, dadurch gekennzeichnet, dass die strukturierte Grenzfläche (7) der fotoempfindlichen Halbleiterschicht (2) Strukturen mit einer Flächendichte von mindestens 10^4 cm^{-2} aufweist.

14. Halbleiterbauelement nach einem der vorhergehenden Ansprüche, dadurch gekennzeichnet, dass die strukturierte Grenzfläche (7) der fotoempfindlichen Halbleiterschicht (2) Strukturen aufweist, die überwiegend eine Flankensteilheit von mehr als 45° aufweisen.

15. Halbleiterbauelement nach einem der vorhergehenden Ansprüche,

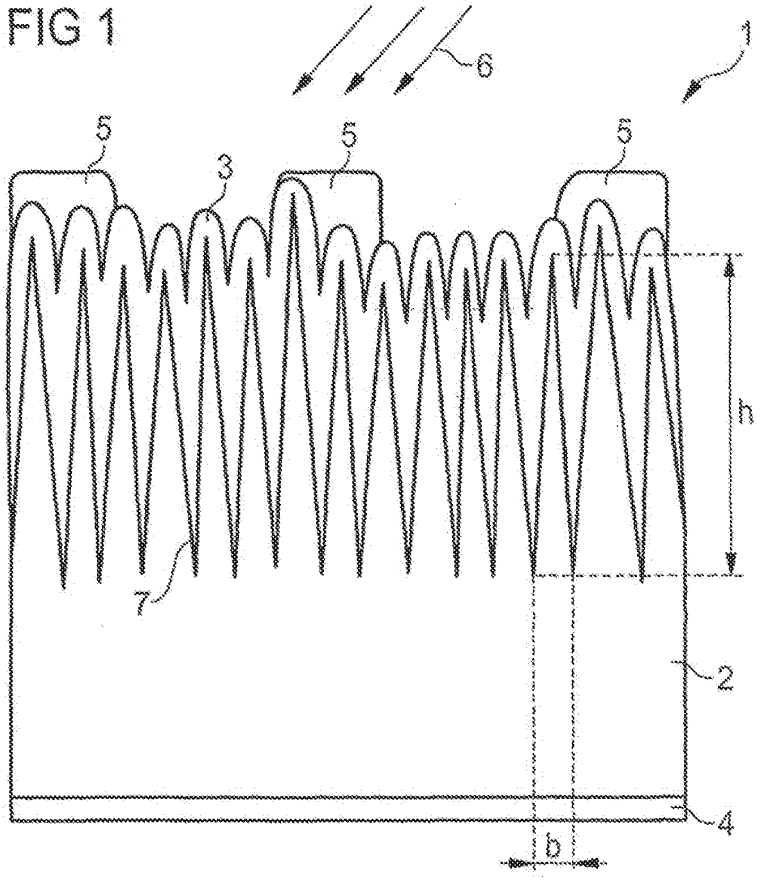
SAMSUNG EX. 1002 - 2374/4148

dadurch gekennzeichnet, dass
die strukturierte Grenzfläche (7) der fotoempfindlichen Halbleiterschicht (2) eine stochastische Struktur aufweist.

16. Halbleiterbauelement nach einem der Ansprüche 1 bis 14, dadurch gekennzeichnet, dass
die strukturierte Grenzfläche (7) der fotoempfindlichen Halbleiterschicht (2) eine deterministische Struktur aufweist.

17. Halbleiterbauelement nach einem der vorhergehenden Ansprüche,
dadurch gekennzeichnet, dass
die strukturierte Grenzfläche (7) der fotoempfindlichen Halbleiterschicht (2) mittels eines Ätzverfahrens strukturiert ist.

FIG 1



SIONYX1403000024.0065

SAMSUNG EX. 1002 - 2376/4148

FIG 2

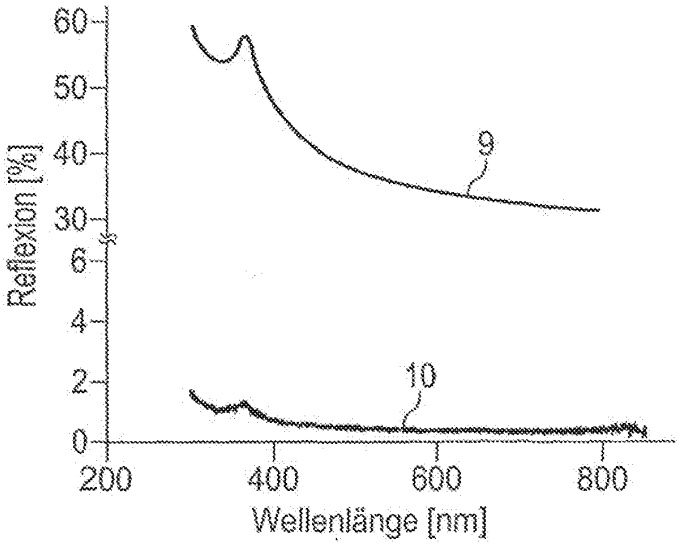
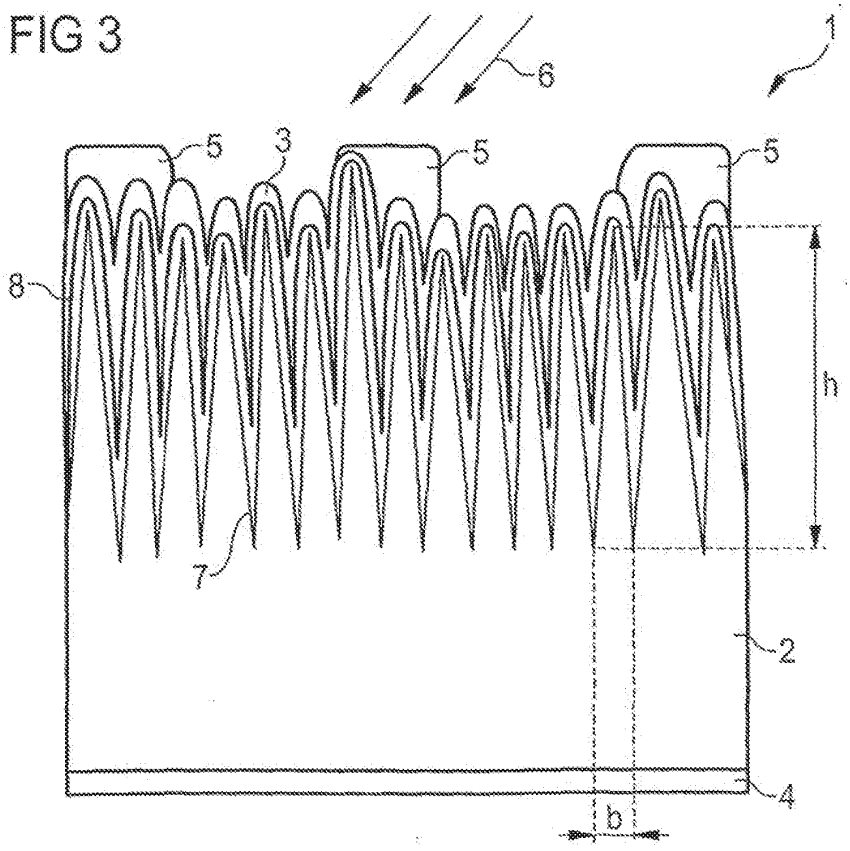


FIG 3



SIONYX1403000024.0066

SAMSUNG EX. 1002 - 2377/4148

(12) INTERNATIONAL APPLICATION PUBLISHED UNDER THE PATENT COOPERATION TREATY (PCT)

(19) World Intellectual Property Organization
International Bureau

(43) International Publication Date
25 March 2010 (25.03.2010)

PCT

(10) International Publication Number
WO 2010/033127 A1

(51) International Patent Classification:
H01L 27/146 (2006.01)

(21) International Application Number:
PCT/US2008/077209

(22) International Filing Date:
22 September 2008 (22.09.2008)

(25) Filing Language: English

(26) Publication Language: English

(71) Applicant *(for all designated States except US)*: **SIONYX, INC.** [US/US]; 100 Cummings Street, Suite 243F, Beverly, Massachusetts 01915 (US).

(72) Inventor; and

(75) Inventor/Applicant *(for US only)*: **VEEDER, Kenton** [US/US]; 143 Grovers Avenue, Winthrop, Massachusetts 02152 (US).

(74) Agent: **HALLAJ, Ibrahim**; Pepper Hamilton Llp, 500 Grant Street, 50th Floor, Pittsburgh, Pennsylvania 15219 (US).

(81) Designated States *(unless otherwise indicated, for every kind of national protection available)*: AE, AG, AL, AM, AO, AT, AU, AZ, BA, BB, BG, BH, BR, BW, BY, BZ, CA, CH, CN, CO, CR, CU, CZ, DE, DK, DM, DO, DZ, EC, EE, EG, ES, FI, GB, GD, GE, GH, GM, GT, HN, HR, HU, ID, IL, IN, IS, JP, KE, KG, KM, KN, KP, KR, KZ, LA, LC, LK, LR, LS, LT, LU, LY, MA, MD, ME, MG, MK, MN, MW, MX, MY, MZ, NA, NG, NI, NO, NZ, OM, PG, PH, PL, PT, RO, RS, RU, SC, SD, SE, SG, SK, SL, SM, ST, SV, SY, TJ, TM, TN, TR, TT, TZ, UA, UG, US, UZ, VC, VN, ZA, ZM, ZW.

(84) Designated States *(unless otherwise indicated, for every kind of regional protection available)*: ARIPO (BW, GH, GM, KE, LS, MW, MZ, NA, SD, SL, SZ, TZ, UG, ZM, ZW), Eurasian (AM, AZ, BY, KG, KZ, MD, RU, TJ, TM), European (AT, BE, BG, CH, CY, CZ, DE, DK, EE, ES, FI, FR, GB, GR, HR, HU, IE, IS, IT, LT, LU, LV, MC, MT, NL, NO, PL, PT, RO, SE, SI, SK, TR), OAPI (BF, BJ, CF, CG, CI, CM, GA, GN, GQ, GW, ML, MR, NE, SN, TD, TG).

Published:

— *with international search report (Art. 21(3))*

WO 2010/033127 A1

(54) **Title**: RESPONSE-ENHANCED MONOLITHIC-HYBRID PIXEL

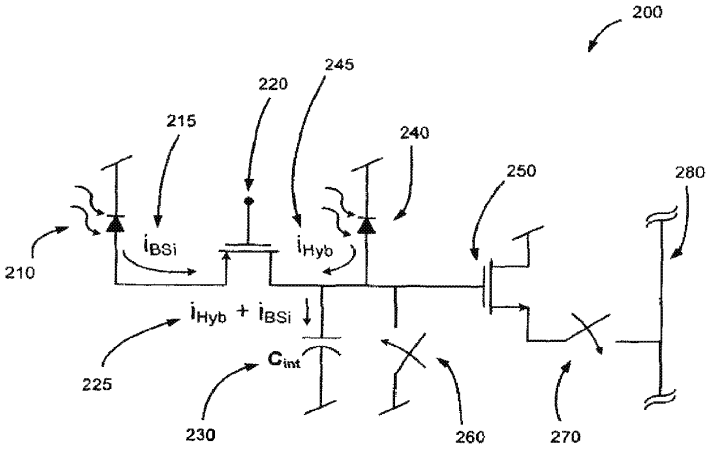


Fig. 2

(57) **Abstract**: A light-sensing pixel is described that includes more than one detector element, each of which is sensitive to a range of wavelengths of the electromagnetic spectrum. The detectors are arranged in a readout circuit that can be constructed on a monolithic semiconductor product such that one or more of the detectors can be switched on or off to include or exclude an output contribution from said detectors and enhance the response of the pixel. Also, the detectors can included a laser-treated semiconductor sensor for efficient sensing of radiation in one or more regions of the spectrum. Arrays and imaging products using such pixels are disclosed.

SAMSUNG EX. 1002 - 2378/4148

RESPONSE-ENHANCED MONOLITHIC-HYBRID PIXEL

I. TECHNICAL FIELD

[0001] The present disclosure relates to the detection of electromagnetic radiation, and more particularly, to methods and articles for detecting such radiation using monolithic or hybrid semiconductor-based designs that have improved response to incident radiation.

II. RELATED APPLICATIONS

[0002] N/A

III. GOVERNMENT FUNDING

[0003] N/A

IV. BACKGROUND

[0004] Pixels, or "picture elements," are the basic light- or color-detection and display elements that form a digital image. Typical digital video and imaging systems use a collection of detector pixels to capture a two-dimensional image field at a capture end (such as a camera) and another corresponding collection of display pixels to display the corresponding two-dimensional image at a display end (such as a monitor). In digital imaging systems, an array of light-sensitive pixels, each including a light sensor or detector, respond to an intensity of incident light at each pixel location, providing an electrical output representative of the incident light. The output of an imager can be referred to as an image.

[0005] Motion or video cameras repeat the process described above, but permit a time-sequence to be captured, for example at regular intervals, so that the captured images can be replayed to recreate a dynamic scene or sequence.

[0006] Most film and digital pixel imagers include wavelength-specific sensors or detectors. The chemical composition of the film or the design of the digital pixels and associated filters determines the range of wavelengths of light to which the film or pixels respond. Practically, a detector or imager has a frequency response that is optimized to provide images of light in the range of wavelengths the imager is designed for. The most common examples are sensitive to visible light (e.g., red, green, blue, and combinations thereof). Visible light corresponds to

SIONYX1403000024.0068

SAMSUNG EX. 1002 - 2379/4148

the range of wavelengths of electromagnetic radiation to which our eyes are sensitive, and is generally in the range of 400 to 750 nanometers (nm).

[0007] Special film and digital pixel imagers are designed for low-light operation to provide night vision capability for military, security, or other special applications in which an illumination source is not available to cause a visible light image. Low-light or night vision imagers rely on detecting and imaging frequencies below (wavelengths longer than) the visible (red) wavelengths, and are sometimes called infra-red (IR) detectors. IR detection is more suited for picking up heat emissions from objects such as a person's body or a vehicle. IR radiation itself can be roughly divided into sub-spectra including the near-infra-red (NIR) having wavelengths between about 750 to 1100 nm, short-wave-infra-red (SWIR) having wavelengths between about 1100 and 2500 nm, medium-wave-infra-red (MWIR) having wavelengths between about 2500 and 8000 nm, and long-wave-infra-red (LWIR) having wavelengths between about 8000 and 12000 nm. These ranges are defined somewhat arbitrarily, and are given merely for simplifying the following discussion, and those skilled in the art will appreciate the generality of the discussion as it relates to the bands of wavelengths of the electromagnetic spectrum.

[0008] Present visible light imaging cameras have used silicon devices made with CID, CCD, or CMOS APS architectures. The low cost and efficient collection of photons from 400-750nm wavelengths has enabled silicon devices. Extending the use of silicon imagers into the near infrared (NIR) band requires a greater volume of material to detect these wavelengths because of silicon's relatively low absorption coefficient in this wavelength range. This increases the size of the detectors and causes increased leakage current and requires expensive manufacturing processes or higher voltages to operate. The use of thick silicon substrates also limits the ability to integrate other devices.

[0009] Present low-light or night vision IR imagers are usually less sensitive than would be desired, lack color definition, and have limited frequency response. Also, low-light imagers can be more costly, noisy, and require greater circuit resources than visible light imagers to achieve useful gains in low-signal conditions. Furthermore, IR sensors are larger than would be desired for compact portable applications because most IR sensitive materials must be cooled significantly to achieve good performance. Most sensors that can detect long-

SIONYX1403000024.0069

SAMSUNG EX. 1002 - 2380/4148

wavelength portions of the electromagnetic spectrum remain poor at detecting visible light, especially in the short-wavelength portions of the spectrum, for example blue and violet light.

[0010] One presently-available solution is a stacked detector, as described for example in U.S. Pat. No. 6,111,300 to Cao, et al. However, this detector fails to adequately capture radiation in a range suitable for some applications with sufficient sensitivity. In addition, present systems do not generally provide for efficient cost and space-efficient readout circuitry for use with stacked detector elements. Also, such systems lack the flexibility in their design to selectively optimize the detectors for a variety of uses under corresponding conditions.

[0011] In summary, present imaging sensors and pixels do not sufficiently capture the full range of wavelengths useful for developing good images across long and short wavelength portions of the spectrum, and improved detector designs and readout circuit integration is needed for such detectors.

V. SUMMARY

[0012] From the discussion given above it can be appreciated that better detectors capable of operating in a variety of wavelength ranges are desirable. The following discussion provides such improved detection methods and apparatus, including methods and apparatus for detecting light in the IR ranges as well as shorter visible ranges, including in the blue range. Greater bandwidth detectors allow imaging in a variety of lighting conditions, for example in day and night. Embodiments hereof provide silicon-based imagers and detector elements capable of imaging across a range of electromagnetic wavelengths, including in various portions of the IR spectrum and in a wide range of lighting conditions. Additionally, the present embodiments provide compact, thin designs that offer increased sensitivity and resolution at a lower cost than presently available systems. Embodiments hereof provide improved manufacturing and process handling capability for producing the detectors and for implementing readout circuits associated therewith.

[0013] A specific embodiment hereof is directed to a light-sensing pixel for detecting at least a portion of the electromagnetic spectrum, including a first detector element having a laser-treated detector portion for detecting a first range of wavelengths of the electromagnetic spectrum; a second detector element for

SIONYX1403000024.0070

SAMSUNG EX. 1002 - 2381/4148

detecting a second range of wavelengths of the electromagnetic spectrum; a collection point for accumulating a first electrical output of said first detector element as well as a second electrical output of said second detector; a bias point for applying a biasing voltage to said first detector element and capable of affecting the first electrical output of said first detector element; and an output point for providing an electrical output of said light-sensing pixel.

[0014] Another embodiment hereof is directed to a light-sensitive array comprising a plurality of pixels as described above, wherein said plurality of pixels each provides an electrical output that can be addressably sensed and contributes to a collective output of said array.

[0015] Yet another embodiment is directed to an imaging apparatus comprising an array of pixels as described above such that an image corresponding to said collective output of said array or pixels can be captured or displayed.

[0016] Other embodiments and uses for the methods and systems given herein can be developed by those skilled in the art upon comprehending the present disclosure.

VI. Brief Description of the Drawings

[0017] For a fuller understanding of the nature and advantages of the present invention, reference is be made to the following detailed description of preferred embodiments and in connection with the accompanying drawings, in which:

[0018] Fig. 1 illustrates an exemplary light-sensing pixel including a black silicon detector element;

[0019] Fig. 2 illustrates an exemplary light-sensing pixel including both a black silicon detector element and another detector element which can be hybridized onto the pixel for enhanced response; and

[0020] Fig. 3 illustrates an exemplary cross-sectional view of a response-enhanced pixel.

VII. Detailed Description

[0021] The present disclosure describes systems and articles of manufacture for providing light sensors, pixels, detectors, or imagers and methods for making and using the same. These methods and apparatus are useful in many applications, including applications benefiting from imaging in a variety of light

SIONYX1403000024.0071

SAMSUNG EX. 1002 - 2382/4148

conditions. In some embodiments the detectors and techniques provided herein can be adapted to small, inexpensive, low-power, portable applications such as hand-carried, helmet-mounted and similar applications.

[0022] Some or all embodiments hereof include a sensor or detector sensitive to certain electromagnetic wavelengths and formed into a device on a semiconductor substrate. In some embodiments, the detector includes a portion comprising a semiconductor material, for example silicon, which is irradiated by a short pulse laser to create modified micro-structured surface morphology. The laser processing can be the same or similar to that described in U.S. Patent No. 7,057,256 to Carey et al., which is hereby incorporated by reference. The laser-processed semiconductor is made to have advantageous light-absorbing properties. In some cases this type of material has been called "black silicon" due to its visually darkened appearance after the laser processing and because of its enhanced absorption of light and IR radiation compared to other forms of silicon.

[0023] Generally, the wavelength of the irradiating laser pulse for making black silicon, its fluence, and pulsewidth can affect the morphology of the microstructured surface. In some embodiments, the laser fluence may be between about 1.5 kJ/m^2 and 12 kJ/m^2, but can vary depending on the substrate composition. The choice of the fluence of laser pulses irradiating a silicon wafer to generate a microstructured layer therein can also affect the gettering performance (capacity and/or specificity) of a microstructured substrate. In general, in various embodiments of the invention, the laser pulse fluence is selected to be greater than about 3 kJ/m^2. More preferably, the fluence may be chosen to be in a range of about 3 kJ/m^2 to about 10 kJ/m^2, or a range of about 3 kJ/m^2 to about 8 kJ/m^2.

[0024] Additionally, the laser pulse length can affect the morphology and absorption properties of the treated silicon. Irradiation of a substrate according to the invention can be with femtosecond laser pulses or picosecond or nanosecond pulses. Other factors that can affect microstructures morphology include laser polarization and laser propagation direction relative to the irradiated silicon surface.

[0025] In some embodiments, the laser microstructuring of a substrate is performed in the presence of a mixture of two or more substances where needed to accomplish the present purposes. For example, silicon samples treated in the

SIONYX1403000024.0072

SAMSUNG EX. 1002 - 2383/4148

presence of a mixture of SF_6 and Cl_2 exhibit an increase in the microstructure density at higher partial pressure of SF_6.

[0026] We now turn to a description of an exemplary apparatus for detecting electromagnetic radiation or light in at least a range of wavelengths of the electromagnetic spectrum.

[0027] **Fig. 1** illustrates an exemplary pixel 100 comprising a photonic detector 110 of the laser-treated type described above (sometimes referred to as 'black silicon' detector) which can be integrated into a same substrate as the readout circuitry for the pixel. Radiation in certain wavelength ranges incident on pixel 100 is detected by detector 110 and creates a corresponding current i_{BSi} 115, which represents an electrical output, to flow from the detector. A direct injection detector bias 120 is applied to hold a relatively constant voltage across the detector 110.

[0028] Integration capacitance C_{int}, 150 which may be physical or parasitic and represents a collection point, integrates the charge collected by flow of current i_{BSi} 125 through the capacitor 150 over some time. Note that in this embodiment, currents 125 and 115 are equivalent and integrate on C_{int}, 150. A resultant output voltage is provided at the input of signal buffer 160, which represents an output point. Contact post 130 in this exemplary embodiment is not used but may be exposed at the surface of pixel 100, and can be used as will be described below to couple to a hybridized detector element to enhance the response of a pixel. Signal buffer 160 is addressed by column 190 and row enable switch 180 for non-destructive reading of pixel 100. It should be appreciated that a source follower buffer, row switch, and column line are merely examples of a generally-realizable output port, which here includes circuit elements 160, 190, and 180 only by way of example. A reset switch 170 shorts out capacitor 150 thus resetting the collection process. During normal operation detector 110 is reverse biased by the bias voltage applied to terminal 120 as mentioned above.

[0029] In some applications, the pixel 100 and its laser-treated detector 110 allow for detection and sensitivity to long wavelength radiation including in ranges beyond the visible range of the electromagnetic spectrum, such as the near infra-red or the infra-red ranges.

[0030] **Fig. 2** illustrates an exemplary response-enhanced pixel 200 having both a first laser-treated detector element 210 similar to those described above, but

SIONYX1403000024.0073

SAMSUNG EX. 1002 - 2384/4148

also includes another light sensitive detector element 240. Second detector 240 may be sensitive to a range of the electromagnetic spectrum that is different from the range of wavelengths that first detector 210 is sensitive to. For example, second detector 240 may be sensitive to shorter wavelengths than first detector 210. More specifically, second detector 240 may be sensitive to wavelengths nearer the blue light or ultraviolet (short) wavelengths of the visible spectrum. As will be described below, this can allow for an overall pixel 200 that has sensitivity to a broad range of wavelengths ranging across those detected by first detector 210 (e.g. longer wavelengths) to those detected by second detector 240 (e.g. shorter wavelengths).

[0031] In this embodiment, a first current or electrical output i_{BSi} 215 from first detector 210 as well as a second current or electrical output i_{Hyb} 245 from second detector 240 are summed and cause an integrated collected charge on collection point or capacitor C_{int} 230 to develop an output voltage at output point or signal buffer 250.

[0032] The pixel 200 can be addressed and read on column 280 and row enable 270 and can contribute to an array of pixels 200 in an imaging product as discussed earlier. Again, a reset switch 260 can be provided to zero out or reset or short out integration capacitor C_{int} 230. As discussed earlier, an generic output port can be used in the present context, of which the present embodiment includes circuit elements 250, 270, and 280 only by way of example.

[0033] In manufacturing such enhanced response detector pixels 200, the second detector element 240 may be hybridized over a monolithic pixel array using the previously-unused post 130 of Fig. 1. The second detector 240 can be selected and constructed such that it provides a great enough output resistance to the circuit of Fig. 2 so that a change in voltage on capacitor C_{int} 230 not to substantially affect the generated photocurrent i_{Hyb} 245 of second detector 240.

[0034] The combination of the detected light and corresponding outputs of detectors 210 and 240 can be used to form enhanced response pixels and enhanced response imaging products having a plurality of pixels such as the exemplary pixel of Fig. 2. Such imaging products can couple a grid of pixels 200 in a two-dimensional format to form sensors such as cameras and scanners that are responsive to a wide range of electromagnetic wavelengths. The output voltage at

SIONYX1403000024.0074

SAMSUNG EX. 1002 - 2385/4148

non-destructive signal buffer 250 will thus correspond to, and in some cases be a function of, the photon flux detected at each detector element, 210, 240.

[0035] It should be appreciated that the present disclosure can apply to more than just two detector elements, but rather, three or more detectors could be used, each sensitive to a range of wavelengths in a pixel structure.

[0036] In some embodiments, the structure of the present monolithic-hybrid pixels and the low reverse bias voltages required to bias the black silicon detectors allows selective shutting off of the black silicon detectors in situ. That is, the detectors 110 and 210 of Figs. 1 and 2 may be secured by proper application of bias voltage at terminals 120 and 220, respectively. In the example of the pixel 200 of Fig. 2, this can be used to provide unique and useful integration qualities to pixel 200, and can provide useful discrimination in color detection by pixel 200. The non-destructive read buffer 250 allows varying integration times without destroying or losing the collected charge on integration capacitor C_{int} 230.

[0037] In some embodiments the present pixels provide multi-color sensing, multi-integration sensors that enhance the overall response and usefulness of an associated sensing array or imaging product.

[0038] Fig. 3 illustrates a representative cross-sectional view of an exemplary response-enhanced pixel 300 similar to that described earlier with respect to Fig. 2.

[0039] Another feature of the present embodiments that facilitates its use in practical applications is that the present laser treated silicon is compatible with most standard CMOS readout circuit substrates, and can leverage known silicon MEMS and amorphous silicon MEMS technologies such as silicon MEMS cantilever technology.

[0040] The present invention should not be considered limited to the particular embodiments described above, but rather should be understood to cover all aspects of the invention as fairly set out in the attached claims. Various modifications, equivalent processes, as well as numerous structures to which the present invention may be applicable, will be readily apparent to those skilled in the art to which the present invention is directed upon review of the present disclosure. The claims are intended to cover such modifications.

[0041] We claim:

SAMSUNG EX. 1002 - 2386/4148

VIII. CLAIMS

1. A light-sensing pixel for detecting at least a portion of the electromagnetic spectrum, comprising:

a first detector element having a laser-treated detector portion for detecting a first range of wavelengths of the electromagnetic spectrum;

a second detector element for detecting a second range of wavelengths of the electromagnetic spectrum;

a collection point for accumulating a first electrical output of said first detector element as well as a second electrical output of said second detector;

a bias point for applying a biasing voltage to said first detector element and capable of affecting the first electrical output of said first detector element; and

an output point for providing an electrical output of said light-sensing pixel.

2. The pixel of claim 1, said first detector element comprising a black silicon detector portion that is sensitive to electromagnetic wavelengths in an infra-red range of the electromagnetic spectrum.

3. The pixel of claim 2, said second detector element comprising a semiconducting photodetector element that is sensitive to electromagnetic wavelengths in a visible range of the electromagnetic spectrum.

4. The pixel of claim 1, further comprising readout circuitry including addressing switch points for addressing said pixel.

5. The pixel of claim 4, said readout circuitry constructed and arranged along with said first detector element in a monolithic semiconductor structure.

6. The pixel of claim 5, said second detector element constructed and arranged in a hybrid arrangement to be coupled to said monolithic semiconductor structure.

7. The pixel of claim 1, further comprising a post for coupling said second detector element to said readout circuitry and said collection point.

SIONYX1403000024.0076

SAMSUNG EX. 1002 - 2387/4148

8. The pixel of claim 1, said collection point comprising a capacitor which collects an electrical charge from said first and second detector elements.

9. The pixel of claim 1, said bias point constructed and arranged to receive a bias voltage and coupled to said first detector element to control the first electrical output of said first detector element.

10. The pixel of claim 9, said bias point providing a reverse bias voltage constructed and arranged to substantially shut off said first electrical output of said first detector element.

11. The pixel of claim 1, further comprising a reset switch coupled to said collection point.

12. The pixel of claim 1, said first and second electrical outputs comprising respective first and second electrical currents, and said bias point comprising a bias voltage terminal electrically coupled to said first and second detector elements and coupled to said collection point so as to control said first and second electrical currents.

13. A light-sensitive array comprising a plurality of pixels as claimed in claim 1, wherein said plurality of pixels each provides an electrical output that can be addressably sensed and contributes to a collective output of said array.

14. An imaging apparatus comprising an array of pixels as claimed in claim 13 such that an image corresponding to said collective output of said array or pixels can be captured or displayed.

SIONYX1403000024.0077

SAMSUNG EX. 1002 - 2388/4148

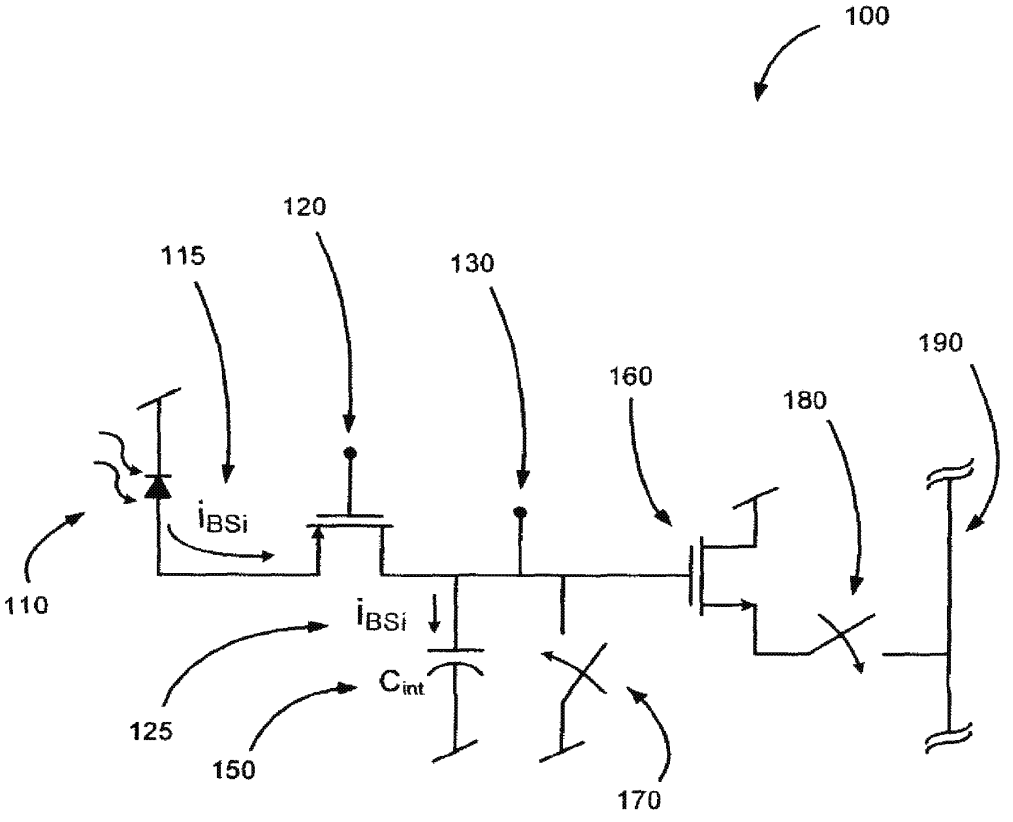


Fig. 1

SIONYX1403000024.0078

SAMSUNG EX. 1002 - 2389/4148

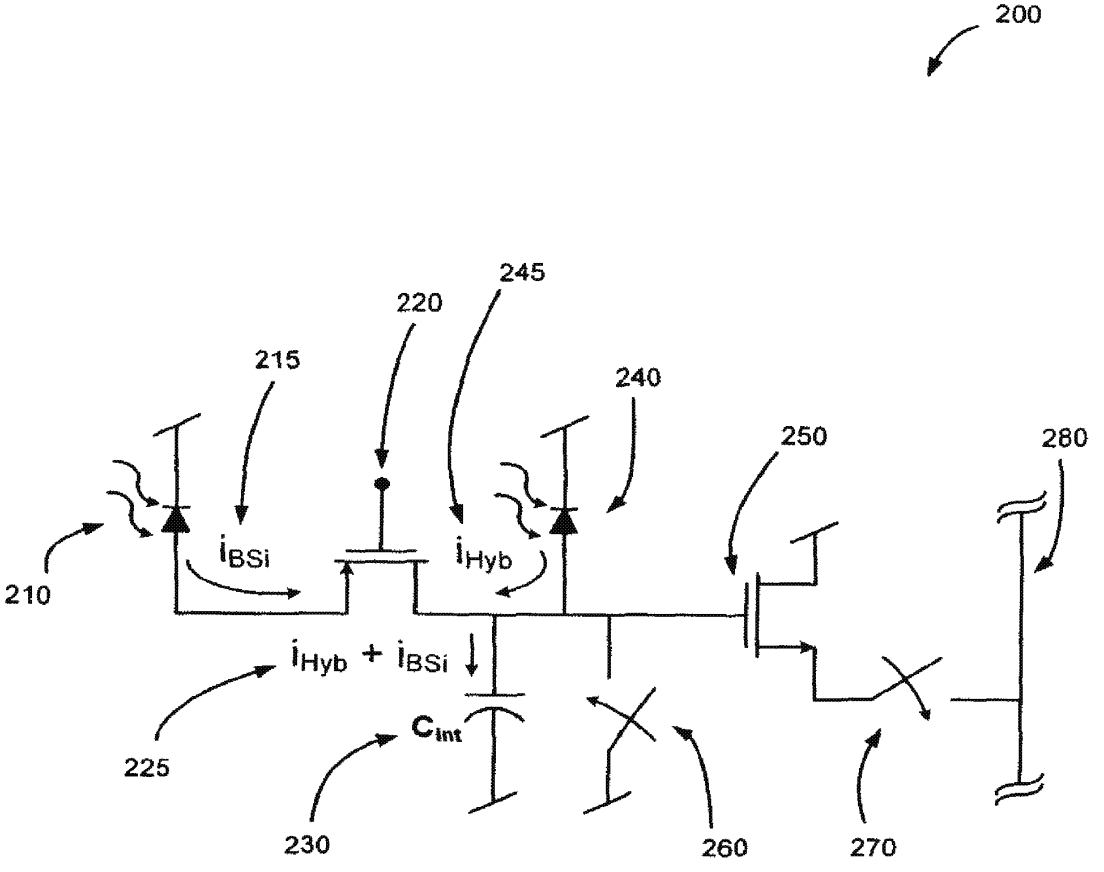


Fig. 2

SAMSUNG EX. 1002 - 2390/4148

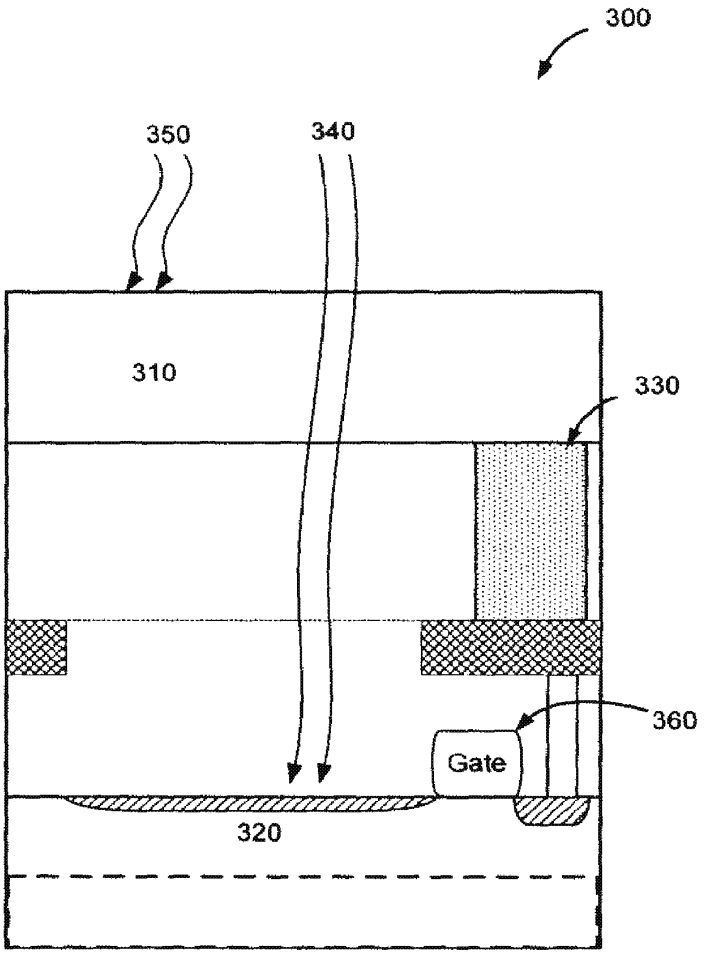


Fig. 3

INTERNATIONAL SEARCH REPORT

International application No
PCT/US2008/077209

A. CLASSIFICATION OF SUBJECT MATTER
INV. H01L27/146

According to International Patent Classification (IPC) or to both national classification and IPC

B. FIELDS SEARCHED

Minimum documentation searched (classification system followed by classification symbols)
H01L

Documentation searched other than minimum documentation to the extent that such documents are included in the fields searched

Electronic data base consulted during the international search (name of data base and, where practical, search terms used)
EPO-Internal

C. DOCUMENTS CONSIDERED TO BE RELEVANT

Category*	Citation of document, with indication, where appropriate, of the relevant passages	Relevant to claim No.
Y	US 5 751 005 A (WYLES RICHARD H [US] ET AL) 12 May 1998 (1998-05-12) cited in the application column 3, lines 50-55; figures 1,2 column 5, lines 34-36 column 7, lines 9-15	1-5,7-14
Y	US 2003/029495 A1 (MAZUR ERIC [US] ET AL MAZUR ERIC [US] ET AL) 13 February 2003 (2003-02-13) cited in the application paragraphs [0030], [0031], [0036], [0042], [0043]; figure 1	1-5,7-14
Y	US 2007/051876 A1 (SUMI HIROFUMI [JP] ET AL) 8 March 2007 (2007-03-08)	1-5
A	figures 21,22	6-14

-/--

[X] Further documents are listed in the continuation of Box C.

[X] See patent family annex.

* Special categories of cited documents :

"A" document defining the general state of the art which is not considered to be of particular relevance

"E" earlier document but published on or after the international filing date

"L" document which may throw doubts on priority claim(s) or which is cited to establish the publication date of another citation or other special reason (as specified)

"O" document referring to an oral disclosure, use, exhibition or other means

"P" document published prior to the international filing date but later than the priority date claimed

"T" later document published after the international filing date or priority date and not in conflict with the application but cited to understand the principle or theory underlying the invention

"X" document of particular relevance; the claimed invention cannot be considered novel or cannot be considered to involve an inventive step when the document is taken alone

"Y" document of particular relevance; the claimed invention cannot be considered to involve an inventive step when the document is combined with one or more other such documents, such combination being obvious to a person skilled in the art.

"&" document member of the same patent family

Date of the actual completion of the international search	Date of mailing of the international search report
6 April 2009	16/04/2009

Name and mailing address of the ISA/	Authorized officer
European Patent Office, P.B. 5818 Patentlaan 2 NL – 2280 HV Rijswijk Tel. (+31-70) 340-2040, Fax: (+31-70) 340-3016	Zakharian, Andre

Form PCT/ISA/210 (second sheet) (April 2005)

SIONYX1403000024.0081

SAMSUNG EX. 1002 - 2392/4148

INTERNATIONAL SEARCH REPORT

International application No
PCT/US2008/077209

C(Continuation). DOCUMENTS CONSIDERED TO BE RELEVANT

Category*	Citation of document, with indication, where appropriate, of the relevant passages	Relevant to claim No.
A	US 5 523 570 A (HAIRSTON ALLEN W [US]) 4 June 1996 (1996-06-04) column 2, lines 17-19; figure 1	6

Form PCT/ISA/210 (continuation of second sheet) (April 2005)

SIONYX1403000024.0082

SAMSUNG EX. 1002 - 2393/4148

INTERNATIONAL SEARCH REPORT

Information on patent family members

International application No
PCT/US2008/077209

Patent document cited in search report	Publication date	Patent family member(s)	Publication date
US 5751005 A	12-05-1998	DE 69723808 D1	04-09-2003
		DE 69723808 T2	15-04-2004
		EP 0849802 A2	24-06-1998
		IL 122556 A	11-01-2001
		JP 3187760 B2	11-07-2001
		JP 10281869 A	23-10-1998
US 2003029495 A1	13-02-2003	US 2008258604 A1	23-10-2008
		US 2005127401 A1	16-06-2005
US 2007051876 A1	08-03-2007	JP 2006238093 A	07-09-2006
US 5523570 A	04-06-1996	NONE	

Form PCT/ISA/210 (patent family annex) (April 2005)

SAMSUNG EX. 1002 - 2394/4148

(12) 特許協力条約に基づいて公開された国際出願

(19) 世界知的所有権機関
国際事務局

(43) 国際公開日
2008 年8 月21 日 (21.08.2008)

PCT

(10) 国際公開番号
WO 2008/099524 A1

(51) 国際特許分類:
H01L 31/04 (2006.01)

(21) 国際出願番号: PCT/JP2007/065386

(22) 国際出願日: 2007 年8 月6 日 (06.08.2007)

(25) 国際出願の言語: 日本語

(26) 国際公開の言語: 日本語

(30) 優先権データ:
特願2007-036432 2007 年2 月16 日 (16.02.2007) JP

(71) 出願人 (米国を除く全ての指定国について): 三菱重工業株式会社 (MITSUBISHI HEAVY INDUSTRIES, LTD.) [JP/JP]; 〒1088215 東京都港区港南二丁目１６番５号 Tokyo (JP).

(72) 発明者; および

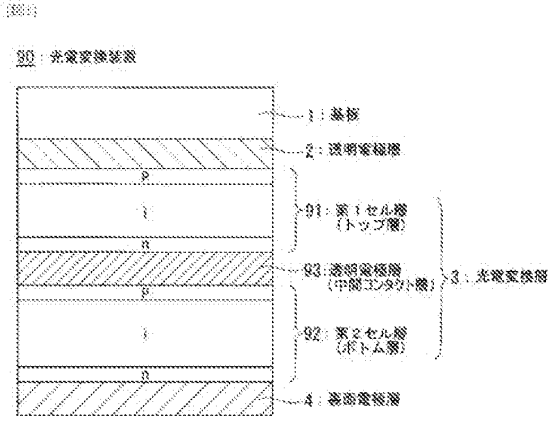
(75) 発明者/出願人 (米国についてのみ): 中野 要治 (NAKANO, Youji) [JP/JP]; 〒8510392 長崎県長崎市深堀町五丁目７１７番１号 三菱重工業株式会社 長崎研究所内 Nagasaki (JP). 竹内 良昭 (TAKEUCHI, Yoshiaki) [JP/JP]; 〒8510392 長崎県長崎市深堀町五丁目７１７番１号 三菱重工業株式会社 長崎研究所内 Nagasaki (JP). 山口 賢剛 (YAMAGUCHI, Kengo) [JP/JP]; 〒8510392 長崎県長崎市深堀町五丁目７１７番１号 三菱重工業株式会社 長崎研究所内 Nagasaki (JP). 山内 康弘 (YAMAUCHI, Yasuhiro) [JP/JP]; 〒8508610 長崎県長崎市鉢の浦町１番１号 三菱重工業株式会社 長崎造船所内 Nagasaki (JP).

(74) 代理人: 藤田 考晴, 外 (FUJITA, Takaharu et al.); 〒2200012 神奈川県横浜市西区みなとみらい３－３－１ 三菱重工横浜ビル２４Ｆ Kanagawa (JP).

(続葉有)

(54) Title: PHOTOELECTRIC CONVERTER AND METHOD FOR FABRICATING THE SAME

(54) 発明の名称: 光電変換装置及びその製造方法



90 PHOTOELECTRIC CONVERTER
1 SUBSTRATE
2 TRANSPARENT ELECTRODE LAYER
3 PHOTOELECTRIC CONVERSION LAYER
91 FIRST CELL LAYER (TOP LAYER)
92 SECOND CELL LAYER (BOTTOM LAYER)
93 TRANSPARENT ELECTRODE LAYER (INTERMEDIATE CONTACT LAYER)
4 BACKSIDE ELECTRODE LAYER

(57) **Abstract:** A photoelectric converter satisfying both high photoelectric conversion efficiency and high productivity, and its fabrication method. The photoelectric converter (90) has a substrate with a transparent electrode where a transparent electrode layer (2) is provided on a transparent insulating substrate (1), and at least a photoelectric conversion layer (92) principally comprising a crystalline silicon based semiconductor and a backside electrode layer (4) that are formed sequentially on the transparent electrode layer (2) side of the substrate with a transparent electrode. The transparent electrode layer (2) on the substrate with a transparent electrode has a surface shape where large and small protrusions and recesses coexist and spectral haze rate is 20% or above at the wavelength of 550-800 nm. The photoelectric conversion layer principally comprising the crystalline silicon based semiconductor has a film thickness of 1.2-2 μm, and a Raman ratio of 3.0-8.0.

(57) 要約: 高い光電変換効率と高い生産性を両立した光電変換装置及びその製造方法を提供することを目的とする。透明絶縁性の基板１上に透明電極層２を設けてなる透明電極付き基板と、該透明電極付き基板の透明電極層２側に順次形成された、結晶質シリコン系半導体を主として有する光電変換層９２ならびに裏面電極層４とを少なくとも有してなる光電変換装置であって、前記透明電極付き基板の透明電極層２表面が、大小の凹凸が混在した形状であり、かつ分光ヘイズ率が５５０ｎｍ以上８００ｎｍ以下の波長で２０％以上であり、前記結晶質シリコン系半導体を主として有する光電変換層の膜厚が１．２μｍ以上２μｍ以下、かつラマン比が３．０以上８．０以下である光電変換装置９０を提供する。

WO 2008/099524 A1

SIONYX1403000024.0084

SAMSUNG EX. 1002 - 2395/4148

(81) 指定国 (表示のない限り、全ての種類の国内保護が可能): AE, AG, AL, AM, AT, AU, AZ, BA, BB, BG, BH, BR, BW, BY, BZ, CA, CH, CN, CO, CR, CU, CZ, DE, DK, DM, DO, DZ, EC, EE, EG, ES, FI, GB, GD, GE, GH, GM, GT, HN, HR, HU, ID, IL, IN, IS, JP, KE, KG, KM, KN, KP, KR, KZ, LA, LC, LK, LR, LS, LT, LU, LY, MA, MD, ME, MG, MK, MN, MW, MX, MY, MZ, NA, NG, NI, NO, NZ, OM, PG, PH, PL, PT, RO, RS, RU, SC, SD, SE, SG, SK, SL, SM, SV, SY, TJ, TM, TN, TR, TT, TZ, UA, UG, US, UZ, VC, VN, ZA, ZM, ZW.

(84) 指定国 (表示のない限り、全ての種類の広域保護が可能): ARIPO (BW, GH, GM, KE, LS, MW, MZ, NA, SD, SL, SZ, TZ, UG, ZM, ZW), ユーラシア (AM, AZ, BY, KG, KZ, MD, RU, TJ, TM), ヨーロッパ (AT, BE, BG, CH, CY, CZ, DE, DK, EE, ES, FI, FR, GB, GR, HU, IE, IS, IT, LT, LU, LV, MC, MT, NL, PL, PT, RO, SE, SI, SK, TR), OAPI (BF, BJ, CF, CG, CI, CM, GA, GN, GQ, GW, ML, MR, NE, SN, TD, TG).

添付公開書類:
— 国際調査報告書

明 細 書

光電変換装置及びその製造方法

技術分野

[0001] 本発明は、光電変換装置及びその製造方法に関し、特に発電層としてシリコンを用いる薄膜シリコン積層型太陽電池に関するものである。

背景技術

[0002] 従来より、太陽電池等の光電変換装置として、シリコン系薄膜光電変換装置が知られている。この光電変換装置は、一般に、基板上に、第1透明電極、シリコン系半導体層（光電変換層）、第2透明電極及び裏面電極膜を順次積層したものである。半導体層はp型、i型及びn型の半導体材料によって形成されるpin接合を有している。光電変換装置が太陽電池である場合においてはこのpin接合がエネルギー変換部となって、太陽光の光エネルギーを電気エネルギーに変換する。このように、光電変換層が1層の光電変換装置の構造は、シングル構造と呼ばれている。

[0003] また、光電変換装置の光電変換効率を高めるために、バンドギャップの異なる半導体からなる光電変換層を複数重ねて用いる方法がある。このように複数の光電変換層を重ねて用いた光電変換装置は多接合型光電変換装置と呼ばれ、吸収波長帯域が異なる光電変換層を2段重ねた構造はタンデム構造、3段重ねた構造はトリプル構造と呼ばれている。タンデム構造の光電変換装置を例にとると、太陽光入射側の光電変換層（以下、「トップセル」ともいう）としては短波長の光を吸収するアモルファス（非晶質）シリコンが用いられ、また、トップセルで吸収されなかった光を吸収するために、太陽光入射側とは反対側の光電変換層（以下、「ボトムセル」ともいう）としては長波長の光を吸収する微結晶シリコン等の結晶質シリコン系半導体を用いることができる。

[0004] このような光電変換装置を用いた太陽電池には、次のような技術課題（1）が存在する。

（1）高効率化：太陽光をエネルギー変換部にいかに効率よく取り込み、電気エネルギーに変換する効率をいかに高めるか。

SIONYX1403000024.0086

SAMSUNG EX. 1002 - 2397/4148

[0005] 上記技術課題(1)の高効率化としては、12%以上の発電効率を得ることが目安となるが、従来、例えばタンデム型太陽電池において12%以上の発電効率を得るためには、2μm以上のボトムセル膜厚が必要であった。更に発電効率を上げるためには、ボトムセルの厚膜化(3μm以上)が検討されている。

[0006] また、上記技術課題(1)の高効率化を実現するために、第1透明電極を含めた基板のヘイズ率を高めることが検討されている。従来は、第1透明電極を含めた基板のヘイズ率を大きくすると、入射光の光散乱による光閉じ込め効果が向上して発電電流は増大するが、第1透明電極を含めた基板表面の大きな凹凸の影響などで開放電圧と形状因子が大幅に低下するので、電池としては好ましくないと、一般的に考えられていた。これを解決するために、前記基板及び第1透明電極として、ガラス基板上に、不連続な複数の山部によるマクロな凹凸(テクスチャ)と、この山部間をうめる複数の平坦部とを有しており、該山部及び該平坦部の外表面が、ミクロの多数の凹凸(テクスチャ)を有する構造(ダブルテクスチャ構造)となっている透明導電性酸化物付き基体を用いることが提案されている(特許文献1、特許文献2参照)。特許文献1及び2の透明導電性酸化物付き基体は、太陽光の全波長域で良好な光散乱性能有するものであり、特許文献2には、これを用いて作製されたアモルファスシリコン太陽電池が、その実施例において、開放電圧と形状因子をほぼ維持しつつ光電変換効率が高められることが示されている。

特許文献1:国際公開第03/036657A1号公報

特許文献2:特開2005-347490号公報

発明の開示

[0007] 光電変換装置を用いた太陽電池を実用化するためには、前記技術課題(1)に加え、下記技術課題(2)も存在する。

(2)生産性向上:生産性のボトルネックとなる結晶質シリコン系光電変換層中のi層をいかに薄膜化できるか。

[0008] 太陽電池の製造時間は、ボトムセル等を構成する結晶質シリコン系光電変換層中のi層の製膜時間に律速するため、上記技術課題(2)の生産性の点からは、結晶質シリコン系光電変換層中のi層の膜厚の薄膜化が極めて有効である。ところが、例え

SAMSUNG EX. 1002 - 2398/4148

ばタンデム型太陽電池においてボトムセルの膜厚を2μmより薄膜化すると、発電電流の低下が著しく、よって発電効率の低下が著しくなる。このため、太陽電池の製造時間が長時間かかっても、2μm以上のボトムセル膜厚が適用されている。

このように、前記技術課題(1)と(2)とは、互いにトレードオフの関係にあった。

[0009] 前記特許文献1に示された技術は、光の吸収波長特性が異なる結晶質シリコン系半導体からなる光電変換層の発電効率を特に考慮したものではなく、また、太陽電池の生産性向上について検討されたものでもなかった。従って、結晶質シリコン系半導体からなる光電変換層を有する太陽電池については、入射光の吸収波長域が特に長波長側で異なるため、透明電極の凹凸による光閉じ込め形状は違うものが必要となるが、結晶質シリコン系半導体の膜厚を薄膜化することを考慮して凹凸形状を適正化することが未確立であり、発電効率の高効率化(技術課題(1)の解決)と太陽電池の生産性向上(技術課題(2)の解決)を両立できる技術が依然として望まれていた。

[0010] また、特許文献1のように大きな凹凸と小さな凹凸の混在する透明導電性酸化膜付き基板を用いて太陽電池を作製すると、大きな凹凸構造のみで構成してヘイズ率を高めた透明導電性酸化物付き基板を用いる場合よりも開放電圧と形状因子の低下を小さくすることはできるものの、やはり開放電圧と形状因子の低下が認められる。

[0011] 本発明は、このような事情に鑑みてなされたものであって、高い光電変換効率と高い生産性を両立した光電変換装置及びその製造方法を提供することを目的とする。

[0012] また、本発明は、大小の凹凸が混在した形状によりヘイズ率を高めた透明電極付き基板を用いた光電変換装置において、開放電圧と形状因子の低下を抑制しつつ高い光電変換効率を実現すること、およびこのような光電変換装置の製造方法を提供することを目的とする。

[0013] 上記課題を解決するために、本発明の第1の態様にかかる光電変換装置は、以下の手段を採用する。

すなわち、本発明の第1の態様にかかる光電変換装置は、透明絶縁性の基板上に透明電極層を設けてなる透明電極付き基板と、該透明電極付き基板の透明電極層側に順次形成された、結晶質シリコン系半導体を主として有する光電変換層ならび

SIONYX1403000024.0088

SAMSUNG EX. 1002 - 2399/4148

に裏面電極層とを少なくとも有してなる光電変換装置であって、前記透明電極付き基板は、表面が大小の凹凸が混在した形状であり、かつ分光ヘイズ率が550nm以上800nm以下の波長で20%以上であり、前記光電変換層の膜厚が1.2μm以上2μm以下であり、かつラマン比が3.0以上8.0以下である光電変換装置である。

[0014] 前記第1の態様にかかる光電変換装置において、結晶質シリコン系光電変換層のラマン比を3.0以上8.0以下とすることにより、結晶の粒界が適度に非晶質シリコンで充填された光電変換装置を得ることができる。これにより、結晶粒界の電流リークを抑制できるので、開放電圧(Voc)及び形状因子(FF)の低下が抑制された光電変換装置を得ることができる。前記透明電極付き基板を用いた場合には、基板の凹凸に起因して欠陥の多い結晶粒界が生成しやすいため、結晶粒界の非晶質シリコンによる充填が特に有効である。

[0015] また、膜厚が1.2μm以上2μm以下の前記結晶質シリコン系半導体を主として有する光電変換層を形成することにより、結晶質シリコン系半導体を主として有する光電変換層のi層の膜厚を薄膜としても、高い発電電流を生じる光電変換装置を製造することができ、更に欠陥数を膜厚分低下でき、また、膜厚方向の電位勾配が大きいので発生電荷が欠陥にトラップされにくくなるので、開放電圧(Voc)及び形状因子(FF)の低下が抑制された光電変換装置を製造することができる。従って、薄膜化と高効率化を同時に達成した光電変換装置を製造でき、さらに、結晶質シリコン系i層を薄膜化することで、この製膜によって律速される光電変換装置の製造時間を短縮することができるので、光電変換装置の生産性が向上する。

[0016] 一般にヘイズ率といえば、ヘイズメータで計測される、波長が約550nmの光のヘイズ率をさす。波長550nmのヘイズ率が高いと波長550nm程度の光はよく散乱されるが、長波長光は該波長のヘイズ率が高ければよく散乱されるが、該波長のヘイズ率が低ければ散乱されにくい。従来の一層の凹凸(テクスチャ)構造の場合、波長550nmのヘイズ率が30%であっても、波長800nmの分光ヘイズ率は5%以下となり、結晶質シリコン系の光電変換層で光を閉じ込めたい700～900nmの波長域の光の散乱増強による光閉じ込めは不十分であった。また、350nm以下の波長域では、前記透明電極基板の透過率が小さくなるためヘイズ率を正しく計測することができない

SAMSUNG EX. 1002 - 2400/4148

。したがって、550nm以上800nm以下の波長のヘイズ率を、波長を特定した光を用いて計測する分光ヘイズ率で定義し、分光ヘイズ率20%以上、より好ましくは30%以上とすることにより、結晶質シリコン系の光電変換層で光閉じ込めの影響を強く受ける700～900nmの波長域の光の散乱、光閉じ込めを増強でき、発電電流を増大することができる。

[0017] 前記第1の態様にかかる光電変換装置において、前記透明電極付き基板と前記結晶質シリコン系半導体を主として有する光電変換層との間に、非晶質シリコン系半導体を主として有する光電変換層を形成してもよい。

[0018] このような構成とすることにより、非晶質シリコン系半導体を主として有する光電変換層では太陽光の短波長側成分の光電変換が行われ、結晶質シリコン系半導体を主として有する光電変換層では太陽光の長波長側成分の光電変換が行なわれるので、より光電変換効率の高い光電変換装置とすることができる。

[0019] 前記第1の態様にかかる光電変換装置において、前記非晶質シリコン系半導体を主として有する光電変換層と前記結晶質シリコン系半導体を主として有する光電変換層との間に、中間コンタクト層を形成してもよい。

[0020] 中間コンタクト層を構成とすることにより、非晶質シリコン系半導体を主として有する光電変換層を薄膜化し、劣化率を改善できる一方で、結晶質シリコン系半導体を主として有する光電変換層への入射光が低下し、電流値が低下する。したがって、非晶質シリコン系半導体を主とする光電変換層の劣化率改善と、結晶質シリコン系半導体を主とする光電変換層の発電電流の低下との相対関係から、中間コンタクト層の膜厚は、90nm以下とすることが好ましく、さらには50nm以上70nm以下とすることがより好ましい。また、中間コンタクト層としては、ZnO系膜（例えば、GZO膜）で形成され、ZnO系単膜での光吸収率がλ＝450nm以上1000nm以下の範囲で1%未満であることがより好ましい。中間コンタクト層の透明性が損なわれると、結晶質シリコン系半導体を主とする光電変換層へ入射する光が低下し、発電電流が低下するため、波長が450nm以上1000nm以下の波長領域に対しては、ほぼ透明であることが好ましい。

[0021] 前記第1の態様にかかる光電変換装置において、前記透明電極付き基板の透明

SAMSUNG EX. 1002 - 2401/4148

電極層表面が、複数の山部と複数の平坦部とで構成され、該山部及び該平坦部の表面がミクロの多数の凸部を連続して有してなり、前記山部の前記基板面垂直方向における高さが0．4μm以上0．7μmであり、基板面10μm角における前記山部の数が15以上50以下であり、前記ミクロの多数の凸部の底面径が0.1μm以上0.3μm以下であり、高さ／底面径の比が0.7以上1.2以下であるものが好ましい。

[0022] 前記第1の態様にかかる光電変換装置は、前記特性を有する透明電極付き基板を適用することで、結晶質シリコン系半導体を主として有する光電変換層（例えば、タンデム型太陽電池のボトムセル）のi層の膜厚を例えば1．5μmの薄膜としても、高い発電電流を生じる。更に結晶質シリコン系半導体を主として有する光電変換層のi層を薄膜化することにより、開放電圧（Voc）及び形状因子（FF）の低下も抑制できる。すなわち、結晶質シリコン系半導体を主として有する光電変換層を薄膜とすることにより、欠陥数を膜厚分低下でき、また、膜厚方向の電位勾配が大きいので発生電荷が欠陥にトラップされにくくなる。従って、光電変換装置の薄膜化と高効率化を同時に達成できる。さらに、結晶質シリコン系光電変換層中のi層を薄膜化できることにより、この層の製膜時間によって律速される光電変換装置の製造時間を短縮することができるので、前記第1の態様にかかる光電変換装置は、生産性が向上したものとなる。

[0023] 従来の技術において開放電圧と形状因子が低下した原因の1つとして、透明電極の谷の部分から光電変換層の膜厚方向に膜成長相間の不連続な境界（その境界を「異相」と呼ぶことにする）が生じ、キャリアの再結合中心となるためと推定される。この異相は、下地の各々の面からシリコン膜が製膜・成長する際に、その成長面が衝突し、衝突面が格子の欠陥或いは微細な隙間となったものと推定され、キャリアの再結合による損失の原因となる。尚、この光電変換層の膜厚方向の異相は、光電変換層の断面方向の透過顕微鏡分析によって、検出することができる。倍率8万倍以上で光電変換層を長さ100μmの範囲で観察し、亀裂が認められたとき異相がある、貫通する異相が1本でも認められたとき貫通する異相があると判断する。

[0024] この異相の発生自体を抑制するには、透明導電性酸化物基板の凹凸を単純に大型化するのではなく、大きな凹凸と小さな凹凸が混在することが有効である。しかしな

SIONYX1403000024.0091

SAMSUNG EX. 1002 - 2402/4148

がら、前記透明電極を用いた場合においても、例えば製膜速度が1nm／sec以上の高速で製膜すると完全に異相の発生を抑制することは難しく、異相発生の抑制には光電変換層を形成する製膜条件選定における制限がある。このため、本発明者らは、特に高速で製膜する場合において異相が発生しても光電変換層を貫通する異相を遮断する知見を得るに至った。

[0025] 従って、本発明者らは、この異相を抑制すること、または完全に抑制はできなくても光電変換層を貫通する異相を遮断できれば、開放電圧低下、形状因子低下を抑制できるという知見を得た。

[0026] この知見から、上記課題を解決するために、本発明の第2の態様にかかる光電変換装置及び第3の態様にかかる光電変換装置の製造方法は、以下の手段を採用する。

すなわち、本発明の第2の態様にかかる光電変換装置は、透明絶縁性の基板上に透明電極層を設けてなる透明電極付き基板と、該透明電極付き基板の透明電極層側に順次形成された、非晶質シリコン系半導体を主として有する光電変換層ならびに裏面電極層とを少なくとも有し、前記透明電極付き基板は、表面が大小の凹凸が混在した形状であり、かつ分光ヘイズ率が550nm以上800nm以下の波長で20%以上、特に好ましくは30%以上であり、前記非晶質シリコン系半導体を主として有する光電変換層中に、該光電変換層の透明電極層側表面から裏面電極層側表面に貫通する異相（膜成長相間の不連続な境界）を遮断する層（異相遮断層と呼ぶこととする）を設けた光電変換装置、もしくは前記基板と前記非晶質シリコン系半導体を主として有する光電変換層の間に、該光電変換層の透明電極層側表面から裏面電極層側表面に貫通する異相の形成を防止する異相防止層を設けた光電変換装置である。

[0027] 第2の態様にかかる光電変換装置によれば、非晶質シリコン系半導体を主として有する光電変換層の透明電極層側表面から裏面電極層側表面に貫通する異相を遮断または防止できるので、このような異相による電流リークを抑えることができ、開放電圧低下、形状因子低下が抑制される。

[0028] また、本発明の第3の態様にかかる光電変換装置の製造方法は、透明絶縁性の基

SIONYX1403000024.0092

SAMSUNG EX. 1002 - 2403/4148

板上に透明電極層を形成して透明電極付き基板を作製し、該透明電極付き基板の透明電極層側に非晶質シリコン系半導体を主として有する光電変換層ならびに裏面電極層とを少なくとも順次形成する光電変換装置の製造方法であって、前記透明電極付き基板の透明電極層表面が多数の凸部を連続して有してなり、前記非晶質シリコン系半導体を主として有する光電変換層中に、該光電変換層の透明電極層側表面から裏面電極層側表面に貫通する異相を遮断する異相遮断層を形成するか、もしくは前記透明電極層の形成と前記非晶質シリコン系半導体を主として有する光電変換層形成の間に、該光電変換層の透明電極層側表面から裏面電極層側表面に貫通する異相の形成を防止する異相防止層を形成する、光電変換装置の製造方法である。

[0029] 第3の態様にかかる光電変換装置の製造方法によれば、非晶質シリコン系半導体を主として有する光電変換層の透明電極層側表面から裏面電極層側表面に貫通する異相が遮断または防止されるので、このような異相による電流リークが抑えられ、開放電圧低下、形状因子低下が抑制された光電変換装置を製造することができる。

[0030] 前記第2の態様にかかる光電変換装置及び第3の態様にかかる光電変換装置の製造方法において、前記非晶質シリコン系半導体を主として有する光電変換層をp層、i層、n層を順次形成してなる層とし、前記異相遮断層を前記i層の一部分において、p層、n層、あるいはi層の他の部分より低速で製膜された層とすることができる。低速で製膜することにより、製膜面表面での製膜粒子の拡散・移動時間が増大し、より安定なサイトに堆積して低欠陥の層、即ち異相が少ない層を形成することができる。また、低速で製膜された層はi層の一部分と薄いため、低速で製膜する製膜時間にかかる処理時間は、全体の生産時間に与える影響としては少なくなり、生産性を維持したまま異相が少ない層を形成することができる。

[0031] あるいは、前記非晶質シリコン系半導体を主として有する光電変換層をp層、i層、n層を順次形成してなる層とし、前記n層の一部或いは全体を非晶質の層として、前記n層が前記異相遮断層の機能を有することができる。なお、非晶質とは、ラマン分光分析で分析したとき、Si結晶のピークが全く検出されないものであり、製膜条件では、水素ガス／シランガス希釈率を低下する方向、又はRFパワーを低下する方向で得る

SAMSUNG EX. 1002 - 2404/4148

ことができる。積層膜で再表面のみ非晶質膜にする場合は，ラマン分光分析で下地のSi結晶質膜のピークが検出されることがあり，ガラス基板又は透明電極つきガラス基板上に、単一条件の膜のみを形成してラマン分光分析を実施してSi結晶ピークの有無を判断することとする。非晶質の膜は、欠陥が水素で終端されるので、結晶質と比較して欠陥が連続しにくいために異相となりにくく、異相を遮断する機能を有するものである。

あるいは、前記非晶質シリコン系半導体を主として有する光電変換層をp層，i層、n層を順次形成してなる層とし、前記n層の少なくともその一部を200Pa以上の圧力下で製膜した層とすることにより，前記n層が異相遮断層の機能を有することができる。高圧で製膜すると、製膜される原料ガスの気相中での衝突拡散が促進され、下地の凹部にも原料ガスが到達しやすいために、凹部にも均一に製膜されるので、欠陥上にも均一に良好な膜が形成される，すなわち異相を抑制できると考えられる。

あるいは、前記異相防止層を、前記凸部を円滑化した前記透明電極層とすることができる。前記凸部の円滑化とは、凸部が連続して形成されることにより凸部の境界に生成する谷部について、通常は平面どおしの組合せのため谷の底は明瞭な線状であるが，その線がないように底面を円滑化したもの、例えば、スプーンカットのような形状を有することである。

[0032] 前記異相防止層を、前記透明電極層表面にイオン処理を施して形成してもよい。イオン処理とは、例えば真空中でのアルゴンイオン照射によるイオンエッチングであり、透明電極の表面形状を原子レベルのエッチング、再付着により制御できる。イオンエッチングのイオン照射角度とイオンエネルギーを調整することで，透明電極の凹凸の特に斜面部の原子をエッチング除去し、谷部の底に再付着させることができ、結果として鋭利な谷形状を円滑化することができる。

[0033] 前記第2の態様にかかる光電変換装置及び第3の態様にかかる光電変換装置の製造方法において、前記透明電極付き基板は、550nm以上800nm以下の波長における分光ヘイズ率が20％以上であるものが好ましい。前記分光ヘイズ率が30％以上であるものが特に好ましい。

上述のとおり、従来の凹凸(テクスチャ)構造の場合、波長550nmの分光ヘイズ率

SIONYX1403000024.0094

SAMSUNG EX. 1002 - 2405/4148

が30%であっても，波長800nmの分光ヘイズ率は5%以下となり、結晶質シリコン系半導体の光電変換層で光を閉じ込めたい700～900nmの波長域の光の散乱増強による光閉じ込めは不十分であった。そこで、前記第2の態様にかかる光電変換装置及び第3の態様にかかる光電変換装置の製造方法においては，凹凸を大型化して、長波長光に対しても高ヘイズとなるようにする。また、350nm以下の波長域では、前記透明電極の透過率が小さくなるためヘイズメータにより分光ヘイズ率を計測することができない。したがって、550nm以上800nm以下の波長の分光ヘイズ率を20%以上、好ましくは30%以上とすることにより、結晶質シリコン系半導体の光電変換層で光閉じ込めの影響を強く受ける700～900nmの波長域の光の散乱、光閉じ込め効果を増強でき、発電電流を増大することができる。

[0034] 前記第2の態様にかかる光電変換装置及び第3の態様にかかる光電変換装置の製造方法において、前記非晶質シリコン系半導体を主として有する光電変換層と前記裏面電極の間に、結晶質シリコン系半導体を主として有する光電変換層を形成してもよい。

[0035] このような構成とすることにより、非晶質シリコン系半導体を主として有する光電変換層では太陽光の短波長側成分の光電変換が行われ、結晶質シリコン系半導体を主として有する光電変換層では太陽光の長波長側成分の光電変換が行なわれるので，より光電変換効率の高い光電変換装置とすることができる。

[0036] また、結晶質シリコン系半導体を主として有する光電変換層は結晶質シリコン系半導体に限らず、結晶質もしくは非晶質シリコン系半導体、結晶質もしくは非晶質シリコンゲルマニウム系半導体を主として有しても同等の効果が得られる。

[0037] また、結晶質シリコン系半導体を主として有する光電変換層とさらに第3の光電変換層を積層して3層構造以上の光電変換装置としても良い。この場合、結晶質シリコン系半導体を主として有する光電変換層及び第3の光電変換層は、結晶質もしくは非晶質シリコン系半導体、結晶質もしくは非晶質シリコンゲルマニウム系半導体を主として有する光電変換層とすることともでき、非晶質シリコン系半導体を主として有する光電変換層、結晶質シリコン系半導体を主として有する光電変換層光電変換層、第3の光電変換層の順に長波長側成分へと吸収が増大するように，各光電変換層の

SAMSUNG EX. 1002 - 2406/4148

材料や膜質、膜厚を設定すれば良い。

[0038] 本発明によれば、高い光電変換効率と高い生産性を両立した光電変換装置及びその製造方法を提供することができる。本発明の光電変換装置は、太陽電池として好適に利用することができる。

[0039] また、本発明によれば、表面が大小の凹凸が混在した形状であり、かつ分光ヘイズ率が550nm以上800nm以下の波長で20%以上、特に好ましくは30%以上である透明電極付き基板を用いた光電変換装置において、開放電圧と形状因子の低下を抑制しつつ高い光電変換効率を実現することができる。さらに、このように優れた光電変換装置の製造方法を提供することができる。本発明の光電変換装置は、太陽電池として好適に利用することができる。

[0040] また、光電変換層を薄膜化しても高い光電変換効率が得られる。薄膜化により、発電電流は多少は低下するが、従来の基板に対し薄膜化による発電電流低下は大幅に改善できている。また、薄膜化により、開放電圧と形状因子が向上される。薄膜化による光電変換層の薄膜化により、光電変換層に含まれる欠陥を膜厚相当分低下できること、および光電変換層内に発生する起電力に対する電位勾配が拡大することによる生成電荷の再結合(欠陥による消滅)確率を低下できるためである。

[0041] 薄膜化は、生産性の点でメリットが大きい。光電変換装置ひとつあたりの生産時間を短縮でき、さらに生産装置の製膜室内部のメンテナンス頻度も低下でき、結果として、時間あたり或いは装置あたりの生産量を薄膜化の膜厚の比率以上に増大できる。従って、生産を考慮すると、光電変換効率の向上以上に、生産性向上のメリットが大きいといえる。

図面の簡単な説明

[0042] [図1]本発明の光電変換装置の構成を示す概略図である。

[図2]本発明の第1実施形態で用いられる透明電極付き基板の形状及び構成を示す一部切欠き断面図である。

[図3]図2に示す山部112の拡大図である。

[図4]本発明の太陽電池パネルの製造方法の実施形態の一部を示す概略図である。

SAMSUNG EX. 1002 - 2407/4148

[図5]本発明の太陽電池パネルの製造方法の実施形態の一部を示す概略図である。

[図6]本発明の太陽電池パネルの製造方法の実施形態の一部を示す概略図である。

[図7]本発明の太陽電池パネルの製造方法の実施形態の一部を示す概略図である。

[図8]本発明の第2実施形態のイオン処理前における透明電極付き基板の透明電極表面の電子顕微鏡写真である。

[図9]本発明の第2実施形態のイオン処理後における透明電極付き基板の透明電極表面の電子顕微鏡写真である

[図10]本発明の第2実施形態の透明電極付き基板を用いて作製したタンデム型太陽電池の断面の透過型電子顕微鏡写真である。

[図11]本発明の第2実施形態の透明電極付き基板を用いて作製したタンデム型太陽電池の断面の透過型電子顕微鏡写真である。実施例7に示したように非晶質Si—i層の製膜後期を位相遮断層として、非晶質Si層を貫通する異相を抑制したものである。

[図12]実施例11のタンデム型太陽電池における、ボトムセルのn層製膜後のラマン比と太陽電池特性の関係を示す図である。

符号の説明

[0043] 1 基板

2 透明電極層

3 光電変換層

4 裏面電極層

6 太陽電池モジュール

90 光電変換装置

91 第1セル層(トップ層)

92 第2セル層(ボトム層)

93 中間コンタクト層

SAMSUNG EX. 1002 - 2408/4148

110 透明電極付き基板

111 基板

112 山部

114 透明電極

115 小山部

116 連続層

117 凸部

H_a 山部の高さ

P_a 山部間の平均ピッチ

H_c 小山部H_cの高さ

P_c 小山部間の平均ピッチ

H_b 凸部の高さ

P_b 凸部間のピッチ

15 絶縁溝

21 バックシート

23 出力ケーブル

50 太陽電池パネル

発明を実施するための最良の形態

[0044] 第1実施形態

以下に、本発明の第1実施形態について、図面を参照して説明する。

[0045] まず、本実施形態の光電変換装置の製造方法により製造される光電変換装置の構成について説明する。

[0046] 図1は、本実施形態の光電変換装置の構成を示す概略図である。光電変換装置90は、シリコン系太陽電池であり、基板1、透明電極層2、太陽電池光電変換層3としての第1セル層(トップ層)91ならびに第2セル層(ボトム層)92、及び裏面電極層4を具備する。本実施形態において、第1セル層91は非晶質シリコン系半導体を主として有する光電変換層であり、第2セル層は結晶質シリコン系半導体を主として有する光電変換層である。第2セル層92は、膜厚が1.2μm以上2.0μm以下、かつ、第

SAMSUNG EX. 1002 - 2409/4148

2セル層92のラマン比が3．0以上8．0以下であることが好ましい。より好ましくは、ラマン比が3．5以上8．0以下であり、更に好ましくは5．0以上7．5以下である。

[0047] 第2セル層92のラマン比を3．0以上8．0以下とすることにより、結晶の粒界が適度に非晶質シリコンで充填された光電変換装置を得ることができ、結晶粒界の電流リークを抑制できるので、開放電圧(Voc)及び形状因子(FF)の低下が抑制された光電変換装置を得ることができる。

[0048] ここで「ラマン比」とはラマン分光評価で520cm^{-1}の結晶Siの強度と480cm^{-1}の非晶質Siの強度の比(結晶Siの強度／非晶質Siの強度)をいう(以下同じ)。ラマン比の測定方法としては、光電変換装置の裏面電極を過酸化水素水等の溶剤で溶剤除去して供試体とする。まず、第2セル層92の膜面側から測定用光を照射する。測定用光としては、レーザー単色が用いられ、例えば、YAGレーザー光の2倍波(波長532nm)が好適に用いられる。第2セル層92の膜面側から測定用光を入射すると、ラマン散乱が観測されるが、測定用光、及び散乱光の一部は第2セル層92中で吸収される。したがって、例えば、YAGレーザー光の2倍波を測定用光として用いた場合は、入射面から約0．1μmの深さまでの情報を得ることができる。なお、第2セル層92と裏面電極層4との間に第2の透明電極層を形成している場合は、第2の透明電極層のラマンピークはバックグランドとして差し引くことができるので、第2の透明電極層を希塩酸等の溶剤により溶剤除去しなくてもしてもよい。

[0049] 上記したように、ラマン比は光電変換層i層(実質的に真性な層)を評価するが、一般的に用いられるレーザー波長532nmでは、0．1μmの侵入深さにより、表面から約0．1μmの膜の結晶化率を評価することとなる。本実施形態においては、第2セル層92のi層製膜後のラマン比が3．0以上8．0以下であることが直接的な意味であるが、最表面にn層が製膜されてもn層は膜厚が0．03μm程度と薄いのでi層からの情報が支配的であること、および一般的なn層の結晶性も2～10であることにより、n層製膜後にn層を含めたラマン比を計測してもn層製膜前と近い値となる。したがって、第2セル層92のラマン比は、3．0以上8．0以下が好ましい範囲となる。

また、ラマン比は製膜において製膜装置構造などにより基板1上で分布が発生する、例えば製膜時に基板1表面上での原料ガス組成変化による局所的なラマン比分布

SAMSUNG EX. 1002 - 2410/4148

や、プラズマや温度分布による全体的なラマン比分布がある。このため、評価する基板1上で極力全体的な平均値として評価する。例えば、1m角以上の基板サイズであれば、均等に区分けした少なくとも10箇所以上の領域で計測し、この平均値で評価することが好ましい。

[0050] ラマン比が3．0以上8．0以下という値は、一般的に結晶化が進んだ結晶質シリコンの値より、非晶質シリコンを多く含むものである。特にダブルテクスチャ基板のような高ヘイズ基板を用いる場合、基板の凹凸に起因する結晶粒界の欠陥が生じるため、粒界を適度に非晶質シリコンで充填することが重要となる。ラマン比が3．0以上が好ましい理由は、結晶シリコン部で発生した電荷が断面方向につながった結晶構造を導通することができるように大部分の結晶構造が膜厚方向に連続するために必要なラマン比が3．0以上であるためで、これは断面観察により確認できる。ラマン比が8．0以下が好ましい理由は、柱状結晶の粒界が電流リークポイントとなり電圧が発生しなくなるのを抑制するために非晶質で結晶粒界を充填することが好ましく、実験的にその場合のラマン比が8．0以下であるためである。

[0051] なお、ここで、「シリコン系」とはシリコン(Si)やシリコンカーバイド(SiC)やシリコンゲルマニウム(SiGe)を含む総称である。また、「結晶質シリコン系」とは、アモルファスシリコン系すなわち非晶質シリコン系以外のシリコン系を意味するものであり、微結晶シリコンや多結晶シリコン系も含まれる。

[0052] 第1セル層91及び第2セル層92の間には、透明導電膜からなる中間コンタクト層93を設けても良い(但し、本発明の光電変換装置は、中間コンタクト層93を設けたものに限定されない)。中間コンタクト層93
を設けた場合、この中間コンタクト層93で入射太陽光の一部が反射されて、第1セル(トップ層)91に再度入射される。これにより、第1セル層(トップセル)91における発電電流が増加する。そして、第1セル層91の膜厚を薄くしても、中間コンタクト層93が積層されない場合と同等の発電電流を得ることができる。したがって、第1セル層91非晶質シリコン系半導体の膜厚を薄くすることにより、当該第1セル層91における光劣化を抑制でき、光電変換装置全体としての安定化効率を向上させることができる。

[0053] 中間コンタクト層93の膜厚を厚くすることにより、第1セル層91である非晶質シリコ

SAMSUNG EX. 1002 - 2411/4148

ン系半導体の発電電流を増加させることができる。このとき、中間コンタクト層93により反射される太陽光の波長における第2セル層92での発電電流は減少する。実際には、第2セル層92である結晶質シリコン系半導体においては、第1セル層91である非晶質シリコン系半導体よりも長波長領域の太陽光による電気エネルギーへの変換が行われている。

[0054] 従って、中間コンタクト層93の膜厚を最適化することにより、中間コンタクト層93による、第2セル層92である結晶質シリコン系半導体が吸収すべき長波長領域の太陽光の吸収率を抑制することが必要になる。

[0055] 本実施の形態に係わる光電変換装置の中間コンタクト層93の膜厚と、第2セル層92における波長800nm(太陽光の長波長領域に対応)の量子効率(入射のうち発電に寄与する割合)との関係から、中間コンタクト層93の膜厚が厚くなると、中間コンタクト層93での長波長領域の太陽光の反射率も増大して、第2セル層92に入射する光量が減少する。中間コンタクト層93は、光吸収率がλ=450nm以上1000nm以下の範囲で1%未満であることが好ましく、この波長領域に対しては、ほぼ透明であることが好ましい。

[0056] 一方、中間コンタクト層93の膜厚が厚くなると、中間コンタクト層93と裏面電極層4との間で光の閉じ込め効果が増大する。このため、第2セル層92に入射した光吸収率が増大する。波長800nmの太陽光に対して、第2セル層92における光の閉じ込め効果が有効に作用する(量子効率を一定の値に維持することができる)中間コンタクト層93の膜厚は100nm以下である。

[0057] 上述したように、第1セル層91と第2セル層92との発電電流バランスを考慮して、最適な中間コンタクト層93の膜厚値は実験的に90nm以下となり、より好ましくは50nm以上70nm以下となる。これにより、より高い安定化効率を有する光電変換装置が実現される。

[0058] 次に、本発明の第1実施形態による光電変換装置において用いられる、透明電極を形成した透明絶縁性基板(以下、「透明電極付き基板」ともいう)の形状及び構成を、図2及び図3を用いて詳細に説明するが、本発明の光電変換装置及びその製造方法は、これらの図面によって限定されない。

SAMSUNG EX. 1002 - 2412/4148

[0059] 図2は、本実施形態で用いられる透明電極付き基板の形状及び構成を示す一部切欠き断面図であり、図3は、図2に示す山部112の拡大図である。図2に示すように、本実施形態において用いられる、透明電極付き基板110は、ガラス基板111上に、不連続な複数の山部112によるマクロな凹凸(テクスチャ)と、この山部間をうめる複数の平坦部113とを有しており、該山部112及び該平坦部113の外表面は、ミクロの多数の凹凸(テクスチャ)を有する構造となっている。以下、このような2つの凹凸を有する構造を、ダブルテクスチャ構造という。

[0060] また、本実施形態においては、図2に示すように、透明電極114は、第1の酸化物からなる不連続な小山部115と、その上に形成される第2の酸化物からなる連続層であって該連続層の表面にミクロの多数の凸部を連続して有する連続層116とからなるのが好ましい。小山部115の密度は、基板111面の10μm角あたり15以上50以下とされ、20以上45以下がより好ましい。この小山部115間の平均ピッチP_sは、1.0μm以上3μm以下に相当する。

第2の酸化物からなる連続層116は、小山部115上及び小山部115が形成されていない部分のガラス基板111上に連続的に形成されている。

[0061] 本実施形態においては、上記山部112の平均の高さH_s(平坦部上のミクロの凸部の頂部からの高さの平均値)は、0.4μm以上0.7μm以下であり、0.5μm以上0.6μm以下であることがより好ましい。

また、隣接する上記山部間の平坦部の距離(以下、単に「山部間の間隔」ともいう。)W_sは、直線上に0μm以上1.5μm以下であることが好ましく、0μm以上1.0μm以下であることがより好ましく、0.1μm以上0.4μm以下(いずれの山部112も不連続である)であることがさらに好ましい。本実施形態においては、複数の山部112は不連続である部分と連続している部分があってもよく、山部間の間隔W_sが0μm以上1.5μm以下であるということは、平坦部がないところがあってもよいということである。なお、平坦部が無い場合には、上記山部に隣接していなくても、上記山部付近の平坦部を用いてH_sを計測でき、または断面の顕微鏡観察を行うことでH_sは計測することができる。

さらに、上記山部112の密度は、小山部115の密度と同様の値となり、基板111面

SAMSUNG EX. 1002 - 2413/4148

の10μm角あたり15以上50以下となり、20以上45以下がより好ましい。この山部112間の平均ピッチP_sは、1.0μm以上3μm以下に相当する。

[0062] 本実施形態においては、上記小山部115の高さH_cは、上記山部の高さH_sと同様の値、すなわち0.4μm以上0.7μm以下であり、0.5μm以上0.6μm以下であることがより好ましい。

[0063] 本実施形態においては、山部112及び平坦部113の表面、すなわち、第2の酸化物からなる連続層116の表面は、図3に示されるように、ミクロの多数の凸部117を有している。ミクロの多数の凸部の底面径が0.1μm以上0.3μm以下であり、高さ／底面径の比が0.7以上1.2以下である。尚、ミクロの凸部の連続層は、表面全体においてミクロの凸部が存在する状況を示していて、一部にミクロの凸部が欠損した領域が存在しても、連続している状況とみなすものである。

[0064] また、図3において、上記小山部115上の連続層116の厚さH_g(ミクロの凸部を含む)は、0.5μm以上1.0μm以下であることが好ましく、0.5μm以上0.7μm以下であることがより好ましい。同様に、上記ガラス基板111上の連続層116の厚さH_g(ミクロの凸部を含む)は0.5μm以上1.0μm以下であることが好ましく、0.5μm以上0.7μm以下であることがより好ましい。

[0065] 本実施形態においては、上記山部112及び上記平坦部113の外表面を、このような山部による凹凸(マクロな凹凸)よりも小さな凹凸(ミクロな凹凸)とすることにより、短波長の光を強く散乱することができ、全体として広い領域の光を有効に散乱することが可能になる。すなわち、大きな凹凸である山部により長波長の光を散乱し、小さな凹凸表面より短波長の光を散乱することができるため、全体として高い光散乱性を達成することができる。

特に本実施形態においては、山部112の高さと密度を制御することにより、長波長の光の散乱を最適化し、結晶質シリコン系半導体からなる光電変換層の発電効率の向上と、製膜時間の短縮が実現される。

[0066] 前記透明電極付き基板110におけるこのような表面性状は、例えば、以下に示す方法により確認することができる。

(1)表面形状の解析:膜表面の凸部を走査型電子顕微鏡(SEM)で観察し、得ら

SAMSUNG EX. 1002 - 2414/4148

れる顕微鏡写真より，凸部の底面径を測定することができる。また、膜表面の凹凸形状をSEM、原子間力顕微鏡（AFM）により観察し，得られる顕微鏡写真より、膜表面の凹凸形及び凸部の高さを解析することができる。

（2）表面被覆率の測定：第1の酸化物からなる小山部の基板上への被覆率をSEM写真から測定し，基板上を小山部が占める面積を、基板の当該被覆面全体の面積で割った値を表面被覆率として評価することができる。

また、質量膜厚とは、基板上の一定面積中にある不連続の金属酸化物に対し、蛍光X線装置でその金属酸化物の金属量に比例する検出量を調べ、別途用意してある基板上に連続し，膜厚の既知の同種の金属酸化物における蛍光X線装置の検出量と比較して、不連続な酸化物の体積が連続になったと仮定して得られた膜厚を示す。

[0067] また、このような形状及び構成を有する透明電極付き基板110は、基板全体において、550nm以上800nm以下の波長における分光ヘイズ率が30%以上、好ましくは40%以上である。

[0068] ここで、「分光ヘイズ率」とは、透過光における散乱成分の割合を示すものである。分光ヘイズ率は波長に依存し、分光ヘイズ率を$Hz(\lambda)$、全透過率を$T_{total}(\lambda)$、透過光の直進成分を$T_{direct}(\lambda)$，透過光の散乱成分を$T_{diffuse}(\lambda)$とすると、下記式に示す関係が成り立つ。

$$T_{total}(\lambda)=T_{direct}(\lambda)+T_{diffuse}(\lambda)$$

$$Hz(\lambda)=T_{diffuse}(\lambda)/T_{total}(\lambda)\times 100[\%]$$

[0069] 以下に，上述した本実施形態の透明電極付き基板の形状及び構成ならびに特性を満たす基板（透明基板）、第1の酸化物及び第2の酸化物について詳述する。

[0070] ＜基板（透明基板）＞

本実施形態の透明電極付き基板に用いられる基板は、必ずしも平面で板状である必要はなく、曲面でも異型状でもよい。

このような基板としては，少なくともその表面が後述する第1の酸化物と異なる材料であることが好ましく，具体的には、ガラス基板、セラミックス基板、プラスチック基板、金属基板等や、これらの基板表面に酸化ケイ素膜、酸化アルミニウム膜、酸化ジルコ

SAMSUNG EX. 1002 - 2415/4148

ニウム膜、酸化チタン膜などのアルカリバリヤ層を施したもの等が挙げられる。これらのうち、透光性に優れた透明の基板であることが好ましく、ガラス基板もしくはアルカリバリア層を施したガラス基板であることが強度及び耐熱性の点から好ましい。

また、このような基板は、光電変換層の主たる吸収波長域である550nm以上800nm以下の波長領域において高い透過率、例えば80%以上の透過率を有することが好ましく、十分絶縁性で、かつ化学的、物理的耐久性が高いことが望ましい。

[0071] 上記ガラス基板としては、具体的には、例えば、無色透明なソーダライムシリケートガラス、アルミノシリケートガラス、ボレートガラス、リチウムアルミノシリケートガラス、石英ガラス、ホウ珪酸ガラス基板、無アルカリガラス基板、その他の各種ガラスからなる透明ガラス板を用いることができる。

また、本実施形態の透明電極付き基板を太陽電池用基板に用いる場合においては、ガラス基板の厚さは0.2mm以上6.0mm以下であることが、強度及び透過率の点から好ましい。

[0072] なお、ソーダライムシリケートガラス等のナトリウムを含有するガラスからなるガラス基板または低アルカリ含有ガラスからなるガラス基板の場合には、ガラスからその上面に形成される透明電導膜へのアルカリ成分の拡散を最小限にするために、上述したアルカリバリヤ層を施したガラス基板を用いることが好ましい。

また、ガラス基板の表面に、ガラス基板の表面と、その上に設けられる層との屈折率の差異を軽減するための層をさらに有していてもよい。

[0073] <第1の酸化物>

本実施形態の透明電極付き基板の透明電極膜を構成する第1の酸化物は、可視光域で高透明な酸化物であれば特に限定されず、その具体例としては、TiO_2、SnO_2、In_2O_3、ZnO、CdO、$CdIn_2O_4$、$CdSnO_3$、$MgIn_2O_4$、$CdGa_2O_4$、$GaInO_3$、$InGaZnO_4$、$Cd_2Sb_2O_7$、Cd_2GeO_4、$CuAlO_2$、$CuGaO_2$、$SrCu_2O_2$、Al_2O_3等が挙げられる。これらのうち、TiO_2、SnO_2及びフッ素を含有するSnO_2からなる群より選択される少なくとも1種を用いることが好ましい。

本実施形態においては、小山部を形成するこのような第1の酸化物の屈折率は、波長400nm以上800nm以下において、1.8以上2.2以下であることが好ましく、さら

SAMSUNG EX. 1002 - 2416/4148

に、1．9以上2．1以下であることが好ましい。

第1の酸化物の形成方法として一例を示す。上述したアルカリバリア層付きガラス基板をベルトコンベア炉において520℃に加熱し、四塩化錫、水、塩化水素ガスを同時にガラス基板に吹き付けて酸化錫核を形成する。この際、四塩化錫、水は、あらかじめ加熱し、窒素ガスをバブリングして塩化水素ガスと同時に移送することでガラス基板上に吹き付ける。

酸化錫核を形成した後、四塩化錫と水を同時にガラス基板に吹き付けることで第1の酸化物であるSnO_2を形成する。この際、四塩化錫、水は、あらかじめ加熱し、窒素ガスをバブリングして移送することでガラス基板上に吹き付けた。

[0074] なお、このような第1の酸化物からなる小山部は、上述したように、不連続な突起物であって連続膜ではないので、該突起物に覆われていない透明基板部分は、当然ながら小山部による入射光の吸収損はゼロであるため、光電変換層への入射光量を増やすことができる。

これらの小山部は、長波長光の分光ヘイズ率を高める（光の散乱度を上げる）部分であり、自由電子による吸収を抑えて、高透明にするために、電気導電性はないのが好ましい。したがって、上記第1の酸化物としてSnO_2を用いた場合は、SnO_2のみからなるか、フッ素を含有する場合でもフッ素は、SnO_2に対して0．01mol%以下の含有量であることが好ましく、0．005mol%以下の含有量であることがより好ましい。

[0075] ＜第2の酸化物＞

本実施形態の透明電極付き基板の透明電極膜を構成する第2の酸化物は、可視光域で透明であり、さらに導電性を有している透明導電性酸化物であることが必要であり、その具体例としては、SnO_2、ZnO、In_2O_3等が挙げられ、2種以上を併用してもよく、さらに、導電性発現のためのドーパントを含有していることが好ましい。

これらのうち、SnO_2はドーパントとしてフッ素またはアンチモンをSnO_2に対して0．01mol%以上4mol%以下含有することが好ましい。ZnOはドーパントとしてホウ素、Al及びGaからなる群から選択される少なくとも1種をZnOに対して0．02mol%以上5mol%以下含有することが好ましい。In_2O_3はドーパントとしてSnをIn_2O_3に対して0．02mol%以上4mol%以下含有することが好ましい。なお、これらのドーパントを用い

SAMSUNG EX. 1002 - 2417/4148

たドーピングは、ハロゲン化水素によるものであってもよい。このようなハロゲン化水素としては、具体的には、例えば、HF、HBr等が挙げられる。

本実施形態においては、連続層を形成するこのような第2の酸化物の屈折率は、波長400nm以上800nm以下において、1．8以上2．2以下であることが好ましく、さらに、1．9以上2．1以下であることが好ましい。

[0076] また、上記第2の酸化物としてフッ素を含有するSnO_2を用いることにより、導電電子密度が向上する。太陽電池に用いる基板としては、導電電子密度は、$5\times10^{19}cm^{-3}$以上$4\times10^{20}cm^{-3}$以下であることが好ましく、$1\times10^{20}cm^{-3}$以上$2\times10^{20}cm^{-3}$以下であることがより好ましい。導電電子密度がこの範囲であれば、第2の酸化物からなる連続層の光吸収量が少なく、高透明で、かつ活性水素種に対して高い耐久性があるので、薄膜シリコン系太陽電池を形成する際に一般に用いられる水素プラズマ照射によっても、透明性は損なわれないため好ましい。

[0077] 上述した第1の酸化物と第2の酸化物とは、同じ酸化物を用いてもよく、本実施形態においては、いずれもSnO_2を用いることが好ましい。また、第1の酸化物及び第2の酸化物層の屈折率は、同等程度であることが好ましく、具体的には、1．8以上2．2以下であることが好ましい。第1の酸化物と第2の酸化物の屈折率がともにこの範囲であると、第1の酸化物と第2の酸化物との界面における光の反射が制御され、透過率が低下しないことから好ましい。

[0078] また、本実施形態においては、上述した第1の酸化物からなる小山部と、上述した第2の酸化物からなる連続層との間に、該第1の酸化物及び該第2の酸化物とは組成が異なる酸化物からなる酸化物層（以下，単に「異なる酸化物層」ともいう。）を有していることが好ましい。

このような異なる酸化物層を有していることにより、第2の酸化物からなる連続層の表面にミクロの多数の凸部が形成されやすく、山部と平坦部とを有する構造を容易に形成することができる。

[0079] また、このような異なる酸化物層を有する多層構造の透明電極膜においては、各層の界面での反射を軽減し、後述する光電変換層への入射光量を最大にする必要がある。すなわち、ガラス基板、第1の酸化物からなる小山部、異なる酸化物層、第2の

SAMSUNG EX. 1002 - 2418/4148

酸化物からなる連続層の各界面での光反射をできるだけ低減することが望ましい。そのためには、第1の酸化物、異なる酸化物及び第2の酸化物の屈折率ができるだけ近いこと、または屈折率が離れている場合は、異なる酸化物層ができるだけ薄いことが望ましい。

このような異なる酸化物としては、具体的には、例えば、Si、Sn、Al、Zr及びTiからなる群から選ばれる1種以上の原子の酸化物が挙げられ、これらのうち、Siの酸化物を主成分とすることが好ましい。また、上記異なる酸化物は、高い透光性を有する必要があるため、非結晶性であるSiO_xであることがより好ましい。

なお、異なる酸化物層の膜厚は2nm以上40nm以下であることが好ましく、10nm以上30nm以下であることがより好ましい。

[0080] 本実施形態の透明電極付き基板は、上述したように、複数の山部とその間をうめる複数の平坦部とで構成され、該山部及び外平坦部の表面がミクロの多数の凸部を連続して有するものであるが、基板上から山部の頂上(ミクロの凸部を含む)までの高さは0.8μm以上3.0μm以下であることが好ましく、0.8μm以上1.0μm以下であることがより好ましい。ミクロの多数の凸部の底面径が0.1μm以上0.3μm以下であり、高さ／底面径の比が0.7以上1.2以下であることが望ましい。また、膜全体のシート抵抗が8Ω／□以上20Ω／□以下であることが好ましく、8Ω／□以上12Ω／□以下であることがより好ましく、550nmにおける透過率(透明性)は、浸漬法で測定した場合、80%以上90%以下であることが好ましく、85%以上90%以下であることがより好ましい。

また、上記構成からなる本実施形態の透明電極付き基板を、光電変換装置の透明電極に用いると、基板を経て入射された光は、透明電極により屈折、散乱されて光電変換部に入射し、光電変換部中を長い距離にわたって通過する。その結果、多くの光が光電変換部にて吸収され、光電変換効率が向上する効果を奏するものとなる。特に、太陽電池に用いた場合には、開放電圧及び曲線因子を低下させずに短絡電流を高く維持することが可能となるため、光電変換効率が向上するものとなる。

[0081] 次に、本実施形態の太陽電池パネルの製造方法について説明する。ここでは、基板1としてのガラス基板上に太陽電池光電変換層3として非晶質シリコン系半導体を

SAMSUNG EX. 1002 - 2419/4148

主として有する光電変換層及び結晶質シリコン系半導体を主として有する光電変換層を順次積層する例について説明する。図4～図7は、本実施形態の太陽電池パネルの製造方法を示す概略図である。

[0082] (1)図4(a):

基板1としてソーダフロートガラス基板(1、4m×1、1m×板厚:4mm)を使用する。基板端面は破損防止にコーナー面取りやR面取り加工されていることが望ましい。

[0083] (2)図4(b):

前記実施形態に基づき、基板1上に透明電極層2を製膜し、透明電極付き基板を形成する。透明導電層2として、透明電極膜に加えて、基板1と透明電極膜との間にアルカリバリア膜(図示されず)を形成しても良い。アルカリバリア膜は、酸化シリコン膜(SiO_2)を50nm以上150nm以下、熱CVD装置にて約500℃で製膜処理する。

[0084] (3)図4(c):

その後、基板1をX－Yテーブルに設置して、YAGレーザーの第1高調波(1064nm)を、図の矢印に示すように、透明電極膜の膜面側から入射する。加工速度に適切となるようにレーザーパワーを調整して、透明電極膜を発電セル5の直列接続方向に対して垂直な方向へ、基板1とレーザー光を相対移動して、溝10を形成するように幅約6mm以上12mm以下の短冊状にレーザーエッチングする。

[0085] (4)図4(d):

プラズマCVD装置により、減圧雰囲気:30Pa以上150Pa以下、基板温度:約200℃、プラズマRF発生周波数:13MHz以上100MHz以下にて光電変換層3の第1セル層(トップ層)91として、非晶質シリコン薄膜からなるp層膜／i層膜／n層膜を順次製膜する。第1セル層91は、SiH_4ガスとH_2ガスとを主原料に、透明導電層2の上に製膜される。太陽光の入射する側からp層、i層、n層がこの順で積層される。

[0086] 本実施形態において、第1セル層91のp層は、SiH_4、H_2、CH_4、B_2H_6ガスをRFプラズマで反応生成させた、非晶質のBドープSiC膜であり、膜厚は4nm以上16nm以下とすることが好ましい。第1セル層91のi層は、SiH_4とH_2をRFプラズマで反応生成させた、非晶質Si膜であり、膜厚は100nm以上400nm以下とすることが好ましい。第1セル層91のn層は、SiH_4、H_2、PH_3ガスをRFプラズマで反応生成させた、結晶

SAMSUNG EX. 1002 - 2420/4148

成分を含むSi膜であり、n層単膜のラマン比は2以上であり、膜厚は10nm以上80nm以下とすることが好ましい。なお、ここで「ラマン比」とはラマン分光評価で520cm^{-1}の結晶Siの強度と480cm^{-1}の非晶質Siの強度の比（結晶Siの強度／非晶質Siの強度）をいう（以下同じ）。また、前記p層（SiC膜）とi層（Si膜）の界面でのバンド不整合を抑制するために、バッファー層（図示略）として、バンドギャップが中間の物質を挿入しても良い。

[0087] 次に、第1セル層91の上に、プラズマCVD装置により、減圧雰囲気：3kPa以下、基板温度：約200℃、プラズマRF発生周波数：40MHz以上200MHz以下にて、第2セル層（ボトム層）92としての微結晶シリコン薄膜からなる微結晶p層膜／微結晶i層膜／微結晶n層膜を順次製膜する。

[0088] 本実施形態において、第2セル層92のp層は、SiH_4, H_2, B_2H_6ガスをRFプラズマで反応生成させた、結晶成分を含むSi膜であり、p層単膜のラマン比は2以上であり、膜厚は10nm以上60nm以下とすることが好ましい。第2セル層92のi層は、SiH_4とH_2をRFプラズマで反応生成させた、結晶成分を含むSi膜であり、このi層を1．5μm膜厚に積んだときのラマン比は3．0以上8．0以下であり、膜厚は1200nm以上2000nm以下とすることが好ましい。より好ましくは、ラマン比を3．5以上8．0以下、さらに好ましくは5．0以上8．0以下とすると好適である。ラマン比の下限値は、結晶シリコン部で発生した電荷が断面方向につながった結晶構造を導通することができるように、大部分の結晶構造が膜厚方向に連続するために必要なラマン比が3．0以上であることから決まり、これは断面観察により確認することができる。また、ラマン比の上限値は柱状結晶の粒界が電流リークポイントとなり、電圧が発生しなくなるのを抑制するために、非晶質で結晶粒界を充填することが好ましく、ラマン比が8．0以下であることが実験的に求められる。

[0089] 第2セル層92のn層は、SiH_4, H_2, PH_3ガスをRFプラズマで反応生成させた、結晶成分を含むSi膜であり、n層単膜のラマン比は2以上であり、膜厚は10nm以上80nm以下とすることが好ましい。

[0090] 微結晶シリコン薄膜、特に微結晶i層膜をプラズマCVD法で形成するにあたり、プラズマ放電電極と基板1の表面との距離dは、3mm以上10mm以下にすることが好ま

SAMSUNG EX. 1002 - 2421/4148

しい。3mmより小さい場合、大型基板に対応する製膜室内の各構成機器精度から距離dを一定に保つことが難しくなるとともに、近過ぎて放電が不安定になる恐れがある。10mmより大きい場合、十分な製膜速度(1nm／s以上)を得難くなるとともに、プラズマの均一性が低下しイオン衝撃により膜質が低下する。第2セル層92のi層は、RF周波数40MHz以上200MHz以下、ガス圧力0．5kPa以上3kPa以下、製膜速度1nm／s以上3nm/s以下で製膜されることが好ましく、本実施形態においてはRF周波数60MHz、ガス圧力1．6kPa、製膜速度2nm／sで製膜される。

[0091] 第1セル層91と第2セル層92の間に電流整合性を取るために半反射膜となることを目的に、中間コンタクト層93として、膜厚0nm以上90nm以下のZnO系膜(例えばGZO(Gaドープ ZnO)膜)をスパッタリング装置により製膜して設けても良い。この中間コンタクト層93は、ZnO単膜での光吸収率がλ＝450nm以上1000nm以下の範囲で1％未満であることが好ましい。

[0092] (5)図4(e)

基板1をX－Yテーブルに設置して、レーザーダイオード励起YAGレーザーの第2高調波(532nm)を、図の矢印に示すように、光電変換層3の膜面側から入射する。パルス発振:10kHz以上20kHz以下として加工速度に適切となるようにレーザーパワーを調整して、透明導電層2のレーザーエッチングラインの約100μm以上150μm以下の横側を狙い、溝11を形成するようにレーザーエッチングする。レーザーエッチングラインの位置は、逆転していなければ問題ないものであるが、位置決めの公差を考慮して、前記数値を狙ったものである。

[0093] (6)図5(a)

裏面電極層4としてAg膜をスパッタリング装置により減圧雰囲気、約150℃にて順次製膜する。裏面電極層4は本実施形態では、Ag膜を膜厚150nm以上で製膜し、さらにn層と裏面電極層4との接触抵抗低減と光反射向上を目的に、光電変換層3と裏面電極層4との間に膜厚10nm以上のZnO系膜(例えばGZO(Gaドープ ZnO)膜)をスパッタリング装置により製膜して設ける。

[0094] (7)図5(b)

基板1をX－Yテーブルに設置して、レーザーダイオード励起YAGレーザーの第2

SAMSUNG EX. 1002 - 2422/4148

高調波(532nm)を、図の矢印に示すように、基板1側から入射する。レーザー光が光電変換層3で吸収され、このとき発生する高いガス蒸気圧を利用して裏面電極層4が爆裂して除去される。パルス発振:1kHz以上10kHz以下として加工速度に適切となるようにレーザーパワーを調整して、透明導電層2のレーザーエッチングラインの約250μm以上400μm以下の横側を狙い、溝12を形成するようにレーザーエッチングする。レーザーエッチングラインの位置は、逆転していなければ問題ないものであるが、位置決めの公差を考慮して、前記数値を狙ったものである。

[0095] (8)図5(c)

発電領域を区分して、基板端周辺の膜端部においてレーザーエッチングによる直列接続部分が短絡し易い影響を除去する。基板1をX-Yテーブルに設置して、レーザーダイオード励起YAGレーザーの第2高調波(532nm)を、基板1側から入射する。レーザー光が透明導電層2と光電変換層3で吸収され、このとき発生する高いガス蒸気圧を利用して裏面電極層4が爆裂して、裏面電極層4/光電変換層3/透明導電層2が除去される。パルス発振:1kHz以上10kHz以下として加工速度に適切となるようにレーザーパワーを調整して、基板1の端部から5mm以上15mm以下の位置を、X方向絶縁溝15を形成するようにレーザーエッチングする。このとき、Y方向絶縁溝は後工程で基板1周囲領域の膜面研磨除去処理を行うので、設ける必要がない。

絶縁溝15は基板1の端より5mm以上10mm以下の位置にてエッチングを終了させることにより、太陽電池パネル端部からの太陽電池モジュール6内部への外部湿分浸入の抑制に、有効な効果を呈するので好ましい。

[0096] (9)図6(a)

後工程のEVA等を介したバックシートとの健在な接着・シール面を確保するために、基板1周辺(周囲領域14)の積層膜は、段差があるとともに剥離し易いため、この膜を除去する。まず、基板の端から5mm以上20mm以下で、前述の図5(c)工程で設けた絶縁溝15よりも基板端側における裏面電極層4/光電変換層3/透明導電層2において、砥石研磨やブラスト研磨などを用いて除去を行う。研磨屑や砥粒は基板1を洗浄処理して除去した。

SAMSUNG EX. 1002 - 2423/4148

[0097] (10)図6(b)

端子箱取付け部分はバックシートに開口貫通窓を設けて集電板を取出す。この開口貫通窓部分には絶縁材を複数層を設置して外部からの湿分などの侵入を抑制する。

直列に並んだ一方端の太陽電池発電セル5と、他方端部の太陽電池発電セル5とから銅箔を用いて集電して太陽電池パネル裏側の端子箱部分から電力が取出せるように処理する。銅箔は各部との短絡を防止するために銅箔幅より広い絶縁シートを配置する。

集電用銅箔などが所定位置に配置された後に、太陽電池モジュール6の全体を覆い、基板1からはみ出さないようにEVA(エチレン酢酸ビニル共重合体)等による充填材シートを配置する。

EVAの上に、防水効果の高いバックシート21を設置する。バックシート21は本実施形態では防水防湿効果が高いようにPTEシート／AL箔／PETシートの3層構造よりなる。

バックシート21までを所定位置に配置したものを、ラミネータにより減圧雰囲気で内部の脱気を行い約150℃でプレスしながら、EVAを架橋させて密着させる。

[0098] (11)図7(a)

太陽電池モジュール6の裏側24に端子箱を接着剤で取付ける。

[0099] (12)図7(b)

銅箔と端子箱の出力ケーブル23とをハンダ等で接続し、端子箱内部を封止剤(ポッティング剤)で充填して密閉する。これで太陽電池パネル50が完成する。

[0100] (13)図7(c)

図7(b)までの工程で形成された太陽電池パネル50について発電検査ならびに、所定の性能試験を行う。発電検査は、AM1．5、全天日射基準太陽光(1000W／m^2)のソーラシミュレータを用いて行う。

[0101] (14)図7(d)

発電検査(図7(c))に前後して、外観検査をはじめ所定の性能検査を行う。

[0102] 上記実施形態では太陽電池として、トップセルとして非晶質(アモルファス)シリコン

SAMSUNG EX. 1002 - 2424/4148

系光電変換層を有し、ボトムセルとして結晶質(微結晶)シリコン系光電変換層を有するタンデム型太陽電池を用いたものについて説明したが、本発明は、この例に限定されるものではない。

例えば、光電変換層として微結晶シリコンをはじめとする結晶質シリコン系光電変換層のみを有するシングル型太陽電池や、前記トップセルと前記ボトムセルに加えてさらに1層もしくは2層以上の別の光電変換層を設けた多接合型太陽電池のような他の種類の薄膜太陽電池にも同様に適用可能である。

[0103] [実施例及び比較例]

比較例1:

透明電極付き基板として、不連続な複数の山部によるマクロな凹凸(テクスチャ)は形成せず、ミクロの多数の凹凸(テクスチャ)を有する、一層のテクスチャ構造を用いた。ミクロの多数の凸部の底面径が0.2～0.3μm、凸部の高さは0.1～0.2μmであり、高さ/底面径の比が0.7～1.0であった。分光ヘイズ率は、波長550nmにおいて20%、波長800nmでは4%である。一層のテクスチャ構造の透明電極付き基板を用いた以外は、本発明の前記実施形態に従って、タンデム型太陽電池を作製した。

透明電極付き基板上に形成した各層において、トップセルp層は膜厚8nm、トップセルn層は膜厚40nm、ボトムセルp層は膜厚30nm、ボトムセルn層は膜厚30nm、裏面電極のZnO層は膜厚80nm、裏面電極のAg層は膜厚300nmで、各比較例及び実施例において共通とした。本例のトップセルi層、ボトムセルi層の膜厚は、表1に示す通りとし、中間コンタクト層は形成しなかった。

得られた太陽電池の電池性能を表2に示す。トップセルi層の膜厚300nmに対し、ボトムセルi層の膜厚を2μmに設定した本例の太陽電池の発電効率初期値は12.0%だった。なお、このときのボトムセルi層の膜厚は、基板上の太陽電池として構成される領域における膜厚分布を考慮して、その平均値で評価したものである。

なお、表2において、電池性能評価項目であるIsc、Voc、FF、Effは、それぞれ短絡電流、開放電圧、形状因子、発電効率(初期値)を表す。Iscの(a－Si/c－Si)は、分光感度から求めたa－Si(非晶質)トップセルのIsc及びc－Si(結晶系)ボトムセルのIscである。タンデムのIscはトップセルIscとボトムセルIscの低い方で律速される

SAMSUNG EX. 1002 - 2425/4148

。本実施例及び比較例は、ボトムセル律速であり、ボトムセルのIscがタンデムのIscとなっている。また、表2に示す比較例及び実施例において、電池性能評価結果は、比較例1を1とした相対値で記載する。本結果は、劣化前の初期値を記載したが、劣化率は本試験の範囲内では同等と考えられ、相対値で表すなら劣化後も同等である。

[0104] 比較例2:

トップセルi層、中間コンタクト層、ボトムセルi層を表1に示す膜厚で形成した以外は前記比較例1と同様の方法に従って、タンデム型太陽電池を作製した。

得られた太陽電池の電池性能を表2に示す。トップセルi層の膜厚250nmとZnO中間コンタクト層の膜厚50nmに対し、ボトムセルi層の膜厚を2μmに設定した本例の太陽電池の発電効率初期値は12.0%だった。

[0105] 比較例3:

トップセルi層、ボトムセルi層を表1に示す膜厚で形成した以外は前記比較例1と同様の方法に従って、タンデム型太陽電池を作製した。

得られた太陽電池の電池性能を表2に示す。トップセルi層の膜厚300nmに対し、ボトムセルi層の膜厚を1.5μmに設定した本例の太陽電池の発電効率初期値は10.8%に低下した。これは、発電電流が大幅に低下したためであり、比較例で用いた基板ではボトムセル膜厚が2μmなければ所望の電流が得られないということが分かった。

[0106] 実施例1:

本発明の前記実施形態に従って、タンデム型太陽電池を作製した。透明電極付き基板として、不連続な小山部とミクロの多数の凸部を有する層状のSnO_2を積層したダブルテクスチャ構造の基板(山部の高さ500nm、山部の密度は10μm角に30個)を適用した。本例のトップセルi層、ボトムセルi層の膜厚は、表1に示す通りとし、中間コンタクト層は形成しなかった。

得られた太陽電池の電池性能を表2に示す。トップセルi層の膜厚300nmに対し、ボトムセルi層の膜厚を2μmに設定した本例の太陽電池の発電効率初期値は13.3%に向上できた。これは、ボトムセルの電流を大幅に増大できた効果である。

SAMSUNG EX. 1002 - 2426/4148

本発明においては、ダブルテクスチャ構造の透明電極により、山部による大きな凹凸(マクロな凹凸)と、これよりも小さな凹凸(ミクロな凹凸)とすることにより、大きな凹凸である山部により長波長の光を散乱し、小さな凹凸表面より短波長の光を散乱することができる。このため、透明電極全体として広い波長領域の光において高い光散乱性を達成することができる。また山部による大きな凹凸があるため、太陽電池層の裏面電極にまで大きな凹凸形状が発生する。これにより、裏面電極からの反射光が太陽電池層内で有効に散乱するので、ボトムセルの電流を大幅に増大させることができる。

特に本発明においては、透明電極の山部の高さと密度を制御して太陽電池層の膜厚を最適化したので、長波長の光の散乱を最適化して、結晶質シリコン系半導体からなる光電変換層の発電効率が向上している。

[0107] 実施例2:

トップセルi層、ボトムセルi層を表1に示す膜厚で形成した以外は前記実施例1と同様の方法に従って、実施例2(1)のタンデム型太陽電池を作製した。

得られた太陽電池の電池性能を表2に示す。トップセルi層の膜厚300nmに対し、ボトムセルi層の膜厚を1.5μmに設定した本例の太陽電池の発電効率初期値は12.8%であり、比較例1に対し効率向上とボトムセル膜厚の25%薄膜化を同時に達成できた。本実施形態による透明電極付き基板の適用により、実施例1に記載したものと同様な効果によりボトムセルを薄膜化しても高い発電電流が得られ、ボトムセルを薄膜化できたためにVocとFFを向上できたためである。また、ボトムセルi層を薄膜化により、ボトムセルi層が厚かったためにこの製膜時間によって律速されていた光電変換装置の製造時間を大幅に短縮することができる。これにより、高速製膜との相乗効果で光電変換装置の生産性を向上させることができる。

さらに、電池性能のボトムセルi層膜厚依存性を調べるために、前記実施例2(1)のボトムセルi層の膜厚を変えて実施例2(2)～実施例2(5)のタンデム型太陽電池を作製した。各実施例におけるボトムセルi層の膜厚を表1に示す。また、各実施例の太陽電池の電池性能を表2に示す。

実施例2において、ボトムセルi層の膜厚が1.2μm以上2.4μm以下の範囲で、

SAMSUNG EX. 1002 - 2427/4148

比較例1のボトムセル層膜厚が2μmの場合と同等以上の効率が得られた。ボトムセル層の膜厚のさらに好ましい範囲は1．5μm以上2μm以下である。
低下するのを抑制でき）VocとFFを向上できたためである。

[0108] 実施例3：

トップセル層、中間コンタクト層、ボトムセル層を表1に示す膜厚で形成した以外は前記実施例2（1）と同様の方法に従って、タンデム型太陽電池を作製した。

得られた太陽電池の電池性能を表2に示す。トップセル層の膜厚250nmとZnO中間コンタクト層の膜厚50nmに対し、ボトムセル層の膜厚を1．5μmに設定した本例の太陽電池の発電効率初期値は12．8％だった。効率向上とボトムセル薄膜化を同時に達成できた。

[0109] 実施例4：

透明電極付き基板の山部の高さを表1に示す値に変えた以外は実施例2（1）と同様の方法に従って、実施例4（1）～実施例4（5）のタンデム型太陽電池を作製し、山部の高さと電池性能の関係を調べた。

得られた太陽電池の電池性能を表2に示す。山部の高さは0．4μm以上0．7μm以下が適正であった。山部の高さが0．4μm以上で高い発電電流が得られ、0．7μmを超えるとVocとFFが著しく低下するためである。

[0110] 実施例5：

透明電極付き基板の山部の密度を表1に示す値に変えた以外は実施例2（1）と同様の方法に従って、実施例5（1）～実施例5（6）のタンデム型太陽電池を作製し、山部の密度と電池性能の関係を調べた。

得られた太陽電池の電池性能を表2に示す。山部の密度が10μm角内に15個以上50個以下のとき、比較例1のi層膜厚2μmの場合と同等以上の効率が得られる。さらに好ましい範囲は10μm角内に20個以上45個以下である。密度が低すぎるとJsc（電流密度）が低下し、高すぎるとJscは飽和しVocとFFが低下して、効率が低下する。

[0111] [表1]

SAMSUNG EX. 1002 - 2428/4148

		透明電極付き基板の山部	トップセルi層膜厚	中間層	ボトムセルi層膜厚	ボトムセルn層製膜後ラマン比
比較例1		—	300nm	なし	2μm	6.5
比較例2		—	250nm	50nm	2μm	6.5
比較例3		—	300nm	なし	1.5μm	5.8
実施例1		高さ0.5μm, 密度30	300nm	なし	2μm	6.5
実施例2	(1)	高さ0.5μm, 密度30	300nm	なし	1.5μm	5.8
	(2)		↑	↑	1μm	6.0
	(3)		↑	↑	1.2μm	5.4
	(4)		↑	↑	1.7μm	6.2
	(5)		↑	↑	2.4μm	6.8
実施例3		高さ0.5μm, 密度30	250nm	50nm	1.5μm	5.8
実施例4	(1)	高さ0.4μm, 密度30	300nm	なし	1.5μm	5.8
	(2)	高さ0.5μm, 密度30	↑	↑	↑	5.8
	(3)	高さ0.6μm, 密度30	↑	↑	↑	5.8
	(4)	高さ0.7μm, 密度30	↑	↑	↑	5.8
	(5)	高さ0.9μm, 密度30	↑	↑	↑	5.8
実施例5	(1)	高さ0.5μm, 密度10	300nm	なし	1.5μm	5.8
	(2)	高さ0.5μm, 密度15	↑	↑	↑	5.8
	(3)	高さ0.5μm, 密度20	↑	↑	↑	5.8
	(4)	高さ0.5μm, 密度30	↑	↑	↑	5.8
	(5)	高さ0.5μm, 密度45	↑	↑	↑	5.8
	(6)	高さ0.5μm, 密度50	↑	↑	↑	5.8

[0112] [表2]

SAMSUNG EX. 1002 - 2429/4148

		電池性能			
		Isc (a-Si/c-Si)	Voc	FF	Eff
比較例1		1 (1/1)	1	1	1
比較例2		1 (1/1)	1	1	1
比較例3		0.89(1/0.89)	1	1	0.89
実施例1		1.15(1/1.15)	0.99	0.97	1.11
実施例2	(1)	1.06(1/1.06)	1.00	1.01	1.07
	(2)	0.80(1/0.80)	1.02	1.04	0.86
	(3)	0.96(1/0.96)	1.01	1.02	0.99
	(4)	1.03(1/1.03)	0.99	1.01	1.03
	(5)	1.13(1/1.13)	0.97	0.92	1.02
実施例3		1.06(1/1.06)	1.00	1.01	1.07
実施例4	(1)	1.00(1/1.00)	1.01	1.01	1.02
	(2)	1.06(1/1.06)	1.00	1.01	1.07
	(3)	1.08(1/1.08)	0.99	0.99	1.06
	(4)	1.10(1/1.10)	0.97	0.96	1.03
	(5)	1.10(1/1.10)	0.92	0.88	0.90
実施例5	(1)	0.93(0.9/0.9)	1.00	0.99	0.92
	(2)	0.99(1/0.99)	1.00	1.00	0.99
	(3)	1.04(1/1.04)	1.00	1.01	1.05
	(4)	1.06(1/1.06)	1.00	1.01	1.07
	(5)	1.06(1/1.06)	0.98	0.98	1.02
	(6)	1.05(1/1.05)	0.97	0.96	0.98

[0113] 第2実施形態

以下に、本発明の第2実施形態について、説明する。

本実施形態において、透明電極つき基板は、大型の凹凸と小型の凹凸が混在する

SAMSUNG EX. 1002 - 2430/4148

ことが望ましく、小型の凹凸(ミクロな凹凸)と大型の凹凸(マクロな凹凸)により、ピッチが0．1μmから1．2μm、高さが0．1μmから1．0μmの凹凸が混在している。ピッチ0．8μm以上の大きな凹凸により800nm以上の長波長の光を拡散、閉じ込めでき、ピッチ0．3μm以下の小さな凹凸により500nm以下の短波長の光も有効に散乱、利用できる。すなわち、大きな凹凸により長波長の光を散乱し、小さな凹凸表面より短波長の光を散乱することができるため、全体として高い光散乱性を達成することができる。また分光ヘイズ率が550nm以上800nm以下の波長で20%以上である。

[0114] 本実施形態においても、透明電極つき基板は、第1実施形態と同様であり、透明電極つき基板は、大型の凹凸(マクロな凹凸)の山部112の平均の高さHa(平坦部上のミクロの凸部の頂部からの高さの平均値)が、0．4μm以上0．7μm以下であり、0．5μm以上0．6μm以下であることがより好ましい。山部の密度は，基板111面の10μm角あたり15以上50以下となり、この平均ピッチPaは、1．0μm以上3μm以下に相当する。一方、小型の凹凸(ミクロな凹凸)のミクロの多数の凸部の底面径が0.1μm以上0.3μm以下であり、高さ／底面径の比が0.7以上1.2以下である。

[0115] 前記透明電極付き基板におけるこのような表面性状は，例えば，前記第1実施形態で説明した表面形状の解析を行うことにより確認することができる。

[0116] また、このような形状及び構成を有する透明電極付き基板は、基板全体において、550nm以上800nm以下の波長における分光ヘイズ率が20%以上、好ましくは30%以上であることが好ましい。

ここで、「分光ヘイズ率」の定義は、上記第1実施形態において説明したとおりである。

[0117] 以下に、上述した本実施形態の透明電極付き基板の形状及び構成ならびに特性を満たす基板(透明基板)及び酸化物は、それぞれ前記第1実施形態で説明した基板および第1酸化物と同様であるので、これらの詳しい説明は省略する。

[0118] 本実施形態の透明電極付き基板は、大型の凹凸と小型の凹凸が混在することが望ましく、ピッチが0.1μmから1.2μm、高さが0.1μmから1．0μmの凹凸が混在している。ピッチ0.8μm以上の大きな凹凸により800nm以上の長波長の光を拡散、閉じ込めでき、ピッチ0.3μm以下の小さな凹凸により500nm以下の短波長の光も有効

SAMSUNG EX. 1002 - 2431/4148

に散乱、利用できる。また、膜全体のシート抵抗が8Ω／□以上20Ω／□以下であることが好ましく、8Ω／□以上12Ω／□以下であることがより好ましく、550nmにおける透過率（透明性）は、浸液法で測定した場合、80%以上90%以下であることが好ましく、85%以上90%以下であることがより好ましい。

[0119] また、本実施形態の透明電極付き基板を、光電変換装置の透明電極に用いると、基板を経て入射された光は、透明電極により屈折、散乱されて光電変換部に入射し、光電変換部中を長い距離にわたって通過する。その結果、多くの光が光電変換部にて吸収され、光電変換効率が向上する効果を奏するものとなる。特に、太陽電池に用いた場合には、開放電圧及び曲線因子を低下させずに短絡電流を高く維持することが可能となるため、光電変換効率が向上するものとなる。

[0120] 本実施形態の光電変換装置の製造方法により製造される光電変換装置の構成および太陽電池パネルの製造方法は、後述の異相遮断層または異相防止層を設けたこと以外は前記第1実施形態と同様であるので、第1実施形態で用いた図1および図4ないし図7を参照する。前記第1実施形態と共通の部材については同一の参照符号を用いることとし、詳細な説明は省略する。

[0121] 本実施形態の光電変換装置においては、非晶質シリコン系半導体を主として有する光電変換層からなる第1セル層（トップ層）91の透明電極層側表面から裏面電極層側表面に貫通する異相を遮断または防止するために、後述の光電変換装置の製造方法に係る実施形態に示した方法により、第1セル層（トップ層）91中に異相遮断層（図示略）が設けられるか、もしくは、基板1と第1セル層（トップ層）91の間に異相防止層（図示略）が設けられる。

第1セル層（トップ層）91及び結晶質シリコン系半導体を主として有する光電変換層からなる第2セル層（ボトム層）92の間には、透明導電膜からなる中間コンタクト層93を設けても良い（但し、本発明の光電変換装置は、中間コンタクト層93を設けたものに限定されない）。

[0122] 本実施形態の太陽電池パネルの製造方法においては、まず、前記第1実施形態の図4の（a）および（b）と同様の方法を行い、透明電極基板が形成される。

[0123] 次に、製膜した透明電極層2の表面に対してイオン処理を行い、本実施形態の異

SAMSUNG EX. 1002 - 2432/4148

相防止層を形成することができる。イオン処理は、例えば真空中でのアルゴンイオン照射によるイオンエッチングとすることができる。イオン処理に用いられる装置としては、フィラメントタイプのイオン源を使用したイオンミリング装置が挙げられる。この装置を用いてイオン処理を行う場合は、例えば容器内を10^{-4}Pa台に真空排気し、アルゴンガスを供給して5×10^{-3}Paの条件で、Arイオンを発生させ、加速電圧1kVでイオン照射してイオン処理を行うことができる。イオンは透明電極付き基板の透明電極層2表面に垂直に照射することが好ましい。照射時間は例えば180sec程度とすることができる。

[0124] 次に、前記第1実施形態の図4の(c)と同様の方法により透明電極膜のレーザーエッチングを行い、次いで異相遮断層または異相防止層を設けたこと以外は図4の(d)と同様の方法を行い、光電変換層3を形成する。

光電変換層3の第1セル層(トップ層)91として、非晶質シリコン薄膜からなるp層膜／i層膜／n層膜を順次形成する。太陽光の入射する側からp層, i層、n層がこの順で積層される。

なお、第1セル層91を製膜する前に、透明電極付き基板を真空容器で10^{-1}Pa以下の圧力とし、ヒータで100℃以上の温度に予備加熱(ベーキング)することが、異相の発生を防ぐために特に好ましい。

[0125] 本実施形態において、第1セル層91のp層は、SiH_4, H_2, CH_4, B_2H_6ガスをRFプラズマで反応生成させた、非晶質のBドープSiC膜であり、膜厚は4nm以上16nm以下とすることが好ましい。

[0126] また本実施形態において、第1セル層91のi層は、標準構成としては非晶質Si膜である、SiH_4とH_2をRFプラズマで反応生成される。膜厚は100nm以上400nm以下とすることが好ましい。標準の製膜条件として、SiH_4とH_2を1:5の比率で供給して圧力を600Paに制御し、60MHzの高周波0．15W／cm^3で放電して、非晶質のi層を製膜することができる。この標準の製膜条件における製膜速度は、例えば1．1nm／sとすることができる。

[0127] 本実施形態の異相遮断層として、第1セル層91のi層中に、標準製膜条件よりも低パワーで製膜された層(例えば、i層製膜の初期に製膜される初期層，あるいはi層製

SAMSUNG EX. 1002 - 2433/4148

膜の後期に製膜される後期層）を設けてもよい。このような層を製膜する場合は、高周波出力を例えば0．02W／cm^3の低パワーにして、低速で製膜すればよい。製膜速度は例えば0．2nm／s程度である。初期層及び後期層は、例えば60s（膜厚12nm相当）～120s（膜厚24nm相当）で製膜される。初期層または後期層を設けた層は、プラズマ放電中にパワーを変更することにより、連続膜として形成される。

[0128] また本実施形態において、第1セル層91（トップ層）のn層は、標準構成としては結晶質（結晶成分を含む）のSi膜であり，SiH_4，H_2，PH_3ガスをRFプラズマで反応生成される。このn層単膜のラマン比は2以上であり、膜厚は10nm以上80nm以下とすることが好ましい。標準の製膜条件として、SiH_4とH_2とPH_3を1：80：0．02の比率で供給して圧力を100Paに制御し、基板と電極の間の間隔を20mmとし、60MHzの高周波0．3W／cm^2で放電して、微結晶（結晶とアモルファスが混在する膜質）のn層を製膜することができる。製膜速度は0．2nm／sとすることができる。製膜速度は例えば0．2nm／s程度とすることができる。

[0129] 本実施形態の異相遷断層として非晶質（結晶成分は存在しない）のn層を形成してもよい。この場合は、前記結晶質のn層の前に非晶質のn層が製膜される。この非晶質n層は、SiH_4とH_2とPH_3を1：1：0．05の比率で供給して圧力を20Paに制御し、基板と電極の間の間隔を20mmとし、60MHzの高周波を0．04W／cm^2で放電して製膜される。製膜速度は例えば0．2nm／s程度とすることができる。非晶質Si－n層と微結晶Si－n層を積層するときは、一旦放電を停止して流量／圧力を変更し、安定後再度放電させて行われる。例えば、非晶質Si製膜条件で15nm程度製膜し、さらに標準の結晶質製膜条件で25nm程度製膜すればよい。

[0130] 本実施形態の異相遷断層として、結晶質（結晶成分を含む）のn層を標準製膜条件より高圧で製膜してもよい。この場合は、例えば、SiH_4とH_2とPH_3を1：80：0．02の比率で供給して、圧力を200Paに制御し、基板と電極の間の間隔を標準条件の1／2である10mmに狭くして、60MHzの高周波を出力0．1W／cm^2で放電して、微結晶Si（結晶とアモルファスが混在する膜質）のn層を製膜することができる。

[0131] 本実施形態において、前記p層膜とi層膜の間には界面特性の向上のためにバッファー層（図示略）を設けてもよい。バッファー層として、バンドギャップが中間の物質を

SAMSUNG EX. 1002 - 2434/4148

挿入することにより、p層（SIC膜）とi層（Si膜）の界面でのバンド不整合を抑制することができる。

本実施形態において、p層の製膜ガス（SiH_4、H_2、CH_4、B_2H_6）に対し、i層ではSiH_4及びH_2しか用いないため、ドーパント（B_2H_6）濃度及びバンド調整のためのCH_4濃度を調整する。具体的には、p層製膜室において、B_2H_6ガスの供給を停止し、B_2H_6の供給は壁面吸着量のみとし、CH_4ガスの供給量をp層に対し1/10～1/3に調整することで0．02～0．1μmの膜厚のバッファー層を形成した。これにより、p層及びi層と原子拡散が進行した結果、膜厚方向の炭素含有率及びバンドエネルギー構造は滑らかに変化する状態となり、p層とi層との界面特性が向上されることとなる。

[0132] 次に、第1セル層（トップ層）91の上に、前記第1実施形態と同様の方法、製膜条件により、微結晶シリコン薄膜からなる微結晶p層膜／微結晶i層膜／微結晶n層膜を順次製膜し、前記第1実施形態と同様の第2セル層（ボトム層）92を形成する。

[0133] 前記第1実施形態と同様に、第1セル層（トップ層）91と第2セル層（ボトム層）92の間に電流整合性を取るために半反射膜となることを目的に、中間コンタクト層93として、膜厚0nm以上90nm以下、より好ましくは5nm以上50nm以下のZnO系膜（例えばGZO（GaドープZnO）膜）をスパッタリング装置により製膜して設けても良い。この中間コンタクト層93は、ZnO単膜での光吸収率がλ＝450nm以上1000nm以下の範囲で1％未満であることが好ましい。

[0134] 第2セル層92を形成した後、第1実施形態における図4の（e）から図7の（b）と同様の方法により太陽電池パネル50が完成する。次いで第1実施形態における図7の（c）および（d）と同様の方法により、発電検査および所定の性能試験ならびに外観検査をはじめ所定の性能検査を行う。

[0135] 上記実施形態では太陽電池として、トップセルとして非晶質シリコン系光電変換層を有し、ボトムセルとして結晶質（微結晶）シリコン系光電変換層を有するタンデム型太陽電池を用いたものについて説明したが、本発明は、この例に限定されるものではない。

例えば、光電変換層として非晶質シリコン系光電変換層のみを有するシングル型太陽電池や、前記トップセルと前記ボトムセルに加えてさらに1層もしくは2層以上の

SAMSUNG EX. 1002 - 2435/4148

別の光電変換層を設けた多接合型太陽電池のような他の種類の薄膜太陽電池にも同様に適用可能である。

[0136] 〔実施例、参考例及び比較例〕

参考例1:

透明電極付き基板として、微細な凹凸のみのものを用いた。微細な凹凸の凸部の高さは0.1μm以上0.2μm以下、ピッチは0.1μm以上0.3μm以下、凸部の高さと底面径の比は0.7～1.0、波長550nmの分光ヘイズ率は20%、800nmの分光ヘイズ率は3%であった。透明電極付き基板が異なる以外は、本発明の前記実施形態における標準の製膜条件に従って、タンデム型太陽電池を作製した。

[0137] 透明電極付き基板上に形成した各層において、トップセルp層は膜厚8nm、トップセルn層は膜厚40nm、ボトムセルp層は膜厚30nm、ボトムセルn層は膜厚30nm、裏面電極のZnO層は膜厚80nm、裏面電極のAg層は膜厚300nmで、各参考例、比較例及び実施例において共通とした。本例のトップセルi層、トップセルn層の膜厚及び製膜条件は、表3に示す通りとし、中間コンタクト層は形成しなかった。

[0138] なお、表3に記載した各参考例、比較例及び実施例の「製膜条件」とは、以下の通りである。

トップセルi層の標準製膜条件: SiH_4とH_2を1:5の比率で供給して、圧力を600Paに制御し、60MHzの高周波を出力0.15W／cm^3で放電して、非晶質i層を製膜した。製膜速度は1.1nm／sとした。

[0139] トップセルi層の初期層または後期層の低速製膜条件: 標準条件と高周波出力のみを変更し、0.02W／cm^3とした。製膜速度は0.2nm／sとした。標準製膜条件による膜との積層は、プラズマ放電中にパワーを変更することにより、連続膜とした。

[0140] トップセルn層の標準製膜条件: SiH_4とH_2とPH_3を1:80:0.02の比率で供給して、圧力を100Paに制御し、基板と電極の間の間隔を7mmとし、60MHzの高周波を出力0.3W／cm^3で放電して、微結晶(結晶と非晶質が混在する膜質)のn層を製膜した。製膜速度は0.2nm／sとした。

[0141] トップセルn層の非晶質Si製膜条件: SiH_4とH_2とPH_3を1:1:0.05の比率で供給して、圧力を20Paに制御し、基板と電極の間の間隔を7mmとし、60MHzの高周波

SAMSUNG EX. 1002 - 2436/4148

を出力0．04W／cm^{2}で放電して、非晶質Si（結晶成分は存在しない）のn層を製膜した。製膜速度は0．2nm／sとした。非晶質Si－n層と微結晶Si－n層を積層するときは、一旦放電を停止して流量／圧力を変更し、安定後再度放電させた。

[0142] トップセルn層の高圧製膜条件：SiH_4とH_2とPH_3を1：80：0．02の比率で供給して、圧力を200Paに制御し、基板と電極の間の間隔を標準条件の1／2である10mmに狭くして、60MHzの高周波を出力0．3W／cm^{2}で放電して、微結晶Si（結晶と非晶質が混在する膜質）のn層を製膜した。

[0143] 参考例1で得られた太陽電池の電池性能を表4に示す。トップセルi層の膜厚300nmに対し、ボトムセルi層の膜厚を2μmに設定した本例の太陽電池の発電効率（初期値）は12％だった。

なお、表4において、電池性能評価項目であるIsc、Voc、FF、Effは、それぞれ短絡電流、開放電圧、形状因子、発電効率（初期値）を表す。また、表4に示す参考例、比較例及び実施例において、電池性能評価結果は、参考例1を1とした相対値で記載する。本結果は、劣化前の初期値を記載したが、劣化率は本試験の範囲内では同等と考えられ、相対値で表すなら劣化後も同等である。

[0144] 参考例2：

トップセルi層、ボトムセルi層を表3に示す膜厚で形成した以外は前記参考例1と同様の方法に従って、タンデム型太陽電池を作製した。

得られた太陽電池の電池性能を表4に示す。トップセルi層の膜厚300nmに対し、ボトムセルi層の膜厚を1．5μmに設定した本例の太陽電池の発電効率は10．8％に低下した。これは、発電電流が大幅に低下したためであり、参考例で用いた基板ではボトムセル膜厚が2μmなければ所望の電流が得られないということが分かった。

[0145] 比較例4：

本発明の前記実施形態における標準の製膜条件に従って、タンデム型太陽電池を作製した。透明電極付き基板として、実施例6と同じく大小の凹凸が混在する基板を適用した。本例のトップセルi層、トップセルn層の膜厚及び製膜条件は、表3に示す通りとし、中間コンタクト層は形成しなかった。すなわち、トップセルi層は製膜速度1．

SAMSUNG EX. 1002 - 2437/4148

1nm／sで300nmの膜厚に、トップセルn層は結晶と非晶質が混在する微結晶となる条件で40nmの膜厚に製膜した。ボトムセルi層の膜厚は1．5μmとした。

[0146] 得られた太陽電池の電池性能を表4に示す。表4に示したように、本例の太陽電池は、電流は増大したものの、開放電圧と形状因子が低下して、発電効率初期値は参考例1のボトムセルi層膜厚が2μmの場合より低下していた。

[0147] 比較例4の太陽電池において開放電圧と形状因子が低下した原因を調査検討した。図10に大小の凹凸が混在する透明電極付き基板を用いて作製したタンデム型太陽電池の断面の透過型電子顕微鏡写真を示す。この電子顕微鏡写真において、透明電極の谷の部分（点線で囲んだ部分）でトップセルを上下に貫通する線が見える。これは、下地の隣接する面に製膜・成長する膜成長相間の不連続な境界が線状に見えるもので、異相と呼んでおり、キャリア再結合中心が集中すると考えられ、電流リーク箇所に相当する。この異相が生じた場合に開放電圧と形状因子が低下していた。従って、本発明者らは、この異相を抑制すること、または完全に抑制はできなくても透明電極から中間コンタクト層又はボトムセルに至るまでトップセルを貫通する異相を遮断できれば、開放電圧低下、形状因子低下を抑制できると考えた。

[0148] 実施例6～実施例9：

トップセルi層、トップセルn層の膜厚及び製膜条件を表3に示す通りとした以外は前記比較例4と同様の方法に従って、実施例6～実施例9のタンデム型太陽電池を作製した。

得られた太陽電池の電池性能を表4に示す。

[0149] 実施例6においては、トップセルの非晶質Si－i層を製膜初期（p層との界面）のみ低パワーで製膜することにより、開放電圧低下、形状因子低下を抑制し、太陽電池性能を向上できた。これは、非晶質Si－i層の初期層によってトップセルを貫通する異相が遮断され、電流リークを抑制することができたためと考えられる。ボトムセルが膜厚1．5μmという薄膜で発電効率初期値13.0%という高効率が得られたことは、生産性と効率向上の両方で非常に大きな成果である。

[0150] 実施例7においては、トップセルの非晶質Si－i層を製膜後期（n層との界面）のみ低パワーで製膜することにより、開放電圧低下、形状因子低下を抑制し、太陽電池

SAMSUNG EX. 1002 - 2438/4148

性能を向上できた。これは、非晶質Si－i層の後期層によってトップセルを貫通する異相が遮断され、電流リークを抑制することができたためと考えられる。この実施例7でも、ボトムセルが膜厚1．5μmという薄膜で発電効率初期値13.0%という高効率が得られたことは、生産性と効率向上の両方で非常に大きな成果である。

[0151] 実施例8においては、トップセルn層の製膜後期のみを標準製膜条件により製膜して結晶質とし、製膜初期の層を非晶質にすることで、開放電圧低下、形状因子低下を抑制し、太陽電池性能を向上できた。これは、トップセルn層において非晶質とした初期層がi層との界面で異相を埋めるため、トップセルを貫通する異相が遮断され、電流リークを抑制することができたためと推察される。ボトムセル膜厚1.5μmの薄膜で発電効率初期値13.2%が得られたのは、実施例6、実施例7と同様の異相遮断効果と、更にn層による界面改善効果が得られたためである。

[0152] 実施例9においては、トップセルn層を200Paの高圧で製膜して微結晶膜を形成することにより、開放電圧低下、形状因子低下を抑制し、太陽電池性能を向上できた。なお、実施例9において、トップセルn層の製膜の際の圧力を400Paとした場合も同様の効果が得られた。これは、高圧で製膜することによりトップセルn層がi層との界面の谷の部分に付きやすくなり、これによってトップセルを貫通する異相が遮断され、電流リークを抑制することができたためと考えられる。

[0153] [表3]

SAMSUNG EX. 1002 - 2439/4148

	トップセルi層の製膜条件と膜厚	トップセルn層の製膜条件と膜厚
参考例1	標準製膜条件で300nm	標準製膜条件で2μm
参考例2	標準製膜条件で300nm	標準製膜条件で1.5μm
比較例4	標準製膜条件で300nm	標準製膜条件(結晶質)で40nm
実施例6	初期層：低速製膜条件で24nm(120s)；続けて標準製膜条件で残り276nm	標準製膜条件(結晶質)で40nm
実施例7	標準製膜条件で276nm；さらに後期層として低速製膜条件で24nm(120s)	標準製膜条件(結晶質)で40nm
実施例8	標準製膜条件で300nm	非晶質Si製膜条件で15nm；さらに標準製膜条件で25nm
実施例9	標準製膜条件で300nm	高圧製膜条件(結晶質)で40nm

[0154] 実施例10:

透明電極付き基板の透明電極表面に対してイオン処理を行った以外は、前記比較例4と同様の方法に従って、実施例10のタンデム型太陽電池を作製した。

イオン処理は、真空中でのアルゴンイオン照射によるイオンエッチングであり、装置としては、フィラメントタイプのイオン源を使用したイオンミリング装置を用いた。容器内を10^{-4}Pa台に真空排気し、アルゴンガスを供給して5×10^{-3}Paの条件で、Arイオンを発生させ、加速電圧E1kVでイオン照射してイオン処理を行った。イオンは透明電極付き基板の透明電極表面に垂直に照射し、照射時間は180secとした。図8は、イオン処理前における透明電極付き基板の透明電極表面の電子顕微鏡写真(倍率5万倍)であり、図9は、イオン処理後における透明電極付き基板の透明電極表面の電子顕微鏡写真(倍率5万倍)である。

[0155] 得られた太陽電池の電池性能を表4に示す。なお、表4において、電池性能評価項目であるIsc、Voc、FF、Effは、それぞれ短絡電流、開放電圧、形状因子、発電効率を表す。Iscの(a－Si／c－Si)は、分光感度から求めたa－Si(非晶質)トップセルのIsc及びc－Si(結晶系)ボトムセルのIscである。

実施例10においては、前記イオン処理により、開放電圧低下、形状因子低下を抑

SAMSUNG EX. 1002 - 2440/4148

制し、太陽電池性能を向上できた。これはイオン処理によって基板の凹形状が円滑になり、トップセルにおける異相の形成が抑制されたため、電流リークを抑制することができたためと考えられる。

実施例1～10においては、ボトムセルi層製膜条件は固定であり、ボトムセルn層製膜後のラマン比は表1に示すとおり、5.0～7.0の間にあった。

[0156] 実施例11；

ボトムセルi層のH_2/SiH_4希釈率比を表5に示すように変えた以外は、実施例1と同様の方法に従って実施例11(1)～実施例11(6)のタンデム型太陽電池を作製し、ボトムセルのn層製膜後のラマン比と太陽電池特性の関係を調べた。その結果を図12に示す。なお、表5、及び図12において、H_2希釈率比、及び電池性能結果は、比較例1を1とした場合の相対値である。本結果は、劣化前の初期値を記載したが、劣化率は本試験の範囲内では同等と考えられ、相対値で表すなら劣化後も同等である。

表5及び図12からわかるように、n層製膜後のラマン比でみて3.0以上8.0以下のとき、比較例1よりも太陽電池性能が向上している。これは、ラマン比が3.0より低下するとVocが向上する一方で、Iscが著しく低下していることから、非晶質成分が多すぎて抵抗損失が生じたと推定される。ラマン比が8.0より増大すると、VocとFFが大きく低下していることより電流リークによる電圧損失が生じたと考えられ、結晶粒界の電流リークが想定される。第2セル層において、適度な非晶質相が存在することにより、結晶質シリコンの粒界に存在する欠陥を不活性にし、これにより、Iscの低下を抑制することに寄与しているものと考えられる。

また、図12において、H_2希釈率比0．9でEffの上昇が緩和し、H_2希釈率比1．1でEffが低下している。H_2希釈率比0．9以上1．1以下でのEff値は、実施例11(3)～実施例11(5)に示すように、比較例1に対し1.1倍以上の性能を得ることができた。したがって、ラマン比は、H_2希釈率比と電池性能との相関関係からみて、実験的に5.0以上7.5以下が最適値となる。

[0157] [表4]

SAMSUNG EX. 1002 - 2441/4148

	電池性能			
	Isc (a-Si/c-Si)	Voc	FF	Eff
参考例1	1 (1/1)	1	1	1
参考例2	0.89(1/0.89)	1	1	0.89
比較例4	1.10(1/1.10)	0.95	0.92	0.97
実施例6	1.10(1/1.10)	0.99	0.99	1.08
実施例7	1.10(1/1.10)	0.99	0.99	1.08
実施例8	1.10(1/1.10)	1.00	1.00	1.10
実施例9	1.10(1/1.10)	0.99	0.98	1.07
実施例10	1.03(1/1.03)	1.01	1.01	1.05

[0158] [表5]

SAMSUNG EX. 1002 - 2442/4148

No	H2 希釈率比	ラマン比	電池性能				
			(タンデム) Isc	(c-Si) Isc	Voc	FF	Eff
実施例11(1)	0.8	2	0.98	0.98	1.03	0.95	0.96
実施例11(2)	0.8	3	1.03	1.03	1.01	1.00	1.04
実施例11(3)	0.8	5	1.11	1.11	1.00	0.99	1.10
実施例11(4)	1.0	6.5	1.15	1.15	0.99	0.97	1.11
実施例11(5)	1.1	7.5	1.17	1.17	0.98	0.96	1.10
実施例11(6)	1.2	10	1.15	1.15	0.94	0.89	0.96
比較例1	1.0	6.5	1.00	1.00	1.00	1.00	1.00(12%)

SAMSUNG EX. 1002 - 2443/4148

[0159] 以上、実施例6から実施例11によれば、分光ヘイズ率を高めた透明電極付き基板を適用しても開放電圧と形状因子の低下を抑制でき、薄いボトムセルで、高効率と高生産性を兼ね備えたタンデム太陽電池を作製可能となった。

なお、トップセル(非晶質Si層)全体を低パワーで製膜すると製膜速度が著しく低下するため、生産性が悪化する。しかし、上記実施例6、実施例7のように初期あるいは後期の20%程度の膜厚を低速で作製するだけであれば、生産性の悪化を極力抑えられて、高い生産効率で太陽電池を製造できる。また、実施例9のようにn層の製膜条件を改善した場合は、生産性の悪化はまったくなく、高い生産効率で太陽電池を製造できる。

SAMSUNG EX. 1002 - 2444/4148

請求の範囲

[1] 透明絶縁性の基板上に透明電極層を設けてなる透明電極付き基板と、該透明電極付き基板の透明電極層側に順次形成された、結晶質シリコン系半導体を主として有する光電変換層ならびに裏面電極層とを少なくとも有してなる光電変換装置であって、

前記透明電極付き基板は、表面が大小の凹凸が混在した形状であり、かつ分光ヘイズ率が550nm以上800nm以下の波長で20%以上であり、

前記結晶質シリコン系半導体を主として有する光電変換層の膜厚が1.2μm以上2μm以下、かつラマン比が3.0以上8.0以下である光電変換装置。

[2] 前記透明電極付き基板と前記結晶質シリコン系半導体を主として有する光電変換層との間に、非晶質シリコン系半導体を主として有する光電変換層を有する請求項1に記載の光電変換装置。

[3] 前記非晶質シリコン系半導体を主として有する光電変換層と前記結晶質シリコン系半導体を主として有する光電変換層との間に中間コンタクト層を有する請求項2に記載の光電変換装置。

[4] 前記透明電極付き基板の透明電極層表面が、複数の山部と複数の平坦部とで構成され、該山部及び該平坦部の表面がミクロの多数の凸部を連続して有してなり、

前記山部の前記基板面垂直方向における高さが0.4μm以上0.7μm以下であり、

基板面10μm角における前記山部の数が15以上50以下であり、

前記ミクロの多数の凸部の底面径が0.1μm以上0.3μm以下であり、高さ／底面径の比が0.7以上1.2以下である請求項1から請求項3のいずれか1項に記載の光電変換装置。

[5] 透明絶縁性の基板上に透明電極層を形成して透明電極付き基板を作製し、

該透明電極付き基板の透明電極層側に非晶質シリコン系半導体を主として有する光電変換層ならびに裏面電極層とを少なくとも順次形成する光電変換装置の製造方法であって、

前記透明電極付き基板は、表面が大小の凹凸が混在した形状であり、かつ分光ヘ

SAMSUNG EX. 1002 - 2445/4148

イズ率が550nm以上800nm以下の波長で20%以上であり、

前記非晶質シリコン系半導体を主として有する光電変換層中に、該光電変換層の透明電極層側表面から裏面電極層側表面に貫通する異相を遮断する異相遮断層を形成する光電変換装置の製造方法。

[6] 前記非晶質シリコン系半導体を主として有する光電変換層の形成においてp層、i層、n層を順次形成し、

前記i層の形成において該i層の他の部分より低速で製膜することにより前記異相遮断層を形成する、請求項5に記載の光電変換装置の製造方法。

[7] 前記非晶質シリコン系半導体を主として有する光電変換層の形成においてp層、i層、n層を順次形成し、

前記n層の形成において少なくともその一部に非晶質の層を形成することにより前記異相遮断層を形成する、請求項5に記載の光電変換装置の製造方法。

[8] 前記非晶質シリコン系半導体を主として有する光電変換層の形成においてp層、i層、n層を順次形成し、

前記n層の形成において少なくともその一部を200Pa以上の圧力下で製膜することにより前記異相遮断層を形成する、請求項5に記載の光電変換装置の製造方法。

[9] 透明絶縁性の基板上に透明電極層を形成して透明電極付き基板を作製し、

該透明電極付き基板の透明電極層側に非晶質シリコン系半導体を主として有する光電変換層ならびに裏面電極層とを少なくとも順次形成する光電変換装置の製造方法であって、

前記透明電極付き基板は、表面が大小の凹凸が混在した形状であり、かつ分光ヘイズ率が550nm以上800nm以下の波長で20%以上であり、

前記透明電極層の形成と前記光電変換層形成の間に、該光電変換層の透明電極層側表面から裏面電極層側表面に貫通する異相の形成を防止する異相防止層を形成する光電変換装置の製造方法。

[10] 前記透明電極層の凸部を円滑化して前記異相防止層を形成する、請求項9に記載の光電変換装置の製造方法。

[11] 前記透明電極層表面にイオン処理を施して前記異相防止層を形成する、請求項9

SAMSUNG EX. 1002 - 2446/4148

または請求項10に記載の光電変換装置の製造方法。

[12] 前記非晶質シリコン系半導体を主として有する光電変換層と前記裏面電極の間に、結晶質シリコン系半導体を主として有する光電変換層を形成する請求項5から請求項11のいずれか1項に記載の光電変換装置の製造方法。

[13] 透明絶縁性の基板上に透明電極層を設けてなる透明電極付き基板と、該透明電極付き基板の透明電極層側に順次形成された、非晶質シリコン系半導体を主として有する光電変換層ならびに裏面電極層とを少なくとも有し、

前記透明電極付き基板は、表面が大小の凹凸が混在した形状であり、かつ分光ヘイズ率が550nm以上800nm以下の波長で20%以上である光電変換装置であって、

前記非晶質シリコン系半導体を主として有する光電変換層中に、該光電変換層の透明電極層側表面から裏面電極層側表面に貫通する異相を遮断する異相遮断層を設けた光電変換装置。

[14] 前記非晶質シリコン系半導体を主として有する光電変換層において、p層、i層、n層が順次形成され、

前記非晶質シリコン系半導体を主として有する光電変換層のn層が非晶質シリコン系半導体を主として有する層と、結晶質シリコン系半導体を主として有する層で形成される請求項2又は13に記載の光電変換装置。

[15] 前記非晶質シリコン系半導体を主として有する光電変換層のp層とi層との間にバッファー層を設けた請求項2, 13又は14に記載の光電変換装置。

[16] 前記非晶質シリコン系半導体を主として有する光電変換層と前記裏面電極層との間に結晶質シリコン系半導体を主として有する光電変換層を有する請求項13に記載の光電変換装置。

[17] 前記結晶質シリコン系半導体を主として有する光電変換層の膜厚が1.2μm以上2μm以下、かつラマン比が3.0以上8.0以下である請求項16に記載の光電変換装置。

[18] 前記非晶質シリコン系半導体を主として有する光電変換層と前記裏面電極の間に、結晶質シリコン系半導体、結晶質もしくは非晶質シリコンゲルマニウム系半導体を

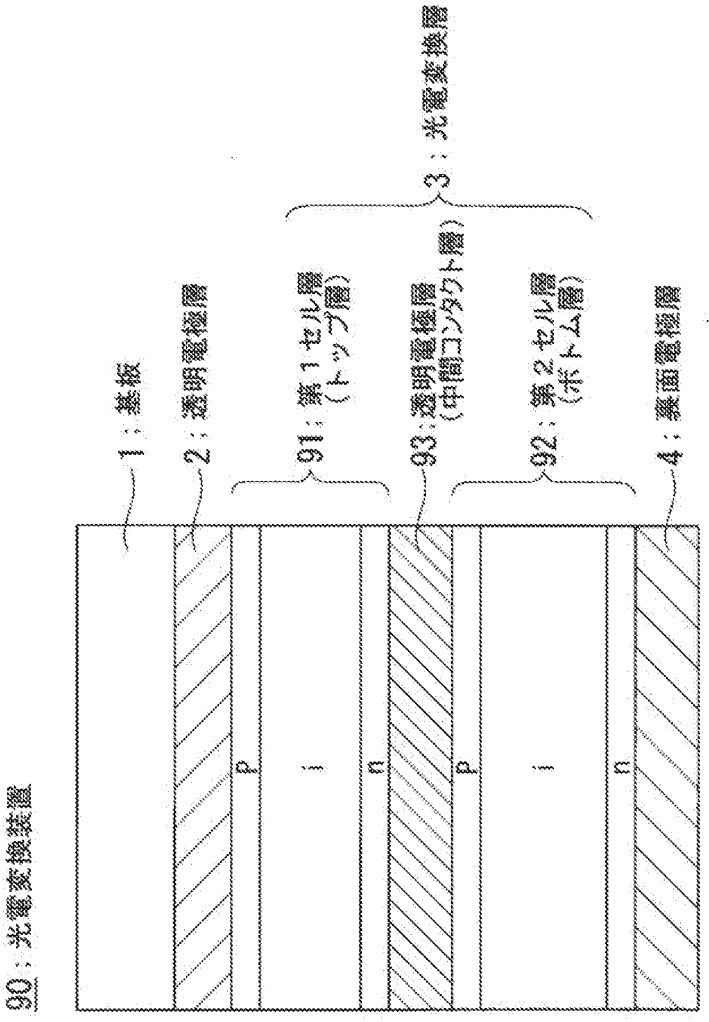
SAMSUNG EX. 1002 - 2447/4148

主として有する光電変換層を有する請求項13に記載の光電変換装置。

[19] 前記非晶質シリコン系半導体を主として有する光電変換層と前記裏面電極の間に、結晶質もしくは非晶質シリコン系半導体、結晶質もしくは非晶質シリコンゲルマニウム系半導体を主として有する光電変換層を複数有する請求項13に記載の光電変換装置。

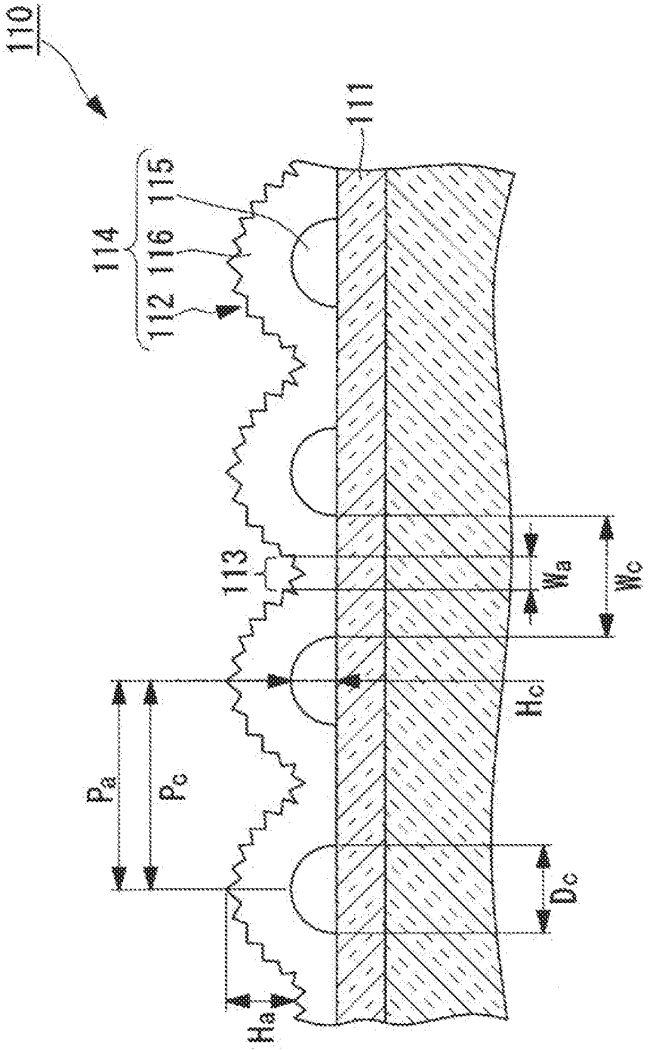
SAMSUNG EX. 1002 - 2448/4148

[図1]

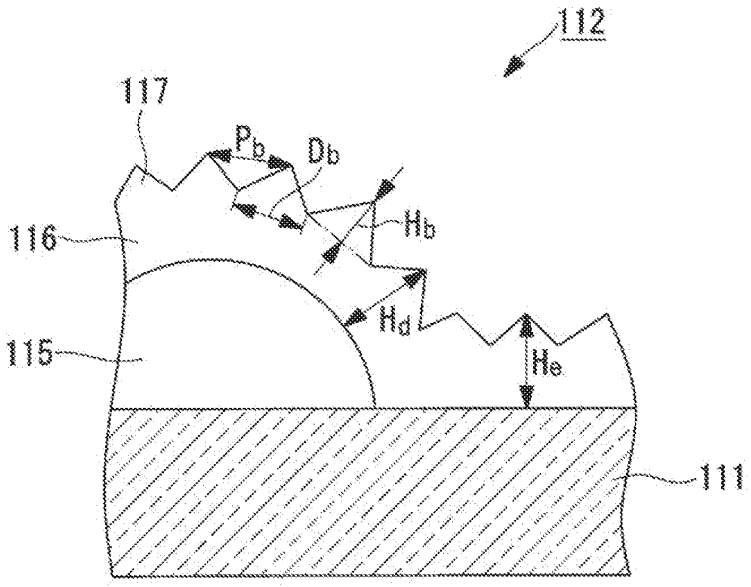


SAMSUNG EX. 1002 - 2449/4148

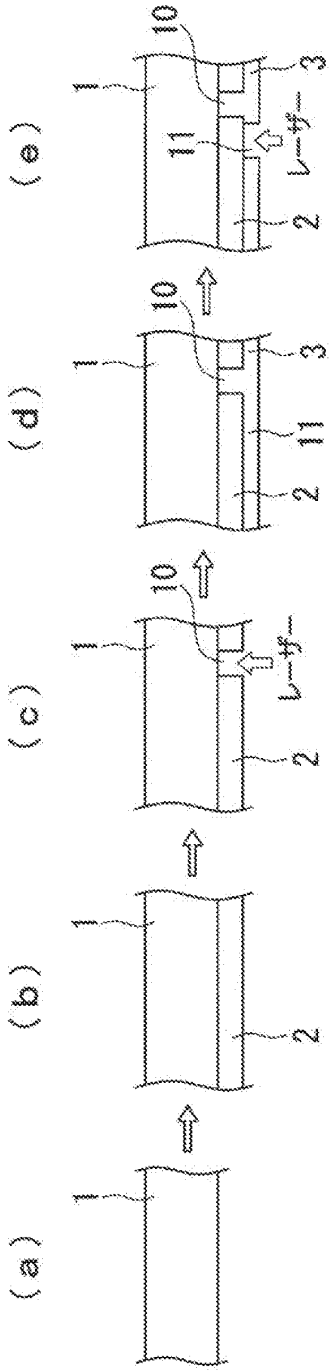
[図2]



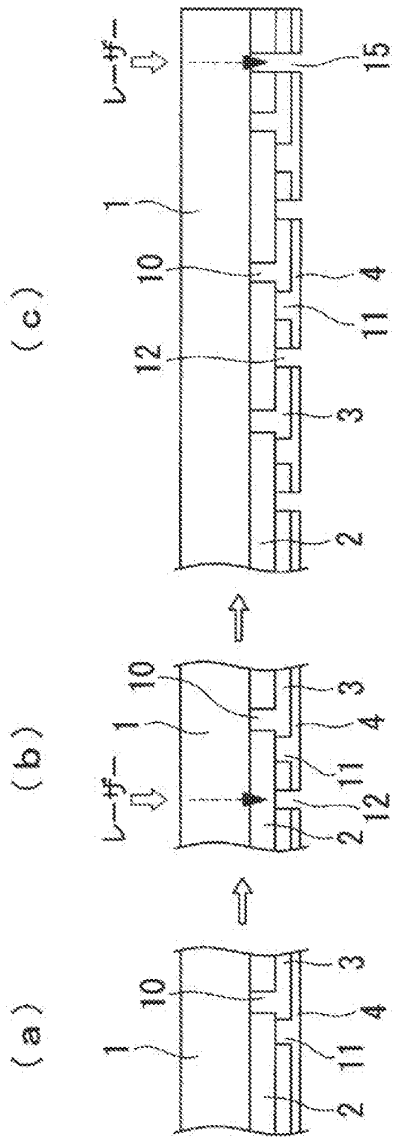
[図3]



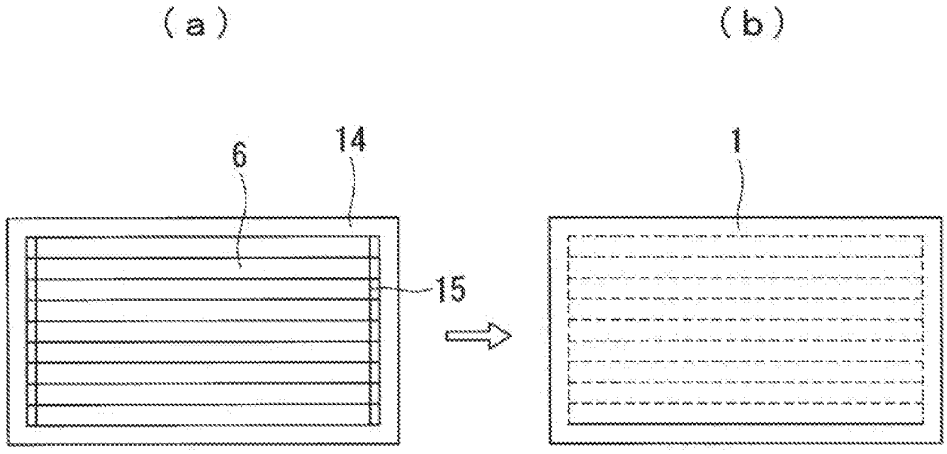
[図4]



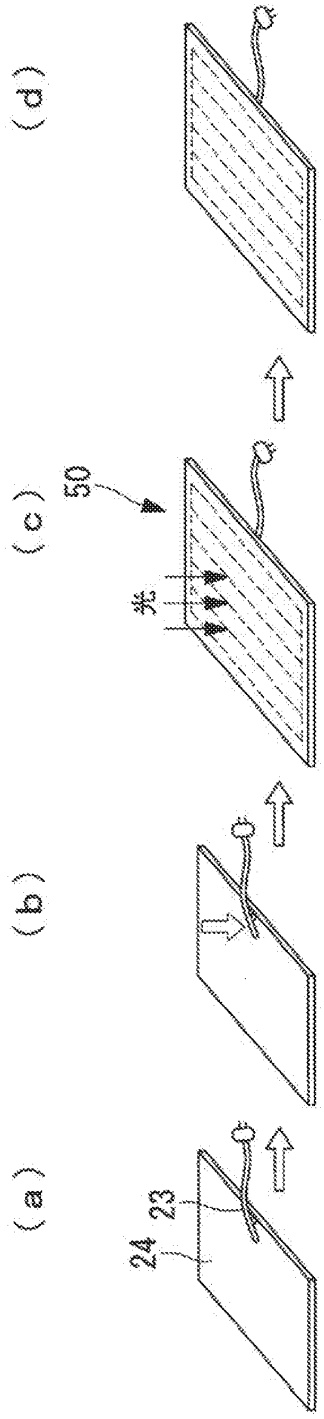
[図5]



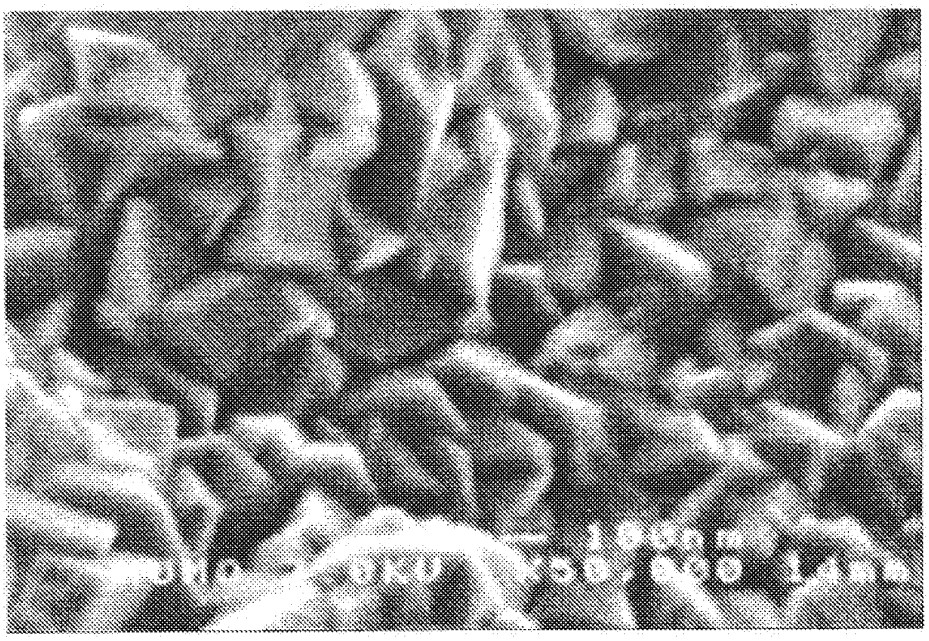
[図6]



[図7]



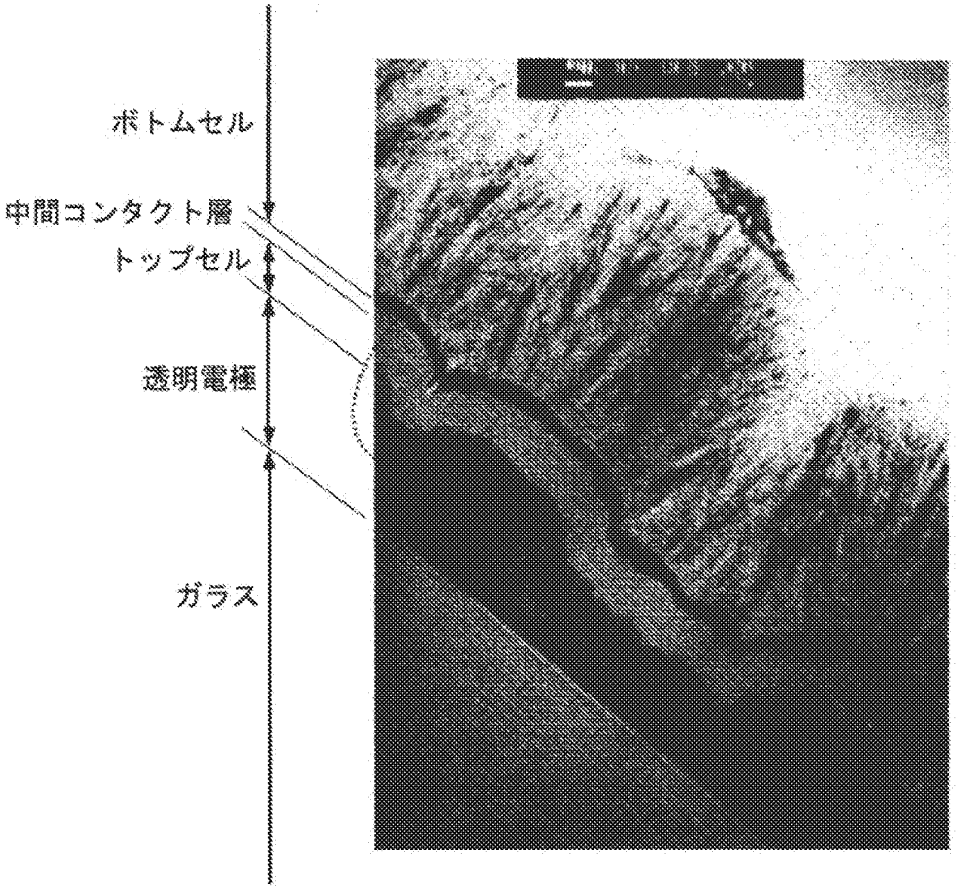
[図8]



[図9]



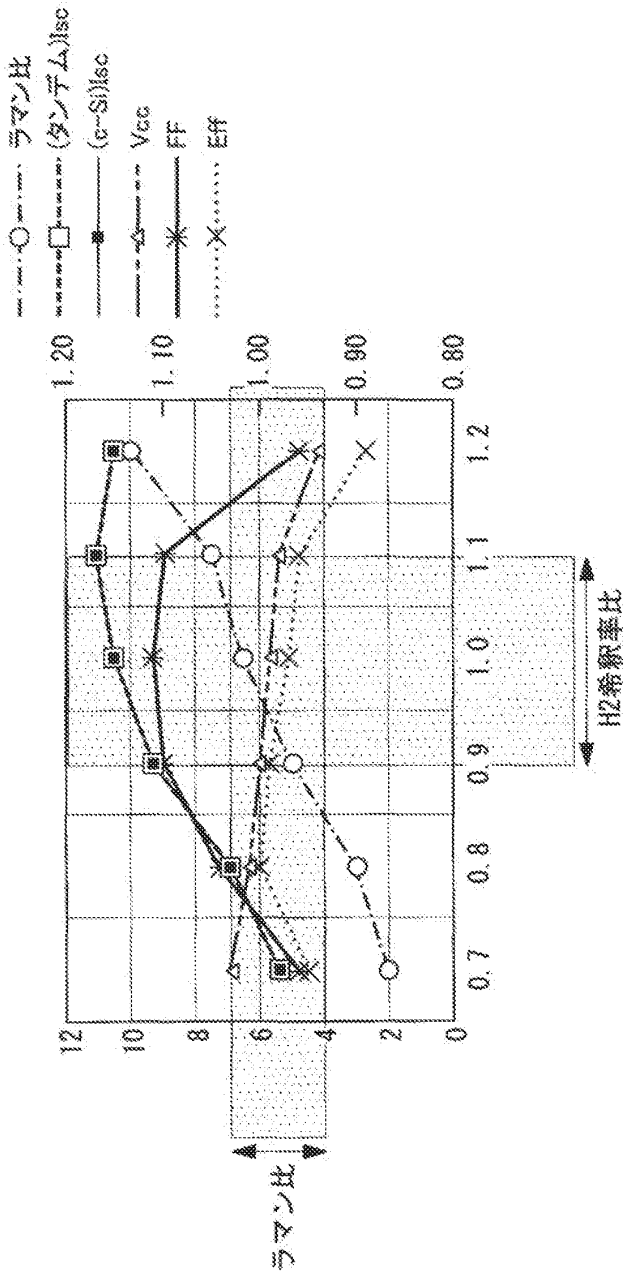
[図10]



[図11]



[図12]



SAMSUNG EX. 1002 - 2459/4148

INTERNATIONAL SEARCH REPORT

International application No.
PCT/JP2007/065386

A. CLASSIFICATION OF SUBJECT MATTER
H01L31/04(2006.01)i

According to International Patent Classification (IPC) or to both national classification and IPC

B. FIELDS SEARCHED

Minimum documentation searched (classification system followed by classification symbols)
H01L31/04

Documentation searched other than minimum documentation to the extent that such documents are included in the fields searched
Jitsuyo Shinan Koho 1922-1996 Jitsuyo Shinan Toroku Koho 1996-2007
Kokai Jitsuyo Shinan Koho 1971-2007 Toroku Jitsuyo Shinan Koho 1994-2007

Electronic data base consulted during the international search (name of data base and, where practicable, search terms used)

C. DOCUMENTS CONSIDERED TO BE RELEVANT

Category*	Citation of document, with indication, where appropriate, of the relevant passages	Relevant to claim No.
Y	JP 2005-347490 A (Asahi Glass Co., Ltd.), 15 December, 2005 (15.12.05), Full text; all drawings (Family: none)	1-4,14,15
Y	JP 2002-26348 A (Mitsubishi Heavy Industries, Ltd.), 25 January, 2002 (25.01.02), Par. No. [0036] (Family: none)	1-4,14,15
Y	JP 2006-216921 A (Mitsubishi Heavy Industries, Ltd.), 17 August, 2006 (17.08.06), Par. No. [0044]; Fig. 5 (Family: none)	1-4,14,15

☒ Further documents are listed in the continuation of Box C. ☐ See patent family annex.

* Special categories of cited documents:
"A" document defining the general state of the art which is not considered to be of particular relevance
"E" earlier application or patent but published on or after the international filing date
"L" document which may throw doubts on priority claim(s) or which is cited to establish the publication date of another citation or other special reason (as specified)
"O" document referring to an oral disclosure, use, exhibition or other means
"P" document published prior to the international filing date but later than the priority date claimed
"T" later document published after the international filing date or priority date and not in conflict with the application but cited to understand the principle or theory underlying the invention
"X" document of particular relevance; the claimed invention cannot be considered novel or cannot be considered to involve an inventive step when the document is taken alone
"Y" document of particular relevance; the claimed invention cannot be considered to involve an inventive step when the document is combined with one or more other such documents, such combination being obvious to a person skilled in the art
"&" document member of the same patent family

Date of the actual completion of the international search	Date of mailing of the international search report
30 October, 2007 (30.10.07)	13 November, 2007 (13.11.07)
Name and mailing address of the ISA/ Japanese Patent Office	Authorized officer
Facsimile No.	Telephone No.

Form PCT/ISA/210 (second sheet) (April 2007)

SAMSUNG EX. 1002 - 2460/4148

INTERNATIONAL SEARCH REPORT

International application No.
PCT/JP2007/065386

C (Continuation). DOCUMENTS CONSIDERED TO BE RELEVANT

Category*	Citation of document, with indication, where appropriate, of the relevant passages	Relevant to claim No.
Y	JP 2007-5345 A (Mitsubishi Heavy Industries, Ltd.), 11 January, 2007 (11.01.07), Par. No. [0041]; Fig. 15 (Family: none)	1-4,14,15

Form PCT/ISA/210 (continuation of second sheet) (April 2007)

SAMSUNG EX. 1002 - 2461/4148

INTERNATIONAL SEARCH REPORT

International application No.
PCT/JP2007/065386

Box No. II Observations where certain claims were found unsearchable (Continuation of item 2 of first sheet)

This international search report has not been established in respect of certain claims under Article 17(2)(a) for the following reasons:

1. ☐ Claims Nos.:
because they relate to subject matter not required to be searched by this Authority, namely:

2. ☐ Claims Nos.:
because they relate to parts of the international application that do not comply with the prescribed requirements to such an extent that no meaningful international search can be carried out, specifically:

3. ☐ Claims Nos.:
because they are dependent claims and are not drafted in accordance with the second and third sentences of Rule 6.4(a).

Box No. III Observations where unity of invention is lacking (Continuation of item 3 of first sheet)

This International Searching Authority found multiple inventions in this international application, as follows:
A matter common to the inventions in claims 1-19 is "a photoelectric converter comprising a substrate with a transparent electrode where a transparent electrode layer is provided on a transparent insulating substrate, and at least a photoelectric conversion layer principally comprising a silicon based semiconductor and a backside electrode layer that are formed sequentially on the transparent electrode layer side of the substrate with a transparent electrode, wherein the substrate with a transparent electrode has a surface shape where large and small protrusions and recesses coexist and spectral haze rate is 20% or above at the wavelength of 550-800 nm.
(Continued to extra sheet.)

1. ☐ As all required additional search fees were timely paid by the applicant, this international search report covers all searchable claims.

2. ☐ As all searchable claims could be searched without effort justifying additional fees, this Authority did not invite payment of additional fees.

3. ☐ As only some of the required additional search fees were timely paid by the applicant, this international search report covers only those claims for which fees were paid, specifically claims Nos.:

4. ☒ No required additional search fees were timely paid by the applicant. Consequently, this international search report is restricted to the invention first mentioned in the claims; it is covered by claims Nos.: 1-4, 14, 15

Remark on Protest

the

☐ The additional search fees were accompanied by the applicant's protest and, where applicable, payment of a protest fee.

☐ The additional search fees were accompanied by the applicant's protest but the applicable protest fee was not paid within the time limit specified in the invitation.

☐ No protest accompanied the payment of additional search fees.

SIONYX1403000024.0151

SAMSUNG EX. 1002 - 2462/4148

Continuation of Box No.III of continuation of first sheet(2)

However, our search has found the above "photoelectric converter" is disclosed in Japanese Laid-open No. 2005-347490, and therefore it is not clearly novel. Consequently the common matter is not a special technical feature within the meaning of PCT Rule 13.2, second sentence, because the above "photoelectric converter" makes no contribution over the prior art.

Therefore, there is no matter common to all the inventions in claims 1-19 as a special technical feature, and there exists no other common matter to be considered to be a special technical feature within the meaning of PCT Rule 13.2, second sentence, therefore no technical relationship within the meaning of PCT Rule 13 can be found among those different inventions.

Accordingly, the inventions in claims 1-19 do not fulfill the requirement of unity of invention.

SIONYX1403000024.0152

SAMSUNG EX. 1002 - 2463/4148

国際調査報告

国際出願番号 PCT／JP2007／065386

A. 発明の属する分野の分類（国際特許分類（IPC））

Int.Cl. H01L31/04(2006.01)

B. 調査を行った分野

調査を行った最小限資料（国際特許分類（IPC））

Int.Cl. H01L31/04

最小限資料以外の資料で調査を行った分野に含まれるもの

日本国実用新案公報	1922－1996年
日本国公開実用新案公報	1971－2007年
日本国実用新案登録公報	1996－2007年
日本国登録実用新案公報	1994－2007年

国際調査で使用した電子データベース（データベースの名称、調査に使用した用語）

C. 関連すると認められる文献

引用文献のカテゴリー＊	引用文献名 及び一部の箇所が関連するときは、その関連する箇所の表示	関連する請求の範囲の番号
Y	JP 2005-347490 A(旭硝子株式会社), 2005.12.15, 全文, 全図 (ファミリーなし)	1-4, 14, 15
Y	JP 2002-26348 A(三菱重工業株式会社), 2002.01.25, [0036] (ファミリーなし)	1-4, 14, 15
Y	JP 2006-216921 A(三菱重工業株式会社), 2006.08.17, [0044], 図5 (ファミリーなし)	1-4, 14, 15

☑ C欄の続きにも文献が列挙されている。　　☐ パテントファミリーに関する別紙を参照。

＊ 引用文献のカテゴリー
「A」特に関連のある文献ではなく、一般的技術水準を示すもの
「E」国際出願日前の出願または特許であるが、国際出願日以後に公表されたもの
「L」優先権主張に疑義を提起する文献又は他の文献の発行日若しくは他の特別な理由を確立するために引用する文献（理由を付す）
「O」口頭による開示、使用、展示等に言及する文献
「P」国際出願日前で、かつ優先権の主張の基礎となる出願
「T」国際出願日又は優先日後に公表された文献であって出願と矛盾するものではなく、発明の原理又は理論の理解のために引用するもの
「X」特に関連のある文献であって、当該文献のみで発明の新規性又は進歩性がないと考えられるもの
「Y」特に関連のある文献であって、当該文献と他の1以上の文献との、当業者にとって自明である組合せによって進歩性がないと考えられるもの
「&」同一パテントファミリー文献

国際調査を完了した日	国際調査報告の発送日
30.10.2007	13.11.2007

国際調査機関の名称及びあて先	特許庁審査官（権限のある職員）	2K	9010
日本国特許庁（ISA／JP） 郵便番号100－8915 東京都千代田区霞が関三丁目4番3号	吉野 三寛		
	電話番号 03－3581－1101 内線 3255		

様式PCT／ISA／210（第2ページ）（2007年4月）

SAMSUNG EX. 1002 - 2464/4148

Ｃ（続き）．　関連すると認められる文献

引用文献のカテゴリー＊	引用文献名　及び一部の箇所が関連するときは、その関連する箇所の表示	関連する請求の範囲の番号
Y	JP 2007-5345 A(三菱重工業株式会社), 2007.01.11, [0041], 図 15 (ファミリーなし)	1-4, 14, 15

SIONYX1403000024.0154

SAMSUNG EX. 1002 - 2465/4148

国際調査報告

国際出願番号 PCT／JP2007／065386

第II欄 請求の範囲の一部の調査ができないときの意見（第1ページの2の続き）

法第8条第3項（PCT17条(2)(a)）の規定により、この国際調査報告は次の理由により請求の範囲の一部について作成しなかった。

1. ☐ 請求の範囲＿＿＿＿＿＿＿＿ は、この国際調査機関が調査をすることを要しない対象に係るものである。
つまり、

2. ☐ 請求の範囲＿＿＿＿＿＿＿＿ は、有意義な国際調査をすることができる程度まで所定の要件を満たしていない国際出願の部分に係るものである。つまり、

3. ☐ 請求の範囲＿＿＿＿＿＿＿＿ は、従属請求の範囲であってPCT規則6.4(a)の第2文及び第3文の規定に従って記載されていない。

第III欄 発明の単一性が欠如しているときの意見（第1ページの3の続き）

次に述べるようにこの国際出願に二以上の発明があるとこの国際調査機関は認めた。

請求の範囲1－19に係る発明の共通の事項は、「透明絶縁性の基板上に透明電極層を設けてなる透明電極付き基板と、該透明電極付き基板の透明電極層側に順次形成された、シリコン系半導体を主として有する光電変換層からなる光電変換装置であって、前記透明電極付き基板は、表面が大小の凹凸が混在した形状であり、かつ分光ヘイズ率が520nm以上800nm以下の波長で20%以上である光電変換装置」である。

しかしながら、調査の結果、上記「光電変換装置」は、特開2005－347490号公報に開示されており、新規でないことが明らかとなり、結果として、上記「光電変換装置」は先行技術の域を出ないから、PCT規則13．2の第2文の意味において、この共通事項は特別な技術的特徴ではない。

それは、特別な技術的特徴として請求の範囲1－19に係る発明全てに共通の事項3など、PCT規則13．2の第2文の意味において特別な技術的特徴と考えられる他の共通の事項も存在しないので、それらの相違する発明の間にPCT規則13の意味における技術的な関連を見いだすことはできない。

よって、請求項1－19に係る発明は、発明の単一性の要件を満たしていない。

1. ☐ 出願人が必要な追加調査手数料をすべて期間内に納付したので、この国際調査報告は、すべての調査可能な請求の範囲について作成した。

2. ☐ 追加調査手数料を要求するまでもなく、すべての調査可能な請求の範囲について調査することができたので、追加調査手数料の納付を求めなかった。

3. ☐ 出願人が必要な追加調査手数料を一部のみしか期間内に納付しなかったので、この国際調査報告は、手数料の納付のあった次の請求の範囲のみについて作成した。

4. ☑ 出願人が必要な追加調査手数料を期間内に納付しなかったので、この国際調査報告は、請求の範囲の最初に記載されている発明に係る次の請求の範囲について作成した。

請求項1－4，14，15

追加調査手数料の異議の申立てに関する注意

☐ 追加調査手数料及び、該当する場合には、異議申立手数料の納付と共に、出願人から異議申立てがあった。

☐ 追加調査手数料の納付と共に出願人から異議申立てがあったが、異議申立手数料が納付命令書に示した期間内に支払われなかった。

☐ 追加調査手数料の納付はあったが、異議申立てはなかった。

様式PCT／ISA／210（第1ページの続葉（2））（2007年4月）

SAMSUNG EX. 1002 - 2466/4148

OPTICAL PROPERTIES OF THE COMSAT NON-REFLECTIVE CELL*

R. A. Arndt, J. F. Allison, J. G. Haynos,† and A. Meulenberg, Jr.
COMSAT Laboratories
Clarksburg, Maryland 20734

SUMMARY

A new generation of silicon solar cell, called the COMSAT Non-Reflective (CNR) cell, which shows a marked improvement over previous cells, has been developed. Under AM0 illumination these cells typically produce a maximum power of about 21 mW/cm^2 and short-circuit current of about 46 mA/cm^2. The improvements stem from a new surface structure and related optical properties of the cell, both of which are discussed herein.

INTRODUCTION

Recently an improved silicon solar cell, called the COMSAT Non-Reflective (CNR) cell, was announced (1). This cell typically produces a maximum power of 21 mW/cm^2 and short-circuit current of 46 mA/cm^2 under AM0 illumination. Figure 1 shows the current-voltage (I-V) curves under AM0 illumination for the CNR cell and the Violet cell. The fabrication of the CNR cell builds upon the technology of the Violet cell (2) and employs a new surface structure to reduce reflection losses. This paper describes the structure of this surface and the optical properties of the cell which lead to its improved output.

BACKGROUND AND THEORY

Traditionally, the light-incident surface of silicon solar cells is flat and polished. The reflectance of normally incident light as a function of wavelength is shown as the upper solid curve of Fig. 2. If a single-layer antireflective (AR) coating of tantalum oxide is added to the surface, the reflectance is reduced considerably, as is also shown in Fig. 2 by the lower solid curve. The rise of these two curves at short wavelengths is due to the anomalous dispersion of silicon; the asymmetric shape of the lower curve with respect to the upper curve is due to the fact that a single-layer AR coating can provide blooming at only one wavelength.

The surface treatment in the CNR cell results in the formation of a random distribution of regular pyramids (Fig. 3) with an average base length of several micrometers and an included angle of 70.5° between opposite faces. An idealized cross section of such a surface, perpendicular to the plane of the cell, is pictured in Fig. 4. A ray of light incident normal to the plane of the cell strikes the face of a pyramid at an angle of incidence of about 55°. The reflected part of this ray strikes the side of an adjacent pyramid at an angle of incidence of about 16°. If the reflectivity (R) of silicon is independent of angle of incidence, as it is for angles up to about 70°, the reflected intensity is R^2I_o, where I_o is the incident intensity. In comparison, for a flat polished surface the reflected intensity is RI_o and the double interaction at the CNR cell surface therefore reduces the overall reflectance.

The measured reflectance of a bare CNR cell surface is shown as the upper dashed curve of Fig. 2. At a given wavelength, if the reflectance of the upper solid curve is squared, the reflectance value in the upper dashed curve is obtained. The reflectance of a CNR cell surface with a single-layer AR coating of tantalum oxide is shown by the lower dashed curve of Fig. 2. The asymmetry introduced into the lower dashed curve by the single-layer AR coating is present although it is difficult to see since the overall reflectance has been reduced to such a low value. It should be noted that the measurements of Fig. 2 were made without cover slides on the cells to facilitate calculations and their comparison with measurements.

Light is attenuated in an absorbing medium according to

$$I = I_o' e^{-\alpha x} \tag{1}$$

where I is the intensity after the light has traveled a distance x, I_o' is the intensity entering the absorber, and α is the absorption coefficient. The generation rate (g) of carriers is proportional to the amount of light absorbed and the expression for g is therefore

$$g \propto \frac{dI}{dx} = -\alpha I_o' e^{-\alpha x} = -\alpha I_o (1 - R) e^{-\alpha x} \tag{2}$$

since $I_o' = I_o(1 - R)$.

For a cell with a flat polished surface, x is equal to t, the distance from the front of the cell in a direction perpendicular to the plane of the cell. This is no longer true for the CNR cell, as can be seen in Fig. 4. The refracted light enters the cell at different angles at each of the two pyramidal faces considered and the magnitudes of these angles will depend on the index of refraction of silicon and that of the medium surrounding the cell.* To simplify the calculations it will be assumed that the cell interface is with air. The angles shown in Fig. 4 are based upon this assumption and a refractive index of silicon of 3.8. Equation (1) must be modified to take into account the double reflection and the angles of the two refracted rays. For the CNR cell, then

$$I = (1 - R) I_o e^{-\alpha x'} \tag{3a}$$

*The presence of an AR coating will not alter the magnitude of these angles.

*This paper is based upon work performed at COMSAT Laboratories under the sponsorship of the Communications Satellite Corporation.
†Deceased.

SIONYX1403000026.0002

SAMSUNG EX. 1002 - 2467/4148

and

$$I = R(1 - R)\ I_o\ e^{-\alpha x''} \qquad (3b)$$

where the single prime refers to the light entering the cell at the first pyramidal face and the double prime refers to the light entering at the second pyramidal face. The equation for the carrier generation rate is

$$g \propto -1.39\ \alpha(1 - R)\ I_o\ e^{-1.39\alpha t} - 1.94\ \alpha R(1 - R)\ I_o\ e^{-1.94\alpha t} \qquad (4)$$

where the appropriate values for x' and x" have been used.

RESULTS AND DISCUSSION

Short-circuit currents of covered cells are 88 and 78 percent of the theoretical maximum (~53 mA/cm^2) under AM0 illumination for the CNR and the Violet cell, respectively. The reflectance, weighted according to the solar spectrum (R_s), and computed for uncovered cells with AR coating from the data of Fig. 2, was 0.025 for the CNR cell and 0.137 for the flat polished-surface cell. Computation of R_s for covered cells resulted in values of 0.025 and 0.113, respectively. For covered cells the ratio of the short-circuit current of the CNR cell to that of the Violet cell is 1.13, whereas the corresponding ratio of $1 - R_s$ is 1.10. Most of the improvement in short-circuit current is thus attributable to reduced reflectance. The rest is attributable to the increased red response of the CNR cell relative to the Violet cell (3).

With equations (2) and (4) the carrier generation rates were computed for incident light of 0.90-μm wavelength. At this wavelength the absorption coefficient is sufficiently low (~300 cm^{-1}) so that all of the light is not absorbed close to the cell junction and yet the carrier collection efficiency is still very high. Figure 5 shows the carrier generation rate at 0.90 μm in arbitrary units as a function of depth for a CNR cell and a cell with a flat polished surface. Both cells were assumed to be covered with a tantalum oxide AR coating, without cover slides and infinitely thick. It can be seen that, near the junction, the generation rate in the CNR cell is greater than that in the cell with a flat polished surface.

The increased generation rate in the CNR cell is not due solely to the increased light entering the cell, since this accounts for an increase by a factor of only 1.10 at 0.90 μm (see Fig. 2), but is also due to the fact that the light traverses the cell in a direction away from the normal to the cell (see Fig. 4). The two lines of Fig. 5 are seen to cross at a depth of about 45 μm. By integration, it was found that 84 percent of all the carriers produced in the CNR cell are produced within the first 45 μm, whereas only 26 percent of all carriers produced in the cell with a flat polished surface are produced within the same distance. This should make the long wavelength part of the spectral response of a CNR cell more resistant to radiation.

Calculations on the CNR cell are more complicated to handle analytically when the light is incident other than normal and are therefore not considered. However, reflectance at 0.9 μm and power output under AM0 illumination were measured as functions of angle of incidence; the results are shown in Fig. 6 for a CNR cell complete with cover slide. The reflectance shown here is slightly higher at normal incidence than in Fig. 2 because of contributions from the grid lines and the cover slide. Both curves can be fitted with a cosine function. Similar measurements on a Violet cell reveal an identical angular dependence.

In Fig. 4 it can be seen that the angle of incidence for light reaching the back face of the CNR cell is 44° for the first refracted ray and 59° for the second. If the back of the cell is flat and polished, both of these angles exceed the critical angle for total internal reflection and the light will be reflected through the cell a second time without any reflection loss at the back face. (The critical angle for a silicon-air interface is 15.3° for a silicon index of 3.8.) In contrast, if the light were traversing the cell perpendicular to the plane of the cell as in a polished-surface cell, only about 33 percent of the light arriving at the back face would be reflected back into the cell.

Figure 7 shows the fraction of incident light of 0.90-μm wavelength that is absorbed as a function of cell thickness for a CNR cell with a flat polished back and a cell in which both surfaces are flat and polished. In both cases the calculations were performed by assuming an AR coating on the light-incident face. If each cell were reduced in thickness to about 50 μm, the fraction of absorbed light in the CNR cell would be reduced by only about 1 percent, whereas the reduction of absorbed light for the other cell would be about 25 percent. The total internal reflection would thus allow use of thinner cells without sacrificing much of the long wavelength sensitivity.

CONCLUSIONS

The CNR cell provides higher short-circuit current due to a reduction in the reflectance of incident light. The long wavelength sensitivity of the CNR cell should not be affected by radiation as much as that of a cell with a flat polished surface because of the higher carrier generation rate near the junction. Finally, the CNR cell should maintain its high short-circuit current in thin cells (~2 mils) due to the total internal reflection at the back surface.

ACKNOWLEDGMENTS

The authors thank Dr. E S. Rittner for his encouragement of this work and many helpful discussions. The members of the Semiconductor Technology Department at COMSAT Labs were helpful in making measurements and preparing samples.

SIONYX1403000026.0003

SAMSUNG EX. 1002 - 2468/4148

REFERENCES

(1) J. Haynos, J. Allison, R. Arndt, and A. Meulenberg, "The COMSAT Non-Reflective Silicon Solar Cell: A Second Generation Improved Cell," International Conference on Photovoltaic Power Generation, Hamburg, Germany, Sept. 25–27, 1974.

(2) J. Lindmayer and J. F. Allison, "The Violet Cell, An Improved Silicon Solar Cell," COMSAT Technical Review, Vol. 3, No. 1, 1973.

(3) A. Meulenberg, Jr., J. F. Allison, R. A. Arndt, and J. G. Haynos, "Radiation Damage to the COMSAT Non-Reflecting Cell," to be presented at the 11th Photovoltaic Specialists Conference, Phoenix, Arizona, May 6–8, 1975.

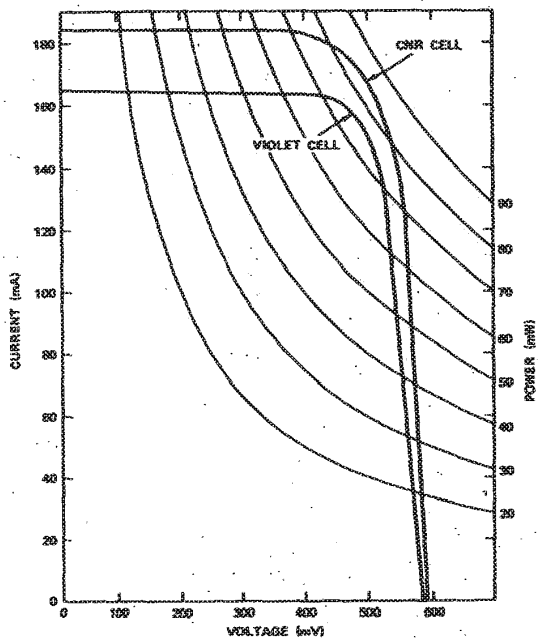


Fig. 1. Current-Voltage Characteristics under AM0 Illumination for a CNR Cell and a Violet Cell

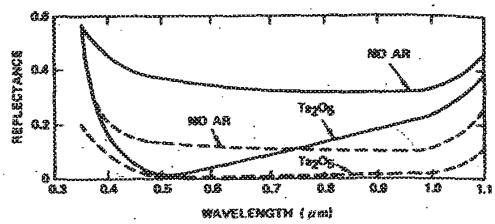


Fig. 2. Reflectance as a Function of Wavelength for Normal Incidence Light. (Upper solid curve is for silicon with a flat polished surface and no AR coating and the lower solid curve is for the same surface with a quarter-wavelength AR coating of tantalum oxide. The upper and lower dashed curves are for a CNR cell surface, without and with a quarter-wavelength AR coating, respectively.)

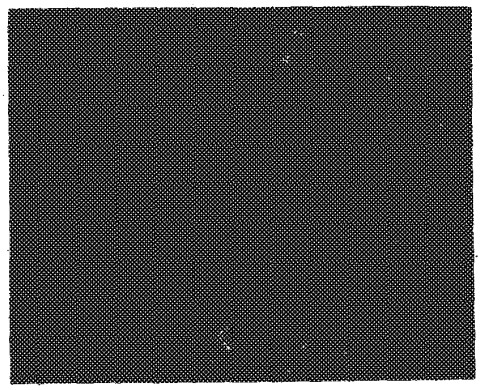


Fig. 3. Scanning Electron Micrograph of the CNR Cell Surface

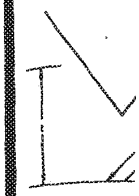


Fig. 4. Re
Cell Surfa
a surrounc
of 1.0 an
3.8. X
ray and
tance i
to

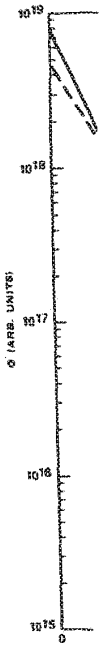


Fig. 5
Rates
Light
a C
(

SIONYX1403000026.0004

SAMSUNG EX. 1002 - 2469/4148

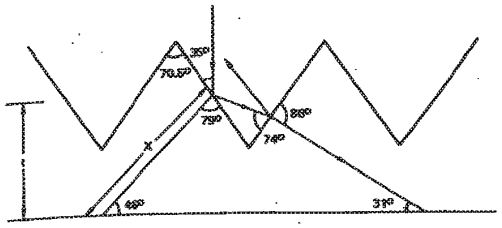


Fig. 4. Representation of an Idealized CNR Cell Surface. (The angles shown are for a surrounding medium of refractive index of 1.0 and a silicon refractive index of 3.8. X is the distance along a light ray and t is the corresponding distance in a direction perpendicular to the plane of the cell.)

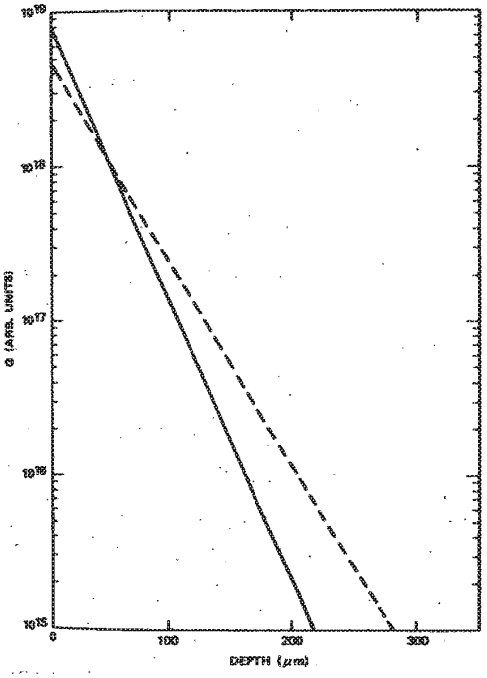


Fig. 5. Calculated Carrier Generation Rates (arbitrary units) from 0.90-μm Light in a CNR Cell (solid line) and a Cell with a Flat Polished Face (dashed line), Both Having AR Coating of Tantalum Oxide

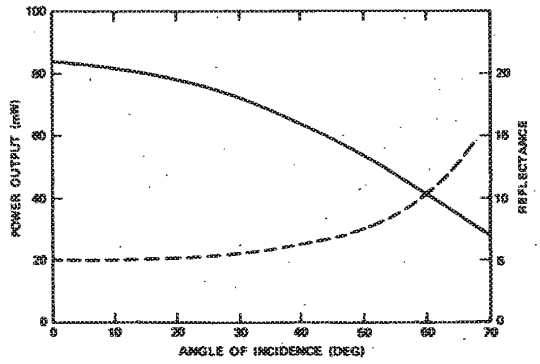


Fig. 6. Maximum Power Output (solid line) under AM0 Illumination and Reflectance at 0.90 μm as a Function of Angle of Incidence (dashed line) for a CNR Cell Complete with Cover Slide

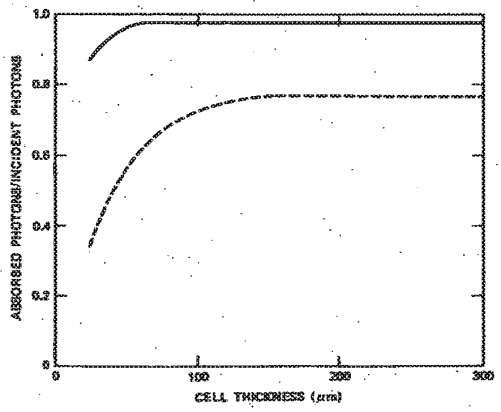


Fig. 7. Fraction of Incident Photons (0.90 μm) That Are Absorbed in a CNR Cell (solid line) and a Cell with Flat Polished Surface (dashed line) as a Function of Cell Thickness

SIONYX1403000026.0005

SAMSUNG EX. 1002 - 2470/4148

Interstitial defect reactions in silicon

M. T. Asom, J. L. Benton, R. Sauer, and L. C. Kimerling
AT&T Bell Laboratories, Murray Hill, New Jersey 07974

(Received 11 March 1987; accepted for publication 27 May 1987)

Deep level transient spectroscopy has been employed in a study of impurity-interstitial defect reactions in silicon following room-temperature electron irradiation. Three defects have been isolated and identified from their reactions and electrical properties as C_s-C_i, C_i-O_i, and P_s-C_i. The C_s-C_i, *ME*[(0.10), (0.17)] and P_s-C_i, *ME* [(0.21), (0.23), (0.27), (0.30)] defects exhibit metastable structural transformations. Our results reveal the multistructural nature and chemical reactivity of the silicon self-interstitial.

Vacancies and interstitials in silicon act as vehicles for various diffusion mechanisms and interact with impurities in the crystal to form complex defects. In phosphorus-doped silicon, the isolated vacancy and vacancy-impurity interactions have been extensively studied and their inventory soundly established.[1–3] Vacancies migrate through the lattice and form pairs with both substitutional (s) and interstitial (i) impurities such as P_s-V, O_i-V, and B_s-V. However, an understanding of interstitial defects and interstitial impurity interactions has not been similarly established. The silicon self-interstitial, Si_i, is reported to be highly mobile, with essentially athermal migration kinetics at 4.2 K[4]; thus, it has been difficult to obtain direct experimental information. While there exist studies of group III interstitials (B_i, Al_i) in p-type Si,[5,6] no interstitial group V element has been observed[7] and the only identified group IV interstitial in silicon is interstitial carbon (C_i).[2,8] The acceptor state assignment for C_i, however, has been recently challenged, and a vacancy-related defect was proposed.[9] This letter resolves this discrepancy and defines, for the first time, impurity-interstitial defect reactions in phosphorus-doped silicon.

The materials used in this study were phosphorus-doped silicon, grown by either the float zone (*FZ*) (low oxygen) or Czochralski (CZ) (high oxygen) methods. Both Schottky-barrier and p-n junction samples were employed. The samples were irradiated with 1.5 MeV electrons at a flux of 4×10^{12} e^-/cm^2 s. Capacitance transient spectra were generated using deep level transient spectroscopy (DLTS) techniques outlined elsewhere.[10] Injection anneals were performed at current densities ranging from 1 to 11 Å/cm^2 using a constant current source.

Figure 1 depicts typical DLTS spectra obtained on a single diode, following room-temperature electron irradiation and a premeasurement forward bias anneal of 1 A/cm^2 at 300 K for 3 min. Each spectral feature is identified by assigned structure and defect state energy (eV). *E* and *H* refer to hole and electron emission energies, respectively. A prefix *M* denotes that the state represents an alternative, metastable defect structure

The solid line spectrum was recorded after the diode was cooled to 50 K with an applied reverse bias. This procedure freezes-in the defect structures associated with unoccupied states in the upper half of the energy gap. Several previously identified spectral features[3] are observed and labeled as V-P_s, V-O_i, and V-V. In this work we justify assignment of the remainder of the defect states to C_s-Si_i-C_s, C_s-C_i *ME*[(0.1), (0.17)], and P_s-C_i, [*ME* 3(0.27), *ME* 2(0.23)], as shown. The defect designated as P_s-C_i possesses two additional configurations which are represented by defect states *ME* 1(0.21) and *ME* 4(0.30) but which are not revealed under these measurement conditions.[9,11,12] As is typical for metastable systems, the defect can be cycled repeatedly through the four configurations.[11]

The dashed spectrum was taken after the sample was cooled to 50 K under zero bias, a condition that stabilizes defect structures associated with filled states. The features are identical to those in the solid line spectrum except that the signal *ME*(0.1) is decreased and *ME*(0.17) is increased. Spectral changes which are dependent on cooling bias conditions are a fingerprint of charge-state controlled, structural

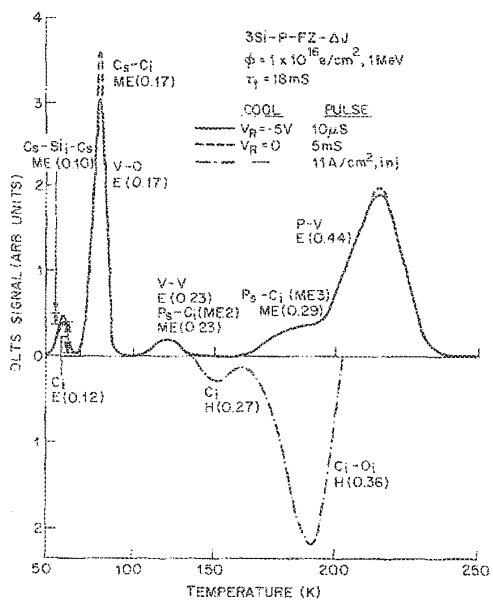


FIG. 1. DLTS spectra of samples 5Si-P-FZ-DJ following room-temperature electron irradiation and injection of 1 A/cm^2 for 3 min at 300 K, taken under three measurement conditions in order to show the interstitial carbon-related defects.

 0003-6951/87/300256-03$01.00 © 1987 American Institute of Physics
Downloaded 26 May 2009 to 146.186.238.18. Redistribution subject to AIP license or copyright; see http://apl.aip.org/apl/copyright.jsp

SIONYX1403000026.0006

SAMSUNG EX. 1002 - 2471/4148

TABLE I. Impurity concentrations and measured interstitial/vacancy ratios.

Sample ID	$[C_s]$	$[O_i]$	$[P_s]$	$\frac{\Sigma I}{\Sigma V}$	$\frac{P_s\text{-}C_i}{\Sigma V}$	$\frac{C_i\text{-}C_i}{\Sigma V}$	$\frac{C_i\text{-}O_i}{\Sigma V}$
1Si-P-CZ-DJ	$\approx 10^{16}$	10^{18}	5×10^{14}	0.95	0.0	0.0	0.95
2Si-P-CZ-DJ	···	$\geqslant 10^{17}$	1×10^{16}	1.0	0.16	0.0	0.84
3Si-P-FZ-DJ	$< 10^{16}$	$< 10^{16}$	2×10^{16}	$\geqslant$0.38	0.37	0.01	···
4Si-P-FZ-SB	$< 10^{16}$	$< 10^{16}$	3×10^{14}	$\geqslant$0.70	0.14	0.56	···
5Si-P-FZ-SB	$\approx 10^{16}$	$\approx 10^{16}$	3×10^{15}	$\geqslant$0.65	0.20	0.45	···
5Si-P-FZ-DJ	$\approx 10^{16}$	$> 10^{16}$	3×10^{15}	$\geqslant$0.68	0.18	0.03	$\geqslant$0.47

transformations. The $ME(0.1)$ defect has been analyzed in detail as a carbon-related, metastable defect.[13]

The dot/dashed spectrum was recorded using an injection pulse of 11 A/cm^2 in order to saturate the minority-carrier traps with holes. Two defect states $H(0.27)$ and $H(0.36)$ are observed as hole traps. $H(0.27)$ and $E(0.12)$ are always present in equal concentrations and have been identified as the donor $(0/+)$ and acceptor $(-/0)$ states[2] of C_i, respectively, by correlation of thermal annealing properties with the interstitial carbon electron paramagnetic resonance spectrum (EPR).[8] $H(0.36)$ has received several assignments in the literature, but it is shown here to represent the C_i-O_i associate.

We show first that all of the three new defect states, $ME[(0.1), (0.17)]$, $ME[(0.21), (0.23), (0.27), (0.30)]$, and $H(0.36)$ are related to interstitial carbon. Immediately following irradiation $E(0.12)$ and $H(0.27)$ are present in equal concentrations which decay simultaneously, at 300 K, as the three new defect states appear. In lightly doped, CZ silicon the post-irradiation concentration of $E(0.12)$ or $H(0.27)$ is equal to the sum of the concentrations of the vacancy-related defects $[\Sigma(O_i\text{-}V) + (P_s\text{-}V) + 2(V\text{-}V)]$ which form during room-temperature irradiation.[2] As shown in Table I, the total concentration of the new defect states (where observable) approaches the sum of the vacancy concentrations. Since the total vacancy introduction rate is constant in all materials, a value approaching unity in the $\Sigma I/\Sigma V$ column supports the conclusion that the total *interstitial component* of the radiation displacement damage is being counted.

Figure 2(a) shows the electronically stimulated dissociation of the defect represented by $ME3(0.29)$ to produce the $E(0.12)/H(0.27)$ states. We identify the reappearance of the $E(0.12)$ and $H(0.27)$ states as the liberation of C_i from a bound impurity complex as follows: (1) the states are, again, observed in equal concentrations and react at 300 K as does C_i as reported in Ref. 2; (2) the subsequent decay of $E(0.12)/H(0.27)$ produces as one product, the states $ME[(0.1), (0.17)]$ which are shown in Fig. 3 to correlate in stability with the 969-meV photoluminescence signal which has been identified as the C_s-C_i/C_s-Si_i-C_s defect by optically detected magnetic resonance.[14]

The above evidence yields the following reaction sequence in n-type silicon at 300 K: (1) interstitial silicon Si_i is captured solely by substitutional carbon C_s to produce interstitial carbon C_i by the Watkins replacement mechanism[4]; (2) mobile C_i reacts with impurities to form stable associates

$$Si_i + C_s \rightarrow Si_s + C_i, \tag{1}$$

$$C_i + X \rightarrow C_i\text{-}X, \tag{2}$$

where X may be oxygen, carbon, or phosphorus. The decay of C_i, $[E(0.12)$ and $H(0.27)]$, follows first-order kinetics[2] indicating that *one C_i is involved in each associate*. This conclusion is supported by the one-to-one relationship between product and reactant concentrations in Figs. 2(a)–2(c).

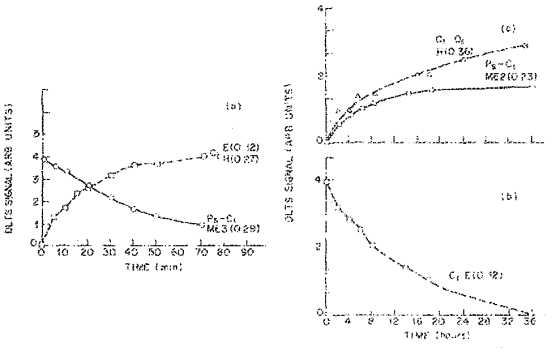


FIG. 2. Interstitial carbon reactions in n-type silicon. (a) The dissociation of P_s-C_i under 10 A/cm^2 injection at 300 K and the corresponding growth of C_i in sample 5Si-P-FZ-DJ. (b) Room-temperature annealing of C_i, following injection dissociation of P_s-C_i in sample 5Si-P-FZ-DJ. (c) The growth of P_s-C_i (solid line) in sample 3Si-P-FZ-DJ, and the alternative growth of C_i-O_i (dashed line) in sample 5Si-P-FZ-DJ is simultaneous with the decay of C_i shown in (b).

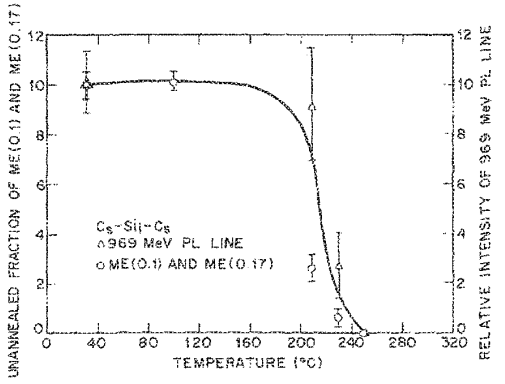


FIG. 3. Annealing curves for $ME[(0.10), (0.17)]$ DLTS signals and the 969-meV photoluminescence line which has been assigned to C_s-Si_i-C_s (Ref. 14).

Downloaded 26 May 2009 to 146.186.238.18. Redistribution subject to AIP license or copyright; see http://apl.aip.org/apl/copyright.jsp

SIONYX1403000026.0007

SAMSUNG EX. 1002 - 2472/4148

The injection-stimulated anneal provides a unique window for the reaction intermediate, C_i. It is particularly noteworthy that the decay of C_i following injection-stimulated dissociation of P_s-C_i displays kinetics with the same time constant and distribution of reaction products as observed after irradiation. This result reveals, for the first time, that C_i *undergoes long range, recombination enhanced diffusion* and suggests that it, too, exhibits configurational instabilities. Since each product defect is an associate involving one C_i, identification is reduced to definition of the impurity constituent. Table I is instructive in this task.[15]

C_i-O_i, $H(0.36)$ is the dominant interstitial-related defect state in oxygen-rich samples, Si-P-CZ. It accounts for practically all interstitial defects in material of low phosphorus content. Its presence correlates[16] with the 790-meV photoluminescence line which has been ascribed to C_i-O_i.[17,18]

P_s-C_i, $ME[(0.30), (0.29), (0.23), (0.21)]$ is the primary interstitial state in material of low oxygen, low carbon, and high phosphorus content. We have shown previously[12] that the introduction rate of the defect has the same dependence on phosphorus concentration as (P_s-V). This result means that the interaction cross section has the same basis in both cases (electrostatic attraction and confirms the assignment of $E(0.12)$ to the negatively charged acceptor state of C_i. The acceptor state of the vacancy, $E(0.10)$, is similarly positioned.[3] The generation of C_i by injection-stimulated dissociation of P_s-C_i is unambiguous evidence of the role of C_i as a constituent of this four-structured defect.

C_s-C_i/C_s-Si_i-C_s, $ME[(0.10), (0.17)]$ is a dominant defect in carbon-rich, low oxygen samples. It becomes less important as oxygen is added. As shown in Table I, a decrease in C_s-C_i in sample 5Si-P-FZ is observed (an increase in O_i-V is also seen) following p-n junction processing. This result directly demonstrates the competing role of O_i as a trap for C_i. The assignment of C_s-C_i/C_s-Si_i-C_s is strongly supported by the data of Fig. 3. The introduction of these defect states correlates with the 969-meV photoluminescence signal (G line), and the recovery kinetics follow the reduction of the signal as shown. This spectrum has been associated with a puckered C_s-Si_i-C_s structure by optically detected magnetic resonance.[14] We assign the $ME(0.10)$ configuration to this structure because the conditions which simulate photoluminescence experiments (forward bias injection at 20 K) produce the $ME(0.10)$ signal, independent of the sample cooling procedure. The $ME(0.17)$ signal is tentatively assigned to the C_s-C_i configuration observed by EPR.[19]

In conclusion, we have isolated and identified, by DLTS and photoluminescence measurements, three interstitial-related defects in n-type silicon. The defect reactions reveal a competition between carbon, oxygen, and phosphorus to trap carbon interstitials in parallel with similar reactions for vacancy defects. In n-type silicon, nearly all of the Si_i can be accounted for through the reactions of C_i. If C_i is a paradigm of group IV interstitials, then similar reactions should occur for Si_i (though the products may have less stability due to the larger size and lower electronegativity of the silicon atom). In particular, association of a group V impurity with an interstitial defect in silicon gives microscopic support to proposals of an interstitial diffusion path for phosphorus in silicon.

[1]G. D. Watkins, in *Radiation Effects on Semiconductor Components*, edited by F. Cambon (Journées d'Electronique, Toulouse, 1967), Vol. 1, A1.
[2]L. C. Kimerling, P. Blood, and W. M. Gibson, in *Defects and Radiation Effects in Semiconductors*, edited by J. H. Albany (Inst. of Phys. Conf. Ser. 46, Bristol and London, 1978), p. 273.
[3]L. C. Kimerling, in *Radiation Effects in Semiconductors*, edited by N. B. Urli and J. M. Corbett (Inst. of Phys. Conf. Ser. 31, London, 1977), p. 221.
[4]G. D. Watkins, in *Radiation Damage in Semiconductors*, edited by P. Baruch (Dunod, Paris, 1965), p. 97.
[5]G. D. Watkins, Phys. Rev. B **12**, 5824 (1975).
[6]G. D. Watkins, Phys. Rev. **155**, 802 (1967).
[7]Interstitial nitrogen has been reported but due to its small size and high electronegativity it is regarded as anomalous with respect to other group V impurities; see K. L. Brower, Phys. Rev. B **26**, 6040 (1982).
[8]G. D. Watkins and K. L. Brower, Phys. Rev. Lett. **36**, 1329 (1976).
[9]L. W. Song, B. W. Benson, and G. D. Watkins, Phys. Rev. B **33**, 1452 (1986).
[10]G. L. Miller, D. W. Lang, and L. C. Kimerling, Annu. Rev. Mater. Sci. **7**, 377 (1977).
[11]A. Chantre and L. C. Kimerling, Appl. Phys. Lett. **48**, 1000 (1986).
[12]A. Chantre, J. L. Benton, M. T. Asom, and L. C. Kimerling, in *Defects in Semiconductors*, edited by H. J. von Bardeleben (Trans. Tech., Switzerland, 1986), Vol. 10–12, p. 1111.
[13]J. L. Benton and M. Levinson, in *Defects in Semiconductors II*, edited by S. Mahajan and J. Corbett (North-Holland, New York, 1983), p. 95.
[14]K. D. O'Donnell, K. M. Lee, and G. D. Watkins, Physica (Ultrecht) B **116**, 258 (1983).
[15]In Schottky-barrier samples (SB), $H(0.36)$ is not accessible because there is no means of forward bias injection of holes. In addition, injection levels high enough to saturate $H(0.36)$ with holes are not attainable in samples doped with $P_s > 10^{16}$ cm^{-3}.
[16]R. Sauer, M. T. Asom, J. L. Benton, and L. C. Kimerling (unpublished).
[17]K. Thonke, G. D. Watkins, and R. Sauer, Solid State Commun. **51**, 127 (1984).
[18]G. Davis, E. C. Lightowlers, R. Woolley, R. C. Newman, and A. S. Oates, J. Phys. C **17**, L499 (1984).
[19]K. L. Brower, Phys. Rev. B **9**, 2607 (1974).

Downloaded 26 May 2009 to 146.186.238.18. Redistribution subject to AIP license or copyright; see http://apl.aip.org/apl/copyright.jsp

SIONYX1403000026.0008

SAMSUNG EX. 1002 - 2473/4148

Available online at www.sciencedirect.com
ScienceDirect
Solar Energy Materials & Solar Cells 91 (2007) 1215–1221
Solar Energy Materials and Solar Cells
www.elsevier.com/locate/solmat

Commercial white paint as back surface reflector for thin-film solar cells

Olaf Berger, Daniel Inns, Armin G. Aberle*

Photovoltaics Centre of Excellence, The University of New South Wales, UNSW, Sydney, NSW 2052, Australia

Received 28 March 2007; accepted 3 April 2007
Available online 8 May 2007

Abstract

In this work, commercially available white paint is applied as a pigmented diffuse reflector (PDR) on the rear surface of thin-film crystalline silicon (c-Si) solar cells with a silicon thickness in the 1–2 μm range. We show that white paint increases the short-circuit current density of the solar cells enormously, with a boost of 41% observed for very thin planar solar cells illuminated with the global AM1.5 solar spectrum. We also show that white paint is a better back surface reflector (BSR) than aluminium, air, a transparent conductive oxide (TCO)/aluminium stack, and even a detached aluminium mirror. While previous studies have investigated the influence of PDRs on silicon solar cells with thicknesses of over 27 μm, this work closes the gap that has existed for much thinner cells.
© 2007 Elsevier B.V. All rights reserved.

Keywords: Light trapping; Thin-film solar cell; Pigmented diffuse reflector; Back surface reflector; Silicon solar cells; Paint

1. Introduction

Light trapping is of crucial importance for crystalline silicon (c-Si) thin-film solar cells [1–4]. An important component of any light trapping scheme for thin-film solar cells is an efficient back surface reflector (BSR). An important sub-class of BSRs are pigmented diffuse reflectors (PDRs) [5–7]. Pigmented materials offer several advantages for solar cell applications: First, they are capable of high optical reflectance over a broad wavelength band. Second, they scatter light in a diffuse pattern which is generally beneficial for solar cells because this maximises the fraction of photons that are trapped inside the solar cell due to total internal reflection at both cell surfaces. Finally, pigmented materials have potential for low cost. PDRs have been shown to be effective BSRs on silicon solar cells having thicknesses of over 27 μm [5–7].

An excellent example for a PDR is white paint [7]. In this work, we apply commercially available white paint to the rear surface of less than 2 μm thick c-Si thin-film solar cells on glass and show that this dramatically enhances both the optical absorption and the external quantum efficiency (EQE) of the devices. We also show that additional EQE gains can be obtained by increasing the pigment volume concentration value of the paint. As a test vehicle for the demonstration of the enormous potential of white paint as BSR for thin-film solar cells we use the ALICIA poly-Si thin-film cell [8] presently under development at the University of New South Wales (UNSW).

2. The operating principle of pigmented diffuse reflectors

In this work, white paint is used as a BSR. Most commonly, white paint consists of rutile titanium dioxide pigments dispersed in an oil or latex-based binder ("medium"). Titanium dioxide is non-toxic, chemically stable, light-resistant and abundant. Optical reflection is achieved by random optical Mie scattering of photons by the pigments held in suspension by an optical binder [9], as schematically depicted in Fig. 1.

The Lorenz-Mie theory [10] describes the scattering of electromagnetic radiation by spherical particles. In general, the reflectance of a PDR is highest when the scattering efficiency is highest. According to the Mie theory, three factors improve the scattering efficiency S of a PDR:

- Increasing the value of the ratio of the refractive indices of the pigments and the medium.

*Corresponding author. Tel.: +61 2 9385 4031; fax: +61 2 9385 7762.
E-mail address: a.aberle@unsw.edu.au (A.G. Aberle).

0927-0248/$ - see front matter © 2007 Elsevier B.V. All rights reserved.
doi:10.1016/j.solmat.2007.04.008

SIONYX1403000026.0009

SAMSUNG EX. 1002 - 2474/4148

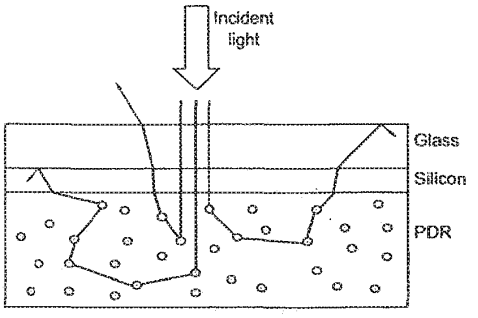


Fig. 1. The operating principle of a pigmented diffuse reflector (PDR) on the rear surface of a thin-film silicon solar cell on glass. A PDR consists of pigments held in suspension by a medium.

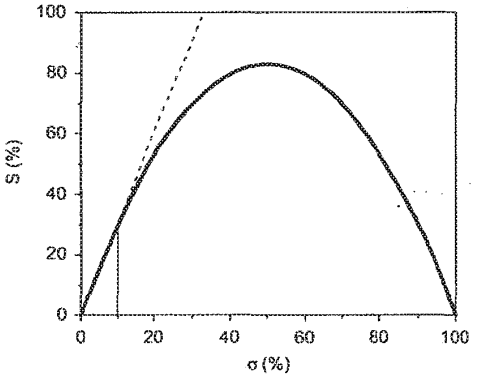


Fig. 2. Schematic representation of the relationship between the scattering efficiency S and the pigment volume concentration σ of a PDR.

- Optimising the pigment diameter.
- Optimising the pigment volume concentration σ.

The dependence of the scattering efficiency S of a PDR as a function of the pigment volume concentration σ is schematically shown in Fig. 2. Up to a σ value of about 10% the scattering efficiency depends approximately linearly on σ, and hence can be described by Beer's law [11]. With further increasing σ value the scattering effect of the pigments in the binder is increasingly reduced because of the smaller distances between the pigment particles, causing multiple scattering events, which hinder reflection. This creates a maximum scattering efficiency at intermediate σ values. In the limiting case of large σ values the roles of pigment and medium become reversed, and the scattering efficiency drops again to zero. Based on the Kubelka–Munk theory [9], an increasing scattering efficiency S in turn leads to a higher internal reflectance of an infinitely thick PDR:

$$R_{\mathrm{int}}^{\infty} = 1 + \frac{K}{S} - \sqrt{\frac{K}{S}\left(\frac{K}{S} + 2\right)}, \tag{1}$$

where K is the PDR's optical absorption coefficient, which shows a linear dependence on the pigment volume concentration σ.

3. Experimental details

3.1. Solar cell structure

The solar cell structure used in this work is termed ALICIA (Aluminium-Induced Crystallisation Ion-Assisted deposition) and is a polycrystalline silicon thin-film solar cell on a glass superstrate [8,12]. The term 'superstrate' indicates that the sunlight enters the solar cell through the glass. An overview on the fabrication and characterisation methods of c-Si thin-film solar cells is given in Ref. [13]. The silicon film of ALICIA cells typically has a thickness in the 1–2 μm range. The cells are made by electron-beam vacuum evaporation of silicon onto a thin large-grained doped poly-Si seed layer, using an epitaxial low-temperature Si deposition process called ion-assisted deposition (IAD) [13]. The poly-Si seed layer is made by aluminium-induced crystallisation (AIC) of amorphous silicon [14] and is p^+-type due to the presence of Al atoms. ALICIA solar cells are made on a commercially available borosilicate float glass (Borofloat33 from Schott AG, Germany [15]), which additionally can be textured on the silicon-facing side. The texture is realised with the UNSW-developed aluminium-induced texture (AIT) method [16]. Then a 70–80 nm thick silicon nitride (SiN) film is deposited onto the textured surface of the glass sheet by plasma-enhanced chemical vapour deposition (PECVD). After the creation of the large-grained, p^+-type poly-Si seed layer with the AIC method, the desired diode structure is epitaxially grown at high rate (~300 nm/min) onto the seed layer by IAD at about 600 °C. During the IAD process dopant atoms are co-evaporated using effusion cells ("Knudsen cells") for gallium and phosphorus, giving the desired solar cell structure of glass/SiN/p^+nn^+. The lightly n doped absorber layer ("base") is typically 1–2 μm thick, whereas the thicknesses of the heavily doped layers ("emitter" and "back surface field") are usually kept below 200 nm to minimise optical absorption in these low-lifetime layers. Fig. 3 schematically shows a Mesa-type ALICIA solar cell structure as used in the present work. The experiments reported in this paper were performed on the following three rectangular Mesa-type ALICIA solar cells:

- Sample P1.0: A planar cell with a silicon thickness of 1.0 μm and an area of 1.5 cm^2.
- Sample P1.6: A planar cell with a silicon thickness of 1.6 μm and an area of 0.7 cm^2.
- Sample T1.6: A textured cell with a silicon thickness of 1.6 μm and an area of 0.7 cm^2.

SIONYX1403000026.0010

SAMSUNG EX. 1002 - 2475/4148

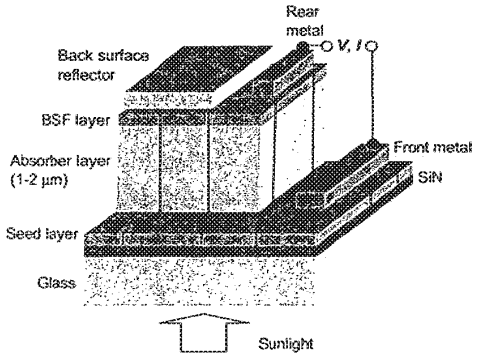


Fig. 3. Schematic view of a Mesa-type ALICIA polycrystalline silicon thin-film solar cell on glass as used in the present work. The sunlight enters the solar cell through the glass. The p–n junction is at the interface between the p^+-type seed layer and the n-type absorber layer. Note that the drawing is not to scale with respect to grain size and layer thicknesses.

3.2. Measurement methods

Light trapping in ALICIA cells is experimentally investigated by a double-beam spectrophotometer (hemispherical reflectance R and transmittance T) and spectral response measurements (SR, in A/W), covering the wavelength range 300–1200 nm. The optical absorption A of the solar cells is

$$A(\lambda) = 1 - R(\lambda) - T(\lambda), \tag{2}$$

where λ is the wavelength (in m). The external quantum efficiency EQE of a solar cell is defined as

$$\mathrm{EQE}(\lambda) = \frac{1}{q} \times \frac{hc}{\lambda} \times \mathrm{SR}(\lambda), \tag{3}$$

where q is the electrical charge of an electron (in C), h is Planck's constant (in Js) and c is the speed of light in vacuum (in m/s). From the EQE curve the short-circuit current density J_{SC} (in A/cm^2) of the cell can be calculated via

$$J_{SC} = q \times \int_0^{\infty} \frac{P_{beam}(\lambda)}{E_{photon}(\lambda)} \times \mathrm{EQE}(\lambda)\,\mathrm{d}\lambda, \tag{4}$$

where $P_{beam}(\lambda)$ is the wavelength-dependent incident optical power density (in W/cm^2) of the AM1.5 G spectrum and $E_{photon}(\lambda)$ is the corresponding photon energy (in J).

4. Results

4.1. White paint as a back surface reflector

An 80 μm thick layer of matt white outdoor spray paint was applied to the rear surface of samples P1.6 and T1.6. Then the transmission T and reflectance R of the samples were measured and the optical absorption calculated according to Eq. (2). The results are plotted in Fig. 4. As can be seen the white paint enormously improves the absorption over a large part of the spectrum, confirming

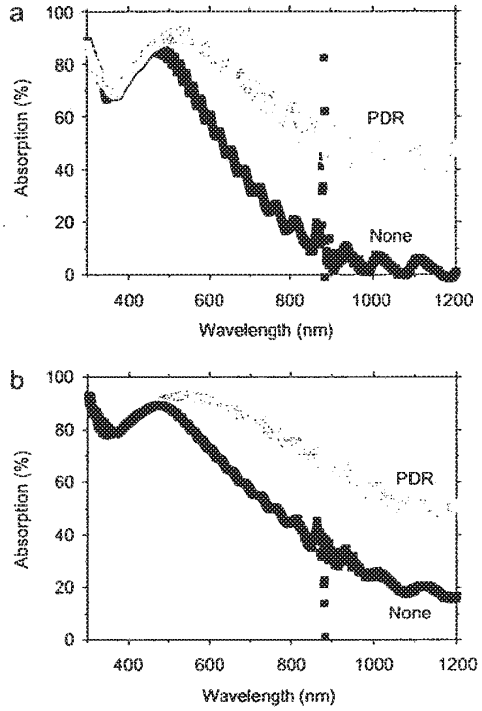


Fig. 4. Measured absorption of (a) sample P1.6 and (b) sample T1.6 with and without a 80 μm thick layer of matt white paint on the back surface. The discontinuities at about 880 nm are due to the change of the detector in the spectrophotometer at this wavelength.

that it acts as an efficient BSR on silicon. Due to the pigments in the paint, many of the photons reaching the BSR are diffusively scattered back into the silicon. This enhances the fraction of photons that undergo total internal reflection at the solar cell surfaces, and thus increases the optical pathlength for weakly absorbed light. For example, at a wavelength of 900 nm in Fig. 4, the paint layer improves the optical absorption A of sample P1.6 by a factor of about 8 and of sample T1.6 by a factor of about 2. The smaller benefit of the paint layer for the textured sample is due to the fact that the textured glass surface already provides significant scattering of the light when it enters the silicon. In this situation, the air at the back surface of the cell provides a good BSR due to total internal reflection of a large fraction of the scattered light reaching that interface. These absorption measurements can be integrated with the AM1.5 G spectrum to get an absorption-limited current. For this, we exclude photons with an energy below the Si bandgap ($\lambda > 1120$ nm) and assume that each absorbed photon creates one electron–hole pair (i.e. no parasitic absorption). The calculations show that the addition of the PDR to the rear surface of the planar cell almost doubles this current limit from 16.2 to 29.3 mA/cm^2. On the textured device, the corresponding change is 23.3 to 33.3 mA/cm^2, a substantial increase of 40%.

SIONYX1403000026.0011

SAMSUNG EX. 1002 - 2476/4148

4.2. The influence of the paint layer thickness

To determine the influence of the paint layer thickness, an approximately 10 μm thick layer of glossy white outdoor paint (5 Star spray-paint, Stalyce Holdings Aust Pty Ltd) was sprayed onto the rear surface of samples P1.0 and T1.6, followed by the measurement of the EQE of the solar cells. This procedure was repeated until the short-circuit current value determined from the EQE curve approached a saturation effect. The measured J_{sc} data points are plotted in Fig. 5 as a function of the total paint layer thickness. As can be seen, the planar sample requires a total paint thickness of about 160 μm to approach a saturation effect, whereas the corresponding paint thickness is only about 50 μm for the textured ALICIA sample. For the planar sample (Si thickness 1.0 μm), the optimal paint layer thickness of 160 μm increased the J_{sc} by about 37%. For the textured sample (Si thickness = 1.6 μm), the optimal paint layer thickness of 50 μm increased the J_{sc} by about 12%. The reason for the smaller benefit of the paint layer for the textured sample compared to the planar sample has already been given in Section 4.1.

4.3. Comparison of specular and diffuse reflectors

To gain additional insight into the performance of white paint compared to other potential BSRs, five different BSRs (see Table 1) were sequentially applied to the rear surface of samples P1.6 and T1.6. After formation of a particular BSR, the EQE curve was measured, the BSR then removed (for example by etching in phosphoric acid in the case of the Al reflector), followed by the formation of the next BSR. The J_{sc} values obtained from the EQE measurements are listed in Table 1, while Fig. 6 shows the measured EQE curves before and after application of white paint as a PDR.

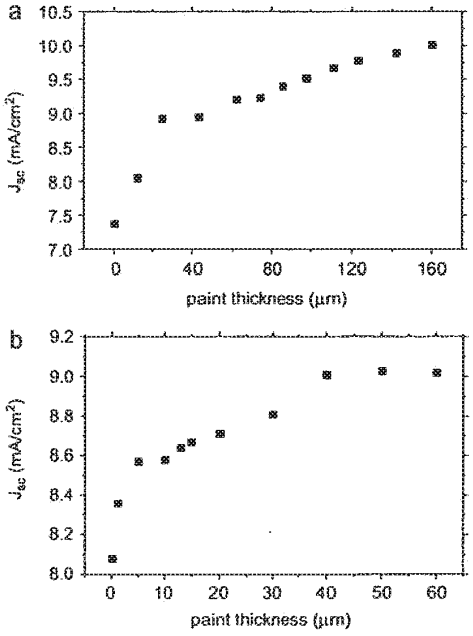


Fig. 5. The influence of the paint thickness on the short-circuit current density J_{sc} of (a) sample P1.0 and (b) sample T1.6.

A number of interesting conclusions can be drawn from Table 1. First, aluminium is a worse BSR than air, both for the planar sample (−2%) and, particularly, for the textured sample (−12%). This shows that significant optical absorption is occurring in evaporated Al films and hence they are relatively bad BSRs. The reason why Al is particularly bad on a textured rear surface is the multiple-bounce effect caused by the texture, increasing parasitic absorption in the Al whenever a ray of light undergoes a multiple-bounce at the rear surface of the solar cell. Considering that a planar silicon sample with an air BSR has a rear reflectance of about 30%, the reflectance of our planar Si–Al interface is also close to this value.

A thin layer of a transparent conductive oxide (TCO) covered by a metal film is a relatively good BSR [17]. The TCO layer listed in Table 1 is a 700 nm thick, Al-doped zinc oxide film with a refractive index of 1.90 at 633 nm, and it is coated with a 500 nm thick evaporated aluminium film. As can be seen, this BSR provides a J_{sc} boost of about 3% on the textured sample and about 12% on the planar sample. The fabrication details of this TCO layer are described in Ref. [18]. The dielectric separation between the aluminium film and the silicon surface allows reflection at the Si–TCO interface, while the aluminium film reflects some of the light which passes through the TCO, giving these photons another chance for absorption in the silicon film. The reflection at the Si–TCO interface is the reason why this BSR performs better than the standard Al BSR.

The TCO has a finite absorption and a refractive index greater than 1, so is not as ideal a dielectric separation as air. This explains why a detached Al mirror (i.e. a silicon-air-aluminium configuration) performs slightly better than the TCO/Al reflector. For a 0.5 mm wide air gap between

Table 1
J_{sc} values (AM1.5G, 100 mW/cm^2, room temperature) of ALICIA solar cells P1.6 and T1.6 with different back surface reflectors, as obtained from external quantum efficiency measurements. Silicon thickness is 1.6 μm in both solar cells

Back surface reflector	J_{sc} of planar sample P1.6		J_{sc} of textured sample T1.6	
	(mA/cm^2)	(%)	(mA/cm^2)	(%)
Aluminium	6.90	98	7.78	88
Air	7.01	100	8.81	100
TCO/Al	7.85	112	9.02	103
Detached Al mirror	7.93	113	9.23	105
Glossy white paint (σ~5%, thickness 80 μm)	8.31	119	10.00	114

SIONYX1403000026.0012

SAMSUNG EX. 1002 - 2477/4148

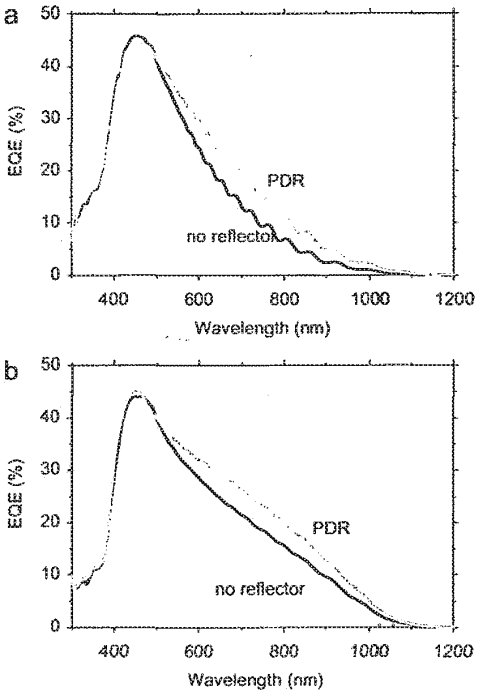


Fig. 6. EQE of (a) sample P1.6 and (b) T1.6, with and without white paint as a pigmented diffuse reflector (PDR). "No reflector" refers to the case where the rear silicon surface faces air.

the Si surface and a thick Al film (> 500 nm), we found a J_{sc} boost of 5% (textured sample) and 13% (planar sample) compared to the air BSR.

Also shown in Table 1 is a BSR that uses white glossy paint as PDR, with a pigment volume concentration of about 5%. The J_{sc} boost provided by this PDR is about 14% for the textured cell and about 19% for the planar cell. This shows that paint outperforms all other BSRs investigated in this study, and particularly so for textured samples. The low refractive index of the paint satisfies the conditions for total internal reflection for scattered light, and most light which is transmitted out of the silicon will be returned in a somewhat diffuse manner by the PDR. This added scatter is the reason why the paint outperforms all of the other dielectric reflectors, including the detached mirror. A metal backing was added to this paint layer and did not influence the J_{sc} at all, showing that the layer can be assumed to be "infinitely" thick on these cells.

5. The influence of thickness and diffusion length of the absorber layer

In addition to the absorber layer ("base") thickness, the current gain provided by the BSR also depends on the ratio of the minority-carrier diffusion length in the base to the base thickness. Using the solar cell simulation program PC1D [19], the influence of the base diffusion length, the base thickness and the light trapping properties on the thin-film solar cell's short-circuit current have been determined. The simulated thin-film solar cell structure consists of a 1 mm thick planar glass superstrate with a refractive index of 1.50 and a 65 nm thick SiN layer with a refractive index of 2.30 on the Si-facing side of the glass. The SiN-coated glass acts as a good antireflection coating for a silicon solar cell. The silicon thin-film solar cell consists of a 40 nm thick p^+ emitter ($2 \times 10^{19}\,cm^{-3}$) on the SiN, followed by an n-type ($1 \times 10^{16}\,cm^{-3}$) absorber layer with variable thickness and a 40 nm thick n^+ BSF layer ($2 \times 10^{19}\,cm^{-3}$). In order to model light trapping effects, the specular internal reflectance at the front and rear surface of the silicon film can be adjusted. For a planar device with air as the BSR, the internal reflectance at the rear of the Si film was set to 33%, while the front internal reflectance was set to 10%. For a planar device with a PDR, the internal reflectance at the rear was set to 75%, while at the front surface it was set to 60%. This is reasonable as the PDR returns light to the cell in a scattered pattern, enhancing total internal reflection at both the front and rear surface of the silicon film and thereby providing efficient light trapping. The relative current gain from the use of a PDR as BSR is then given by

$$J_{sc,gain}(\%) = 100 \times [(J_{sc,PDR}/J_{sc,air}) - 1]. \quad (5)$$

This current gain due to a PDR on a planar cell was calculated with PC1D for a range of base diffusion lengths and base layer thicknesses. The results are summarised in Fig. 7 as a function of the ratio L_n/W of base diffusion length and base layer thickness. It can be seen that, for a given value of the base diffusion length, the thinner the base, the larger the current gains from the application of a PDR.

For the investigated ALICIA cells, PC1D determines a base diffusion length L_n of about 0.5 μm from fitting the measured EQE curves (such as those of Fig. 6). Hence, the L_n/W ratio of the solar cells of Table 1 (base thickness ~1.4 μm) is about 0.35. From Fig. 7 it follows that the PC1D model predicts a current gain of about 20%, which agrees well with the experimental result for the planar cell of Table 1.

According to Fig. 7, for a given base diffusion length, higher J_{sc} gains can be obtained from a PDR if the base thickness is reduced. The thin-base ALICIA cell P1.0 (i.e. base thickness of about 0.75 μm, L_n/W ratio of about 0.7) is well suited to test this model prediction. As shown in Fig. 5(a), application of a thick (~150 μm) glossy white outdoor paint layer provides an experimental J_{sc} gain of 37%, which agrees well with the model predictions of Fig. 7. In an effort to further boost this current gain, the experiment was repeated with an improved version of a commercial white acrylic indoor paint (DULUX® one coat ceiling paint). By adding TiO_2 particles (diameter ~200 nm) to this paint, its σ value was increased from 9.5% to about 20%.

SIONYX1403000026.0013

SAMSUNG EX. 1002 - 2478/4148

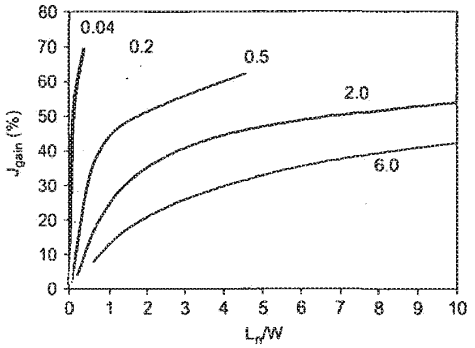


Fig. 7. PC1D-calculated short-circuit current gain from adding a PDR with an internal reflectance of 75% onto the rear surface of a planar silicon thin-film solar cell, as a function of the ratio of base diffusion length L_n and base layer thickness W. The current gain shown is relative to the baseline case of air as the BSR. The parameter shown next to each curve is the corresponding fixed base diffusion length (in microns). The internal front reflectance is 60% for all curves.

Table 2
Measured 1-Sun J_{sc} values of ALICIA samples P1.0 and T1.6 without and with an approximately 600 μm thick pigmented diffuse reflector (with $\sigma = 20\%$) on the back surface. The Ln/W ratio of the planar cell is about 0.7 and that of the textured cell about 0.35

Back surface reflector	J_{sc} of planar sample (1.0 μm)		J_{sc} of textured sample (1.6 μm)	
	(mA/cm^2)	(%)	(mA/cm^2)	(%)
Air	7.04	100	5.91	100
PDR (~600 μm, $\sigma = 20\%$)	9.91	141	7.07	120

According to Fig. 2, this should lead to a significant increase of the scattering efficiency and hence an improved reflectance of the PDR (see Eq. (1)). For comparison, the same improved paint was also applied to the rear surface of a textured cell with thicker base (T1.6). Paint thickness was about 600 μm on both solar cells. From the measured EQE curves, the short-circuit currents shown in Table 2 have been determined. The experimentally obtained gain in J_{sc} is now 41% for the planar cell, well above the 19% result achieved with the thicker-base planar cell (see Table 1) and also higher than the 37% result obtained with the non-optimised paint. This experimental result confirms that the increased pigment volume concentration (20% vs. 9.5%) is indeed very beneficial for the paint's reflectance.

6. Conclusions

In this work, commercially available white paint has been applied as a PDR to the rear surface of thin-film polycrystalline silicon solar cells with a silicon thickness of less than 2 μm. We have shown that white paint increases the short-circuit current density J_{sc} of the solar cells enormously, with a boost of 41% observed for very thin (1.0 μm) planar solar cells illuminated with the AM1.5G solar spectrum. On 1.6 μm thick solar cells made on textured glass, the corresponding J_{sc} gain due to the white paint was still as high as 20%. An optical model has been presented that calculates the short-circuit current gain provided by a PDR as a function of the base layer thickness, the diffusion length in the base layer and the solar cell's light trapping properties. Good agreement between the model's predictions and experimental results has been found. While all commercial paints investigated in this study performed well as PDR, the best current gains were observed when the pigment volume concentration of the paints was increased significantly (by a factor of about 2) by adding TiO_2 particles. We have also shown experimentally that white paint is a better BSR than aluminium, air, a TCO/Al stack and even a detached mirror. White paint is inexpensive and it offers the potential to be optimised. This work proves that pigmented materials are an excellent option for light trapping in thin-film c-Si solar cells with a silicon film thickness of less than 2 μm. Since the studies of Cotter et al. [5,6] and Shaw [7] investigated the influence of PDRs on silicon solar cells with thicknesses of over 27 μm, this work closes the gap that has existed for much thinner cells.

Acknowledgements

This work was supported by the Australian Research Council (ARC) via its Centres of Excellence scheme. The help of various staff at UNSW's School of Photovoltaic and Renewable Energy Engineering is also acknowledged, particularly Oliver Kunz.

References

[1] R. Brendel, R.B. Bergmann, P. Lölgen, M. Wolf, J.H. Werner, Appl. Phys. Lett. 70 (1997) 390.
[2] D. Thorp, P. Campbell, S.R. Wenham, Progr. Photovoltaics 4 (1996) 205.
[3] P. Campbell, M.A. Green, Appl. Phys. 62 (1987) 243.
[4] P.A. Basore, Simplified processing and improved efficiency of crystalline silicon on glass modules, in: Conference Record 19th European Photovoltaic Solar Energy Conference, Paris, pp. 455–458 (WIP, Munich, 2004), 2004
[5] J.E. Cotter, Pigmented materials for light trapping in thin-film polycrystalline silicon solar cells, Ph.D. Thesis, University of Delaware, USA, 1996.
[6] J.E. Cotter, R.B. Hall, M.G. Mauk, A.M. Barnett, Progr. Photovoltaics 7 (1999) 261.
[7] N. Shaw, Increasing light generated current in thin-film silicon solar cells using pigmented diffuse reflectors and static optical concentrators, Ph.D. Thesis, The University of New South Wales, Sydney, Australia, 2003.
[8] A.G. Aberle, A. Straub, P.J. Widenborg, A.B. Sproul, Y. Huang, P. Campbell, Progr. Photovoltaics 13 (2005) 37–47.
[9] H. Völz, Industrial Color Testing: Fundamentals and Techniques, Second ed., Wiley-VCH, Weinheim, 2001.
[10] G. Mie, Ann. Phys. 25 (3) (1908) 377.
[11] G. Smestad, Optoelectronics of Solar Cells, SPIE, Bellingham, 2002.

SIONYX1403000026.0014

SAMSUNG EX. 1002 - 2479/4148

[12] A.G. Aberle, J. Cryst. Growth 287 (2006) 386.
[13] A.G. Aberle, Thin Solid Films 511–512 (2006) 26–34.
[14] O. Nast, S. Brehme, D.H. Neuhaus, S. Wenham, IEEE Trans. Electron Devices 46 (1999) 2062.
[15] Schott AG, Germany, 2007, http://www.schott.com/german/.
[16] N. Chuangsuwanich, P.I. Widenborg, P. Campbell, and A.G. Aberle, "Light trapping properties of thin silicon films on AIT-textured glass," Tech. Digest, in: 14th International Photovoltaic Science and Engineering Conference, Bangkok, 2004, pp. 325–326.
[17] J. Springer, A. Poruba, L. Mullerova, M. Vanecek, O. Kulth, B. Rech, Appl. Phys. 95 (2004) 1427.
[18] D. Song, P. Widenborg, W. Chin, A.G. Aberle, Sol. Energy Mater. Sol. Cells 73 (2002) 1–20.
[19] P.A. Basore, IEEE Trans. Electron Devices 37 (1990) 337.

SIONYX1403000026.0015

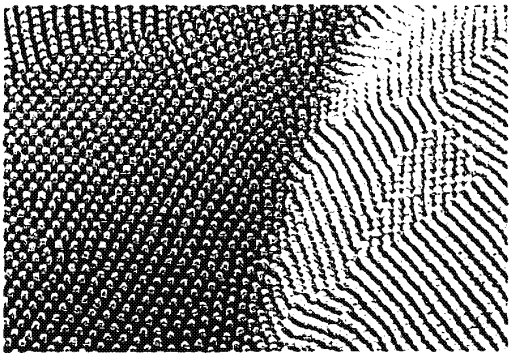
SAMSUNG EX. 1002 - 2480/4148

Moth eyes inspire self-cleaning antireflection nanotechnology coatings

(*Nanowerk Spotlight*) Antireflection coatings have become one of the key issues for mass production of silicon solar cells. Silicon solar cells are the most common solar cells on the market today. They are constructed with layers of n-type silicon having many electrons and p-type silicon having many electron holes (portions with missing electrons). When hit by sunlight, an equal number of electrons and electron holes are generated at the interface between the two silicon layers and, as the electrons migrate from the n-type silicon to the p-type silicon, an electric flow is generated.

One of the problems with silicon solar cells is the high refractive index of silicon, which causes more than 30% of incident light to be reflected back from the surface of the silicon crystals. Solar cell manufacturers have therefore developed various kinds of antireflection coatings (ARCs) to reduce the unwanted reflective losses. Currently, quarter-wavelength silicon nitride thin films deposited by plasma-enhanced chemical vapor deposition (PECVD) are the industrial standard for ARCs on crystalline silicon substrates. Unfortunately, current top-down lithographic techniques for creating subwavelength silicon gratings, such as electron-beam lithography, nanoimprint lithography, and interference lithography, require sophisticated equipment and are expensive to implement, thus contributing to the still high costs of this type of solar cells.

Borrowing from Mother Nature's millions of years old design book, researchers have now come up with a nanotechnology antireflection coating inspired by the eyes of moths.



Details of the moth eye structure.

"We have developed a simple and scalable spin-coating technique that enables wafer-scale production of colloidal crystals with nonclose-packed (ncp) structures" Wei-Lun Min tells Nanowerk.

Min, a student in Peng Jiang's group in the Department of Chemical Engineering at the University of Florida, is first author of a recent paper in *Advanced Materials* that

SAMSUNG EX. 1002 - 2481/4148

describes this new coating technique ("Bioinspired Self-Cleaning Antireflection Coatings").

Min explains that commercial silicon nitride ARCs are typically designed to suppress reflection efficiently at wavelengths around 600 nm. "The reflective loss is rapidly increased for near-infrared and other visible wavelengths, which contain a large portion of the incident solar energy" he says. "In contrast, our subwavelength-structured moth-eye ARCs directly patterned in the substrates are broadband and intrinsically more stable and durable than multilayer ARCs since no foreign material is involved."

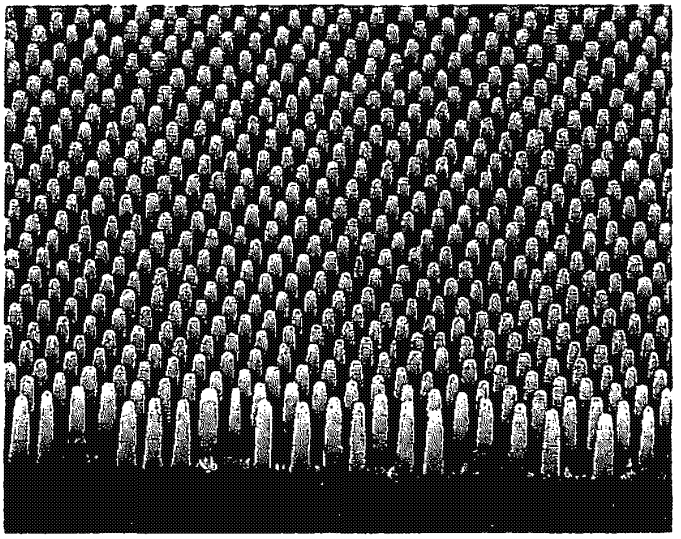
The team in Florida has developed a simple and scalable templating technique for making subwavelength ARCs. Knowing that moths use hexagonal arrays of nonclose-packed nipples as antireflection coatings to reduce reflectivity from their compound eyes, they designed a colloidal templating approach for fabricating such moth-eye ARCs on both glass and silicon substrates.

"The outer surface of the corneal lenses of moths consists of ncp arrays of conical protuberances, termed corneal nipples, typically of sub-300nm height and spacing" explains Min. "These arrays of subwavelength nipples generate a graded transition of refractive index, leading to minimized reflection over a broad range of wavelengths and angles of incidence."

In similar fashion, the templated pillar arrays that the researchers designed have a high aspect ratio and exhibit excellent broadband antireflection and nonwetting properties.

The team points out that transparent polymer moth-eye ARCs with good antireflective properties has been demonstrated before but, in contrast to their own ARC, the low aspect ratio (ca. 0.5) of the previously templated nipples had hampered the realization of superhydrophobic coatings.

In their approach, Min and his colleagues used a simple and scalable spin-coating technique to generate ncp colloidal monolayers of hexagonally ordered silica particles on silicon wafers. These particles are then used as etching mask during a reactive ion etch (RIE).



Templated silicon pillar arrays. (Image: Wei-Lun Min, University of Florida)

"As the etching rate of silica is much lower than that of silicon under RIE conditions, silica particles protect silicon immediately underneath them from being etched, resulting in the formation of pillar arrays directly on silicon surface" Min explains the process.

Once the silicon pillars are deep enough, the process is stopped by removing the templating silica spheres with a solution.

Min points out that their technique can be easily utilized to generate wafer-scale silicon pillar arrays, is compatible with standard industrial manufacturing and is promising for developing self-cleaning ARCs for a large variety of technological applications ranging from solar cells and photodiodes to flat panel displays and optical components.

By Michael Berger. Copyright 2008 Nanowerk LLC

SAMSUNG EX. 1002 - 2483/4148

Nuclear Instruments and Methods in Physics Research A 395 (1997) 344–348

ELSEVIER

NUCLEAR INSTRUMENTS & METHODS IN PHYSICS RESEARCH Section A

Si-PIN X-ray detector technology

G.F. Dalla Betta[a], G.U. Pignatel[a,*], G. Verzellesi[a], M. Boscardin[b]

[a] *Dipartimento di Ingegneria dei Materiali, Università di Trento, I-38050 Mesiano (TN), Italy*
[b] *IRST-Microelectronics, 38050 Povo (TN), Italy*

Abstract

PIN diodes and other test structures have been fabricated on both n- and p-type, high-resistivity, Floating-Zone (FZ) silicon substrates. Different alternative extrinsic-gettering techniques have been adopted to the purpose of meeting the required specification of a detector leakage current density lower than 1 nA/cm^2. Phosphorus-doped polysilicon gettering provided the best results on n-type Si with a leakage current density lower than 0.2 nA/cm^2 at 100 μm depletion width. On the contrary, devices made on p-type substrates exhibited a leakage current density two orders of magnitude higher. A proper control of the oxide charge at the silicon–silicon dioxide interface was found to be crucial in obtaining a predictable behavior of PIN diode detectors. Some degradation of the reverse leakage current has been observed after device dicing and bonding.

1. Introduction

The aim of this work was to test the technology presently available at the Institute for Scientific and Technological Research (IRST) in Trento, Italy, for the fabrication of PIN radiation detectors suitable for high-energy physics experiments and X-ray spectroscopy. These devices are typically operated under reverse bias conditions in a fully depleted mode, so that they have to sustain a relatively high voltage (about 140 V for 300 μm thick, 2 kΩ cm, n-type substrates) while maintaining a low reverse leakage current density (less than 1 nA/cm^2 at room temperature). Leakage current is the parameter that mainly determines the detector noise, which, in turn, limits the energy resolution. However, it must be stressed that the total noise of the detection system strongly depends also on stray capacitances as well as on impedance matching of the detector with the input device of the preamplifier [1]. This is particularly true for low-capacitance detectors, such as silicon drift chambers and pixel detectors. In this respect, monolithic integration of the detector with the front-end electronics can result in a considerable performance enhancement, reducing parasitic capacitances associated with the detector–preamplifier connection.

The main problem associated with the manufacturing of radiation detectors is the degradation of the carrier lifetime of the high-quality starting material that may occur during the fabrication process due to contamination or defect activation. Moreover, a careful control of oxide charges and surface leakage current (which can be of the same order of the bulk thermally-generated current) is necessary. Finally, a good long-term stability of the detector performance in ambient atmosphere and under irradiation is an important issue.

In the past, two different technological approaches have been proposed, which are able to meet the desired specifications. The first one, developed by Kemmer [2], relies on a very low thermal budget experienced by the detector (maximum annealing temperature of 700°C) after an initial oxidation at 1050°C with HCl. The second, proposed by Holland [3], is based on the use of extrinsic gettering techniques to maintain the carrier lifetime in the range of milliseconds even after relatively high-temperature processing. While the first approach results in ad hoc processes, the second one allows more standard fabrication procedures to be adopted, as demonstrated by the realization of PMOS- and CMOS-compatible detectors [3,4]. We embraced this latter approach, the final goal of our work being the development of a technology suitable for integration of detectors and read-out electronics.

In this paper, after a brief description of the adopted fabrication process, we report on preliminary results obtained from PIN diodes and other test structures fabricated on both n-type and p-type Floating Zone (FZ) silicon substrates.

* Corresponding author. Tel.: +39 461 88 2451; fax: +39 461 88 1977; e-mail: giorgio.pignatel@ing.unitn.it.

0168-9002/97/$17.00 Copyright © 1997 Elsevier Science B.V. All rights reserved
PII S0168-9002(97)00612-8

SIONYX1403000026.0019

SAMSUNG EX. 1002 - 2484/4148

2. Process outline

As p-type substrates, we used 500 μm thick, 4 in diameter, 5 kΩ cm resistivity, boron doped, (1 0 0) silicon wafers. As n-type substrates, we employed 280 μm thick, 4 in diameter, 2 kΩ cm resistivity, phosphorus doped, (1 1 1) silicon wafers. The basic process sequence was the following: after an initial oxidation at 975°C in dry O_2, the heavily-doped front-side regions were formed by ion implantation through a 45 nm thick initial oxide, using photoresist as a mask. Then, having protected the front side with a low-temperature deposited oxide (600 nm, 430°C), the back side was uniformly doped by ion implantation at a dose of 4×10^{15} cm^{-2} to ensure a good ohmic contact, while providing the first type of gettering. The post-implant annealing, necessary to recover the implant damage and to electrically activate the implanted species, was carried out at two different temperatures, namely, 700 and 850°C. Finally, contact opening followed by Al–Si(1%) metal deposition, patterning and sintering, completed the process sequence.

In case of n-type silicon substrates, two alternative backside gettering techniques were adopted: one consists of $POCl_3$ doping followed by segregation annealing [5], the second exploits a polysilicon layer doped by using the same $POCl_3$ source. For p-type substrates, polysilicon deposition followed by p^+ boron implantation was adopted as an alternative to simple boron implantation, while a channel stop BF_2 implant (60 keV, 1×10^{12} cm^{-2}) through the oxide was added on the front side to avoid surface inversion.

The basic process flow is illustrated in Fig. 1 with reference to an n-type substrate and to the backside P implant as gettering technique.

3. Results

Fig. 2 shows a schematic cross section of a detector realized on an n-type substrate. The front side of the detector was patterned to form circular guard rings around a central diode having an active area of 1.8 mm^2. Only the innermost and outermost guard rings were provided with a contact metallisation. The intermediate floating rings have the purpose of evenly distributing the potential drop from the center to the border of the device, when a reverse voltage is applied to the diode with respect to the substrate. The gap between adjacent rings is 50 μm. The width of the innermost guard ring is 600 μm, while that of the floating rings is 100 μm. The complementary PIN diode has the same geometry, except that p^+ and n^+ doped regions are interchanged.

Fig. 3 shows the leakage current versus reverse voltage characteristics of diodes fabricated on both n- and p-type substrates. During measurements, the innermost guard ring was biased at the same potential of the central diode, while the external guard ring was kept at the same potential of the

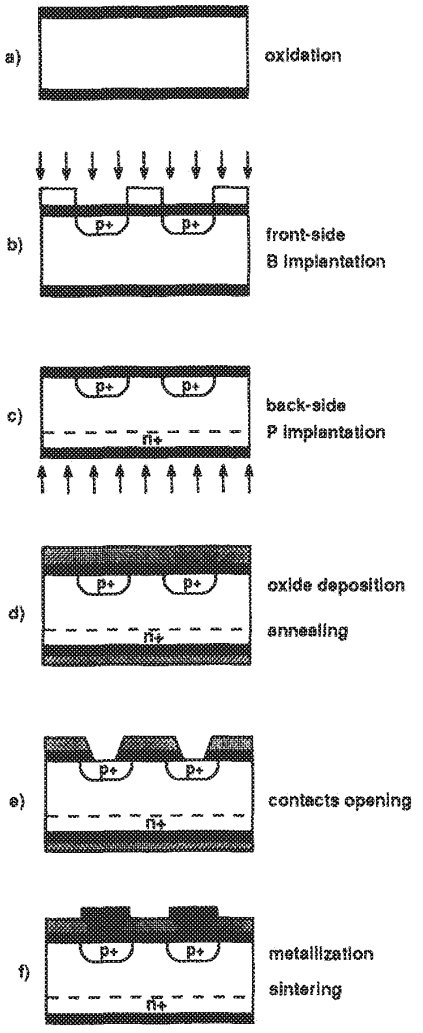


Fig. 1. Flow chart of the fabrication process for an n-type substrate with backside P implant as gettering technique.

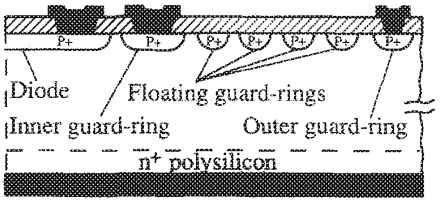


Fig. 2. Schematic cross-section (half device) of a PIN detector on n-type substrate.

SIONYX1403000026.0020

SAMSUNG EX. 1002 - 2485/4148

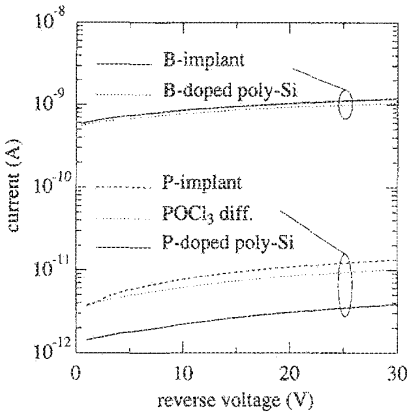


Fig. 3. Reverse I–V characteristics of PIN detectors fabricated on both n-type and p-type substrates with different extrinsic gettering techniques. Diode area of 1.8 mm^2.

backside contact. In Figs. 4(a) and (b) the statistical data – average and standard deviation – of the leakage current density, measured at a reverse voltage of 20 V (corresponding to a depletion width of about 100 μm), are reported. As can be seen, the required specification of less than 1 nA/cm^2 was met on all the diodes on n-type substrate, but not on those built on p-type wafers. In particular, we found that phosphorus-doped polysilicon gettering was the technique that gave the best results on n-type substrates, while about two order of magnitude higher leakage currents were observed in devices on p-type wafers. A difference of only 50% was found between samples annealed at low (700°C) temperature and those annealed at medium (850°C) temperature, in favour, as expected, of low-temperature annealing [6]. Data reported in Fig. 4 also give an indication of the fairly good uniformity and reproducibility of the fabrication processes.

While PIN diodes allow for a direct measurement of the detector leakage current, other test structures can be used to monitor important parameters which characterize the technology. For instance, gated diodes are suitable for extracting surface generation velocity. C–V measurements on Metal-Oxide-Semiconductor (MOS) capacitors enable the density of both oxide fixed charge and interface states to be evaluated. Threshold voltages of MOS transistors are strictly related to substrate doping concentration, oxide thickness and interface charge. All these structures were realized on the same wafer together with PIN diodes, and some results have been reported in Ref. [7]. Here, we present the output characteristics of n-channel MOS transistors realized on p-type substrates and, for comparison, of p-channel MOS transistors realized on n-type substrates. Figs. 5(a) and (b) show that the threshold voltage of p-MOSFETs is about −15 V, while that characterizing n-MOSFETs is about zero. This remarkable difference is primarily due to the fact

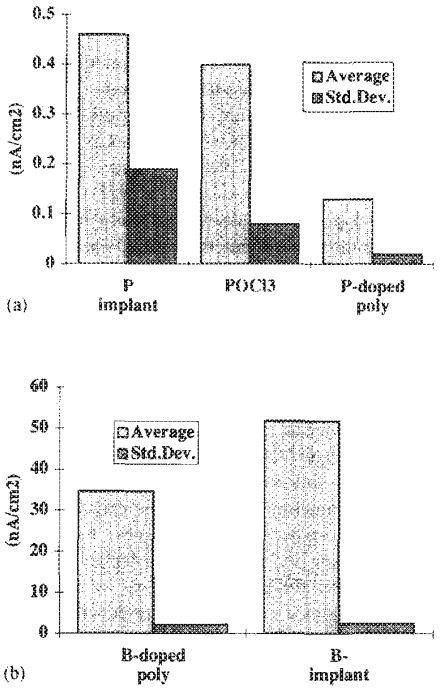


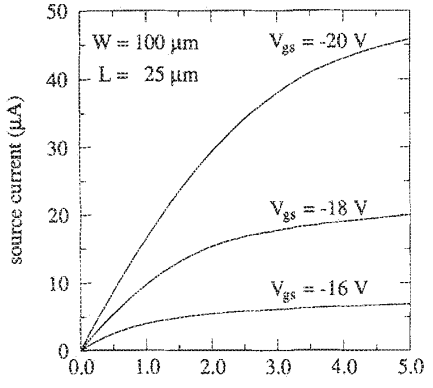
Fig. 4. Average value and standard deviation of leakage current density measured on a statistical sample of 10 dies/wafer and 2 wafers/type, at a reverse voltage corresponding to a 100 μm depletion width. (a) n-type Si substrate; (b) p-type Si substrate.

that p-MOSFETs have a 645 nm thick gate insulator, while n-MOSFETs have a 45 nm thick, thermally grown gate oxide. Therefore, p-MOSFETs exhibit a much lower gate capacitance with respect to n-MOSFETs, due to the higher oxide thickness. Moreover, p-MOSFETs are characterised by a greater oxide-charge density (about 4×10^{11} cm^{-2}), due to the (1 1 1) orientation of n-type substrates (whereas n-MOSFETs are built on (1 0 0) p-type wafers).

These and other results have pointed out the importance of controlling oxide charges for the fabrication of detectors with a predictable behavior. Computer simulations have shown that an oxide-charge density of 4×10^{11} cm^{-2} is large enough to prevent surface inversion between adjacent p^+ regions on n-type substrate [7], thus providing isolation between diode and guard rings and making the implementation of channel-stop implants unnecessary. Another effect of oxide charge is that the surface electric potential does not distribute gradually between the innermost guard ring (which is biased at the same potential of the central diode) and the outermost guard ring (kept at the same potential of the substrate). As a result, avalanche breakdown is more likely to occur at the surface region close to the innermost biased guard ring [8].

SIONYX1403000026.0021

SAMSUNG EX. 1002 - 2486/4148



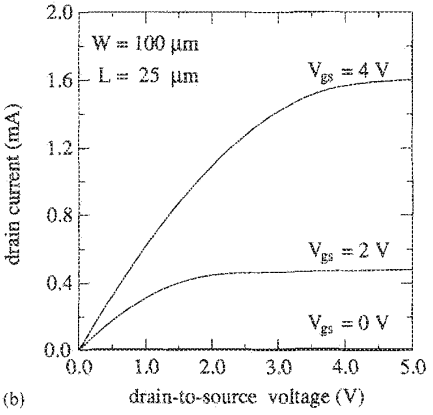


Fig. 5. Output characteristics of a p-channel and an n-channel MOS Field Effect Transistor. (a) p-MOSFET: $t_{ox} = 645$ nm, $V_{th} \simeq -15$ V; (b) n-MOSFET: $t_{ox} = 45$ nm, $V_{th} \simeq 0$ V.

Finally, a PIN diode on n-type substrate was tested under X-ray irradiation using an ^{241}Am radioactive source. Fig. 6 shows the block diagram of the detection system set-up [1]. The diode p^+ cathode is connected to an external charge preamplifier, consisting of an input JFET in the common-source configuration, a transimpedence amplifier and a feedback capacitance. No feedback resistance is required, because the JFET gate junction (which is forward biased at the source end of the gate) provides the path for the discharge of the feedback capacitance and for the detector leakage current. The room-temperature spectrum, obtained with $C_F = 0.2$ pF, $V_{bias} = 100$ V (resulting in a detector capacitance of about 1 pF), and a shaping time of 0.5 μs, is reported in Fig. 7. An ENC of 228 rms. electrons (corresponding to 1930 eV FWHM) was measured on the pulser peak, while a resolution of 1966 eV FWHM was obtained on the 59.54 keV γ-peak. Such a relatively low resolution

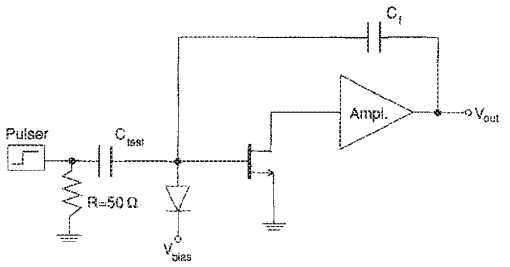


Fig. 6. Block diagram of the detection system set-up.

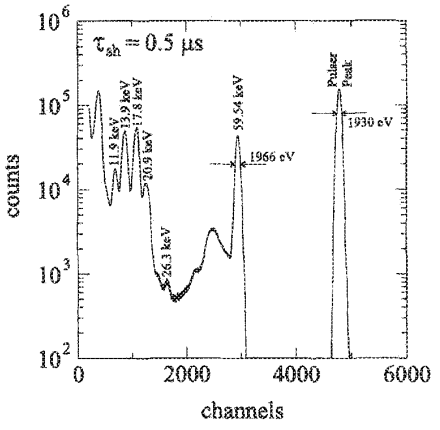


Fig. 7. ^{241}Am spectrum acquired at room temperature and 0.5 μs shaping time.

is mainly ascribed to the fact that the detector leakage current increased by more than one order of magnitude after chip dicing and bonding, reaching a value of about 1 nA at a reverse voltage of 100 V (to be compared with the value of 60 pA measured at wafer-level). We attributed such a behaviour to the absence, in our detectors, of a suitable isolation from current contributions originating at the chip edges.

4. Conclusions

We have reported on the electrical and X-ray characterisation of PIN radiation detectors and other related test structures fabricated on both n- and p-type high-resistivity Si substrates. The effectiveness of different extrinsic-gettering techniques in limiting the detector leakage current has been investigated. Among devices built on n-type Si, those implementing a phosphorus-doped polysilicon backside layer have shown the best results in terms of both leakage current (lower than 0.2 nA/cm^2/100 μm) and process uniformity.

SIONYX1403000026.0022

SAMSUNG EX. 1002 - 2487/4148

On the contrary, B-doped polysilicon gettering in devices built on p-type Si was not as much effective, the resulting average leakage current density exceeding the value of 30 nA/cm^2/100 μm. In spite of the good results obtained at the wafer-level, the experience has shown that some leakage current degradation can occur after device dicing and bonding, adversely affecting the detector X-ray energy resolution.

Acknowledgements

The authors would like to thank A. Fazzi and C. Fiorini (Politecnico di Milano) for the X-ray characterisation of PIN detectors.

References

[1] G. Bertuccio, A. Pullia, IEEE Trans. Nucl. Sci. NS-41(4) (1994) 1704.
[2] J. Kemmer, Nucl. Instr. and Meth. A 226 (1988) 89.
[3] S. Holland, Nucl. Instr. and Meth. A 275 (1989) 537.
[4] W. Snoeys, J.D. Plummer, S. Parker, C. Kenney, IEEE Trans. Electron Devices ED-41(6) (1994) 903.
[5] P.G. Fallica, S. Cannavaro, S. Musumeci, G. Ferla, Nucl. Phys. B (Proc. Suppl.) 23-A (1991) 107.
[6] P.J. Van Wijnen, W.R. Th. Ten Kate, Nucl. Instr. and Meth. A 253 (1987) 351.
[7] G.F. Dalla Betta, M. Boscardin, G. Verzellesi, G.U. Pignatel, A. Fazzi, G. Soncini, Proc. IEEE Int. Conf. on Microelectronics Test Structures (ICMTS), 1996, pp. 231–235.
[8] L. Evensen, A. Hanneborg, B.S. Avset, M. Nese, Nucl. Instr. and Meth. A 337 (1993) 44.

SIONYX1403000026.0023

SAMSUNG EX. 1002 - 2488/4148

Nanoimprinting for Antireflective Moth-Eye Surfaces

Stuart A. Boden* and Darren M. Bagnall
Nano Group, Electronics and Computer Science, University of Southampton,
Highfield, Southampton, SO17 1BJ
*Corresponding Author: sb1@ecs.soton.ac.uk

Abstract

We present our most recent work on the development of a new method of fabricating antireflective moth-eye structures in silicon based on nanoimprint lithography (NIL). Reflectance spectra from test structures show that broadband, low reflectance can be achieved using moth-eyes fabricated by NIL, with reflectance below 1% across wavelengths ranging from 572 to 647 nm. The appearance of interference peaks in the reflectance spectrum of pillars with a square profile is analysed to highlight the importance of tapered pillar profiles in achieving broadband antireflection (AR). Development of a cheap and scalable NIL synthetic moth-eye fabrication method will pave the way for excellent broadband AR surfaces for photovoltaic applications.

Introduction

Various schemes have been developed to reduce reflectance of sunlight from solar cell surfaces. These include the use of thin film antireflection coatings (ARCs) and texturing of the surface. Single or double layer thin film coatings (SLARs and DLARs) employ a destructive interference mechanism to minimise reflectance at specific design wavelengths [1]. However, reflectance for other wavelengths can be high and, due to the broadband nature of sunlight, a broadband antireflective effect is required for solar cells. Thin film ARCs are also limited by the availability of materials with appropriate optical and thermal properties. Texturing on the micron scale is often used, in combination with ARCs, to force light to undergo multiple reflections from the inclined faces of the textured features, thus increasing the amount of light coupled into the cell. An example of such an approach is the use of regular pyramidal arrays on high efficiency c-Si cells [2]. Texturing with large scale features, however, is incompatible with second generation, thin-film solar cell technologies.

A third option is to texture with arrays of features on a scale below the wavelength of light. If these features are tapered, light passing through the interface experiences a graded refractive index which minimizes the amount reflected. This is the mechanism behind the very low reflectance achieved by nature as a form of camouflage on the corneal surfaces of some species of moth (*Figure 1*) [3]. Surfaces employing this type of AR are commonly called "moth-eye" surfaces. Several examples of antireflective, biomimetic silicon moth-eye surfaces have been reported [4, 5], showing antireflection over a wide range of wavelengths.

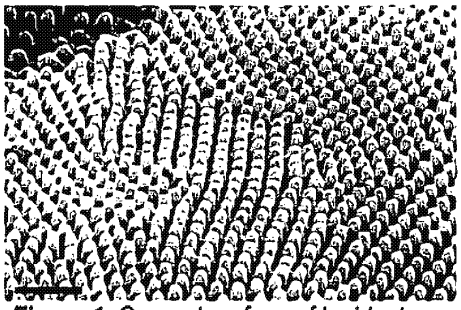


Figure 1. *Corneal surface of lepidopteran moth. Scale bar is 1 μm [6].*

Previously, we showed through simulation that replacing an optimized SLAR with a moth-eye array on a high efficiency c-Si solar cell could lead to approximately 10% more energy over a day [7]. We have also reported the fabrication of test structures using electron beam lithography, the best of which exhibit reflectances of less than 0.5% over a range of wavelengths from 550 nm to 870 nm. However, the long write times (approximately 30-90 mins per mm^2) that result from having to define each individual feature with an electron beam, means that this approach is prohibitively expensive for photovoltaics. We are therefore investigating nanoimprint lithography (NIL) as an alternative scheme. NIL uses electron beam lithography to produce a stamp, which can then be used to reproduce the pattern

SAMSUNG EX. 1002 - 2489/4148

many times over, and so is a cheaper and potentially more scalable way of achieving excellent AR for solar cells. Our aim is to develop an NIL process that produces similar AR surfaces to those we have achieved using our e-beam techniques.

Review of electron-beam work

Measurements of reflectance versus wavelength from the best-performing Si moth-eye samples produced using the e-beam technique are shown in *Figure 2* [7]. A scanning electron micrograph (SEM) of the features of one of the best performing samples (curve D in *Figure 2*) is presented in *Figure 3*. The aim is to produce similar structures using NIL.

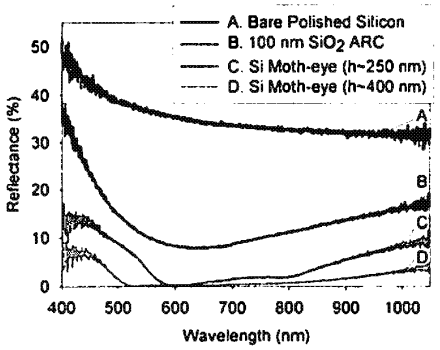


Figure 2. *Reflectance probe results for best-performing silicon moth-eye samples.*

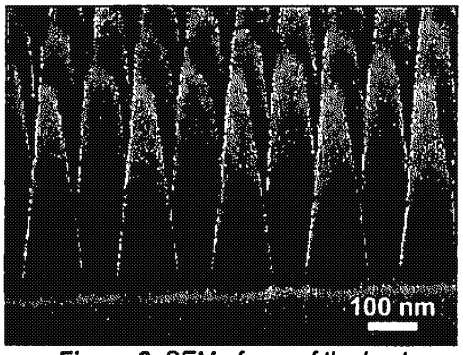


Figure 3. *SEM of one of the best performing silicon moth-eye samples (curve D on Figure 2) fabricated using E-beam method.*

Nanoimprint Lithography

The processes for stamp fabrication and imprinting are presented in *Figure 4* and *Figure 5*, respectively. For the stamp, a metal mask is formed using e-beam lithography and lift-off. A SF_6/C_4F_8 dry etch (STS MESC Multiplex ICP) is then used to form vertical-walled, 150 nm high pillars. The stamp is used in combination with lift-off to reproduce the metal mask on a substrate. The SF_6/C_4F_8 etch is then used to form pillars with heights of approximately 400-500 nm. The metal mask is removed and then a $SF_6/CHF_3/O_2$ reactive ion etch (STS RIE), which is more isotropic than the first etch, is then performed to shape and taper the pillars. Further shaping and damage removal is achieved with an oxidation and oxide strip.

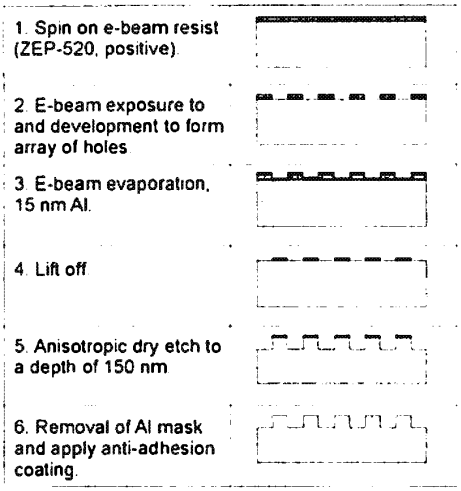


Figure 4. *Stamp fabrication for NIL.*

Profile Development

By varying the time of the second etch (shaping etch) and the oxidation time we have fabricated a variety of pillar profiles. The pillar profile is also dependent on the period and initial size of the features on the metal mask. After an initial development batch involving patterning of 100 μm^2 areas, we fabricated a range of larger samples (1.4 mm^2) from which we could measure reflectance. We found that with a stamp containing a range of patterns with different densities the imprint process is hindered by problems with maintaining an even pressure over the whole stamp. Therefore, the optical samples presented here were patterned using e-beam lithography to create the metal mask (steps 1-4, *Figure 4*). The plan is to select the best performing pattern from the optical samples and create a stamp with a patterned area of 1 cm^2. This will eliminate density variation problems and so enable us to use NIL to pattern the metal mask. We can directly transfer the developed etch process because the metal mask is identical whether patterned using e-beam or NIL.

SAMSUNG EX. 1002 - 2490/4148

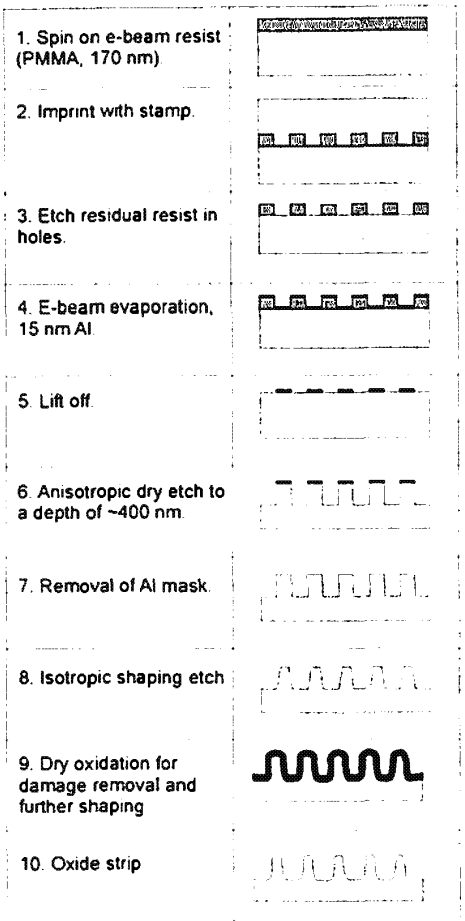


Figure 5. NIL process.

Examples of the pillar structures of two such patterns are shown in Figure 6. We observe that the longer isotropic etch used for wafer B (*Figure 6* (b)) results in a more tapered pillar profile that more closely resembles the profile of the previous reported excellent AR structures shown in *Figure 3*. However, the pillars display concave, hollowed out tips which are in contrast to the convex, rounded pillar tips shown in *Figure 3*. Wafer A (*Figure 6* (a)) exhibits pillars with squarer profiles and flat tops which we predict will lead to poorer AR properties because light will experience sharp changes in refractive index as it passed through a surface textured with these features.

Optical Characterization

We used the reflectance probe technique described in [7] to measure reflectance of near-normal incident light from the samples shown in *Figure 6*. The resulting reflectance spectra are presented in *Figure 7*.

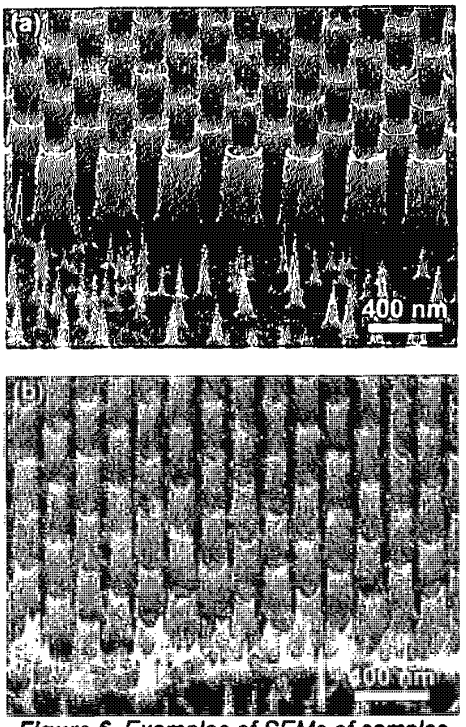


***Figure 6.** Examples of SEMs of samples made with a metal etch mask (a) wafer A: iso. etch 3 mins, oxidation 15 mins; (b) wafer B: iso. etch 12 mins, oxidation 15 mins.*

Results and Discussion

Wafer B exhibits good AR properties, with reflectance reduced to below 2% for the wavelength range 560-769 nm and below 1% for wavelengths between 572 and 647 nm (*Figure 7*). We have not yet achieved AR properties that match the best achieved using the previous e-beam technique. However, by developing the etch process further, we should be able to achieve pillar profiles, and so reflectance properties that more closely resemble those of the sample shown in *Figure 3*. This could including altering the isotropic etch recipe and/or extending the oxidation time further in an attempt to eliminate the concave tip features.

Wafer A exhibits poor AR properties, with various maxima and minima in reflectance across the wavelength range. Minima in reflectance comparable to wafer B are achieved but only over narrow wavelength ranges (e.g. reflectance is less than 1% but only over a 10 nm wavelength range

SAMSUNG EX. 1002 - 2491/4148

around 647 nm). We can reveal a clue as to the cause of such a reflectance spectrum using effective medium theory (EMT). The reflectance spectrum resembles that of a single layer thin film coating of sufficient thickness to cause multiple interference peaks. Treating the structured region as an effective medium with the refractive index dependent on the amount of silicon to air, we notice that for a square pillar profile, the refractive index varies little from the base to the peak of the pillars. Therefore, the structure could be modelled as a single layer with an effective refractive index, n_{eff}, given by [8]

$$n_{eff} = \sqrt{f n_{Si}^{\ 2} + (1-f) n_{air}}$$

where f is the fraction of silicon to air. We can calculate f and the n_{eff} by measuring the radius and period from *Figure 6* (a). We can then calculate the reflectance spectra expected from a single layer thin film on silicon with these parameters. The results of this analysis (*Figure 7*) show that the positions of the maxima and minima predicted with the thin film simulation are similar to those observed in the reflectance spectra of wafer A. Differences will be due to the pillar profiles not exactly matching the ideal square profile assumed for the simulation.

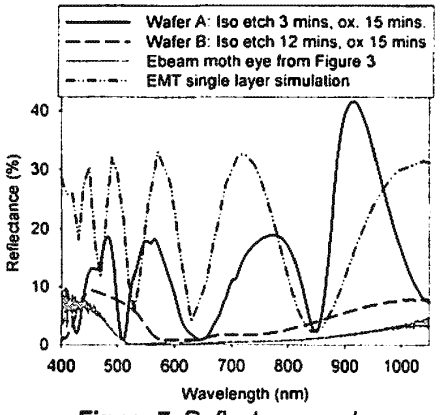


***Figure 7.** Reflectance probe measurements on two samples (Figure 6) etched through a metal mask. The best result from the previous e-beam technique is included, as is the EMT single layer simulation with f= 0.31 and h = 480 nm.*

For PV applications, we would like to avoid moth-eye patterns such as wafer A that exhibit large variations between reflectance maxima and minima. Therefore, we need to avoid square pillar profiles and develop etch techniques to produce tapered pillars. In terms of effective medium theory, tapering has the effect of grading the refractive index and so suppressing the interference effect, resulting in low reflectance over a broad range of wavelengths.

Conclusions

We are developing a new process, based on nanoimprint lithography, for the fabrication of synthetic moth-eye structures in silicon. The aim is to reproduce the excellent AR surfaces we achieved with an e-beam based technique, but with cheaper and potentially more scalable NIL technology. We have demonstrated good AR performance, with reflectances less that 2% over a 209 nm wavelength range. The etch development process has highlighted the importance of a tapered pillar profile: Square profiles lead to large reflectance variations over the spectrum due to interference effects because the structures behave as a single layer coating. We aim to optimize the etch process, and then select the best pattern to create a 1 cm^2 stamp. We can then produce test solar cells from substrates patterned with this stamp.

The authors would like to thank NIL Technology Ltd. for fabricating the test structures.

[1] J. Zhao, M. A. Green, *IEEE Trans. Electron Devices* **1991**, *38*, 1925.
[2] J. Zhao, A. Wang, P. Altermatt, M. A. Green, *Applied Physics Letters* **1995**, *66*, 3636.
[3] C. G. Bernhard, *Endeavour* **1967**, *26*, 79.
[4] Y. Kanamori, M. Sasaki, K. Hane, *Opt. Lett.* **1999**, *24*, 1422.
[5] P. Lalanne, G. M. Morris, *Nanotechnology* **1997**, *8*, 53.
[6] P. Vukusic, J. R. Sambles, *Nature* **2003**, *424*, 852.
[7] S. A. Boden, D. M. Bagnall, "Bio-mimetic nanostructured surfaces for near-zero reflection sunrise to sunset", presented at *PVSAT-3*, Durham, UK, **2007**.
[8] W. H. Southwell, *Journal of the Optical Society of America A (Optics and Image Science)* **1991**, *8*, 549.

SAMSUNG EX. 1002 - 2492/4148

C1

Feature

From bolometers to beetles: the development of thermal imaging sensors

Robert Bogue
Associate Editor, *Sensor Review*

Abstract

Purpose – This paper seeks to describe and discuss the historical development of IR sensors used in thermal imaging and to identify and consider some recent research trends.

Design/methodology/approach – This paper first considers cooled semiconductor photon detectors and their limitations and then traces the historical development of un-cooled IR sensing technologies and their commercialisation. It then discusses certain present-day developments and research trends.

Findings – This paper shows that military-funded research by the USA in the 1980s led to families of un-cooled IR sensors, pyroelectric detectors and microbolometers, that have since been widely commercialised. Research continues in the search for a technology that can yield un-cooled sensors offering the sensitivity of cooled devices, such as Golay cells, microcantilever arrays and biomimetics.

Originality/value – This paper traces the technological evolution of un-cooled thermal imaging sensors and identifies and considers recent research.

Keywords Infra-red devices, Sensors

Paper type Technical paper

Originally developed for the military during the Korean War, thermal imagers are used widely by the armed forces and emergency services and also satisfy many industrial applications such as equipment fault detection and condition monitoring. The heart of all thermal imagers is the sensor that detects the incoming IR radiation and critically these govern the products' cost and performance. The majority fall into either of two categories: high-cost, high-resolution devices based on direct photon detection and less costly, lower resolution devices which detect thermal energy. The former are fabricated from compound semiconductors such as mercury cadmium telluride (HgCdTe), indium antimonide (InSb) and indium arsenic antimonide (InAsSb). They operate through the quantum mechanical interactions that occur between the incident photons and electrons in the detector material. Either of two specific mechanisms may be exploited: photoconductive and photovoltaic. In the former, IR photons are absorbed and elevate an electron from the material's valence band to the conduction band, thus changing its conductivity, whilst photovoltaic detectors absorb the photons to create an electron-hole pair across a p-n junction which can produce a small current. Except when working in the short-wave IR region (i.e. $\lambda = 1\text{-}3\,\mu m$), all IR sensors based on photon detection must be cryogenically or thermo-electrically cooled to eliminate noise arising from thermally generated carriers. As a consequence, reliability suffers: the MTBF (mean time between failures) of cooled-sensor imaging systems is typically 3,000-4,000 h but for un-cooled devices the figure is 40,000-60,000 h. In addition, cooling imposes size, weight, cost and start-up time limitation, leading to the search for a technology which could yield un-cooled detectors that are easy to mass-produce and capable of generating high-quality images.

This has been the topic of military-funded research for several decades and in the 1980s the US Department of Defence (DoD) awarded Honeywell and Raytheon R&D group, then part of Texas instruments (TI), large, classified contracts termed high-density array development (HIDAD) to develop un-cooled IR sensor technology. Both programmes were very successful: TI developed the pyroelectric sensor and Honeywell developed the microbolometer and both have since enjoyed considerable commercial success. In 1992, the US Government de-classified the use of IR imaging for commercial products but maintained close control over the technology. TI developed commercial thermal imagers and Honeywell initially licensed their microbolometers to four companies. These were Loral, the company that purchased the Honeywell Electro-optics Division, Santa Barbara Research that was then part of Hughes, Amber Engineering and Rockwell. Subsequently, Loral was acquired by Lockheed Martin who later put the microbolometer activity into their Sanders operation which was then acquired by British Aerospace; Raytheon acquired Santa Barbara Research from Hughes and also acquired Amber Engineering; and Boeing acquired Rockwell's IR imaging activity and after a few years sold it to DRS Technologies. Several further companies have since acquired licenses.

Pyroelectric detectors are based on ferroelectric ceramic materials which exhibit the pyroelectric effect, whereby incident IR radiation falling on the ceramic causes a temperature change

The current issue and full text archive of this journal is available at
www.emeraldinsight.com/0260-2288.htm

Sensor Review
27/4 (2007) 278–281
© Emerald Group Publishing Limited
[ISSN 0260-2288]
[DOI 10.1108/02602280710821399]

SIONYX1403000026.0028

SAMSUNG EX. 1002 - 2493/4148

which generates an electrical charge. A typical array consists of a number of ceramic elements, effectively pixels, coupled to the signal read-out electronics. TI patented ferroelectric IR detectors based on barium strontium titanate in 1978 and first demonstrated the technology to the military in 1979. Since, then, several companies have exploited the effect. It is important to recognise, however, that unless the signals are chopped, pyroelectric arrays only respond to changes in the IR flux but this makes them particularly well suited to monitoring the movements of people in applications such as retail outlets and safety applications. Figure 1 shows a people counting product based on a 16 × 16 element pyroelectric array, produced in the UK by IRISYS. These respond over the wavelength range 8-14 μm and are now being used in supermarkets, including Tesco, the UK's largest grocery chain. The ceiling-mounted sensors monitor the number of people entering a store and queuing and the data are used to determine the number of check-outs required. The use of this system reduces queuing times and led to Tesco winning the Retail Week Customer Service Initiative of the Year Award in 2006. These arrays are also used in conventional thermal imaging instruments, albeit with relatively low resolution (Figure 2). The technology is not static and efforts are underway to enhance performance. Two notable research themes are the use of alternative pyroelectric materials with improved characteristics and the fabrication of arrays based on thin pyroelectric films deposited onto microengineered silicon substrates.

The bolometer was invented in 1878 by the American astronomer Samuel Pierpont Langley and microbolometers are effectively miniaturised versions of these, fabricated by silicon MEMS technology. They generally respond over the wavelength range 8-14 μm and rely on the incident IR radiation heating a sensing element causing a change in its electrical resistance. The most widely used sensing material is vanadium pentoxide (V_2O_5), often termed "VOx". This is the preferred material because of its high-thermal coefficient of

Figure 1 The IRISYS people counter is based on a 16 × 16 element pyroelectric array

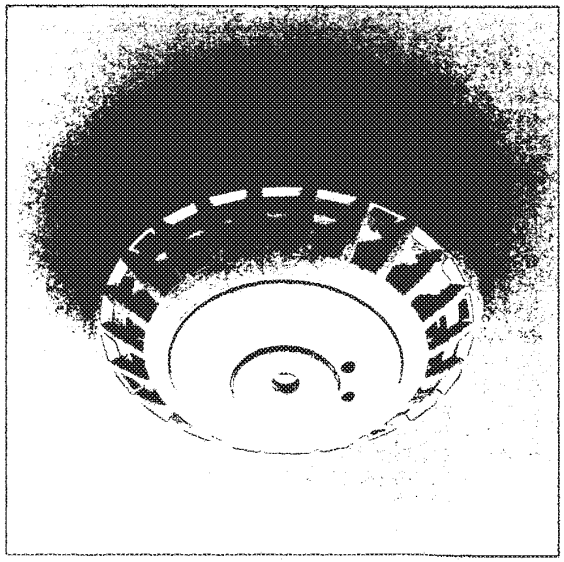
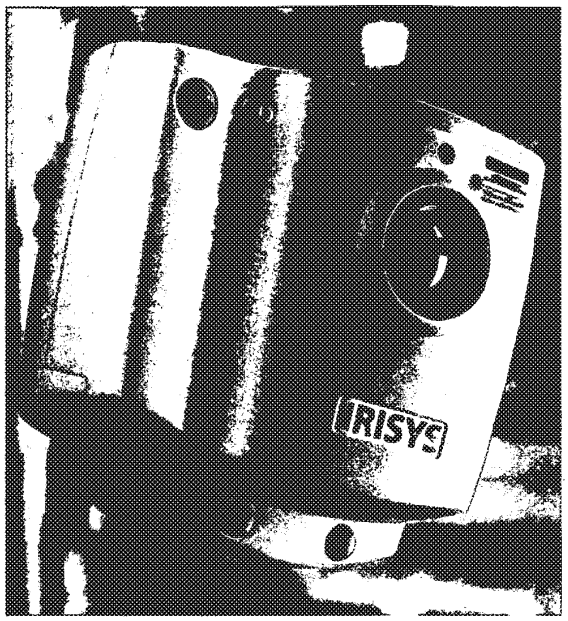


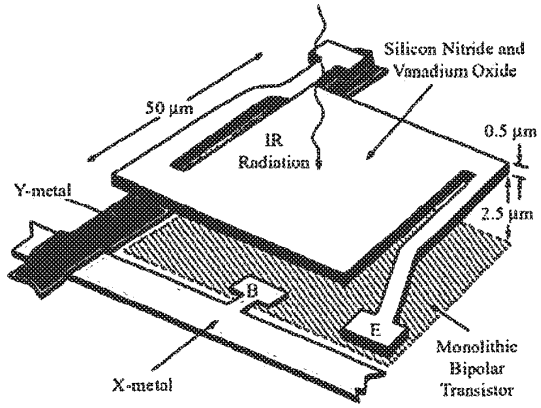
Figure 2 Thermal imager based on a pyroelectric array (IRISYS)



resistance (~3-4 per cent/degree). A microbolometer is a two-layer structure consisting of 80,000 or more sensor elements in a two-dimensional array, where the thermally isolated VOx elements are deposited over the silicon read-out circuitry. Figure 3 shows a schematic of a single sensing element. The two most common sizes are the 320 × 240 array and the less costly 160 × 120 array. Both have the same resolution, although the larger array provides a wider field of view. Larger, 640 × 480 element arrays were announced in 2005. Microbolometer arrays are used widely in thermal imagers and have become the technology of choice for un-cooled devices.

A more recent microbolometer development uses amorphous silicon rather than VOx, a material that has the advantage of being fully compatible with standard IC processing technology. This technology has the potential for low-cost devices due to high-processing yields. Operational

Figure 3 Schematic of a VOx-based microbolometer element



SIONYX1403000026.0029

SAMSUNG EX. 1002 - 2494/4148

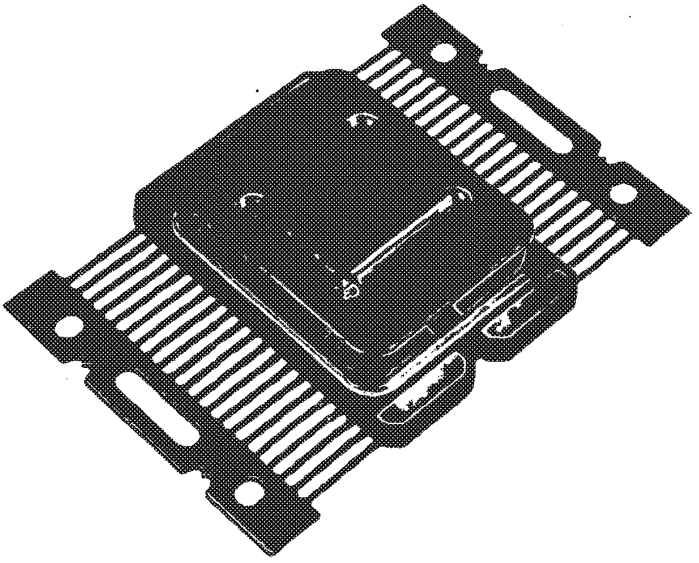
benefits include high-mechanical strength, the ability to sustain high vibration and shock loads and very low-pixel thermal time constants which arise from the extremely thin, thermally isolated suspended membranes. The technology has been the topic of research at the French Laboratoire d'Electronique de Technologie de l'Information (LETI) since 1992 and has recently been commercialised by ULIS. Set up as an array manufacturer in 2002, the company announced its 160 × 120 pixel amorphous silicon array with a pitch of 35 μm and a spectral response of 8-14 μm in 2004. Since, then, the range has been expanded and includes arrays with sizes up to 640 × 490. A packaged array is shown in Figure 4. These and other amorphous silicon microbolometers are now being used in many commercial thermal imagers.

Whilst pyroelectric detectors and microbolometers operate a room temperature and some can be fabricated at relatively low costs, they exhibit lower sensitivities than photon detectors, leading to the search for a high resolution, un-cooled technology continuing during the 1990s. One technique that saw a resurgence of interest during this period was the Golay cell. Invented by its namesake in 1947 and often termed a "pneumatic" IR detector, a Golay cell is a highly sensitive device which exploits the simple principle whereby a confined volume of gas expands when heated. Early devices used a cavity featuring a flexible membrane whose expansion was measured with a displacement sensor but more recent designs aimed at thermal imaging have exploited silicon MEMS technology. Notable is the tunnelling Golay cell developed at the Jet Propulsion Laboratory at the California Institute of Technology in the early 1990s. Here, the membrane's deflection is determined by measuring variations in a quantum mechanical tunnelling current between it and a fixed conducting tip. The device is operated in a force-rebalance mode, which maintains the electron tunnelling distance and thus keeps the current constant, using simple feedback electronics. These devices are yet to exert a commercial impact but work continues at Stanford University on a high-yield wafer-scale process for fabricating tunnelling Golay detectors. Recently, a group from the Department of Materials Science and Engineering at Iowa State University has conducted some innovative but preliminary work on micro-miniaturised arrays based around polymer/inorganic nanocomposite membranes which, they argue, may offer longer term prospects in the thermal imaging context by exploiting the Golay principle (*Chem. Mater.* 2006, 18, 2632-2634).

A type of IR imaging sensor which exploits MEMS technology but which has so far enjoyed mixed fortunes is the microcantilever array, developed originally by the US Oak Ridge National Laboratories (ORNL) in the mid-1990s. These structures have been studied widely in the gas, chemical and physical sensing contexts and for thermal sensing a bi-material coating on the cantilevers absorb IR and the temperature-induced deflection (displacement) causes a change in capacitance which is detected by integrated CMOS electronics. In other, similar devices the deflection is detected by integrated piezoresistors. An image of an early cantilever array is shown in Figure 5. As noted in a previous issue of this journal (Vol. 23, No. 4, pp. 299-301) Sarcon Microsystems, Inc. unveiled a prototype IR camera based on capacitive microcantilever technology in 2003. However, the company encountered technical problems and folded later that year but in 2005, Multispectral Imaging, Inc. (MII) was granted an exclusive, world-wide licence from ORNL to commercialise the technology. Whilst still at the development stage, according to MII, the sensor's calculated conversion sensitivity (the percentage change in output per degree rise in temperature) is 10-50 per cent/K, which far exceeds the figures for VOx and amorphous silicon microbolometers (~1.5-3 per cent/K) and pyroelectric detectors (~2-3 per cent/K).

Whilst cantilever-based sensors appear to offer considerable potential, they are unlikely to bring to an end the search for a high-performance un-cooled thermal sensing array. Indeed,

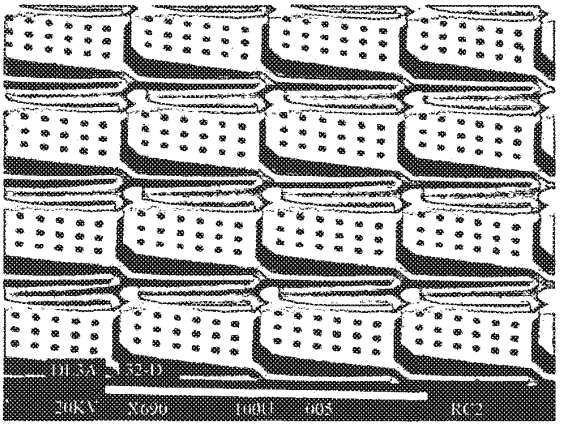
Figure 4 Packaged amorphous silicon microbolometer array



SIONYX1403000026.0030

SAMSUNG EX. 1002 - 2495/4148

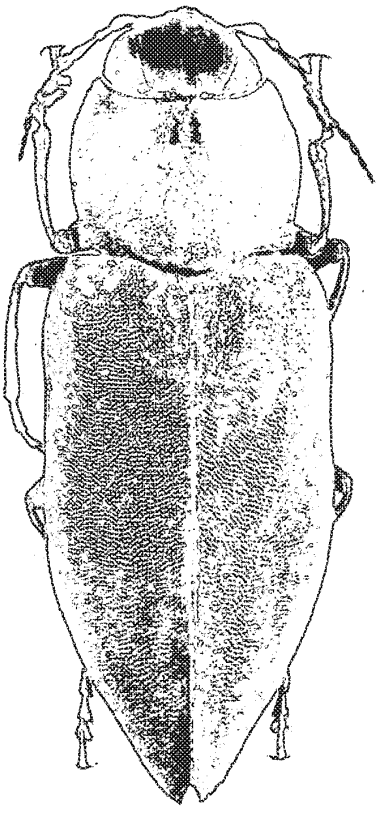
Figure 5 Electron micrograph of an early microcantilever-based thermal sensing array



despite the commercial success of microbolometers, research into these devices continues today, with the dual aims of improving performance and reducing costs. Some research themes include novel sensing materials (polymers, high-Tc superconductors such as YBCO, nanostructured VOx, etc.), more sophisticated silicon microstructures with better thermal isolation and reduced pitch size and advanced material deposition, processing and fabrication technologies.

A more speculative and intriguing body of research concerns biomimetics, the development of products or techniques which mimic the phenomena found in nature. Several US Government and university labs are investigating the application of this to thermal imaging. An example of an organism with a remarkable thermal sensing ability is the beetle *Melanophila acuminata* (Figure 6) which is attracted to fires and smoke up to 50 km away because burned trees provide the environment for their larvae to develop and hatch into adults. The fires emit IR radiation that the beetle detects via a specialised structure known as the pit organ which contains 60-70 IR sensors termed sensilla. Each sensillum consists of a minute sphere made from the same material as the beetle's outer shell and is connected by nerves to a highly sensitive mechanoreceptive sensory cell. Incoming IR radiation is absorbed by the outer sphere and absorption causes the sphere to expand. This micromechanical event is measured by the mechanoreceptor and a neuronal signal is generated. Similar highly sensitive IR pits are also present in snakes such as pythons. By understanding the mechanism and the biological processes involved, one could, in principle, develop new and improved IR materials and sensors. However, understanding these processes and applying them to man-made devices is a huge scientific and technological challenge but researchers at the US Air Force Research Laboratory's Materials and Manufacturing Directorate at Wright-Patterson AFB, Ohio, have successfully created

Figure 6 *Melanophila acuminate*. Could this beetle hold the key to the next generation of high performance thermal imagers?



composite polymer films that electronically report changes in a protein's structure when stimulated by IR radiation. They have since built a prototype imaging array based on this technology, resulting in the world's first biomimetic thermal imager. This is understood to be based on a radiant heat-sensitive biological material embedding in a capacitive polymer substrate. Current efforts aim to reduce the size and weight of the array to allow integration with a micro-air vehicle. A major project dubbed BIRN (Biomimetic Infrared Nanosystems) commenced at the University of California, Berkeley, in 2005, which aims to combine MEMS technology with the thermo-sensitive organs of the beetle to develop high-sensitivity thermal imaging sensors.

Whether microbolometers, cantilever arrays, biomimetics or some other technology will ultimately yield an un-cooled IR detector with performance to match the best cooled devices remains unclear but it is certain that the search for such a technology is not over.

To purchase reprints of this article please e-mail: **reprints@emeraldinsight.com**
Or visit our web site for further details: **www.emeraldinsight.com/reprints**

SIONYX1403000026.0031

SAMSUNG EX. 1002 - 2496/4148

APPLIED PHYSICS REVIEWS

Oxygen precipitation in silicon

A. Borghesi
Dipartimento di Fisica dell'Università, via Campi 213 a, I-41100 Modena, Italy

B. Pivac
Rudjer Boskovic Institute, P.O. Box 1016, HR-41000 Zagreb, Croatia

A. Sassella and A. Stella
Dipartimento di Fisica "A. Volta" dell'Università, via Bassi 6, I-27100 Pavia, Italy

(Received 15 June 1994; accepted for publication 14 December 1994)

A review is presented of the recent advances in the study of oxygen precipitation and of the main properties of oxide precipitates in silicon. After a general overview of the system "oxygen in silicon," the thermodynamics and the kinetics of the precipitate formation are treated in detail, with major emphasis on the phenomenology; subsequently, the most important techniques for the characterization of the precipitates are illustrated together with the most interesting and recent results. Finally, the possible influence of oxygen precipitation on technological applications is stressed, with particular attention to recent results regarding device yield. Actually, the essential novelty of this review rests on the attempt to give an extended picture of what has been recently clarified by means of highly sophisticated diagnostic methods and of the influence of precipitation on the properties of semiconductor devices. © *1995 American Institute of Physics.*

TABLE OF CONTENTS

I. Introduction 4170
II. Oxygen in silicon 4170
A. Growth processes 4170
1. Float-zone growth 4170
2. Czochralski growth 4171
B. Fundamental properties of isolated oxygen atoms in silicon 4174
1. Position of isolated oxygen atoms in the silicon lattice 4174
2. Oxygen segregation 4174
3. Oxygen solubility 4175
4. Oxygen diffusivity 4176
C. Techniques for oxygen content determination in silicon 4179
1. Infrared spectroscopy 4179
2. Gas fusion analysis 4182
3. Secondary ion mass spectrometry 4182
4. Other methods 4183
III. Thermodynamics and kinetics of precipitate formation 4184
A. Nucleation 4184
1. Homogeneous strain-free nucleation 4184
2. Homogeneous nucleation with strain 4187
3. Heterogeneous nucleation 4188
4. Nucleation in as-grown crystals 4190
B. Precipitation 4190
1. Spherical precipitates with fixed radius 4191
2. Spherical precipitates with increasing radius 4194
3. Disc precipitates with varying thickness 4196
C. Precipitate morphology 4197
1. Precipitate free-energy 4197
2. Influence of annealing temperature and time 4198
D. Phenomenology 4199
1. Thermal history effect 4199
2. Effect of single-step annealing 4200
3. Effect of two-step annealing 4205
4. Effect of rapid thermal annealing 4206
5. Effect of dopant and impurities 4206
IV. Techniques for oxide precipitates characterization 4209
A. Wet chemical etching 4209
1. Etch formulation and application 4209
2. Chrystallographic defects evidenced by selective etching 4209
3. Optical microscopy 4210
4. Detection of SiO_x precipitates 4212
B. Transmission electron microscopy 4212
C. Infrared absorption 4215
1. Indirect precipitate detection 4216
2. Direct precipitate detection 4216
D. Small angle neutron scattering 4222
E. Optical scattering 4224
1. Laser scanning tomography 4224
2. Scanning infrared microscopy 4225
F. X-ray topography 4226
1. Transmission topography 4227
2. Reflection topography 4228
V. Technological interest of oxygen precipitation 4229
A. Influence of precipitation on the mechanical properties of silicon 4230

Downloaded 21 Apr 2008 to 146.186.238.16. Redistribution subject to AIP license or copyright; see http://jap.aip.org/jap/copyright.jsp

SIONYX1403000026.0032

SAMSUNG EX. 1002 - 2497/4148

B. Influence of precipitation on the electrical properties of silicon. 4231
C. Denuded zone. 4233
D. Influence of precipitation on the device yield: some examples. 4236

I. INTRODUCTION

Starting from the 1950s, a lot of work has been performed on the behavior of oxygen in silicon. The growing demand to understand and clarify details concerning various aspects of this type of impurity-matrix coupling has encouraged the use of more and more sophisticated techniques.

The recent developments can be extracted from the enormous amount of scientific articles in the field, which have been stimulated by the new and wide-range silicon-based applications, particularly in the direction of very large-scale integration (VLSI) and the related integrated circuit processing. As a matter of fact, Czochralski (Cz) -grown silicon single crystals are used to fabricate VLSI devices, due to the lower cost with respect to the float-zone growth technique. In the Cz growth process oxygen is incorporated into the silicon directly from the silica crucible, as an unavoidable impurity. The presence of oxygen in silicon, however, is not to be superficially and globally considered just as a drawback, since it has effects that are also positive (mainly related to intrinsic gettering properties), in addition to the negative ones (formation of defects in the active regions related to oxygen precipitation). In this connection, one might stress that, aiming at the large-scale applications, fabrication of dislocation-free single crystals with a low concentration of contaminants and a not too high level of oxygen is obviously an important goal to be reached.

As a direct consequence, oxygen in silicon represents a challenging prototype to study solid-state reactions also from a fundamental point of view. Oxygen is incorporated as an interstitial impurity or in complexes. It should be stressed that at temperatures characteristic of device processing ($\leq$1200 °C) Cz silicon containing oxygen is a supersaturated solid solution, since oxygen is incorporated at about 1400 °C. Looking at Fig. 1 it is evident that the amount of oxygen which, at high temperature, gives rise to a solid solution, at lower temperatures leads to a phase separation between silicon and silicon oxide. In other words, at temperatures lower than 1400 °C the equilibrium state of the Si-O system is reached by means of oxygen precipitation, i.e., formation of SiO_2 particles (oxide precipitates) in the silicon crystal. The processing temperature (together with other parameters such as thermal history and initial oxygen concentration) plays an essential role in determining the formation and the morphology of oxide precipitates: In general, we can say that while nucleation is favored in the temperature range 600–900 °C, precipitate growth is predominant from about 1000 to 1200 °C. The variety of possible size, shape, orientation, etc., of the oxide precipitates in silicon imposes the use of high-performance characterization techniques for an adequate understanding of the different and multiple details.

In this article we review the recent developments concerning both precipitate formation and characterization, with the aim of presenting to the reader a picture which, if not complete (unfortunately this could not be avoided due to the huge quantity of articles published in the last years), should be (hopefully) rather homogeneous and up to date.

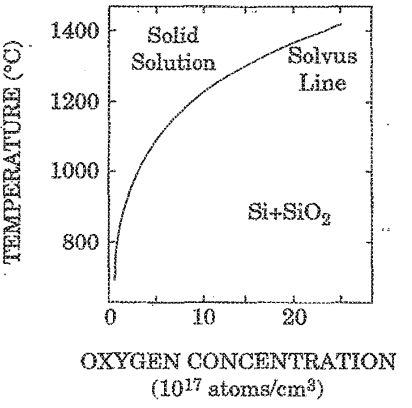


FIG. 1. Partial phase diagram of the Si-O system.

II. OXYGEN IN SILICON

To study oxygen behavior in silicon we briefly review the current techniques for industrial production of single-crystal silicon ingots and describe the mechanisms that lead to oxygen incorporation into the growing crystal, its thermodynamically stable positions in the lattice, its solubility, and diffusion mechanism. We also review the most common techniques used to study isolated oxygen atoms in silicon.

A. Growth processes

1. Float-zone growth

In the float-zone (FZ) technique a radio-frequency (rf) coil is used to melt a narrow zone in a vertically mounted polycrystalline silicon rod. The molten zone is seeded with single-crystal silicon and then passed from one end of the rod to the other. This zoning can be repeated many times to obtain high-purity crystals. Dopants are introduced either by melting pills into the molten zone or by gas-phase doping.

Since the container or crucible is not directly in contact with the molten zone and multiple zone passes are possible, high crystal purity is readily attainable; however, since the molten zone is supported by the lateral surface tension and solid-liquid interface tension, it is difficult to grow crystals much larger than 75 mm in diameter. Furthermore, no techniques have been developed to incorporate significant oxygen amounts (oxygen concentration within the bulk is typically 10^{15}–5×10^{16} atoms/cm^3), which is a prerequisite for successful ultralarge-scale-integration (ULSI) device manufacture. As a result FZ does not play an important role in ULSI silicon application (its applications are limited to about 20% of the market). Therefore, being oxygen free and not widely used for applications, silicon crystals grown by this technique are not considered any longer.

Downloaded 21 Apr 2008 to 146.186.238.16. Redistribution subject to AIP license or copyright; see http://jap.aip.org/jap/copyright.jsp

SIONYX1403000026.0033

SAMSUNG EX. 1002 - 2498/4148

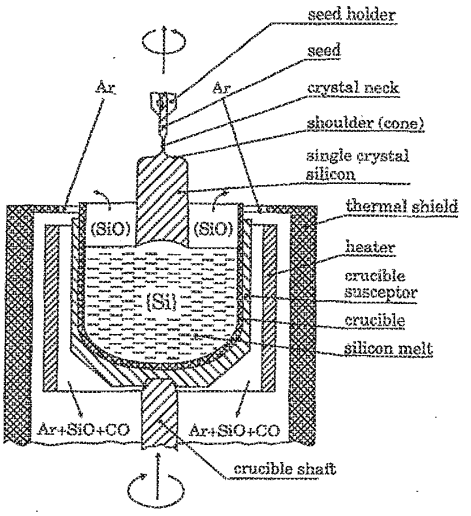


FIG. 2. Cz single-crystal pulling (from Ref. 5).

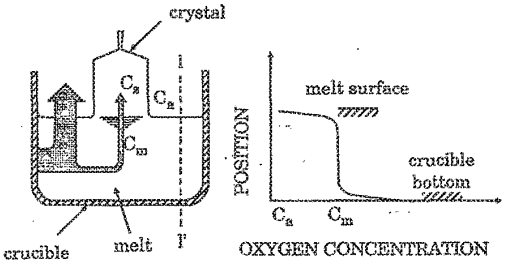


FIG. 3. Diagrams showing oxygen transportation during Cz silicon growth (left-hand side), and oxygen concentration profile in the melt along $l-l'$ (right-hand side) (from Ref. 7).

2. Czochralski growth

The experimental setup for the pulling of single crystals by the Cz method is illustrated in Fig. 2. Molten polycrystalline silicon is held in a crucible, a single-crystal seed is first dipped into the melt and then slowly withdrawn vertically to the melt surface, whereby the liquid Si crystallizes around the seed. The method is named after Czochralski, who introduced it in 1916 in the framework of the study of crystallization velocity of metals.[1] For the growth of silicon and germanium single crystals the Cz method was first applied in 1950 by Teal, Little, and Bühler.[2,3] The silicon single crystals of the early years were not dislocation free. In 1958 Dash[4] developed a special pulling technique to obtain dislocation-free crystals.

Polycrystalline silicon is melted in a crucible that is supported by a graphite susceptor. While rf heating is sometime used, all modern Cz crystal pullers use resistance heaters. The growth chamber is evacuated to ~10–20 Torr and maintained at this pressure with argon or helium flow during the growth process.

Molten silicon reacts to a large extent with every crucible material. This is due to its high binding forces for the light elements and to the high dissolving power of the melt for most elements. It is then essential to find a crucible material that only slightly reacts with the melt, and in addition does not affect the crystal quality required for electronic applications.

Almost all crucible materials, especially metals and their alloys, are quickly dissolved by liquid silicon. Only dense carbon, particularly vitreous carbon, dissolves slowly, so that a silicon melt can be held in such a crucible over a longer period, for example, to pull a polycrystalline rod. There are several compound materials, namely some carbides, nitrides, and oxides, which also react slowly. All these materials are dissolved by liquid silicon with an erosion rate of at least several microns per hour.[5] For example, vitreous silica dissolves with an erosion rate of 7 μm/h at temperatures near the melting point of silicon in a 1 bar argon atmosphere. Due to uninterrupted dissolution, the silicon melt is soon enriched to higher concentrations of the constituents of the crucible material. Therefore, materials containing metals or dopants are not suitable, as, for example, titanium carbide, boron nitride, or aluminum oxide. Only silicon compounds such as silicon carbide, nitride, or oxide, are considered as potential crucible materials.

Up to now only vitreous silica has been used in the production of Cz silicon crystals, since silicon monoxide produced in the reaction between silicon melt and silica crucible evaporates easily from the melt. Therefore, under the usual pulling conditions, oxygen concentration in the melt never reaches the solubility limit and no disturbance of crystal growth by oversaturation occurs. Under the usual pulling conditions less than 1% of the reacting oxygen gets into the crystal and more than 99% of oxygen evaporates out of the melt in the form of gaseous SiO.

Oxygen fluxes in the Cz silicon growth system are shown in Fig. 3. Oxygen enters the melt as the silica crucible dissolves in the liquid silicon. As already mentioned, part of the dissolved oxygen is incorporated into the growing crystal, while another part is lost by evaporation of SiO from the melt surface. In modern conventional growth systems an argon purge is usually introduced somewhere above the melt to help sweep off SiO from the crystal growth area. Due to strong convective flows, mixing in the melt is virtually complete and significant oxygen concentration differences exist only at the three boundaries involved:

(1) the crucible/melt interface;
(2) the solid/melt interface; and
(3) the melt/ambient interface.

At steady state the amount of oxygen leaving the melt must equal the amount entering the melt, so that

oxygen in melt = oxygen from crucible
− oxygen evaporated
− oxygen incorporated.

The steady-state conditions have been studied by many authors.[6–9] The results can be briefly summarized as follows.

Downloaded 21 Apr 2008 to 146.186.238.16. Redistribution subject to AIP license or copyright; see http://jap.aip.org/jap/copyright.jsp

SIONYX1403000026.0034

SAMSUNG EX. 1002 - 2499/4148

(1) At the crucible/melt interface

$$\text{oxygen flux} = A_c D(C_c - C_m)/\delta_c, \tag{1}$$

where A_c is the area of the crucible/melt interface, D is the diffusion coefficient of oxygen in molten silicon (see Sec. II B 4), C_c and C_m are the oxygen concentrations in the crucible and in the melt, respectively, and δ_c is the interface thickness.

(2) At the melt/ambient interface

$$\text{oxygen flux} = A_s D(C_a - C_m)/\delta_s, \tag{2}$$

where A_s is the area of the free melt surface, C_a is the oxygen concentration in the ambient, and δ_s is the interface thickness.

(3) At the solid/melt interface

$$\text{oxygen flux} = A_R v k_e C_m, \tag{3}$$

where A_R is the cross-sectional area of the growing crystal, v the linear growth rate, and k_e the effective segregation coefficient of oxygen in silicon (see Sec. II B 2).

The oxygen fluxes involve, therefore, three diffusion boundary layers and three surface areas. The thickness of the boundary layers depends on the convective flows in the melt and on the purge flow conditions, while the surface areas are determined by the amount of polycrystalline silicon (charge), by the crucible size and shape, and by the crystal diameter.

The large silica crucibles used in contemporary growth systems are approximately cylindrical. During crystal growth the crucible/melt interface constantly decreases with the melt volume, while the free melt surface remains unchanged during most of the growth process. As a result, less oxygen enters the melt but evaporation remains constant as the crystal growth proceeds, thus influencing oxygen distribution along the ingot length.

More uniform distributions can be obtained if the ratio of the crucible/melt surface area to the free melt surface area is maintained constant during crystal growth. This can be realized in crucibles of special shape, e.g., a truncated cone;[10] however, the charge size in such crucibles is limited with respect to conventional crucibles of the same size. A much more practical solution is the continuously recharged system in which feed is continuously supplied during the crystal growth. In this way, the ratio crucible/melt surface area to free surface area can be maintained constant. The uniformity of oxygen axial distribution obtained in such a way was first described by Fiegl.[11]

In general, the oxygen distribution within the silicon ingot on microscopic as well as on macroscopic scale does not correspond to the distribution of the other elements. The effective segregation coefficient of oxygen is close to one and depends only a little on the growth rate (see Sec. II B 2). On the other hand, the incorporation of oxygen into the growing crystal strongly depends on the pattern of the convective flows in the melt. Figure 4 illustrates a few melt flow characteristics in Cz silicon melts for isorotation of crystal and crucible. Clearly, unsteady melt flows cause unsteady supply of oxygen and oxygen striations in the crystals which are thicker than the dopant striations. It is difficult to measure

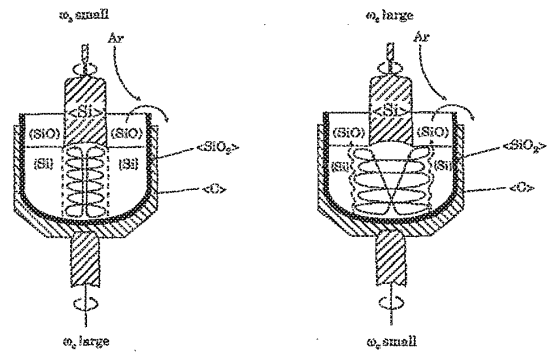


FIG. 4. Melt flow characteristics in Cz silicon melts for isorotation of crystal and crucible (from Ref. 5).

the oxygen striations straightforwardly, but there are ways to visualize them indirectly. For example, one possibility is to generate oxygen-related thermal donors by annealing at 450 °C when their formation takes place with a strict correlation with oxygen concentration. A second possibility is to induce oxygen precipitation and to make the precipitates visible by preferential etching.

The flow patterns in the melt are by far the dominant factor in determining oxygen content and distribution in the crystal. Figure 5 shows the axial oxygen distribution for eight Cz crystals grown from silica crucibles. All crystals have the same length, diameter (50 mm), orientation, and doping, while crystal and crucible rotation during pulling were different. All other pulling and growing parameters were held constant. As shown in the figure, variations of oxygen content in Cz crystals by a factor of about 10 was achieved by simply adjusting crystal and crucible rotation; however, a very good axial homogeneity was obtained. Modern pulling techniques allow one to obtain a nicely flat radial oxygen distribution, as shown in Fig. 6.

To control and/or modify oxygen incorporation in the silicon lattice a new method of Cz growth in magnetic field (MCz) has been developed.

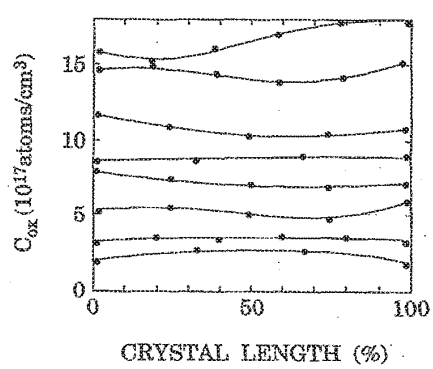


FIG. 5. Axial oxygen distribution for eight Cz crystals grown in the same conditions with different crystal and crucible rotations (from Ref. 5).

Downloaded 21 Apr 2008 to 146.186.238.16. Redistribution subject to AIP license or copyright; see http://jap.aip.org/jap/copyright.jsp

SIONYX1403000026.0035

SAMSUNG EX. 1002 - 2500/4148

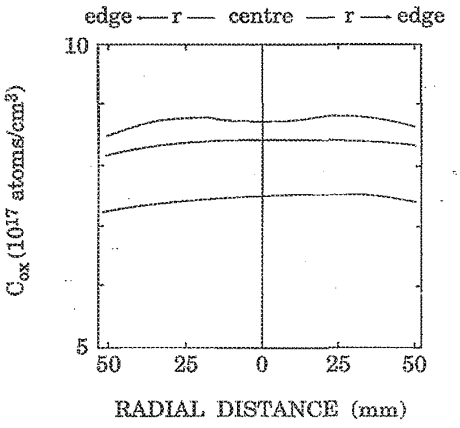


FIG. 6. Radial oxygen distribution in Cz single crystal at three different axial lengths. The higher oxygen concentration values correspond to the seed-end and the lower ones to the tail-end of the crystal (from Ref. 5).

It has been established that a magnetic field can suppress the convection of electrically conductive fluids. In 1966 Chedzey and Hurle[12] and in 1970 Utech and Flemings[13] pointed out that a magnetic field can be used to obtain high-quality InSb crystals by means of a horizontal crystal-growth method. Soon Cz InSb crystal growth in a magnetic field transversal with respect to the growth direction was presented.[14] Recently a transversal magnetic field was applied for Cz silicon crystal growth[15] to improve the quality of the crystals. More specifically, the convection flows are suppressed when a magnetic field of more than 0.15 T is applied to molten silicon, which has an electrical conductivity comparable to that of mercury. Therefore, the applied magnetic field suppresses convection, reduces the growth of striations, and allows to control oxygen concentration in the silicon crystal.

Figure 7 shows the experimental results[15] of the effect of magnetic field on the concentration of oxygen atoms incorporated into a crystal. A substantial amount of oxygen is eliminated from crystals grown under the effect of a magnetic field of 0.15 T. A smooth melt surface was observed with small temperature fluctuations. The suppression of convection in the melt causes a decrease in decomposed oxygen atoms moving from the silica crucible to the growth interface.

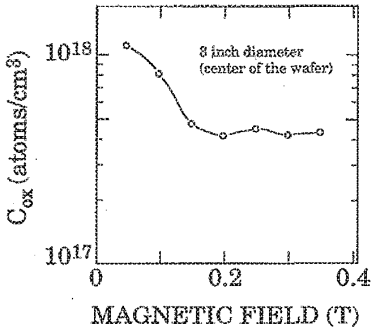


FIG. 7. Effect of magnetic-field strength on the oxygen concentration in silicon crystal (from Ref. 15).

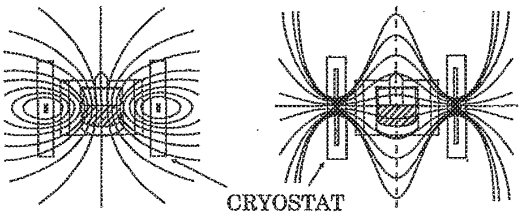


FIG. 8. Two flat coil configurations for magneto-Cz silicon single-crystal growth. Vertical or axial configuration (left-hand side) and horizontal or transversal configuration (right-hand side) (from Ref. 16).

The magnetic field was applied in the two configurations, vertical and horizontal, shown in Fig. 8. The results obtained by comparing[16] vertical and horizontal MCz can be summarized as follows.

For vertical field configuration it is easy to get crystals with an oxygen concentration over 2×10^{18} atoms/cm^3 and eliminate the striations caused by temperature variation under lower magnetic field, that is, less than 0.1 T.

For horizontal field configuration it is easy to get crystals with an oxygen content lower than 1×10^{18} atoms/cm^3, with high pulling speed. A magnetic field of about 0.25–0.3 T is required to reduce temperature variations.

The oxygen content in MCz crystals can be controlled by adjusting the applied magnetic field, or, at fixed value of the magnetic field, by varying the crucible rotation rate during the crystal growth, similar to what is done for the conventional Cz growth.

Figure 9 shows longitudinal oxygen profiles in crystals grown with the MCz method, and typical "low-oxygen" range (shaded area) obtainable with the standard Cz technique.[17]

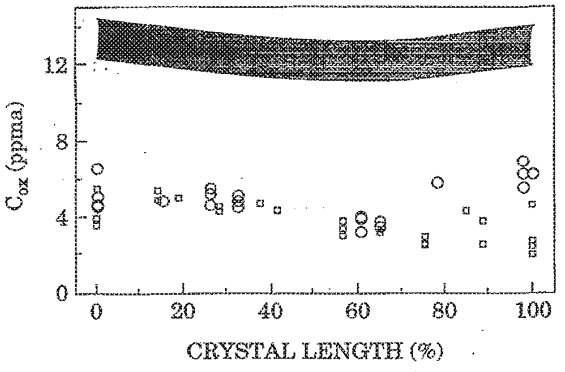


FIG. 9. Longitudinal profiles of oxygen concentration in low-oxygen crystals grown with the MCz method. Circles and squares refer to 6 and 4 in. ingot diameter, respectively. Shaded area on the top of the figure represents the typical low-oxygen range obtainable with the standard Cz technique (from Ref. 17).

Downloaded 21 Apr 2008 to 146.186.238.16. Redistribution subject to AIP license or copyright; see http://jap.aip.org/jap/copyright.jsp

SIONYX1403000026.0036

SAMSUNG EX. 1002 - 2501/4148

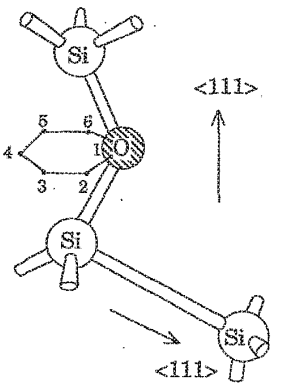


FIG. 10. Interstitial position of oxygen atom in silicon lattice, covalently bonded with two neighboring silicon atoms The equivalent interstitial positions are indicated (1–6).

B. Fundamental properties of isolated oxygen atoms in silicon

The fundamental properties of isolated oxygen atoms placed in a silicon crystal, such as their lattice position, segregation, solubility, and diffusivity, as a prerequisite for its more complex behavior, have been studied for almost 4 decades. It is widely accepted nowadays that oxygen is thermodynamically stable at interstitial sites. Recent studies on the solubility and diffusivity yield convergent indications in a wider temperature range; however, the agreement among data concerning segregation and anomalous diffusion mechanism at lower temperatures is less satisfactory.

1. Position of isolated oxygen atoms in silicon

Infrared (IR) measurements on oxygen-doped silicon led Kaiser, Keck, and Lange[18,19] to conclude that oxygen is placed interstitially in silicon lattice and is covalently bonded with two neighboring silicon atoms (see Fig. 10). Such interstitial oxygen is electrically inactive.

Oxygen interstitial position was further confirmed by x-ray-diffraction measurements of the silicon lattice parameter as a function of the oxygen concentration.[20] Corbett, McDonald, and Watkins[21] by measuring stress-induced dichroism of the IR band at 1107 cm^{-1}, and Stavola[22] for the bands at 1107 and 515 cm^{-1}, confirmed this model as well. Besides this model O'Mara[23] proposed, on the basis of the IR data by Bosomworth *et al.*,[24] that oxygen can be present simultaneously at interstitial and substitutional sites. The key for such a proposal was the observation that the 515 cm^{-1} band does not fit in the band scheme given by Bosomworth *et al.*[24] In the O'Mara model substitutional oxygen manifests double donor activity. This would explain the donor behavior of oxygen (see Sec. III D) as well as the segregation coefficient larger than one, as observed by Yatsurugi *et al.*[25] However, there is no general agreement on the existence of oxygen on substitutional sites, and furthermore Stavola[22] has shown, from stress-induced IR dichroism data, that the 515 cm^{-1} band is not due to substitutional oxygen, but to the symmetric stretching vibration of interstitial silicon, i.e., of the Si-O-Si quasimolecules.

Recently, Chen *et al.*[26] proposed a new model predicting that most of the oxygen atoms in Si are at interstitial sites in bonded Si_2O configuration, with a binding energy $E_b \sim 0.8-1.0$ eV, for temperatures up to 600 K. At higher temperatures a new "quasifree interstitial oxygen" and the bonded Si_2O configuration coexist. In the quasifree interstitial oxygen state the Si—O bonds are broken, but oxygen migration is hindered by the lattice with a potential barrier $E_L \sim 1.5-1.6$ eV. With this model they explained the enhanced oxygen diffusivity (see Sec. II B 4).

It can be concluded that at room temperature the interstitial position of isolated oxygen atoms dissolved in silicon is nowadays widely accepted.

2. Oxygen segregation

The behavior of oxygen in silicon upon various thermal treatments is strictly dependent on the processes leading to its incorporation into the crystal during growth. The distribution of impurities into the solid phase of the crystal growing from the melt is related to its segregation. The equilibrium segregation coefficient k_0 of oxygen in silicon is defined as

$$k_0 = \frac{C_s}{C_m}, \tag{4}$$

where C_s and C_m are the oxygen concentrations in the solid and in the melt, respectively.

The above equation holds for equilibrium processes. Although the Cz growth process is rather slow (the maximum growth speed is a few mm/min), it is still far from equilibrium; therefore, segregation is described by the effective segregation coefficient k_e. A detailed analysis of the phenomena at the growth interface shows that they are related to the thickness δ of the diffusion boundary layer and growth speed v. By using these parameters, Burton, Prim, and Slichter[27,28] could write k_e as a function of δ,

$$k_e = \frac{k_0}{[k_0 + (1-k_0)\exp(-v\,\delta/D)]}, \tag{5}$$

where δ is given by

$$\delta = 1.6 D^{1/3} \nu^{1/6} \omega^{-1/2}. \tag{6}$$

D is the diffusion coefficient of oxygen in the melt, ν the kinematic viscosity of the melt, and ω the rotation rate of the crystal. This theory gave a satisfactory explanation of the actual impurity distribution along the growth direction for several dopants in Cz crystals.[29]

According to Eq. (5), $k_0 = 1$ implies that the oxygen incorporation is not dependent on the growth rate variations, i.e., that the oxygen redistribution within the ingot is uniform. This is, however, in disagreement with experimental findings, which give values of k_0 different from unity.

Several attempts have been made to determine k_0, which displays values in the range from 0.25 to 1.48, as shown in Table I. Such large discrepancies in the experimentally determined values for k_0 are due to the fact that oxygen behavior in the silicon melt is driven by dynamic processes and, therefore, is not simply related to the equilibrium segregation coefficient.

Downloaded 21 Apr 2008 to 146.186.238.16. Redistribution subject to AIP license or copyright; see http://jap.aip.org/jap/copyright.jsp

SIONYX1403000026.0037

SAMSUNG EX. 1002 - 2502/4148

TABLE I. Comparison of k_0 values for oxygen in silicon, as determined by different techniques. FTIR, CPAA, SIMS, and SRP denote Fourier transform infrared spectroscopy, charged particle activation analysis, secondary-ion-mass spectrometry, and spreading resistance probe, respectively.

k_0	Method	Ref.
1.48	growth rate-IR	30
1.25 ± 0.17	CPAA	31
1± 0.25	FTIR	23
1.0 ± 0.1	growth rate	31
1	growth rate-IR, SIMS, SRP	32
~1	FTIR	9
0.36–0.9	calculated	34
0.5	vacuum fusion	35
0.3	growth rate-IR	36
0.25	growth rate	37

One of the difficulties for the determination of the segregation coefficient is the continuous supply of oxygen from the crucible walls and the evaporation of SiO from the melt surface. The balance between supply and evaporation fluctuates so that oxygen concentration in the crystal varies. Consequently, many researchers gave scattered values of the equilibrium segregation coefficient for oxygen in silicon.[9,30–37] Harada *et al.*[32] took into account these effects and furthermore suppressed oxygen evaporation by encapsulation, i.e., they increased the ingot diameter up to the inner diameter of the crucible, to completely cover the melt surface. From the uniform distribution of the oxygen through the P and Sb striations they concluded that the segregation coefficient is equal to unity. Lin and Hill[37] and Lin and Stavola[36] have grown small-diameter silicon crystals under constant growth rate conditions trying to reach equilibrium conditions by keeping the area of the melt in contact with the crucible and of the melt surface nearly constant. By comparing the axial distribution of oxygen and of the doping atoms, they found a value of 0.25 for the segregation coefficient;[37] from the comparison of microscopic arsenic and oxygen striations, a value of 0.3 was found.[36] In similar crystal pulling experiments Series and Barraclough[31] kept the temperature of the melt constant during the crystal growth, thus avoiding changes of the oxygen concentration in the melt. This experiment resulted in a segregation coefficient equal to 1.0±0.1.

Attempts to determine the segregation coefficient from IR measurements[9,23,30–36] are limited by the presence of oxygen complexes and other IR inactive species. Therefore the use of complementary techniques is required to determine the total amount of incorporated oxygen.

From the analysis of the phase diagram Sosman[38] determined a segregation coefficient smaller than one. However, the accuracy of the available phase diagrams for oxygen in silicon is far from being satisfactory, since they were determined in the early days of silicon pulling.

Recently Kim and Langlois[39] developed a model for oxygen segregation in Cz and MCz crystals. This model takes into account the oxygen source (ablation of the silica crucible), the transport in the melt, and the segregation at the growth interface. The sink is represented by evaporation of SiO from the free surface of the melt, which is a fast process compared to O diffusion through the melt and incorporation in the growing crystal. The equilibrium segregation coefficient was set to 1.25, i.e., the melt under the interface is depleted of oxygen. The comparison between simulations and experimental results for the radial oxygen profiles and the ablation of the crucible shows excellent agreement.

TABLE II. Literature data for the constant C_{OI} and the dissolution enthalpy E_s. SIMS, SRP, IR, CPAA, and XRD denote secondary-ion-mass spectrometry, spreading resistance probe, infrared spectroscopy, charged particle activation analysis, and x-ray diffraction, respectively.

C_{OI} (10^{22} atoms/cm^3)	E_s (eV)	Method	Temperature (°C)	Ref.
0.14	2.53	SIMS, outdiffusion	700–1160	42
0.13	2.50	SIMS, implanted O	700–1100	43
1100	2.3 ±0.3	SRP	1250–1400	44
6.3	1.65±0.17	IR	1100–1200	45
9	1.52	SIMS, CPAA, IR	800–1400	40
3.2	1.4	IR	850–1050	41
9.3	1.20±0.13	CPAA (^{16}O)	1000–1375	46
0.27	1.10	XRD	1100–1200	47
	1.08±0.02	CPAA (^{16}O)	1000–1280	48
0.10	1.03	IR	950–1350	49
0.13	0.95±0.1	IR	1000–1250	50
0.055	0.89	IR	460–900	51

3. Oxygen solubility

Oxygen incorporated from the melt into the growing Cz crystals is frozen in during the cooling of the ingots and gives rise to a solid solution. Therefore, in Cz wafers oxygen is present in a supersaturated state for all temperatures of standard processing. At the melting point oxygen solubility in silicon C^*_{ox} was shown to be $2.75\pm0.15\times10^{18}$ atoms/cm^3, as shown by Yatsurugi *et al.*[25] The temperature dependence of C^*_{ox} is expected to have the form

$$C^*_{ox}(T)=C_{OI}\exp\left(-\frac{E_s}{kT}\right), \tag{7}$$

where C_{OI} is a constant and E_s is the dissolution enthalpy. Oxygen solubility at various temperatures has been studied by means of various techniques: Table II shows the data from the literature, scattered up to an order of magnitude. A best fit of the experimental results from different groups is given by Mikkelsen,[40] who found $C_{OI}=9\times10^{22}$ atoms/cm^3 and $E_s=1.52$ eV. Figure 11 gives an overview of the most important experimental results and the line represents Eq. (7). The discrepancies are related to the different analytical techniques used.

Let us first consider the IR solubility measurements. The wide scattering in the published data has been recently discussed by Livingston *et al.*[41] in conjunction with their study of oxygen precipitation in silicon, devoting a particular attention to the different calibration procedures. They have also shown that since the reported IR measurements were not

Downloaded 21 Apr 2008 to 146.186.238.16. Redistribution subject to AIP license or copyright; see http://jap.aip.org/jap/copyright.jsp

SIONYX1403000026.0038

SAMSUNG EX. 1002 - 2503/4148

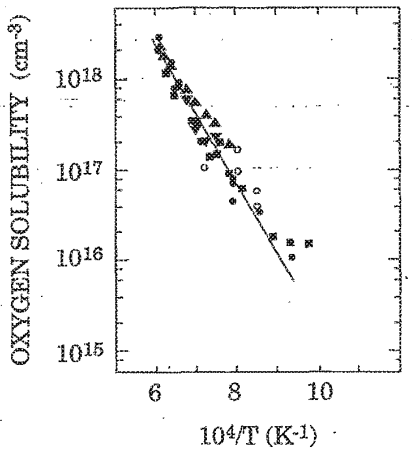


FIG. 11. Oxygen solubility in silicon as determined by SIMS (circles); IR (solid squares), and CPAA (triangles); the solid line represents the best fit (from Ref. 40).

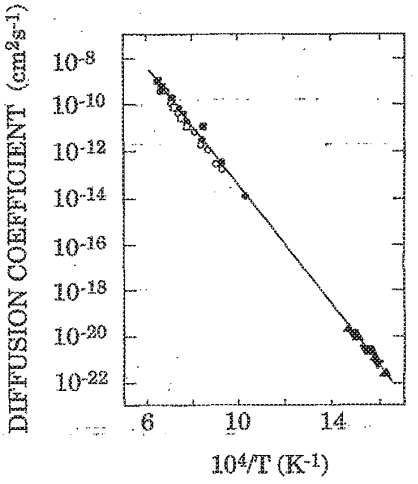


FIG. 12. Oxygen diffusivity in silicon measured by SIMS (circles), CPAA (squares), dichroism (triangles up), and kinetic data (triangles down); solid line: best fit (from Ref. 40).

all performed at 4.2 K, it would be extremely difficult to separate the absorption due to precipitates from that of dissolved oxygen. The data in Table II are recalibrated with the 3.03 calibration constant. A more detailed discussion about calibration factors is given in the next paragraphs. Furthermore, they noticed that most authors have limited the times of heat treatment in precipitation experiments to less than 200 h, apparently too short for the low-temperature anneals. These problems were avoided in the experiments of Craven,[49] who studied silicon wafers doped by nuclear transmutation, thus having high density of heterogeneous nucleation sites. The results of Craven are in close agreement with those of Hrostowski and Kaiser[50] obtained by IR spectroscopy and of Takano and Maki[47] obtained by x-ray diffraction.

Other analytical methods such as secondary-ion-mass spectrometry (SIMS), charged particle activation analysis (CPAA), and x-ray diffraction evaluate the oxygen solubility from the surface oxygen concentration and diffusion profiles. It is assumed that this concentration is established by the intrinsic solubility as a boundary condition for normal (Fickian) diffusion. It is, however, critical to ensure that no oxygen precipitation and/or complexing took place during the thermal treatment, since neither SIMS nor CPAA can distinguish the various forms of oxygen in silicon. Precipitation is likely to greatly affect the x-ray measurements of lattice dilatation, too.

For temperatures above 1000 °C, the oxygen solubility values determined by different techniques are comparable. Significant differences, however, affect the results at low temperatures. Livingston *et al.*[41] have shown that below 850 °C the solubility is enhanced. An increase in oxygen solubility below 650 °C, compared to the exponential dependence given in Eq. (7), was evidenced by Messoloras *et al.*[52] This was attributed to the changes in the structure or in the morphology of the SiO_x precipitates. However, Vanhellemont and Claeys[53] recently attributed this effect to the presence of a high self-interstitial supersaturation and to the higher interface and strain energy of precipitates at these low temperatures, making precipitation more difficult than at higher temperatures.

Mikkelsen[54,55] investigated the influence of oxidizing annealing ambients on the oxygen solubility, which was found much higher than that measured under vacuum annealing conditions. Similar results were obtained both with oxidation in O_2 and in H_2O, but it should be pointed out that these treatments did not lead to equilibrium. Furthermore, they found that oxygen solubility is a factor of 2 higher for steam than for dry ambients and is also a factor of 2 larger for ⟨111⟩ than for ⟨100⟩-oriented wafers. A similar result was obtained by Lee and Nichols[42] from SIMS analysis of the oxygen out-diffusion profile. The observed effect is explained by the increase of the oxygen steady-state solubility in the presence of the high silicon self-interstitial concentrations induced by the oxidation process.[54]

The influence of other chemical impurities on the solubility of oxygen in silicon is not clear. Gass *et al.*[48] showed that the oxygen solubility limit does not depend on B and P doping. Instead, Al and Ga seem to influence the solubility, but this may depend on sample preparation. Mikkelsen[40] reported that silicon crystals heavily doped with As tend to show defect regions which attract oxygen in excess with respect to the solubility limit, but the presence of precipitated oxygen cannot be ruled out. In the case of heavy P doping, both Heck, Tressler, and Monkowski[56] and Lee and Nichols[42] observed that the concentration of oxygen in-diffusion profiles was somewhat lower than that obtained under inert ambient annealing. These results are difficult to interpret due to very complex processes occuring at the surface.

4. Oxygen diffusivity

a. Intrinsic oxygen diffusivity. Different techniques, such as, e.g., x-ray diffraction,[47] CPAA,[48] and Cs^+ ion-beam

Downloaded 21 Apr 2008 to 146.186.238.16. Redistribution subject to AIP license or copyright; see http://jap.aip.org/jap/copyright.jsp

SIONYX1403000026.0039

SAMSUNG EX. 1002 - 2504/4148

TABLE III. Oxygen diffusivity D_0 and activation energy E_D as deduced by CPAA, SIMS, IR, SANS (small-angle neutron scattering), and XRD measurements.

D_0 (cm^2/s)	E_D (eV)	Method	Temperature (°C)	Ref.
22.6	3.15	CPAA (^{18}O)	1100–1280	48
3.2	2.9	CPAA (^{16}O)	1150–1375	46
0.23	2.56	stress-induced dichroism	1100–1280	21,63
0.7	2.54	stress-induced dichroism	330–1240	57
0.14	2.53	SIMS, O out-diff.	700–1160	42
0.13	2.53	SIMS, CPAA, IR	330–1280	40
0.11	2.51	IR, SANS	650–1050	41
0.11	2.51	stress-induced dichroism	330–1200	64
0.07	2.44	SIMS, O in-diff.	700–1240	65
0.091	2.4	lattice parameter XRD	1100–1280	47

SIMS depth profiling,[40,54] have been used to study oxygen diffusivity in silicon in the high-temperature range (700–1200 °C). The agreement among the results obtained by the different techniques is excellent, as shown in Fig. 12. On the other hand, in the low-temperature range (220–360 °C) IR spectroscopy was used to study oxygen diffusivity by means of stress-induced dichroism measurements.[21,57,58] Oxygen diffusivity in the silicon crystal D_0 is related to values of τ through the relation

$$D_0 = a^2/(8\tau), \tag{8}$$

where a is the silicon lattice parameter and τ is the relaxation time.

SIMS measurements have been performed at different experimental conditions. ^{18}O in-diffusion in FZ silicon wafers, as well as ^{16}O out-diffusion from supersaturated Cz crystals were considered.[40,42,43,56,59] It has been shown that oxygen diffusivity does not depend on wafer orientation (⟨100⟩ or ⟨111⟩), annealing ambient (dry or wet oxidizing, or inert), doping concentrations, nor pulling technique.[40,42]

On the other hand, Gass *et al.*[48] have shown by CPAA that B or P doping has no influence on oxygen diffusion, which, however, might be somewhat affected by Al and Ga doping. It has been also suggested that complexing of As may influence the O diffusion.[60] The influence of heavy Sb doping on oxygen diffusivity has been investigated,[60–62] and no effect has been found. Wijaranakula and co-workers[60] studied oxygen diffusivity in a wider range of Sb doping concentrations, concluding that point defects, such as silicon self-interstitials or vacancies, have little or no effect on oxygen diffusion.

The temperature dependence of the diffusion coefficient D is expected to have the form

$$D = D_0 \exp\left(-\frac{E_D}{kT}\right), \tag{9}$$

where D_0 is diffusivity and E_D is the activation energy of diffusion process. Diffusion coefficient data have been obtained in a wide range of temperatures as shown in Table III, and it is now well understood over twelve orders of magnitude (see Fig. 12). Fitting the results of both low and high temperatures Mikkelsen[40] has shown that the values for D_0 and E_D are 0.13 cm^2/s and 2.53 eV, respectively. The interstitial oxygen diffusivity under thermal equilibrium conditions is dominated by the process of jumping from one interstitial site to another.[43,57,63]

Heck and co-workers[56] found differences concerning diffusivity at 1100 °C during steam and HCl oxidation, suggesting that oxygen diffuses via a vacancy-dominant mechanism. According to this model oxygen hopping takes place via a substitutional site previously occupied by a vacancy. This model implies that oxygen hopping directly from one to another interstitial site should involve a too large lattice distortion; therefore, it is suggested that oxygen atoms hop through an intermediate substitutional position. On the other hand, Lee and Nichols[42,43] measured oxygen diffusivity in the temperature range 700–1160 °C, under the various conditions known to lead to a large supersaturation of point defects. They found that over more than two orders of magnitude in point defect concentration oxygen diffusivity is not affected by the variations of such conditions. Their findings clearly indicate that the oxygen diffusion above 700 °C is dominated by an interstitial hop mechanism.

b. Anomalous oxygen diffusivity. The phenomenon of enhanced oxygen diffusivity has been the object of several studies and attributed to different causes. Oates *et al.*[66] found that electron irradiation induced an enhanced oxygen diffusion, while other groups found its dependence on thermal history,[57,67–69] on the presence of metallic contamination,[69] and on interactions with carbon[70,71] or hydrogen.[64,72,73] Enhanced oxygen diffusion is also invoked to explain the formation of thermal donors and rodlike precipitates at low temperatures.

Enhanced oxygen diffusivity observed on electron-irradiated samples was studied by stress-induced dichroism.[66] The effect was explained with the formation of oxygen-vacancy complexes (*A* centers), or dioxygen vacancy complexes.[74] The capture of silicon interstitials by these complexes results in emission of oxygen interstitials. Such a process, i.e., successive capture and emission of vacancies, is assumed to occur faster than the normal oxygen hop, and it dominates the oxygen diffusion process above 300 °C. On the other hand, no evidence of interaction between silicon self-interstitials and oxygen atoms in the temperature range 25–500 °C has been given.

Stavola *et al.*[57] found that the oxygen hopping time is two orders of magnitude shorter in crystals subjected to an "oxygen stabilization" heat treatment (900 °C for 2 h), as compared to crystals in which oxygen has been well dispersed (heated at 1350 °C for 20 h). This suggests that thermal history of silicon wafers may significantly influence oxygen diffusivity.[67,75]

The presence of metallic contaminants (Fe, Cu) can enhance oxygen diffusion[69] up to two orders of magnitude.

Downloaded 21 Apr 2008 to 146.186.238.16. Redistribution subject to AIP license or copyright; see http://jap.aip.org/jap/copyright.jsp

SIONYX1403000026.0040

SAMSUNG EX. 1002 - 2505/4148

This effect is also explained by the presence of vacancies due to metallic contaminants.

Enhancement of oxygen diffusion was observed[64] upon treatment in a hydrogen plasma at low temperatures. At 300 °C an increase of the diffusivity by a factor of 300 is reported. Such an effect was not observed with other kinds of plasma treatments and, therefore, is not related to ion damage. More recently, Newman *et al.*[72] extended these measurements to the temperature range 225–350 °C. They revealed oxygen profiles by measuring the IR dichroism ratio as a function of the depth by grinding the surface after each measurement. It was found that oxygen hopping is favored by collision with diffusing hydrogen atoms, thus causing the enhancement of oxygen diffusion. Very recently, Zhong and Shimura[73] showed, by means of SIMS measurements, that even at higher temperatures (>1000 °C) annealing in hydrogen atmosphere produces an enhanced oxygen diffusion. They interpreted the results with a model based on the direct interaction between hydrogen and interstitial oxygen.

Shimura and co-workers[70] studied the outdiffusion behavior of oxygen and carbon in carbon-doped Cz silicon wafers by SIMS. They showed that the diffusion of both oxygen and carbon is greatly enhanced at 750 °C, but is significantly slowed down at 1000 °C. Enhanced oxygen diffusion is attributed to fast diffusing molecularlike O-C complexes. Wijaranakula[71] found also that at temperatures below 690 °C oxygen diffusion in silicon doped with carbon is enhanced. This phenomenon is attributed to C_i-O_i complexes, which could act either as a mobile species or as an activated state.

A possible explanation of thermal donor formation is based on an enhancement of the oxygen diffusivity at 250–500 °C of 3–4 orders of magnitude;[76] however, such enhancement is no longer a necessary requirement in a recently proposed model in which thermal donors are described as silicon self-interstitial agglomerates.[58,68,74]

Thermal treatment of silicon supersaturated with oxygen in the temperature range 500–625 °C produces rodlike defects. Transmission electron microscopy (TEM) studies of such defects lead to the conclusion that they contain coesite, i.e., the high-pressure phase of SiO_2.[77] This requires, however, that oxygen diffusion be enhanced by four orders of magnitude.[78] Recently, Bourret showed that the concentration of oxygen in the "coesite" particles was, in fact, very low.[79] Such features were reinterpreted as hexagonal silicon inclusions, presumably produced by the stress fields set up by the local condensation of silicon self-interstitial atoms; similar features were found in irradiated silicon. The fact that the defects have not been revealed by small-angle neutron scattering (SANS) measurements provides additional evidence that they do not contain significant amounts of oxygen and the local density of silicon atoms is not very different from that of the matrix. The new interpretation immediately eliminates the need for enhanced oxygen diffusion.

Several models have been proposed to explain enhanced oxygen diffusion in silicon, and are briefly reviewed here.

Gösele and Tan[80] proposed a model that explains enhanced oxygen diffusivity by the fast diffusion of molecular oxygen. Gaslike O_2 quasimolecules oriented along the ⟨111⟩ direction and centered at a tetrahedral site were studied by Needels *et al.*,[81] with evidence of just a small buildup of charge between the silicon and oxygen atoms, indicating that the Si-O interaction is extremely weak, thus supporting the model of a very mobile O_2 molecule. However, Oehrlein and Corbett[82] showed that the assumption of gaslike molecular oxygen diffusion leads to unrealistic values for oxygen diffusivity around and slightly above room temperature.

An alternative model for a fast gaslike oxygen dimer (O_2) with C_{2v} symmetry is proposed by Snyder *et al.*[83,84] From their theoretical modeling they conclude that the diffusivity of oxygen dimers is eight orders of magnitude higher than that of interstitial oxygen atoms.

Several authors proposed models that include complexes formed with point defects such as vacancies or self-interstitials to explain enhanced diffusivity. Oates *et al.*[66] attributed enhanced oxygen diffusion under electron irradiation at room temperature to the formation of V-O complexes which capture silicon self-interstitials so that the O atoms are reinjected in the lattice as interstitials, but at a much higher rate. Furthermore, Newman proposed the following reaction:[74]

$$O_i + O_i \rightarrow [O_i\text{-}O_i\text{-}V] + I, \tag{10}$$

where V is the vacant site occupied originally by a Si atom. I defects would be mobile and it seems likely that $[O_i$-O_i-$V]$ complexes would be more mobile than single O_i atoms, possibly by repeated emission and recapture of I atoms.

Ourmazd, Schröter, and Bourret[85] proposed that the fast diffusing species are oxygen-silicon self-interstitial complexes. In heavily carbon-doped Cz silicon, however, Newman *et al.*[72] showed that the reduction of $[O_i]$ concentration is not distinguishable from that in carbon-free samples, where self-interstitials are expected to have a longer lifetime. Thus, there is no evidence that the presence of self-interstitials enhances oxygen diffusivity.

Moleculelike C_i-O_i complexes or perturbed C(3) centers have been proposed by Shimura and co-workers[70] to explain enhanced oxygen diffusion in carbon-doped Cz silicon; however, from the variations in carbon and oxygen concentrations upon thermal treatment, Wijaranakula[71] deduced that such C_i-O_i complexes may contain more than 35 oxygen atoms. This result is not compatible with two or three oxygen atoms as proposed by Shimura and co-workers.[70] It implies that an enhanced oxygen diffusion could involve several mechanisms, and therefore an alternative model was proposed. The local strain field surrounding an isolated oxygen is compressive along the ⟨111⟩ axis, while that of the interstitial carbon is tensile along the ⟨110⟩ axis. If the C_i-O_i complexes are activated, the local strain field surrounding the complex would lower the energy barrier so that jumping of oxygen atoms is favored. Thus, enhanced oxygen diffusion could be a result of a strain field effect.

Recent reports that oxygen diffusion is enhanced by the presence of hydrogen[72,73] confirmed the model proposed by Estreicher,[86] according to which rapidly diffusing H atoms form complexes with O_i impurities as a transient species, and an oxygen diffusion jump may occur when a complex dissociates.

Downloaded 21 Apr 2008 to 146.186.238.16. Redistribution subject to AIP license or copyright; see http://jap.aip.org/jap/copyright.jsp

SIONYX1403000026.0041

SAMSUNG EX. 1002 - 2506/4148

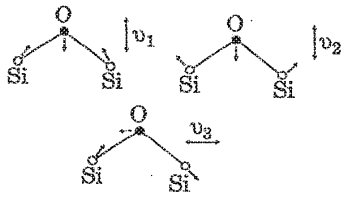


FIG. 13. Normal vibrations of the Si-O-Si defect molecule. $\nu_1=1205\ \mathrm{cm}^{-1}$, $\nu_2=515\ \mathrm{cm}^{-1}$, and $\nu_3=1107\ \mathrm{cm}^{-1}$ are the wave numbers corresponding to symmetric stretching, bending, and antisymmetric stretching vibration modes, respectively.

Not only enhanced, but also retarded oxygen diffusivity has been measured on several occasions. Heck and co-workers[56] reported that under oxidizing conditions at 1100 °C oxygen diffusion is retarded, and this retardation is found to be larger for steam than for dry oxidation. The observed difference was taken as evidence that oxygen diffuses via a vacancy dominant mechanism.

A variation in oxygen diffusivity was also reported by Shimura and co-workers.[70] From SIMS measurements on carbon-free and carbon-doped Cz silicon annealed at 750 °C, where precipitation is small, a good correspondence with the expected profile was obtained. On the other hand, results for annealing at 1000 °C show a strong retardation of oxygen diffusion, and a much stronger retardation in heavily carbon-doped samples. This additional retardation can be related primarily to the stronger oxygen precipitation, resulting in higher densities of silicon self-interstitials in the near-surface region. Consequently, this result suggests that oxygen diffusion is retarded by the presence of silicon self-interstitials and, in turn, supports a vacancy-dominant diffusion mechanism for oxygen in silicon.

C. Techniques for oxygen content determination in silicon

IR spectroscopy, with grating or with Fourier transform infrared (FTIR) spectrometers, is widely accepted and used as a nondestructive technique for routine measurements of interstitial oxygen concentration in silicon. It should be pointed out that IR spectroscopy is the only technique that can discriminate between interstitially dissolved oxygen and oxygen in complexes or precipitates. Other techniques such as SIMS, CPAA, photon activation analysis, x-ray diffraction, and gas fusion analysis are used to detect the total oxygen concentration in the bulk. It has also been shown that low-temperature IR spectroscopy could be used to detect oxygen in Fz or crucibleless-grown silicon crystals, where the oxygen concentration can be 3–4 orders of magnitude less than in Cz crystals.[87] IR spectroscopy can be employed for quantitative analysis after comparison with the results obtained by means of other techniques, as is discussed later. We briefly describe these techniques and underline their main characteristics, relevant for the measurements of oxygen in silicon.

1. Infrared spectroscopy

a. Room-temperature measurements. There are three absorption bands in the mid-IR spectral range observable at room temperature, one at 1205 cm^{-1}, one at 1107 cm^{-1}, and the third one at 515 cm^{-1}. Hrostowski and Kaiser[88] originally assigned these bands to symmetric and antisymmetric stretching and bending vibrations of the triatomic Si-O-Si "defect molecule," respectively (see Fig. 13). The 1107 cm^{-1} is the strongest and has been used for many years to measure the concentration of interstitial oxygen in silicon. This band is broad (~30 cm^{-1}) at room temperature and splits into a number of features at low temperatures: The assignment to an antisymmetric vibration (ν_3 in Fig. 13) is well established.[21,89] The assignment of the 515 cm^{-1} band is much more uncertain. Bosomworth *et al.*[24] have left this band unassigned and suggested that it is due either to a symmetric motion or to impurity-induced lattice absorption. The fact that this band looses intensity more quickly than the band at 1107 cm^{-1} upon oxygen precipitation heat treatments,[23,90,91] as observed by measuring stress-induced IR dichroism, offers a variety of possible interpretations; however, Stavola[22] showed that such a band is due to symmetric vibrations of interstitial oxygen.

The transmittance T, i.e., the ratio of the transmitted to the incident light intensity, depends on the wavelength λ. For accurate measurements the influence of multiple reflections on the wafer surfaces has to be taken into account. This is particularly important when both surfaces are polished. At normal incidence on a plane-parallel plate with polished surfaces the transmittance T is given by[92]

$$T=\frac{(1-R)^2e^{-\alpha d}}{1-R^2e^{-2\alpha d}}, \tag{11}$$

where R is the reflectivity which is related to the refractive index n (when extinction coefficient ~0) by

$$R=\left(\frac{n-1}{n+1}\right)^2. \tag{12}$$

For silicon $n\cong 3.42$ in the wavelength range from 5 to 50 μm, i.e., $R\cong 0.3$.

From Eq. (11) the absorption coefficient α can be derived,

$$\alpha=\frac{-1}{d}\ln\left(\frac{1}{R^2}\left\{\frac{-(1-R)^2}{2T}+\left[R^2+\left(\frac{(1-R)^2}{2T}\right)^2\right]^{1/2}\right\}\right). \tag{13}$$

The absorption coefficient measured at 1107 cm^{-1} is the sum of three contributions due to interstitial oxygen α_O, free carriers α_{FC}, and multiphonon lattice absorption α_L. Thus,

$$\alpha=\alpha_O+\alpha_{FC}+\alpha_L. \tag{14}$$

For lattice absorption at 1107 cm^{-1} the value $\alpha_L=0.85$ cm^{-1} can be used.[93] This value was measured directly at the National Institute of Standards and Technology from the spectrum of a 4.7-mm-thick polished FZ silicon crystal. Nevertheless, the calculation of the absorption coefficient α is not much affected by this value. For example, a change of 10% in this parameter would result in a change of 0.25% in the calculated value of the absorption coefficient.

Downloaded 21 Apr 2008 to 146.186.238.16. Redistribution subject to AIP license or copyright; see http://jap.aip.org/jap/copyright.jsp

SIONYX1403000026.0042

SAMSUNG EX. 1002 - 2507/4148

The term describing the free-carrier absorption α_{FC} depends on the resistivity of the analyzed sample. It is well known that free-carrier absorption can be neglected for concentrations below 10^{15} atoms/cm^3. Above that value, however, the absorption coefficient increases drastically.[94] For highly doped silicon with resistivities in the range of mΩ cm the free-carrier absorption becomes high enough to hide other contributions. Schomann and Graff[94] studied samples with different resistivities and they found that the sum of absorption coefficients $\alpha_L+\alpha_{FC}$ at 1107 cm^{-1} can be given as a function of the free-carrier concentration x (in 10^{15} atoms/cm^3),

$$\alpha=0.825e^{0.07x}\ (\mathrm{cm}^{-1}), \tag{15}$$

with $1\leqslant x\leqslant 20$.

The problem of free-carrier absorption in a highly doped material has been circumvented by Tsuya *et al.*[95] by high-flux electron irradiation, which results in trapping of the free carriers. Oates and Lin[96] have proposed a "short baseline technique" which takes into account the effects of the free carriers for the measurements of interstitial oxygen in heavily doped silicon. Recently, Borghesi *et al.*[97] have discussed an alternative method which uses a curved baseline. It was shown that their technique, which gives results equivalent to those of Oates and Lin, requires a simpler analytical procedure and is quite suitable for computerised routine measurements.

In order to obtain interstitial oxygen concentration C_{ox} (in atoms/cm^3) the absorption coefficient α_0 (in cm^{-1}) has to be multiplied by the calibration constant χ (in atoms/cm^2),

$$C_{ox}=\chi\alpha_0. \tag{16}$$

The exact determination of the calibration constant has been a matter of long studies and interlaboratory round-robin experiments: A wide range of values differing up to a factor of 2.5 is reported. A recent worldwide interlaboratory calibration yields the IOC-88 standard,[93]

$$\chi=(3.14\pm0.09)\times10^{17}\ \text{atoms/cm}^2. \tag{17}$$

This calibration factor is in close agreement with the JEIDA value of 3.03×10^{17} atoms/cm^2 (Iizuki *et al.*[98]). On the other hand, it deviates a lot from the value of the ASTM F 121-83 and the DIN 50 438/1 standards of 2.45×10^{17} atoms/cm^2 and the old ASTM F 121-79 standard of 4.81×10^{17} atoms/cm^2 used previously. A full compilation of all reported calibration factors is given by Baghdadi *et al.*[93] The optimum wafer thickness that results in the best accuracy for α_0 is given by $d=1/\alpha_0$. Therefore, a slice with thickness of 2 mm is recommended for measurement of C_{ox} in Cz silicon. Commercially produced wafers are much thinner (typically of the order of 700 μm for wafers of 150 mm in diameter): This causes a lower accuracy of the measurements of oxygen content. An additional difficulty with measurements of standard wafers is their backside roughness that results in the loss of intensity due to light scattering. This effect can reduce the transmittance of wafers when both surfaces are rough by approximately 40% with respect to that of double-side-polished wafers and by only few percent with respect to single-side-polished wafers.

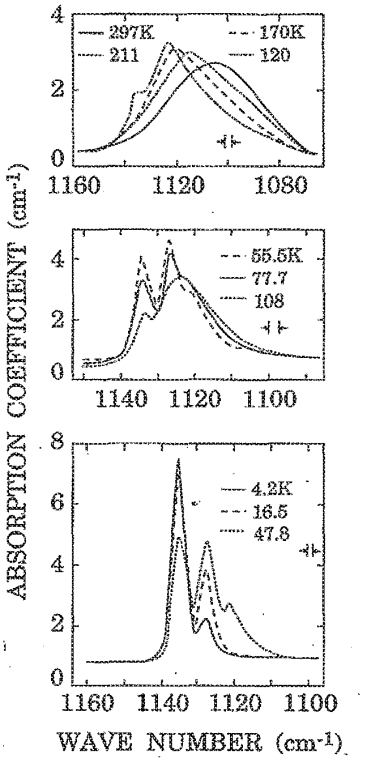


FIG. 14. Absorption coefficient of the antisymmetric vibration mode of Si-O-Si molecule at different temperatures (from Ref. 88).

Schomann and Graff[94] discussed the factors influencing the accuracy of measurements of oxygen content in silicon. They showed that the highest error comes from surface roughness which is important also in single-side-polished wafers. Both the sample temperature during measurement and the free-carrier absorption are also important, while the thickness variations, spectral resolution, and instrumental errors are less significant.

Usually, for the determination of oxygen content, FZ oxygen- and carbon-free silicon wafers are used as reference samples. Optimum measurement conditions require the same doping level, backside polishing, and precisely determined thickness both of the unknown and the reference wafer. Recently, a new method to determine precisely the O_i concentration in single-side-polished wafers was proposed.[99] The method is based on IR transmission measurements performed with p-polarized light impinging on the sample at the Brewster angle. In this case the 1107 cm^{-1} absorption band is easily distinguishable from the contribution due to light scattering at the backside surface from the difference between absorbance spectra of single-side- and double-side-polished wafers. This is due to the lack of multiple reflections for measurements with p-polarized light at the Brewster angle on single-side-polished wafers.

b. Low-temperature measurements. Under progressive cooling from room temperature, the 1107 cm^{-1} band gets distorted and shifts toward higher energies, as shown in Fig.

Downloaded 21 Apr 2008 to 146.186.238.16. Redistribution subject to AIP license or copyright; see http://jap.aip.org/jap/copyright.jsp

SIONYX1403000026.0043

SAMSUNG EX. 1002 - 2508/4148

14. At 77 K there are three bands at 1121.4, 1127.5, and at 1135.8 cm^{-1} and the most intense one is centered at 1127.5 cm^{-1} with a full width at half-maximum (FWHM) of about 5 cm^{-1}. In this case, the ratio $\alpha_{1127.5}(77\ K)/\alpha_{1107}(300\ K)$ is 2.56 ± 0.02, therefore the calibration factors found for room-temperature measurements are no more valid. New calibration constant values were proposed by Pajot[92] to obtain the O_i concentration (in atoms/cm^3) at 77 K,

$$C_{ox}=\chi_{77\ K}\alpha_{1127.5}, \tag{18}$$

where

$$\chi_{77\ K}=1.1\pm0.1\times10^{17}\ \text{atoms/cm}^2. \tag{19}$$

$\alpha_{1127.5}$ is the absorption coefficient (in cm^{-1}) of the 1127.5 cm^{-1} band measured with a resolution equal or better than 1 cm^{-1} to avoid instrumental distorsion.

At liquid-helium temperature the bands at 1121.4 and 1127.5 cm^{-1} disappear.[24] The 1135.8 cm^{-1} line shifts to 1136.4 cm^{-1} getting sharp and prominent with two weaker satellites at 1134.5 and 1132.7 cm^{-1}, due to the silicon isotopes with mass 29 and 30 (see Ref. 22). The FWHM of the 1136.4 cm^{-1} is only 0.6 cm^{-1} and, as the integrated intensity of the band is nearly the same at room temperature and at 8 K, the maximum absorption coefficient rises strongly so that $\alpha_{1136.4}(8\ K)/\alpha_{1107}(300\ K)\sim30$. This fact allows one to detect this band even in FZ silicon at 8 K.

Low-temperature measurements can also be used to measure oxygen absorption in very thin Cz samples: The limit of the sample thickness for observing O_i is calculated to be about 0.2 μm for 8 K transmission measurements. For thicker Cz silicon samples the huge increase of the O_i absorption band at 8 K leads to a saturation of the 1136.4 cm^{-1} band preventing accurate measurements. In this case, room-temperature measurements are more favorable. The detection limit for the O_i concentration reachable with the liquid-He temperature measurements, for a 1-cm-thick silicon sample, with a reasonable integration time, is about 3×10^{13} atoms/cm^3.

To determine the conversion factor for measurements at temperatures near liquid He some difficulties rise, due to the sharpness of the 1136.4 cm^{-1} band. In fact, only by measuring the band profile with an instrumental resolution eight times lower than the FWHM of the band can it be reasonably inferred that the measured profile is free of instrumental distortion. In this case, the maximum absorption coefficient is independent of the instrumental resolution and proportional to the integrated intensity. When the above conditions are not fulfilled, the maximum absorption coefficient measured decreases with the ratio between the FWHM of the band and the instrumental resolution, strongly depending on the latter. Then, for comparative measurements the spectral resolution used must be specified.

Since it is very difficult to measure the profile of the 1136.4 cm^{-1} band with the appropriate instrumental resolution, Pajot[92] proposed a conversion coefficient to determine the O_i concentration from liquid-He measurements, which takes into account $\Delta\omega_{obs}$, the observed FWHM of the 1136.4 cm^{-1} band. The proposed calibration coefficient to obtain C_{ox} in atoms/cm^3 is

TABLE IV. Conversion factors χ for the determination of interstitial oxygen concentration C_{ox} (in atoms/cm^3) from IR-absorption measurements at different temperatures.

Band position (cm^{-1})	χ (10^{17} atoms/cm^2)	T (K)	Ref.
1107	3.14 ± 0.09	300	93
1127.5	1.1 ± 0.1	77	92
1136.4	$0.14\pm0.02\Delta\omega_{obs}$	8	92
1136	0.169[a]	4	100
515	1	300	100

[a]With 1 cm^{-1} resolution.

$$\chi_{8\ K}=1.4\pm0.2\times10^{16}\ \Delta\omega_{obs}\ \text{atoms/cm}^2. \tag{20}$$

It should be pointed out that the measurements of this band at low temperatures are very sensitive to the temperature of the sample and to the resolution of the instrument; therefore, the exact calibration strongly depends on the experimental conditions.

Recently Wagner[100] discussed the influence of the sample temperature on the absorption coefficient; for a resolution of 1 cm^{-1} he gave the calibration factor to determine the O_i concentration in atoms/cm^3, for temperatures close to 4 K, to be

$$\chi=1.69\times10^{16}\ \text{atoms/cm}^2. \tag{21}$$

Low-temperature measurements of interstitial oxygen concentration are of particular importance if oxygen precipitates exist within the bulk, giving rise to the broad band close to 1107 cm^{-1} at room temperature, which significantly hides the real signal. In fact, measurements at low temperature have no influence on this broad band but strongly enhance the interstitial oxygen absorption band, so that precise measurements are possible.

Another approach is based on using the 515 cm^{-1} band, which has no underlying precipitate response, as a measure of interstitial oxygen concentration. The calibration factor for this band is[100]

$$\chi_{515}=1\times10^{17}\ \text{atoms/cm}^2, \tag{22}$$

which is temperature independent. This coefficient gives C_{ox} in atoms/cm^3 with α in cm^{-1}. The 515 cm^{-1} band, however, is much weaker than the 1107 cm^{-1} band and disappears much more quickly, so that it can be used only for samples with very high concentration of interstitial oxygen.

In silicon samples stressed along the ⟨110⟩ directions, the interstitial oxygen atoms are preferentially situated along the ⟨111⟩ directions, where lattice stress is minimized. By reducing the temperature while maintaining the stress, the preferential orientation can be frozen in. The temperature dependence of the reduction rate of the resulting dichroism of the 1107 cm^{-1} absorption band[21,22,58] yields information on the hop frequency of the interstitial atoms. Table IV summarizes the χ values for different temperatures for the 1107 and 515 cm^{-1} absorption bands.

Downloaded 21 Apr 2008 to 146.186.238.16. Redistribution subject to AIP license or copyright; see http://jap.aip.org/jap/copyright.jsp

SIONYX1403000026.0044

SAMSUNG EX. 1002 - 2509/4148

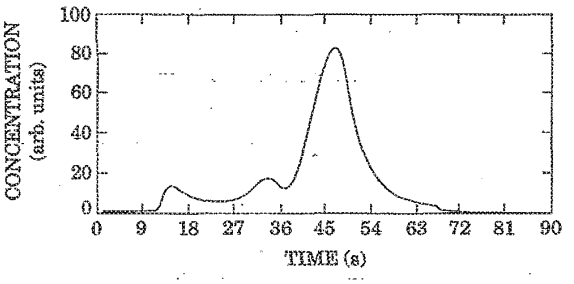


FIG. 15. Oxygen evolution from a silicon sample vs time. The first peak evidences surface contamination, the second one surface oxide, and the third one bulk oxygen (from Ref. 104).

2. Gas fusion analysis

Gas fusion analysis (GFA) is a well established method in metallurgy for the analysis of several gases (e.g., oxygen, nitrogen, and hydrogen) in solids. In the case of silicon, the samples are heated to above the melting point (up to 1500–1700 °C) in a special graphite crucible where the dissolved oxygen reacts with the carbon, producing CO. The developed CO gas is carried by flowing helium through a CuO bed heated at 400 °C where the reaction is completed, so that CO is converted into CO_2. The amount of this gas is subsequently detected by IR-absorption measurements, with a sensitivity about four times higher for the CO_2 than for the CO gas. Before reaching the samples the high-purity He carrier gas is purified by drying agents and by exposure to Cu turnings at 600 °C to remove the oxygen traces.

A different procedure is also possible where the CO gas is extracted into a vacuum system (vacuum fusion analysis) and then analyzed.

Baker, in 1970,[101] used GFA as a comparative tool in the quantitative determination of oxygen in silicon by IR spectroscopy (see Sec. II C 1). Later on it was used to a limited extent.[102–104] GFA has been developed primarily for measuring the oxygen content in heavily doped silicon, since it is suitable for any type or concentration of the doping material, while other methods (e.g., IR spectroscopy) are not suitable for heavily doped samples. The GFA method detects the whole oxygen content, hence, it cannot distinguish between interstitial and precipitated oxygen.

Prior to the measurement the samples are degreased, etched to remove the contaminated area close to the surface (typically in CP 4 etchant), then rinsed in de-ionized water, and etched in HF (40%) to remove any surface oxide. Finally, they are rinsed again and dried at 100 °C at a pressure lower than 5 Torr.

A typical GFA spectrum,[104] i.e., oxygen signal plotted vs time, is illustrated in Fig. 15. The three partially separated peaks indicate three sources of oxygen evolution from the sample. The first peak, occurring after about 15 s, is made up of various easily liberated oxygen-containing species from surface contaminants. The second and third ones are due primarily to surface oxide and bulk oxygen, respectively, although they may have other components. These two peaks can be well separated from each other by appropriate program of power inputs. The third peak is due primarily to bulk

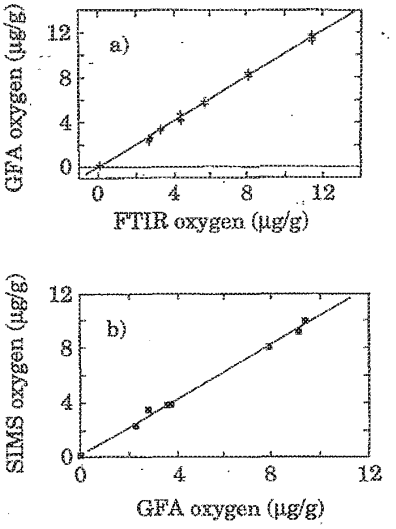


FIG. 16. Correlation of GFA relative oxygen concentration results with (a) FTIR data and (b) SIMS data (from Ref. 105). The continuous line represents the linear regression results.

oxygen but it could also be affected by the oxidation at the surface. Shaw and co-workers[104] demonstrated that such influence could be of the order of 10% of the typical oxygen level in Cz silicon. Such an effect is tentatively attributed to a very stable surface or near-surface oxide. Nonoxidized samples show excellent correlation between SIMS and GFA measurements.

The GFA technique needs calibration which is usually performed in two steps. For precalibration measurements standard steel samples are used. Basic elements of the second step are standard gas mixtures and silicon slices cut from selected ingot positions and measured with FTIR. The bulk oxygen content of the silicon sample is calculated in μg/g or atoms/cm^3. The correlation factor to convert μg/g to atoms/cm^3 is 0.877×10^{17}. The detection limit for a typical instrument can be $<1\times10^{16}$ atoms/cm^3 with a reproducibility of $<\pm2\%$ for 5–10 μg/g and $\pm3\%$–4% for 2–3 μg/g.

Figure 16 shows the correlation of GFA results with FTIR [Fig. 16(a)] and SIMS [Fig. 16(b)] data in the range from 0 to 12 μg/g. Correlation factors of 0.997 and 0.994 are found with FTIR and SIMS, respectively.[105]

3. Secondary-ion mass spectrometry

SIMS has become a very versatile analytical technique in the semiconductor industry aimed at bulk impurity measurements. Determination of oxygen in silicon samples by SIMS is possible independently of doping type and concentration. Generally, the primary ion beam used to bombard the sample surface is constituted by a noble gas; however, the secondary ion yield can be increased through the use of oxygen or cesium primary ion beams. Electropositive gas such as cesium can enhance negative secondary ion yield of electronegative species.[106,107] Williams *et al.*[106] showed the feasibility of using Cs^+ bombardment combined with the detection of negative secondary ions in a depth profiling mode. It

Downloaded 21 Apr 2008 to 146.186.238.16. Redistribution subject to AIP license or copyright; see http://jap.aip.org/jap/copyright.jsp

SIONYX1403000026.0045

SAMSUNG EX. 1002 - 2510/4148

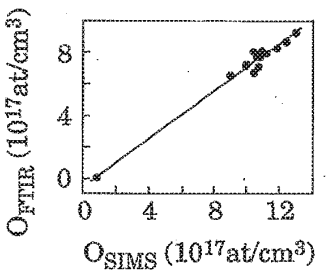


FIG. 17. Regression straight-line fit for oxygen concentration measured by FTIR and SIMS in highly doped silicon samples. The lowest point corresponds to undoped FZ silicon (from Ref. 97).

has been demonstrated that a high sensitivity can be obtained in the detection of oxygen in silicon. Typically, 10 mA/cm^2 of primary current density is used, which yields an oxygen background limit corresponding to 1×10^{17} atoms/cm^3 as calibrated using ion-implanted samples. Usually SIMS instruments use lower current density, implying a worse background limit for oxygen detection. In fact, the detection limit for oxygen in silicon is controlled by the balance established between the adsorption rate of oxygen from the residual gas of the vacuum system and the rate of sample erosion during sputtering with primary ion beam. Thus, ultra high-vacuum (UHV) conditions are necessary in order to obtain reliable results. A further increase in sensitivity is possible using a very high sputter rate. Wittmaack[107] demonstrated the importance of highly focused primary ion beam and UHV conditions in determining the background levels of oxygen in silicon. Moreover, the background level can be further lowered by using a secondary ion optics designed to preferentially extract ions from the central area of the rastered crater.

Bleiler *et al.*[108] developed a methodology for accurate and reproducible measurements of oxygen in heavily doped silicon wafers. Prior to measurements the samples were baked for approximately 30 min at 100 °C to remove adsorbed water. A proper vacuum system and a liquid-nitrogen-cooled shroud surrounds the sample holder ensuring about $2–3\times10^{-9}$ Torr pressure during the analysis. Another factor influencing the detection limit can be the natural abundance of different oxygen isotopes. While for ^{16}O resolution limit is 1×10^{17} atoms/cm^3, for ^{18}O, in-diffused from $H_2{}^{18}O$ or $^{18}O_2$ ambients, a detection limit approximately 500 times better can be obtained.

In addition, it is well known that the SIMS secondary ion yield varies quite drastically for different elements and for the same element in different materials (matrix effect).[109] To obtain quantitative SIMS data is thus not straightforward, and a careful calibration for an accurate comparison with other techniques is essential. Calibration of the oxygen yield by means of a known oxygen ion implantation profile results in an accuracy of about 30%, while the depth scale calibrated with a profile measurement of the sputter crater gives an accuracy of about 10%. The precision of the method is ±2% on a routine basis.[110]

The comparison between SIMS analysis and FTIR transmission measurements performed by Borghesi *et al.*[97] is given in Fig. 17. The figure shows O_{FTIR} vs O_{SIMS} straight-line fits. The correlation between the two sets of data is satisfactory, as indicated by the high value of the linear correlation coefficient (0.97) and by the low standard deviation (0.37×10^{17} atoms/cm^3) of the fits.

4. Other methods

In CPAA a silicon crystal doped with ^{18}O is irradiated with a 4.6 MeV proton beam or with α particles of 18–23 MeV, to produce the nuclear reactions[46,48,98]

$$^{18}O(p,n)\ ^{18}F \tag{23}$$

or

$$^{16}O(^3He,p)\ ^{18}F, \tag{24}$$

respectively. Both reactions produce the unstable fluorine isotope ^{18}F, which decays into ^{18}O with half-lifetime of 109.7 min by emitting a β^+ particle.

Oxygen content depth profiling is possible by repeated measurements after sequential etching of the surface layer.

The presence of the surface native oxide layer interferes with the signal of the oxygen in silicon. Therefore, care has to be taken in completely removing this oxide and the oxygen adsorbed during the measurement (this is usually performed by the *in situ* sputtering with a beam of argon ions). With reaction (24) this problem could be overcome by using highly ^{18}O-enriched oxides as diffusion sources and by etching back this oxide before the measurements, so that a native oxide with the normal low ^{18}O abundance is formed. The detection limit of CPAA is 1×10^{15} atoms/cm^3 and the accuracy about 20%.

The total oxygen content in silicon can also be measured by activation with high-energy photons, generated by bombardment of a tungsten target with 30 MeV electrons with a maximum of bremsstrahlung in the range of about 20 MeV. This technique is known as photon activation analysis (PAA). The mentioned energy range yields a giant resonance for the nuclear reaction[102]

$$^{16}O(\gamma,n)\ ^{15}O, \tag{25}$$

with half-lifetime of 2.03 min. During the irradiation the sample rotates, in order to be homogeneously activated. After irradiation the samples are etched with the solution nitric acid/hydrofluoric acid (1:1) in order to remove the activated surface oxide and to eliminate background problems. GFA (see Sec. II C 2) is then performed with iron as a metallic bath. The sample is completely dissolved at 2000 °C under helium gas flux. The sample collection efficiency is about 100%.

The determination of the activated oxygen is based on the annihilation radiation, generated by β^+ radiation of ^{15}O, which reacts with an electron under emission of two γ rays of 511 keV, that are further measured with two detectors in coincidence to determine oxygen decay curve and content.

Figure 18 shows a comparison of oxygen concentrations determined by PAA versus absorption coefficient of IR oxygen band at 1107 cm^{-1}. The accuracy of the method is typically better than ±15% and the detection limit is 5×10^{15} atoms/cm^3.

Downloaded 21 Apr 2008 to 146.186.238.16. Redistribution subject to AIP license or copyright; see http://jap.aip.org/jap/copyright.jsp

SIONYX1403000026.0046

SAMSUNG EX. 1002 - 2511/4148

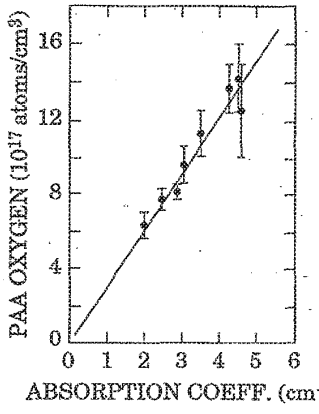


FIG. 18. Least-mean-squares fit of oxygen concentration data obtained by IR spectroscopy and PAA (from Ref. 102).

Two indirect methods of measuring oxygen in silicon also exist:

(1) determination of the lattice dilatation due to interstitial oxygen atoms by x-ray diffraction analysis;
(2) spreading resistance profiling of thermal donors, whose concentration is considered proportional to a power of starting interstitial oxygen concentration.

Takano and Maki[47] quantified the lattice dilatation due to the presence of interstitial oxygen atoms within the silicon lattice, considering the value of oxygen concentration as determined using IR-absorbance measurements. By stepwise removal of silicon from the surface they obtained dilatation profiles that were subsequently converted in oxygen diffusion profile. The sensitivity limit of this method is 1×10^{17} atoms/cm^3, on the basis of the determination of the diffusivities and solubilities only for a temperature range from 1100 to 1200 °C. Nevertheless, these measurements are in excellent agreement with those obtained by means of other methods.

The thermal donor profiling by spreading resistance measurements relies on the formation of thermal donors arising from oxygen related complexes. The rate of formation is proportional to the starting oxygen concentration to the third or fourth power. Thus, the gradient of oxygen concentration is converted in gradient of thermal donor concentration; however, such a correlation would require the comprehension of donor formation process, which has not yet been achieved.

III. THERMODYNAMICS AND KINETICS OF PRECIPITATE FORMATION

A. Nucleation

The first stage of oxygen precipitation in silicon is nucleation, a process leading to the formation of aggregates of a few O atoms, the so-called nuclei or precipitate embryos, within the silicon lattice. Once formed, precipitation nuclei can either further grow and form oxide precipitates or dissolve, depending on the characteristics of silicon crystals and on the thermal treatments performed. The fundamental parameter for nucleation (and, therefore, precipitation) is the degree of supersaturation of the solid solution constituted by the Si crystal (solvent) and the interstitial oxygen (solute), i.e., the ratio between the concentration of oxygen present in the Si crystal C_{ox} and its solubility limit C^*_{ox} (which is a function of temperature).

Nucleation can occur at crystal lattice sites where few interstitial oxygen atoms are close to each other (homogeneous nucleation[111–117]), or at lattice defects (heterogeneous nucleation[118–128]). Both processes lead to the formation of nuclei having different distributions and size.

In this subsection a general discussion about nucleation theory and related experimental results is reported, describing both homogeneous and heterogeneous processes. Moreover, some nucleation models[124] are illustrated and the mechanisms of nucleus dissolution, occurring during particular thermal treatments of silicon wafers, are described.[125]

1. Homogeneous strain-free nucleation

A very important parameter in the theory of nucleation is the critical radius r_c, distinguishing the nuclei which upon thermal treatment grow further ($r>r_c$) from those which are going to dissolve ($r<r_c$). It depends on several characteristics of the silicon crystal such as, for example, self-interstitial and vacancy concentrations, impurity type and content, elastic properties, and temperature.[114,115]

As a first step a theory for strain-free nucleation is illustrated, i.e., a theory that describes nucleation by completely neglecting the strain energy related to the structural difference between silicon and the oxide composing the nuclei. Under this assumption, the free energy ΔG required to form a spherical nucleus with radius r is given by the sum of two contributions: The particle-matrix interface energy and the chemical energy of supersaturation. The first term is positive since energy is needed to increase the nucleus surface, while the second one is negative since chemical energy of supersaturation decreases when solute atoms (oxygen) are removed from the solution and incorporated into the nucleus. The total free energy ΔG is therefore

$$\Delta G=4\pi r^2\gamma-\tfrac{4}{3}\pi r^3\Delta G_v, \tag{26}$$

where γ is the interface energy per unit area and ΔG_v is the volume free energy, related to the variation of the chemical energy of supersaturation per unit volume after oxygen atom removing from the solution. ΔG_v can be written as

$$\Delta G_v=\frac{k_BT}{v_P}\ln\frac{C_{ox}}{C^*_{ox}}, \tag{27}$$

where k_B is the Boltzmann constant, T is the absolute temperature, and v_P is the particle volume per oxygen atom (i.e., volume per oxygen atom in the silicon oxide SiO_x composing the nuclei).

The critical radius is defined as the value $r=r_c$ for which $d(\Delta G)=0$ (equilibrium); in the case of strain-free nucleation it can be derived from Eq. (26),

$$r_c=\frac{2\gamma v_P}{k_BT\ln(C_{ox}/C^*_{ox})}. \tag{28}$$

Downloaded 21 Apr 2008 to 146.186.238.16. Redistribution subject to AIP license or copyright; see http://jap.aip.org/jap/copyright.jsp

SIONYX1403000026.0047

SAMSUNG EX. 1002 - 2512/4148

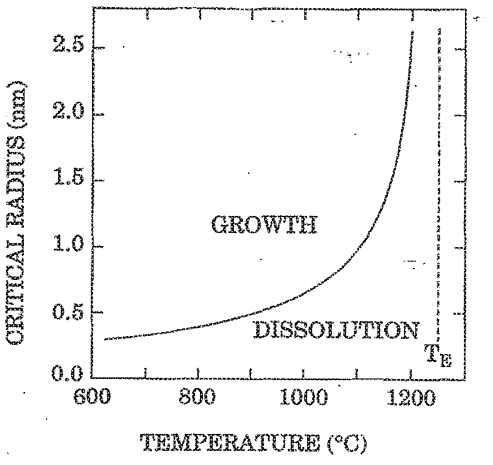


FIG. 19. Temperature dependence of the critical radius as determined from Eq. (28). T_E is the temperature at which the actual C_{ox} should equal C^*_{ox} (from Ref. 113).

When the nucleus radius r is smaller than r_c the volume free energy is lower than the surface free energy and, therefore, the nucleus dissolves. On the contrary, when $r>r_c$ the surface free energy is the smaller term in Eq. (26) and a precipitate can grow. From the expression of r_c it is clear that high temperatures and high oxygen concentrations enhance precipitate growth, reducing the nucleus critical radius. On the other hand, low temperatures correspond to low C^*_{ox}, which also causes r_c to decrease. These trends lead to a monotonically increasing function $r_c(T)$. Figure 19 reports the plot of $r_c(T)$ as deduced from Eq. (28), considering γ=410 erg/cm^2, v_P=37.66 Å^3, and $C_{ox}=11\times10^{17}$ atoms/cm^3. T_E in the figure is the temperature at which the actual value C_{ox} should equal C^*_{ox}.

In the classical theory of nucleation[118] the number N of nuclei of radius r per unit volume follows a Boltzmann distribution,

$$N(r)=c\,\exp\left(-\frac{\Delta G}{k_BT}\right), \tag{29}$$

where c is the number of nucleation sites per unit volume. The nucleation rate $J_0=N/t$, where t is the time, is given by

$$J_0=4\pi r_c^2 c(D/d)Zn(r_c), \tag{30}$$

where D is oxygen diffusion coefficient, d is the so-called atomic jump distance of oxygen, and Z is the Zeldovich factor ($Z\simeq10^{-2}$), corresponding to the fraction of oxygen atoms which are included in the precipitate nuclei immediately after nucleation. The nucleation rate dependence on the interstitial oxygen content and on the temperature as deduced from a best fit of experimental data[129] with Eq. (30) is reported in Figs. 20(a) and 20(b) respectively.[115]

In Fig. 20(a) the experimental data fit very well with the calculated line, while in Fig. 20(b) the agreement is less satisfactory, probably because of the neglected dependence of Z on the temperature. Figure 20(c) reports the function $J(T)$ for different interstitial oxygen contents and shows that for

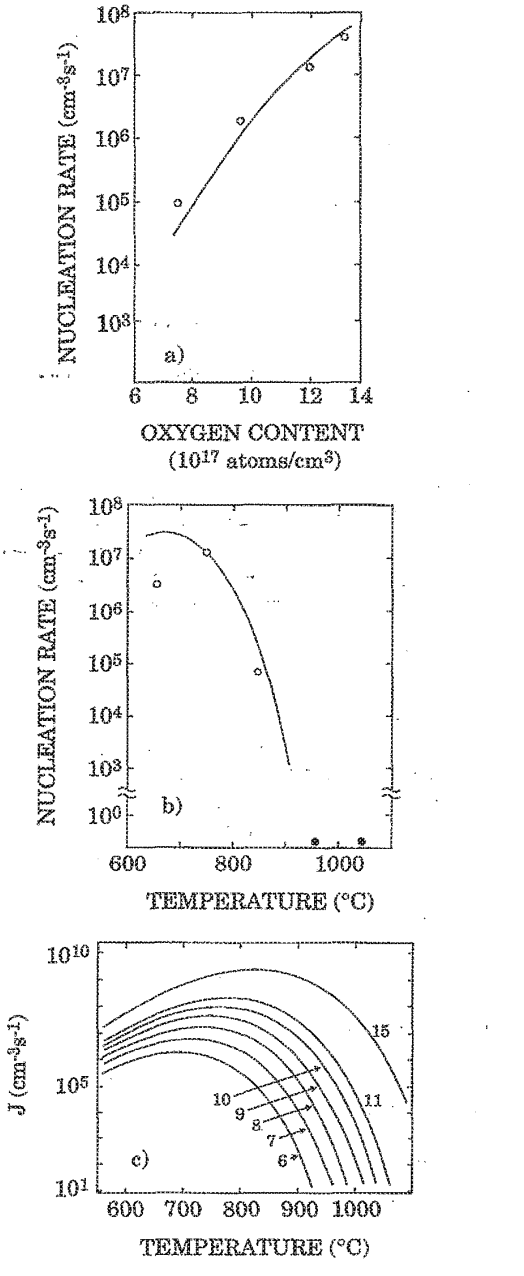


FIG. 20. Dependence of the nucleation rate on (a) the oxygen content and (b) the temperature. Open circles indicate the experimental data, solid circles show the detectability limit for two temperatures, and the lines are the best fit (from Ref. 115). (c) Dependence of the nucleation rate J on the temperature for crystals with different interstitial oxygen content (indicated in 10^{17} atoms/cm^3 units).

typical Cz wafers ($C_{ox}=7$–10×10^{17} atoms/cm^3) the optimum temperature range for nucleation is from 650 to 850 °C.

All the relations derived up to this point disregard the possible time dependence of the thermodynamic state of the solid solution. A nonsteady-state theory of nucleation can be used to describe the process occurring after a sudden cooling

Downloaded 21 Apr 2008 to 146.186.238.16. Redistribution subject to AIP license or copyright; see http://jap.aip.org/jap/copyright.jsp

SIONYX1403000026.0048

SAMSUNG EX. 1002 - 2513/4148

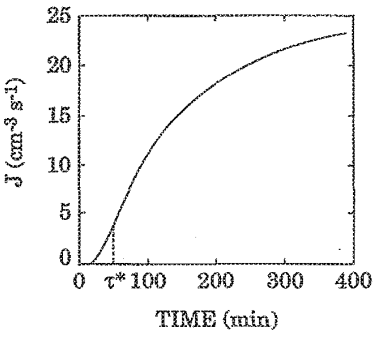


FIG. 21. Time dependence of the nucleation rate J. The value of the induction time τ^* is indicated.

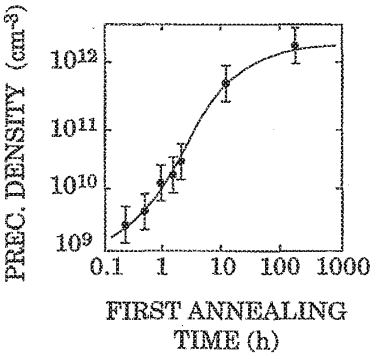


FIG. 23. Precipitate density in a sample with initial $C_{ox}=8.8\times10^{17}$ atoms/cm^3 annealed for 10 h at 1000 °C as a function of the duration of the nucleation annealing at 750 °C (from Ref. 129).

of the Si crystal, where a supersaturation state suddenly develops. Such a theory can be particularly interesting for the comparison with experimental results regarding precipitation rate, being more adequate to the real process. In the nonsteady-state the nucleation rate is

$$J(t)=J_0\exp\left(-\frac{\tau^*}{t}\right), \tag{31}$$

where J_0 is the steady-state nucleation rate of Eq. (30) and τ^* is called the nucleation time (or induction time). Figure 21, which reports the plot of $J(t)$, shows that the nucleation rate reaches its steady-state value J_0 as t approaches infinity (τ^* is also explicitly indicated). The nucleation time can be written as

$$\tau^*=\frac{n^2}{f}, \tag{32}$$

where $n=\frac{4}{3}\pi r_c^3 N$ is the number of oxygen atoms in the nucleus (N is the atomic concentration in the precipitates) and f the frequency of atom sticking to a critical nucleus. τ^* decreases with increasing the temperature, as shown in Fig. 22,[115] which reports $\tau^*(T)$ for different C_{ox} values (indicated in units of 10^{17} atoms/cm^3) obtained by using the same best-fit parameters as in Fig. 20. Higher temperature, as already pointed out and shown in Fig. 19, leads to smaller r_c values and, therefore, to a τ^* decrease. Moreover, at high temperatures the oxygen atomic diffusivity is high and also f increases, leading in turn to low τ^*.

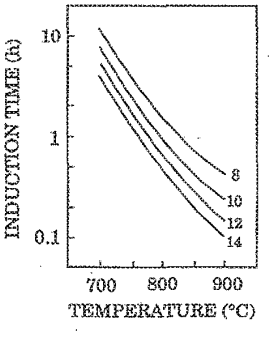


FIG. 22. Temperature dependence of induction time. Each curve is labeled by the C_{ox} value in 10^{17} atoms/cm^3 units (from Ref. 115).

τ^* can be obtained both from Eq. (31) and experimentally from the increase of precipitate density with time. The two evaluations lead to $\tau^*\simeq1$ h and $\tau^*\simeq10^2$ h, respectively,[115] but this discrepancy can be ascribed to the fact that probably not all the oxygen atoms reaching a nucleus remain there.

The nucleation rate has been deduced by Inoue and co-workers[129] to slow down, reaching a saturation value, as the duration of the nucleation annealing increases. Figure 23 shows the precipitate density as a function of nucleation annealing time for samples annealed at 750 °C (nucleation) and then for 10 h at 1000 °C (precipitation). The precipitate density has been measured[129] by the surface etching technique (see Sec. IV A) after the second annealing. The authors propose an explanation for the described saturation. It can take place when the diffusion layers surrounding each nucleus overlap, so that further oxygen diffusion leads to the growth of the existing nuclei more likely than to the creation of new ones. The diffusion layer has been assumed as spherical, with radius $\sqrt{Dt}$, where D is the diffusion coefficient of oxygen in silicon and t is the nucleation time. Saturation occurs when the average distance between two adjacent nuclei is of the order of $\sqrt{Dt}$. The following relation between the number density of nuclei N and $\sqrt{Dt}$ is therefore assumed

$$N^{-1/3}=(Jt)^{-1/3}=\sqrt{Dt}. \tag{33}$$

Then the time t_s when saturation begins and the saturation number density of nuclei N_s can be determined,

$$t_s=(\tfrac{4}{3}\pi D^{3/2}J)^{-2/5} \tag{34}$$

and

$$N_s=J^{3/5}(\tfrac{4}{3}\pi D^{3/2})^{-2/5}. \tag{35}$$

This model for the saturation in nucleation is well confirmed by the good agreement between experimental and calculated $N(t)$ values, shown in Fig. 24 for various annealing temperatures, for a silicon crystal with $C_{ox}=11\times10^{17}$ atoms/cm^3.

Downloaded 21 Apr 2008 to 146.186.238.16. Redistribution subject to AIP license or copyright; see http://jap.aip.org/jap/copyright.jsp

SIONYX1403000026.0049

SAMSUNG EX. 1002 - 2514/4148

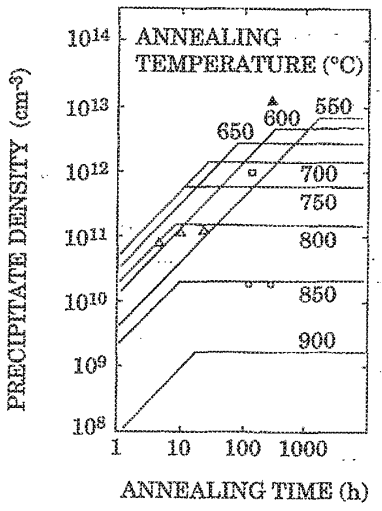


FIG. 24. Experimental data of the density of nuclei as a function of annealing time for different annealing temperatures: 650 °C (solid triangle); 750 °C (open squares); 800 °C (open triangles); and 850 °C (open circles). The lines are the $N(t)$ functions calculated for different temperatures according to Eq. (35) (from Ref. 129).

Homogeneous nucleation has been reported[115,125] as responsible for a phenomenon called time lag in precipitate growth, which is considered the experimental evidence of the time dependence of Eq. (31). Time lag consists in a "delay" of precipitation detected in samples subjected to a short high-temperature preannealing (e.g., 5 min at 1200 °C) before the precipitation treatment (several hours at low temperature). Considering Eq. (31) (or looking at Fig. 21), time lag can simply be related to the initial transient $\Delta t \cong 3-4\tau^*$, when $J(t)$ is still noticeably different from the steady-state value J_0. Some authors[112] disagree, considering time lag a piece of evidence for heterogeneous nucleation (see Sec. III A 3).

Figure 25[115] reports experimental data regarding time lag in precipitation, i.e., the precipitate density detected in silicon wafers subjected to different thermal treatments, which is directly related to the initial concentration of nuclei. The precipitate density in the sample subjected to a short preannealing and then quenched is initially very low, abruptly increasing after about 70 h. This initial delay has been related to the nucleation time.

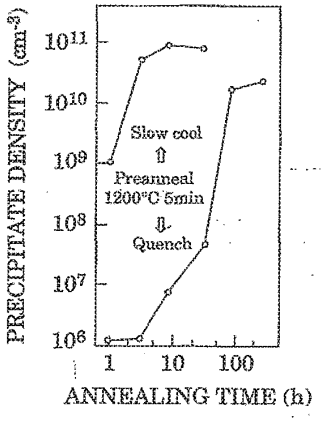


FIG. 25. Time dependence of precipitate density during anneal at 800 °C for two samples subjected to preanneal at 1200 °C for 5 min. The upper curve refers to a slowly cooled sample, the lower one to a quenched sample (from Ref. 115).

2. Homogeneous nucleation with strain

The assumption of nucleation as a strain-free process imposes a serious limit for the theory outlined in Sec. III A 1, even if it results in qualitatively good agreement with experimental data and partially includes (implicitly) the lattice strain when considering the interface energy γ. More adequate models have been proposed[114,116,130,131] to explicitly take into account the strain-energy contribution to the total free-energy variation ΔG. Indeed, the difference between the volume per Si atom in the precipitate V_P and in the silicon crystal V_{Si} (volume misfit) causes an increase of precipitate strain energy during growth (in particular for the case of SiO_2 in Si, $V_P > V_{Si}$). Absorption of n_V vacancies from the bulk of silicon and/or emission of n_I self-interstitial atoms release part of this strain.[116,117] Consideration of this last contribution leads us to include intrinsic point defects in the nucleation process, although the term homogeneous nucleation is still used to distinguish this case from that which involves extrinsic defect contribution or intrinsic defects as the main constituents of the nuclei.

On the basis of these arguments about strain, it is clear that Eq. (26) has to be modified. According to Hu,[114] it is useful to describe the volume variation of a precipitate, when its radius r increases by dr, in terms of elastic properties of silicon. When a few Si atoms are included in a precipitate nucleus, they leave a cavity in the bulk of the silicon. Such a cavity can be described as a sphere of radius r_0 to compare with the growing particle. At the same time the growing particle has a different radius $r=(1+\delta)r_0$, where δ is the linear misfit between Si and SiO_x lattices ($\delta \sim 0.3$ for SiO_2). To reach a common radius r_P (the actual nucleus radius) the cavity must be expanded, while the nucleus must be compressed. The final radius r_P falls between r_0 and r, i.e., $r_P = r_0(1+\epsilon)$, where $0<\epsilon<\delta$. Considering the shear modulus of silicon μ and the bulk compressibility of SiO_x K and assuming $\epsilon, \delta \ll 1$, the strain ϵ compressing the precipitate is

$$\epsilon = \frac{\delta}{1+4\mu/3K}. \tag{36}$$

The final radius r_P can also be written as

$$r_P = r\frac{(1+\epsilon)}{(1+\delta)}. \tag{37}$$

Then, ΔG of a SiO_x spherical precipitate, considering an increase dr of the radius r, is

$$\Delta G = \left[(1+\delta+\epsilon)^3 \frac{xrk_BT}{V_P}\left(-n_I \ln\frac{C_I}{C_I^*} - n_V \ln\frac{C_V}{C_V^*} - \ln\frac{C_{ox}}{C_{ox}^*}\right) + 2\gamma + 6\mu\delta\epsilon r\right] 4\pi r\, dr, \tag{38}$$

Downloaded 21 Apr 2008 to 146.186.238.16. Redistribution subject to AIP license or copyright; see http://jap.aip.org/jap/copyright.jsp

SIONYX1403000026.0050

SAMSUNG EX. 1002 - 2515/4148

where n_I and n_V are the numbers of interstitials and vacancies emitted and absorbed, respectively, C_I and C_V are the concentration of interstitials and vacancies, respectively, and C_I^* and C_V^* are the solubility limits of these defects in silicon. The term $(6\mu\delta\epsilon r)4\pi r\,dr=(6\mu\delta\epsilon)dV$ is the change in the total elastic energy of a spherical nucleus related to a volume variation dV.

From Eq. (38) a more complete expression for the critical radius r_c that also considers strain energy is obtained,

$$r_c=2\gamma\left[\frac{(1+\delta-\epsilon)^3 x k_B T}{V_P}\ln\frac{C_{ox}}{C_{ox}^*}\left(\frac{C_V}{C_V^*}\right)^{n_V}\left(\frac{C_I^*}{C_I}\right)^{n_I}\right]^{-1}. \quad (39)$$

Besides the strain-related contribution, this expression also illustrates the role of interstitial Si atoms and vacancies in strain relief. It is important to note that in the case of strain-free nucleation, i.e., $\epsilon=\delta=0$, Eq. (39) is identical to Eq. (28).

Equation (39) can be rewritten in a useful form using the following expressions for C_{ox}, C_{ox}^*, C_I, C_I^*, C_V, and C_V^*:

$$C_X=c_X\exp\left(-\frac{T_X}{T_s^X}\right) \quad (40a)$$

and

$$C_X^*=c_X\exp\left(-\frac{T_X}{T}\right), \quad (40b)$$

where c_X is a constant and $X=I$, V, ox. T_X is the characteristic temperature derived from the heat of solution $H_X=k_B T_X$ and T_s^X is the temperature at which the actual X content should be soluble ($T_s^{ox}=T_E$ in Fig. 19). By substituting Eqs. (40) in Eq. (39) we obtain

$$r_c=\frac{2\gamma v_P}{x k_B T}\frac{T_s^{ox}}{\xi T_s^{ox}-\lambda T}, \quad (41)$$

where

$$\xi=(1+\delta-\epsilon)\left(1+\frac{n_V T_V}{T_{ox}}\frac{n_I T_I}{T_{ox}}\right)-\frac{6\mu\delta\epsilon v_P}{x k_B T_{ox}}$$

and

$$\lambda=(1+\delta-\epsilon)\left[1+\left(\frac{n_V T_V T_s^{ox}}{T_{ox}T_s^V}-\frac{n_I T_I T_s^{ox}}{T_{ox}T_s^I}\right)\right].$$

In intrinsic thermal equilibrium conditions ($T=T_s^I=T_s^V$), the critical radius becomes

$$r_c=\frac{2\gamma v_P}{x k_B T}\frac{T_s^{ox}}{\xi' T_s^{ox}}, \quad (42)$$

where

$$\xi'=(1+\delta-\epsilon)-\frac{6\mu\delta\epsilon v_P}{x k_B T_{ox}}.$$

Equation (42) relates the critical radius r_c to the temperature at which the actual interstitial oxygen content should be soluble T_s^{ox}. This is very interesting because the initial oxygen concentration is usually a known parameter and can be controlled.

Another interesting model for homogeneous nucleation involves thermal donors, considered as aggregates of several oxygen atoms.[132] Assuming that only one type of thermal donors dominates carrier increase during thermal donor formation and considering the results of the classical nucleation theory about the concentration of nuclei and the nucleation rate [see Eqs. (29) and (30)], the dominant thermal donors are deduced to act as nuclei for oxygen precipitation in Cz silicon above 600 °C. This result allows one to predict the nucleation rate dependence on initial oxygen concentration, annealing temperature, and carrier concentration, which are found to well reproduce the experimental findings. Nevertheless, in Ref. 132 the authors underline that there is also some experimental evidence of heterogeneous nucleation which they believe to simultaneously occur and compete with homogeneous nucleation.

Other nucleation models including intrinsic point defects as active elements have been proposed[112,119,120] and are illustrated in the following subsection as heterogeneous nucleation models.

3. Heterogeneous nucleation

Nucleation of oxide precipitates can occur on lattice defects, mainly substitutional carbon atoms, carbon-oxygen complexes, and point defects. A clear description of the mechanisms involved in this phenomenon is not yet available, but some general trends have been evidenced[119–123,125–127] from the analysis of a lot of experimental data.

Regarding the influence of carbon, several phenomena enhancing oxygen nucleation and precipitation are widely accepted to occur. First of all, in C-rich samples the variation of interstitial oxygen concentration, usually related to precipitation, has been shown to increase. At the same time, substitutional carbon concentration, measured through the IR absorption of Si—C bonds, decreases. Probably, oxygen aggregating on carbon atoms during precipitate nucleation makes C undetectable, due to the variation of the vibrational properties of Si—C—Si bonds.

Carbon atoms in the silicon lattice can form SiC particles, which produce a volume contraction of about 50%. Therefore, C presence can cause the formation of free volume in the silicon crystal, available for nuclei and precipitates. Moreover, this free volume leads to a C_I decrease and, therefore, also to a r_c decrease [see Eq. (39)].

Besides single C atoms, carbon-oxygen complexes have also been proposed to act as heterogeneous nuclei for oxygen precipitation in Cz silicon.[122,133–136] The same experimental data reported in support of the assumption of nucleation related to substitutional C atoms might also lead to the hypothesis of a significant role of C-O complexes. The variation of IR-absorption bands related to C-O complexes has been connected to changes in the interstitial-oxygen peak due to precipitation. Therefore, C-O complexes are deduced to be involved in precipitation as the most probable nuclei. On the basis of these findings heterogeneous nucleation is indicated as predominant at low temperatures, while the homogeneous mechanism predominates at higher temperatures. In Fig. 26 the IR spectra of samples annealed at 900 °C for different

Downloaded 21 Apr 2008 to 146.186.238.16. Redistribution subject to AIP license or copyright; see http://jap.aip.org/jap/copyright.jsp

SIONYX1403000026.0051

SAMSUNG EX. 1002 - 2516/4148

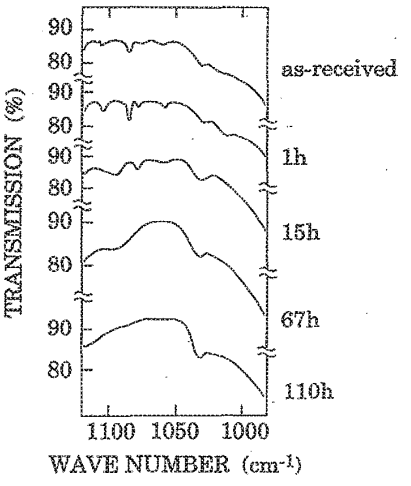


FIG. 26. IR transmission spectra of Cz silicon samples heated at 900 °C for various times in N_2, showing the C-related absorption bands (from Ref. 122).

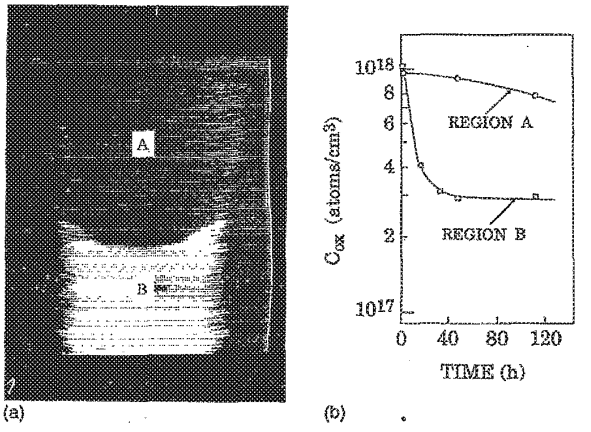


FIG. 27. X-ray topography (left-hand side) of a longitudinal section of a quenched silicon crystal pulled at 1 mm/min and annealed at 1000 °C for 16 h. Region A contains swirl defects, while region B is defect free. Interstitial oxygen concentration vs annealing time at 1000 °C (right-hand side) measured at crystal axis in regions A and B (from Ref. 120).

times are reported.[122] The absorption bands present in the spectrum of the as-received sample related to C-O complexes decrease with the interstitial-oxygen band as the annealing time is increased and precipitation takes place. After 110 h annealing, the intensity of all these bands is below the detection limits.

Intrinsic point defects, in particular vacancy clusters formed in the silicon crystal during growth and including also solute atoms, have been assumed to be possible nuclei[112,119,137] (modified homogeneous nucleation). One of the main arguments supporting this hypothesis is the role of the clusters in releasing the volume misfit associated with precipitate growth. At high temperatures these centers can also dissolve, due to the self-interstitial generation in the Si crystal. This phenomenon has been indicated[112] as responsible for the above-mentioned time lag in precipitation, instead of the explanation based on the homogeneous model for nucleation. Moreover, the hypothesis that clusters of vacancies can be part of the nuclei is supported by the experimental data about precipitation reduction in samples treated in oxidizing ambient,[111,114] where vacancy clusters are known to annihilate. On the basis of the hypothesis of heterogeneous nucleation occurring at vacancy-solute atom clusters, Ravi[119] suggested two possible models for nucleation, which can also explain the Si crystal faceting observed on the sample surface after precipitation. The first one postulates a direct nucleation of SiO_2 at vacancy clusters. The second one is a multistep mechanism, involving stacking faults. Indeed, extrinsic stacking faults can nucleate at vacancy clusters during heat treatments, then becoming nucleation sites for SiO_2 precipitates during further annealing. The mentioned faceting of the Si crystal surface arises from the inhibition of oxidation at the precipitate sites.

Other possible centers for heterogeneous nucleation have been indicated in the so-called swirl defects,[120,121] whose nature is not clear, but in any case related to the condensation of self-interstitials. High concentrations of these defects reduce precipitation, while silicon crystal doping can enhance the process. Indeed, doping reduces swirl-defect concentration, thus preventing their detrimental effect on precipitation. Figure 27 (left-hand side) shows the x-ray topography of a longitudinal section of an undoped Si ingot annealed at 1000 °C for 16 h.[120] Region A is rich in swirl defects, while region B is defect free. In Fig. 27 (right-hand side) the interstitial-oxygen concentration at different stages of the annealing is also reported.[120] In region B the decrease of O_i concentration, connected with precipitation, is much more evident, confirming the retardation role of swirl defects.

On the other hand, self-interstitials seem to help precipitation of oxygen, acting as nuclei, when the oxygen supersaturation ratio s (C_{ox}/C^*_{ox}) is smaller than 5. If s is increased their influence decreases and becomes negligible for $s=20$. Also the mentioned retardation of precipitation in samples treated in oxidizing ambients has been related[111,114] to the decreased self-interstitial concentration in such samples.

Retardation of precipitation, experimentally observed using IR spectroscopy in samples subjected to prolonged nucleation treatments (2–16 h), has also been related[125] to the possible dissolution of the nuclei, described by an interesting model. According to that model, dissolution takes place at the onset stage of the precipitate-growth annealing, due to the large supersaturation of silicon self-interstitials. Indeed, this increases r_c and a large fraction of nuclei dissolve, because the reaction

$$(1+y)\mathrm{Si}+2O_i \rightleftharpoons \mathrm{SiO_2}+yI \tag{43}$$

is driven to the left-hand side. The generation of self-interstitials, also taking place at the initial stage of the growth annealing, is essentially due to the need of an accommodation volume for the precipitates (remember that $V_P > V_{Si}$).

To complete this overview on heterogeneous nucleation it is worth mentioning the findings of Wada *et al.*,[123] who

Downloaded 21 Apr 2008 to 146.186.238.16. Redistribution subject to AIP license or copyright; see http://jap.aip.org/jap/copyright.jsp

SIONYX1403000026.0052

SAMSUNG EX. 1002 - 2517/4148

deduced nucleation in as-grown silicon crystals to be heterogeneous from the characteristic nucleation temperature observed (1000–1250 °C), which is higher than those predicted for the homogeneous process. Moreover, they related precipitation to thermal fluctuations in the crystal during growth, causing the formation of the heterogeneous nucleation centers.

4. Nucleation in as-grown crystals

Oxygen precipitation in as-grown silicon crystals is a very important process, being characteristic of the starting conditions for further precipitation. Several experimental works[113,123,128,131,138] deal with this subject and some models for nucleation in these samples have been proposed.

In the framework of a growth model for precipitates in as-grown crystals,[113] essentially developed using the concept of critical radius, nucleation is assumed to be homogeneous and to proceed at the same rate as during nucleation annealing (about 10^{17} nuclei/cm^3 s at 750 °C).[139] It takes place during the crystal cooling after heating cutoff, which is faster (about 100 °C/h) than crystal seed-end cooling during growth.

Another mechanism of nucleation leading to the formation of precipitates in as-grown silicon crystals has been proposed[123] on the basis of TEM observation and crystal cooling measurements. From the experimental results about precipitate shape, dimensions, and density in as-grown silicon samples the authors deduce that nucleation occurs via an heterogeneous mechanism, at temperatures from 1250 to 1000 °C during crystal cooling.

An interesting nucleation model including both homogeneous and heterogeneous processes has been recently developed[128] on the basis of experimental findings on particular samples. After halting the crystal growth for well-specified time intervals, therefore annealing the growth part of the crystal, the authors studied oxygen precipitation in as-grown samples. Precipitate density was found higher in the regions where the temperature during pulling halt was below 800 °C or above 1200 °C and this inhomogeneity of precipitate distribution was related to a different nucleation rate. Regarding the first regions, nuclei are assumed to be homogeneous, while the nuclei responsible for the high-temperature precipitation are assumed to be heterogeneous, probably clusters of point defects, because at such high temperature (≥1200 °C) C_{ox}^{*} was higher than C_{ox}. Moreover, when the temperature during the halt of pulling is high the density of heterogeneous nuclei depends on C content in the silicon crystal. On the basis of these experimental findings, nucleation is deduced to proceed as follows. First, some nuclei are formed at $T>1200$ °C, remaining essentially inactive (unless the crystal is annealed at low temperature, as during cooling). Then, between 1100 and 900 °C the nuclei can incorporate C atoms and, finally, below 800 °C they become active as centers for precipitation (at this stage nucleation is heterogeneous).

Recently, Puzanov and Eidenzan[131] proposed that the formation of oxygen precipitation nuclei during crystal growth proceeds through the following stages, which depend on the crystal growth regime:

(i) recombination of intrinsic point defects near the crystal-melt interface, which determinates the type and concentration of surviving point defects in the growing crystal;

(ii) redistribution of intrinsic point defects, their annealing at the crystal lateral surface and smoothing of concentration profile (diffusion stage);

(iii) agglomeration of impurities and intrinsic point defects:

(a) vacancy regime: A-defect (V-O complex) nucleation as a result of vacancy-oxygen interaction;
(b) interstitial regime: B-defect generation as a result of coaggregation of self-interstitials and carbon atoms;

(iv) growth and transformation of agglomerates involving consumption of intrinsic point defects:

(a) vacancy regime: transformation of A-defect nuclei and reduction in vacancy concentration;
(b) interstitial regime: transformation of some B-defects into A-defects; reduction in self-interstitial concentration;

(v)

(a) vacancy regime: formation of secondary (low-temperature) nuclei;
(b) interstitial regime: transformation of residual B-defects into centers of oxygen precipitation.

In this model each stage may depend not only upon its conditions, but also upon the results of all previous stages. Vacancy or interstitial regimes depend on the type and concentration of intrinsic point defects remaining in the crystal after recombination, depending on the ratio $\xi = V/G_0$, where G_0 is the longitudinal temperature gradient near the interface and V is the growth rate. For $\xi<\xi_t=3.3\times10^{-5}$ cm^2 s^{-1} K^{-1} the remaining defects are self-interstitials and for $\xi>\xi_t$ they are vacancies. As a rule, crystals produced commercially are grown in the vacancy regime.

B. Precipitation

Oxygen precipitation in silicon is a phenomenon of aggregation of oxygen atoms, normally uniformely distributed within the Si crystal. As a consequence, small particles of SiO_x, $1\leqslant x\leqslant 2$, form within the silicon crystal. Nowadays it is widely accepted that precipitation is driven, in a wide temperature range, by the diffusion kinetics.

In 1958 Ham proposed[140] a general theory to explain the kinetics of precipitation in a supersaturated solution by considering the phenomenon as diffusion limited. The validity of this model has been checked by different authors and experimentally confirmed. In particular, Patrick *et al.*,[141] using a combination of TEM and IR measurements, showed that the growth of precipitates at about 1000 °C in a dislocation-free matrix fits very well the Ham kinetics. Wada *et al.*,[123,142] on the basis of TEM observation, extended the validity of the model to the temperature range from 750 to 1050 °C. A detailed analysis and more extended experimental results were reported for the temperature range from 650 to 1050 °C using different techniques (see Sec. IV) such as chemical etching, optical scattering, cold neutron scattering, and infrared

Downloaded 21 Apr 2008 to 146.186.238.16. Redistribution subject to AIP license or copyright; see http://jap.aip.org/jap/copyright.jsp

SIONYX1403000026.0053

SAMSUNG EX. 1002 - 2518/4148

absorption by Newman *et al.*[143] and by Binns *et al.*[144] Oxygen precipitation below 650 °C follows a kinetics that no longer agrees with Ham's theory since a negligible fraction of atoms is involved in the oxide precipitates.[68]

The starting hypotheses to develop Ham precipitation model are as follows.

(1) The silicon lattice is defect free (i.e., without any extended defects such as dislocations, besides precipitation nuclei).
(2) The initial interstitial oxygen concentration C_0 (atoms/cm^3) in the as-grown crystal is uniform.
(3) The concentration of nuclei N (cm^{-3}) remains constant during the heat treatment. This means that nucleation already occurred in as-grown material, in practice during crystal growth.
(4) In the silicon lattice spherical precipitate nuclei having the same radius r_0 much smaller than their distances are present.
(5) The precipitates (oxygen sinks) are made of a form of silica with oxygen concentration C_P. The oxygen concentration in the silicon matrix immediately adjacent to the precipitates C' is the equilibrium solubility limit C^*_{ox} (see Sec. II B 3) at the considered temperature (after an infinite time). The variation of C' during precipitate growth is neglected.

Assuming the particles are arranged in a simple cubic lattice and dividing the lattice into equivalent symmetrical cubic cells, each one centered at one precipitate nucleus, no oxygen flux is expected to cross the cubic cell boundaries if the distribution of nuclei is uniform.

It is worth noting that the assumption of spatially uniform distribution is not necessary, provided any crystal inhomogeneities are absent. In fact, oxygen atoms follow three-dimensional random walks and only a small probability of sticking to growing particles exists, due to the presence of oxygen concentration gradient only close to the precipitate, as is shown later.

The oxygen concentration profile $C_{ox}(r,t)$ as a function of the distance r from the center of the precipitate and time t fulfills the Fick equation,

$$\frac{\partial C_{ox}(r,t)}{\partial t} = D\nabla^2 C_{ox}(r,t), \tag{44}$$

where D is the oxygen diffusion coefficient, which is assumed to be independent of time, oxygen concentration, and position (see Sec. II B 4). This equation has to fulfill two boundary conditions:

(i) At the precipitate/matrix interface ($r=r_0$) the oxygen concentration is equal to C';
(ii) no solute flux can cross the cell boundary, due to symmetry.

We note that, taking into account the above-mentioned boundary conditions, it is sufficient to solve the Fick equation only for a single cubic cell.

To find the solution of Eq. (44) we first consider spherical precipitates with the value r_0 of precipitate radius constant and equal to its final value $r_0(\infty)$ (steady-state value, i.e., the value after infinite annealing time) and then we study the general case of increasing precipitate radius. Finally, the case of disk-shaped precipitates with increasing thickness is considered.

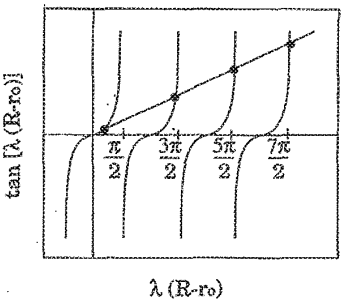


FIG. 28. Illustration indicating the solutions of $\tan\{\lambda(R-r_0)\}=\lambda R$.

1. Spherical precipitates with fixed radius

In order to solve the Fick equation in this case, it is useful to expand $C_{ox}(r,t)-C'$ in terms of the eigenfunctions of the equation

$$\nabla^2\psi_n(r)+\lambda_n^2\psi_n(r)=0, \tag{45}$$

obtaining

$$C_{ox}(r,t)-C'=\sum_{n=0}^{\infty} a_n(t)\psi_n(r). \tag{46}$$

To satisfy the boundary condition (i), $\psi_n(r_0)$ has to be zero $\forall n$. Then, substituting Eq. (46) into Eq. (44) and considering Eq. (45), we obtain

$$\frac{da_n(t)}{dt} = -D\lambda_n^2 a_n(t). \tag{47}$$

Therefore, $a_n(t)$ can be written as

$$a_n(t)=A_n\exp(-D\lambda_n^2 t)=A_n\exp\left(-\frac{t}{\tau_n}\right), \tag{48}$$

where A_n are normalizing constants and $\tau_n=1/D\lambda_n^2$. From Eqs. (46) and (47) the solution of Eq. (44) expressed as $C_{ox}(r,t)-C'$ follows,

$$C_{ox}(r,t)-C'=\sum_{n=0}^{\infty} A_n\exp\left(-\frac{t}{\tau_n}\right)\psi_n(r). \tag{49}$$

Now using the Wigner–Seitz approximation we can replace the cubic cell surrounding each particle by a spherically symmetric region of equal volume with radius R satisfying the relation

$$\tfrac{4}{3}\pi R^3 N=1, \tag{50}$$

where N (cm^{-3}) is the average number of precipitates per unit volume, which has been assumed to be constant during annealing. Therefore, Eq. (49) in spherical polar coordinates is

Downloaded 21 Apr 2008 to 146.186.238.16. Redistribution subject to AIP license or copyright; see http://jap.aip.org/jap/copyright.jsp

SIONYX1403000026.0054

SAMSUNG EX. 1002 - 2519/4148

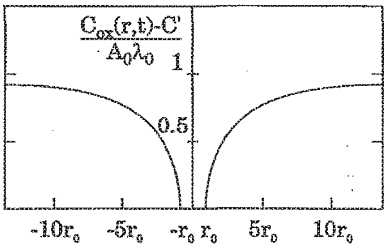


FIG. 29. Plot of interstitial oxygen concentration in the vicinity of an oxide precipitate of radius r_0 as deduced from Eq. (55).

$$C_{ox}(r,t)-C'=\sum_{n=0}^{\infty} A_n \frac{\sin[\lambda_n(r-r_0)]}{r} \exp\left(-\frac{t}{\tau_n}\right). \quad (51)$$

The boundary condition (ii) can be written as $\{\partial[C_{ox}(r,t)-C']/\partial r\}_{r=R}=0$, i.e., from Eq. (51) as

$$\tan[\lambda_n(R-r_0)]=\lambda_n R. \quad (52)$$

The coefficients λ_n have the dimensions of a reciprocal length and can have infinite positive values (see Fig. 28).

The first solution of Eq. (52), considering that the precipitates usually occupy only a small fraction of the whole sphere with radius R (i.e., typically $r_0/R\simeq 0.025$), is approximated as

$$\lambda_0^2\simeq\frac{3r_0}{R^3} \quad (53)$$

and then

$$\tau_0=\frac{R^3}{3Dr_0}, \quad (54)$$

where $1/\tau_0$ is the precipitation rate.

It is possible to show that after a short initial transient, when all the solutions of Eq. (52) are significant, λ_0 gives the most important contribution to the variations of $C_{ox}(r,t)$. Therefore, after a time interval $\Delta t=\tau_0$ a pseudosteady state is reached. In that case, from Eq. (51), the concentration of oxygen remaining in the solution as a function of the distance r from the precipitate center and of the annealing time can be considered equal to

$$C_{ox}(r,t)-C'\simeq A_0\lambda_0\left(1-\frac{r_0}{r}\right)\exp\left(-\frac{t}{\tau_0}\right), \quad (55)$$

where $A_0\lambda_0$ is a constant with the dimension of a concentration, equal to about C_0-C'. This equation leads to interesting considerations. Fixing the annealing time t the spatial oxygen concentration profile can be obtained. In this case, as shown in Fig. 29, the oxygen concentration remaining in the solution is almost constant in the whole sphere of radius R ($R\simeq 40r_0$), except for a central spherical region with radius of about 5 r_0. At a given distance from the precipitate, oxygen concentration decays exponentially to the equilibrium value C' with a time constant τ_0 given by Eq. (54).

The spatial average of oxygen concentration remaining in the solution C_m, usually measured by IR absorption, verifies this relation,

$$\frac{C_m(t)-C'}{C_0-C'}=\exp\left(\frac{-t}{\tau_0}\right), \quad (56)$$

which allows one to determine the value of C' from the intensity of the 1107 cm^{-1} absorption band, which is proportional to $C_m(t)$. For long annealing time ($t\to\infty$), with $C_0\gg C'$, Eq. (56) becomes

$$\lim_{t\to\infty} C_m(t)=C'. \quad (57)$$

Taking into account that the total oxygen content is conserved, we have

$$\tfrac{4}{3}\pi R^3[C_0-C_m(t)]=\tfrac{4}{3}\pi r_0^3[C_P-C_m(t)]. \quad (58)$$

From this equation and considering Eq. (50), we obtain

$$C_0-C_m(t)=\tfrac{4}{3}\pi r_0^3 N[C_P-C_m(t)]. \quad (59)$$

Since for $t\to\infty$ $C_m(t)=C'$, Eq. (58) gives

$$\frac{R}{r_0}=\left(\frac{C_P-C'}{C_0-C'}\right)^{1/3}. \quad (60)$$

Then, substituting this expression into Eq. (54) we can write

$$\tau_0=\frac{R^2}{3D}\left(\frac{C_P-C'}{C_0-C'}\right)^{1/3}. \quad (61)$$

From Eqs. (61) and (50) the precipitate density N can be deduced,

$$N=\frac{3}{4\pi}\left(\frac{C_P-C'}{C_0-C'}\right)^{1/2}(3D\tau_0)^{-3/2}. \quad (62)$$

A comparison between Ham's theoretical predictions and experimental data has been reported in Refs. 143 and 144. The authors studied dislocation-free Cz silicon samples, annealed for a very long time, with interstitial oxygen concentration $C_0\simeq 7\pm 0.7\times 10^{17}$ atoms/cm^3, as determined by IR-absorption measurements. Oxide precipitates were assumed to be constituted by SiO_2 with oxygen concentration $C_P=4.6\times 10^{22}$ atoms/cm^3.

The direct measurement of C' is not always possible, since it requires samples annealed for a very long time, necessary for oxygen to reach the equilibrium concentration value. Furthermore, duration of the suitable annealing depends on the temperature. For example, after 850 °C annealing the value of C' was not yet reached after 800 h heating. For lower temperatures (below 750 °C), even 2000 h were not enough to reach the equilibrium concentration value. This problem can be overcome by measuring at different times the amount of oxygen $C_m(t)$ remaining in the solution after the annealing time t, and extrapolating the value of $C_m(\infty)$ which is equal to C' according to Eq. (57).

Figure 30 (crosses) reports $C_m(t)$ normalized to the initial oxygen concentration C_0 after different annealing times at 850 °C. The figure clearly shows that, after an initial transient (about 50–100 h) where a rapid reduction of oxygen in the solution occurs, the O concentration slowly decreases, thus approaching the equilibrium value C'. Once C' is determined, the value of τ_0 can also be easily deduced, taking into account Eq. (56), from the plot of $[C_m(t)-C']/(C_0-C')$ as a function of time after the initial

Downloaded 21 Apr 2008 to 146.186.238.16. Redistribution subject to AIP license or copyright; see http://jap.aip.org/jap/copyright.jsp

SIONYX1403000026.0055

SAMSUNG EX. 1002 - 2520/4148

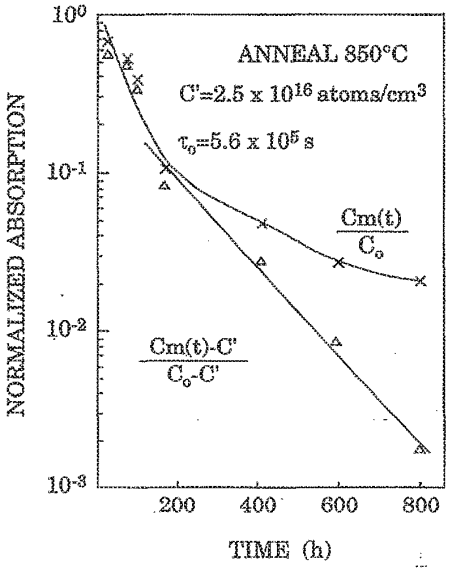


FIG. 30. IR absorption at 1107 cm^{-1} normalized to initial oxygen concentration $C_m(t)/C_0$ (crosses) and $[C_m(t)-C']/(C_0-C')$ (triangles) for different annealing times (from Ref. 144).

transient (see triangles in Fig. 30). The values of τ_0 obtained by Newman *et al.*[143] are reported for different temperatures in Fig. 31. From the values of τ_0 the precipitate density N can then be calculated via Eq. (62) using a known value for the diffusion coefficient D. A comparison between the values of N calculated in this way (open circles) using $D=0.07\exp(-2.44/kT)$ (where kT is in eV, as proposed by Mikkelsen[54,65]) and those obtained from etch-pit (crosses) and SANS measurements (open squares) are reported in Fig. 32. The very good agreement among the N values obtained with different experimental techniques (considering also their uncertainty) gives an important confirmation of the validity of the diffusion-limited kinetic model used to derive Eq. (62).

The radius of precipitates r_0 can be deduced from Eq. (59) using the obtained N values. Figure 33 shows r_0 as a function of the annealing temperature after a long heating time. Furthermore, the figure reports for comparison the ra-

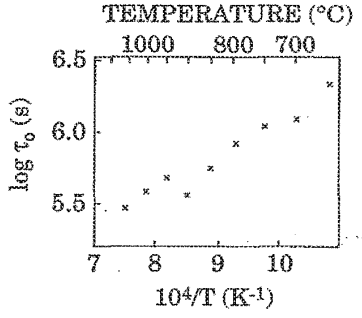


FIG. 31. Time constant τ_0 as a function of annealing temperature (from Ref. 143).

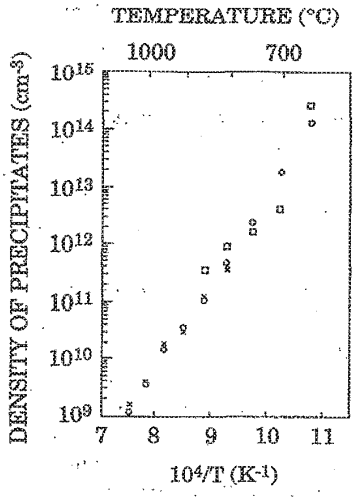


FIG. 32. Density of precipitates as a function of annealing temperature, as determined by etch-pit counts (crosses), kinetic model (circles), and SANS results (squares) (from Ref. 41).

dius of precipitates derived for the same samples by different techniques, such as neutron scattering, etch-pit measurements, and optical scattering (see Sec. IV). It is interesting to underline that the agreement among the values of r_0 obtained by different techniques is remarkably good.

In alternative to calculating of N from the kinetic data using D taken from Ref. 54, one can use the experimental N values obtained from etch-pit measurements together with the kinetic data to obtain the diffusion coefficient D. The

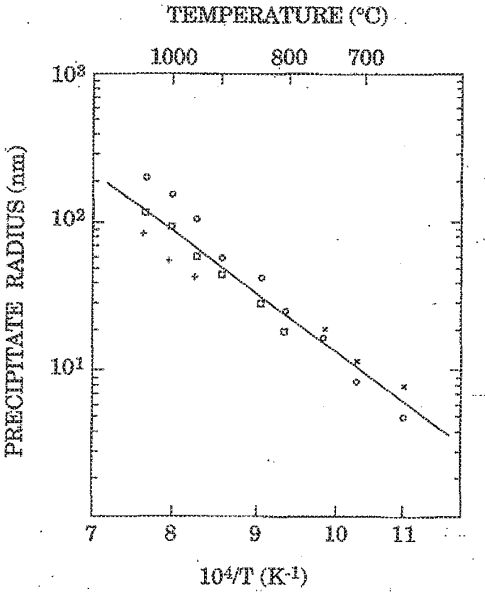


FIG. 33. Temperature dependence of precipitate radius derived from IR data and kinetic model (circles), SANS (crosses), etch-pit density (squares), and optical scattering (+). The solid line represents the best fit (from Ref. 145).

Downloaded 21 Apr 2008 to 146.186.238.16. Redistribution subject to AIP license or copyright; see http://jap.aip.org/jap/copyright.jsp

SIONYX1403000026.0056

SAMSUNG EX. 1002 - 2521/4148

value for D obtained in such a way, for temperatures down to 650 °C, is

$$D=0.02\ \exp(-2.42/kT), \tag{63}$$

where kT is measured in eV. A comparison between the values of D obtained from the kinetic data and those reported in the literature is shown in Fig. 12. A more complete analysis of available experimental data over 12 orders of magnitude has been presented in Ref. 145 (see Sec. II B 4).

2. Spherical precipitates with increasing radius

The above-reported analysis which gives important results on the precipitation mechanism is strongly limited by the hypothesis that the precipitate radius r_0 is constant during annealing and is equal to the steady-state value. This limitation was overcome by an extension of Ham's theory taking into account the growth of the radius of precipitates as a function of annealing time.[140] The analysis can be limited to spherical particles since for the ellipsoidal ones only minor differences in the results are expected. This allows Ham's theory to be applied also to samples subjected to long-time heat treatment, where, as it is well known, precipitates are ellipsoidal. The assumptions for this more general model are:

(i) The precipitates form and grow as identical spheres with $r_0 \ll R$, arranged in a simple cubic lattice, and

(ii) the concentration of precipitates N and the diffusion coefficient of oxygen D remain constant with the annealing time.

Following the same procedure as in Sec. III B 1, the solution of Eq. (44) for growing precipitate radius is given by the relation[140]

$$Kt=\frac{1}{6}\ln\left(\frac{[u^2(t)+u(t)+1][u^2(0)-2u(0)+1]}{[u^2(t)-2u(t)+1][u^2(0)+u(0)+1]}\right) - \frac{1}{\sqrt{3}}\tan^{-1}\left(\frac{2u(t)+1}{\sqrt{3}}\right)+\frac{1}{\sqrt{3}}\tan^{-1}\left(\frac{2u(0)+1}{\sqrt{3}}\right), \tag{64}$$

where

$$K=\frac{D}{R^2}\left(\frac{(C_0-C')(1+Z)}{C_P-C'}\right)^{1/3}, \tag{65}$$

$$Z=\frac{r_0^3(0)(C_P-C')}{R^3(C_0-C')}, \tag{66}$$

$$u(t)=\left(1-\frac{\rho(t)}{\rho(0)(1+Z)}\right)^{1/3}, \tag{67}$$

and

$$\rho(t)=C_m(t)-C'. \tag{68}$$

The parameter Z, known as the Zeldovich factor, is the fraction of oxygen atoms in the precipitate at $t=0$ (i.e., immediately after nucleation). The value of Z in this case is 0.01 and may be assumed zero without any significant errors.

Equation (64) gives therefore the kinetics of oxygen precipitation as predicted by the diffusion-limited model. The

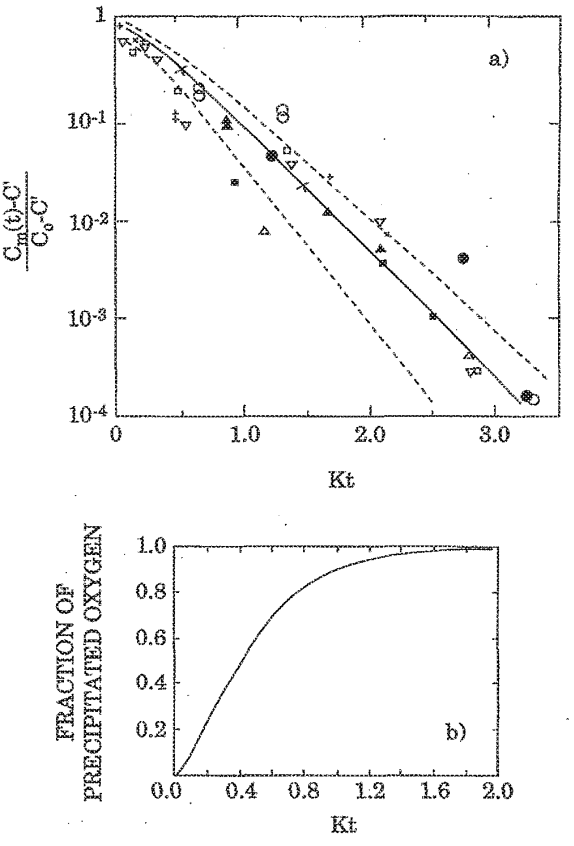


FIG. 34. (a) Interstitial oxygen concentration as a function of the reduced parameter Kt for different temperatures: 650 °C (open circles); 700 °C (closed triangles); 750 °C (+); 800 °C (open triangles up); 850 °C (open triangles down); 900 °C (closed squares); 950 °C (open squares); 1000 °C (solid circles), and 1050 °C (crosses) (from Ref. 41); (b) precipitated oxygen concentration as a function of Kt.

solid line in Fig. 34(a) illustrates the quantity $(C_m-C')/(C_0-C')$ as a function of Kt, as obtained from this equation, while the quantity $1-(C_m-C')/(C_0-C')$, giving the concentration of oxygen precipitated, is shown in Fig. 34(b). The behavior of $(C_m-C')/(C_0-C')$ vs Kt clearly shows two different regions. In the first one, where $(C_m-C')/(C_0-C')>0.5$ (i.e., for very short annealing times), Eq. (64) can be approximated by the simple relation

$$\frac{C_m-C'}{C_0-C'}=\exp(-\beta t^{3/2}), \tag{69}$$

where

$$\beta=\left(\frac{2D}{R^2}\right)^{3/2}\left(\frac{C_0-C'}{C_P-C'}\right)^{1/2}. \tag{70}$$

In the second one, where $(C_m-C')/(C_0-C')\leqslant 0.5$ (i.e., for long annealing times), Eq. (64) can be approximated by a straight line,

$$\frac{C_m-C'}{C_0-C'}=\exp\left(-\frac{t}{\tau}\right), \tag{71}$$

Downloaded 21 Apr 2008 to 146.186.238.16. Redistribution subject to AIP license or copyright; see http://jap.aip.org/jap/copyright.jsp

SIONYX1403000026.0057

SAMSUNG EX. 1002 - 2522/4148

TABLE V. Values of the constant K and the oxygen concentration C' as determined by a fitting procedure, on the basis of IR-absorption data on samples annealed at different temperatures (from Ref. 41).

Temperature (°C)	K (10^{-3} h^{-1})	C' (10^{17} cm^{-3})
650	1.65	0.078
700	2.10	0.110
750	2.30	0.120
800	2.80	0.128
850	3.50	0.142
900	5.00	0.290
950	6.20	0.510
1000	6.50	0.710
1050	6.80	1.640

where

$$\tau=\frac{R^2}{3D}\left(\frac{C_P-C'}{C_0-C'}\right)^{1/3}. \tag{72}$$

Considering that $Z\simeq 0$, from Eqs. (65) and (72) we obtain

$$\tau=\frac{1}{3K}. \tag{73}$$

It is worth noting that Eq. (71), which gives the long-time behavior of $C_m(t)$, generalizes Eq. (56), obtained in the approximation of constant precipitate radius. Indeed, applying the condition of Eq. (60) to the definition of τ [Eq. (72)], the relation $\tau=R^3/3Dr_0$ is obtained, which is exactly the quantity τ_0 defined in Eq. (54). From the analysis performed on the basis of Ham theory the evolution of the precipitate radius r as a function of time can also be deduced,

$$\frac{dr(t)}{dt}=\frac{C_m(t)-C'}{C_P-C'}\frac{D}{r(t)}. \tag{74}$$

Considering Eq. (71), Eq. (74) becomes

$$\frac{dr(t)}{dt}=\frac{C_0(t)-C'}{C_P-C'}\frac{D}{r(t)}\exp\left(\frac{-t}{\tau}\right), \tag{75}$$

and integrating this expression $r(t)$ can be found,

$$r^2(t)=2\tau D\left(\frac{C_0-C'}{C_P-C'}\right)\left[1-\exp\left(\frac{-t}{\tau}\right)\right]. \tag{76}$$

For $t\ll\tau$,

$$r^2(t)\simeq 2D\left(\frac{C_0-C'}{C_P-C'}\right)t. \tag{77}$$

Therefore, in the early stages of precipitation the particle volume increases as $t^{3/2}$.

Comparing the experimental results with the predictions of Ham's theory, Livingston *et al.*[41] determined by a fitting procedure the values of K and C' at different temperatures from Eq. (64), the value of initial interstitial oxygen concentration C_0, and the average concentration of oxygen remaining in the solution $C_m(t)$ after different annealing treatments when measured by IR absorption. The results are reported in Table V. From K and C' the quantity $[C_m(t)-C']/(C_0-C')$ can also be determined as a function of Kt from IR experimental data. These data [experimental points in Fig. 34(a)] for different temperatures are in very good agreement with those predicted by the Ham's theoretical model [solid line in Fig. 34(a)], thus confirming the validity of the model. The spread of some data can be related to the errors affecting C_0 and $C_m(t)$ measurements. The broken lines in Fig. 34(a) take into account the uncertainty of about 10% in these concentration values.

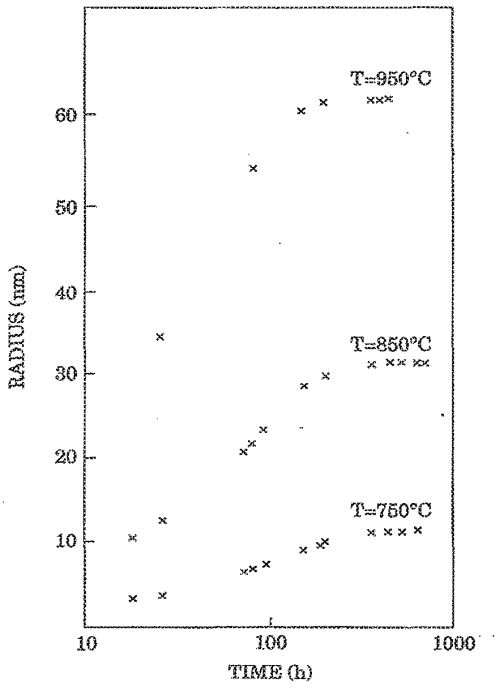


FIG. 35. Time dependence of precipitate radius for different annealing temperatures derived from Eq. (74) (from Ref. 41).

The knowledge of the values of K and C' allows one to calculate the radius of precipitates for different annealing times and temperatures from Eq. (74). As an example, in Fig. 35 the results taken from Ref. 41 for 750, 850, and 950 °C annealing temperatures are shown. It is possible to see that the value of $r(t)$ increases in the early stages of the precipitation process, becoming almost constant for annealing times as long as 200–300 h depending on the temperature.

The experimental assessment of the diffusion-limited model for oxygen precipitation in silicon is very convincing. Nevertheless, an analysis of the data reported in Fig. 34(a) reveals that some values of $[C_m(t)-C']/(C_0-C')$ for Kt in the range from 0.5 to 1 and for heating temperatures from 750 to 900 °C are lower than the values predicted by Ham's theory. This enhanced precipitation has been explained by a systematic decrease of the precipitate concentration N with increasing annealing temperature, whereas Ham's theory assumes N to be constant. This reduction, confirmed by SANS measurements,[146] may be due to the fact that as precipitation proceeds some of the smaller particles dissolve while the larger particles continue to grow. Another possible explanation comes from the fact that the precipitates can assume shapes different from the sphere, as confirmed by TEM and

Downloaded 21 Apr 2008 to 146.186.238.16. Redistribution subject to AIP license or copyright; see http://jap.aip.org/jap/copyright.jsp

SIONYX1403000026.0058

SAMSUNG EX. 1002 - 2523/4148

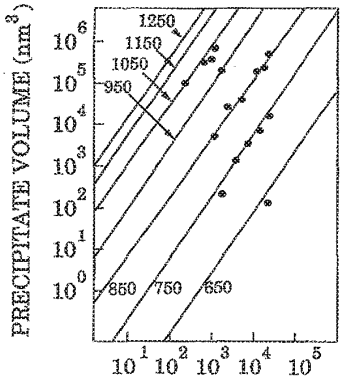


FIG. 36. Time dependence of precipitate volume for different annealing temperatures as determined from Ham theory (solid lines) and from experimental data (solid circles). Annealing temperatures are indicated in °C (from Ref. 123).

SANS results[41] and widely accepted, which are not considered in the model.

Wada *et al.*, who studied silicon samples annealed for different times at the temperatures of 750, 850, and 1050 °C by TEM,[123,142] found that oxide precipitates grow in two dimensions with constant thickness of about 40 Å. The precipitate density ranges from 10^{11} cm^{-3} at 750 °C to 10^{8} cm^{-3} at 1050 °C. On the basis of these data and assuming that the results of the diffusion-limited theory of precipitation are valid also for the actual square-shaped platelet precipitates, they compared experimental values of the precipitate volume to the predicted function $V(T,t)$ derived from Eq. (77). Figure 36 shows the results of Ham's theory (solid lines) and experimental values (solid circles). In spite of the good agreement, the extension of the model to platelet precipitates has not been justified. Furthermore, the two main assumptions made in Refs. 123 and 142, i.e., that the thickness of precipitates remains constant during growth and that the rate of volume change of a platelet precipitate is equal to that of a sphere, have been considered to be incorrect.[126,147] A model for the growth of platelets has been developed and is illustrated in the following subsection.

3. Disk precipitates with varying thickness

The study of the growth of platelet-shaped oxygen precipitates in silicon is of particular interest, since that shape is favored when the Si wafers are heated in the temperature range of device processing. Here the analysis carried out by Hu[114,147] by applying the diffusion-limited growth model is reported.

The author starts from the hypothesis that the thickness h of the precipitates is not constant during the growth and that the rim of the disk is a perfect sink for the excess oxygen atoms. In this case the total diffusion flux through the disk surface giving the rate of volume change is

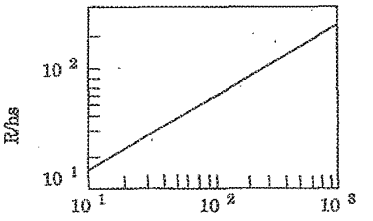


FIG. 37. Dependence of the aspect ratio R/hs on normalized disk radius (from Ref. 147).

$$V_m\{8RD[C_{ox}(\infty)-C_{ox}(0)]\}=\frac{d}{dt}(\pi r^2 h), \tag{78}$$

where R is the radius of the disk, V_m is the precipitate volume per oxygen atom in it, $C_{ox}(\infty)$ and $C_{ox}(0)=C'$ are oxygen concentrations far from and on the Si/precipitate interface, respectively. Considering that at a given volume the disk is the shape which minimizes the strain energy ΔG_σ (see Fig. 40 in Sec. III C) while the interface energy ΔG_γ is maximized (see Fig. 39 in Sec. III C), the equilibrium exists only for one particular value of the ratio R/h, which may vary with R. This value can be found by minimizing the total free energy of precipitates, obtaining the following implicit relation between R and R/h,

$$R/L=\frac{(R/hs)^2}{\ln(R/hs)+\ln(8/e^2)}, \tag{79}$$

where L is a constant that in our case is equal to 0.89 Å and s is the lattice displacement per unit thickness of the disk (about 0.24 for SiO_2 in silicon). Equation (79) is plotted in Fig. 37 which reports the aspect ratio R/sh vs R/L, i.e., the variation of the precipitate thickness at different disc radii. Relation (79) can be written explicitly if the logarithmic factor is regarded as a weak power function of R/h. Introducing the average quantity $\langle R/hs\rangle$ Eq. (79) can be written as

$$h=s^{-1}(L/p)^{1-m}R^m, \tag{80}$$

where

$$m=\frac{1}{2}\frac{2\ln\langle R/hs\rangle+\ln 64-6}{2\ln\langle R/hs\rangle+\ln 64-5}, \tag{81}$$

and

$$p=\langle R/hs\rangle^{(1-2m)/(1-m)}[\ln(\langle R/hs\rangle)+\ln 8-2]. \tag{82}$$

For precipitates with radius very large with respect to the thickness m is about 1/2.

From Eq. (80) an interesting result of the analysis can be obtained. Substituting that expression for h in the total free energy of the platelet precipitates, under the assumption of precipitates with very large R/h (therefore $m\simeq 0.5$) and integrating, one obtains

$$R\propto t^{1/(1+m)}=t^{2/3}, \tag{83}$$

which is exactly the time dependence found in the previous subsection.

Downloaded 21 Apr 2008 to 146.186.238.16. Redistribution subject to AIP license or copyright; see http://jap.aip.org/jap/copyright.jsp

SIONYX1403000026.0059

SAMSUNG EX. 1002 - 2524/4148

C. Precipitate morphology

An interesting feature of precipitate morphology is its dependence on the annealing temperature. Three temperature ranges have been related[77,114,148–150] to the three typical precipitate shapes, i.e., the needle, the disk, and the polyhedron.

At low temperatures (about 400–650 °C) precipitates grow as needles[114,116,127,150] made of a high-pressure SiO_2 polimorph, which is coesite. In this temperature range the strain-energy contribution to the precipitate total free energy dominates, since the stress-relieving processes (which become important at higher temperatures) play a minor role.

At intermediate temperatures (about 650–950 °C) disk-shaped precipitates are typical[20,41,45] (although they can be formed also by short high-temperature annealing). Self-interstitial emission and dislocation-loop formation can partially release the surface strain, therefore making the strain energy less important for shape determination. Moreover, strain energy is further diminished by the decrease of precipitate thickness, with the concomitant increase of surface energy.

At high temperatures (above 950 °C) strain is completely released and the precipitates take the shape with minimum surface energy.[114,123,150,151] Due to the anisotropy of interface energy, such a preferential shape is the octahedron with eight equivalent {111} faces (surface energy of silicon is minimum in the {111} planes) instead of the sphere.

A lot of experimental results, mainly obtained from TEM investigations, confirm these trends (see Sec. IV B). In the following a qualitative description of the factors determining precipitate morphology is presented and some interesting conclusions derived.

1. Precipitate free energy

The general features of precipitate morphology can be justified on the basis of thermodynamics, considering the different contributions to the total free energy ΔG_{tot} associated with the oxygen precipitation process and their dependence on precipitate shape, annealing time, and temperature. Assuming the precipitates to be far apart, i.e., neglecting their possible interactions, and studying precipitate formation in regions of the silicon crystal far away from other defects, ΔG_{tot} can be considered as the volume free energy available for SiO_x formation in the regions far from the growing precipitates and as[150]

$$\Delta G_{\text{tot}} = \Delta G_K + \Delta G_S + \Delta G_E, \tag{84}$$

where ΔG_K is the free-energy contribution associated with the phase change at the silicon/precipitate interface, ΔG_S is the free-energy contribution related to the oxygen transport, and ΔG_E is the excess free energy. This last term is associated with the creation of interface energy ΔG_γ, strain energy ΔG_σ, and interstitial-related energy ΔG_I and can be expressed as their sum,

$$\Delta G_E = \Delta G_\gamma + \Delta G_\sigma + \Delta G_I. \tag{85}$$

In the following the various contributions to ΔG_{tot} are discussed in detail.

Little is known about the energy required for the growth of the Si-SiO_2 interface. The phase-change free energy ΔG_K can be considered proportional to the rate of silicon oxidation and only slightly dependent on crystal orientation. ΔG_K gives in general a small contribution to ΔG_{tot}, because the precipitate growth velocity is small.

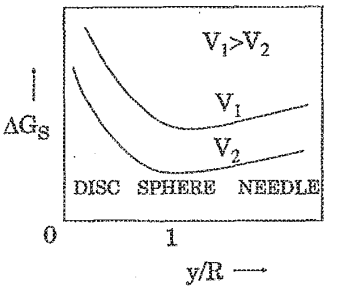


FIG. 38. Dependence of energy contribution of O_i transport on y/R for two precipitate growth velocities and for short annealing times (from Ref. 150).

The energy required for oxygen transport to the precipitate surface is a function of the precipitate shape because also the dependence of C_{ox} on the distance from the precipitate varies with the precipitate shape. ΔG_S can be expressed as a function of precipitate shape aspect ratio y/R, where the general precipitate shape is a spheroid having axes $2R = 2R \neq 2y$, and therefore $y/R = 0$ results in a disk, $y/R = 1$ in a sphere and $y/R = \infty$ in a needle. Figure 38 shows the ΔG_S dependence on y/R in the case of two precipitate growth velocities and for short annealing times. Spherical precipitates clearly dominate, leading to the minimum in ΔG_S. For long times the ΔG_S contribution is minimum for the needle shape, which is therefore favored.

The first contribution to ΔG_E, interfacial energy ΔG_γ, depends on the surface area as well as on the degree of coherence of the Si/SiO_2 interface. Considering a coherent interface, with free energy per unit area γ constant and isotropic, at a fixed particle volume ΔG_γ is minimum for the sphere, and this maximizes the volume/surface ratio. Nevertheless, since perfect coherence only rarely is achieved, the interfacial free energy is usually higher with respect to the ideal case. For semicoherent precipitate interfaces γ is modified as

$$\gamma' = \gamma + g, \tag{86}$$

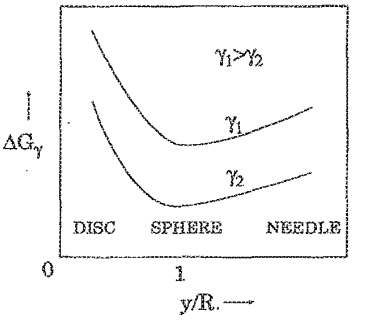


FIG. 39. Interfacial energy dependence on y/R for a coherent (γ_2) and for an incoherent (γ_1) interface (from Ref. 150).

Downloaded 21 Apr 2008 to 146.186.238.16. Redistribution subject to AIP license or copyright; see http://jap.aip.org/jap/copyright.jsp

SIONYX1403000026.0060

SAMSUNG EX. 1002 - 2525/4148

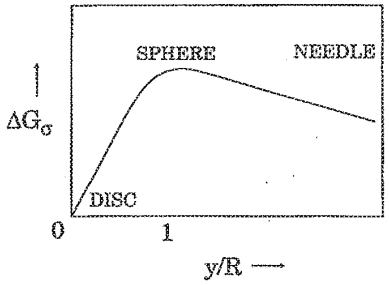


FIG. 40. Strain energy dependence on y/R (from Ref. 150).

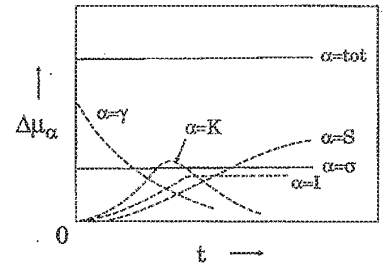


FIG. 42. Time dependence of the different contributions $\Delta\mu_\alpha$, $\alpha=K,S,\sigma,I,\gamma$ and their sum $\Delta\mu_{tot}$ (from Ref. 150).

where g depends on the crystal elastic constants and on the interface degree of coherence, while the ΔG_γ dependence on y/R, illustrated in Fig. 39 for both cases, is qualitatively preserved.

Interface coherence also influences the strain energy contribution ΔG_σ, together with the degree of elastic isotropy of silicon and silicon oxide. Given these factors, the precipitate shape is the only parameter affecting ΔG_σ. In Fig. 40 the dependence of ΔG_σ on the aspect ratio y/R is illustrated and clearly demonstrates that this contribution to the total free energy favors disk-shaped precipitates.

The last contribution to ΔG_E is the free energy of interstitial point defect formation ΔG_I. In the case of constant growth velocity, self-interstitial concentration C_I is maximum close to the precipitate (i.e., at $r=r_P$) and reaches a constant value for very large distances from the precipitate ($r\to\infty$). The value $C_I(r_P)$ is maximum for diskoidal particles, lower for needles, and minimum for spheres, although the differences are very small. Therefore, the ΔG_I follows the same trend, as shown in Fig. 41 for two values of the parameter $D_I\tau_I$, where D_I is the diffusion coefficient for self-interstitials and τ_I their diffusion time. In any case, ΔG_I is small compared to the other contributions to ΔG_{tot}.

2. Influence of annealing temperature and time

The analysis of the time dependence of the free-energy contributions described in the previous subsection gives information about the most probable precipitate shape during annealing, while their temperature dependence allows one to predict the precipitate shape after a particular annealing. On this basis a significant comparison with experimental results can be made, although only qualitative arguments are proposed.

In Fig. 42 the time dependence of the free energy per interstitial O atom $\Delta\mu_\alpha=d(\Delta G_\alpha)/dC_{ox}$, $\alpha=K, S, \gamma, \sigma, I,$ tot, is reported. $\Delta\mu_K$ is proportional to the growth velocity, which reaches a maximum and then slows down for $t\to\infty$, when O transport is limited. Moreover, this long-time limit of oxygen transport makes the contribution $\Delta\mu_S$ increase with time, as shown in the figure. $\Delta\mu_\gamma$ is inversely proportional to the spheroid axis length R which increases with time, so that it decreases with increasing time. Finally, $\Delta\mu_I$ tends to saturate for long times as self-interstitials are created. From Fig. 42 the shape of oxygen precipitates in the early stages of precipitation turns out to be the sphere, which minimizes the dominant contribution $\Delta\mu_\gamma$. This conclusion, confirmed by TEM observations, supports the hypothesis of the Ham precipitation theory about the shape of precipitation nuclei.

To study precipitate shapes after long-time treatments, i.e., in the equilibrium state, the temperature dependence of the free energy per interstitial O atom also has to be analyzed. The general trend of all $\Delta\mu_\alpha$ terms is to increase with decreasing T, while only $\Delta\mu_I$ shows an opposite behavior. At low temperatures the growth velocity decreases, consequently the rate of self-interstitial emission decreases as does $\Delta\mu_I$. Figure 43 shows all the terms $\Delta\mu_\alpha$ as function of $1/T$. Looking at this figure, at low T ΔG_S and ΔG_σ turn out to be the most important contributions to the total precipitate free-energy. From Figs. 38 and 40 ΔG_S appears to give needles,

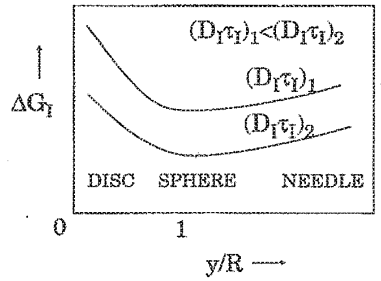


FIG. 41. Dependence of the energy required for self-interstitial creation on y/R for two values of $D_I\tau_I$ (D_I is the diffusion coefficient for self-interstitials; τ_I is the interstitial diffusion time) (from Ref. 150).

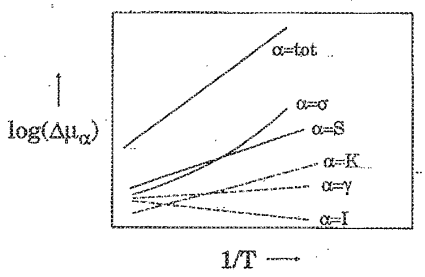


FIG. 43. Temperature dependence of the different contributions $\Delta\mu_\alpha$, $\alpha=K,S,\sigma,I,\gamma$ and their sum $\Delta\mu_{tot}$ (from Ref. 150).

Downloaded 21 Apr 2008 to 146.186.238.16. Redistribution subject to AIP license or copyright; see http://jap.aip.org/jap/copyright.jsp

SIONYX1403000026.0061

SAMSUNG EX. 1002 - 2526/4148

and ΔG_σ disks. Nevertheless, the disk shape is related to a low stress and coesite, which has been found to compose the precipitates grown at low temperatures and which is a high-pressure oxide polimorph, cannot be stable. Considering Fig. 38, the sphere should be even more probable than the needle, but it should not be favored by ΔG_S for long annealing times (see Fig. 42). Therefore, the needle shape is the most likely one for the coesite precipitates, grown at low temperatures.

At intermediate temperatures ΔG_S promotes the formation of needlelike precipitates. On the other hand, ΔG_σ is minimum for the disks, while ΔG_γ is high (see Fig. 39). Nonetheless, this last contribution can be lowered by a good coherence of the interface, achievable along {100} planes by both cristobalite and amorphous SiO_2. Therefore, amorphous SiO_2 disks lying along {100} planes are the most probable precipitates after intermediate-temperature annealing.

Finally, at high temperatures the precipitates are usually octahedra with {111} and {100} faces. Due to the high oxygen diffusivity and solubility limit at high T, ΔG_S is very small. Moreover, stress is almost completely released, i.e., ΔG_σ is also small, and interface coherence is no more critical. Therefore, ΔG_γ is the only contribution to take into consideration. This contribution is minimum for the spherical shape when the surface energy γ is isotropic, while a faceting of the sphere occurs when γ is anisotropic (as in the case of silicon). The planes with minimum surface energy in Si are the {111} and {100}, therefore, the octahedron resulting from faceting presents faces along those planes. These arguments are completely in agreement with the experimental findings.

D. Phenomenology

Oxygen precipitation in dislocation-free single-crystal silicon can be influenced by many factors. Both crystal characteristics and annealing treatments performed on the wafers during device processing are important in determining oxygen precipitation. The main factors to be considered are: interstitial oxygen concentration, interstitial oxygen distribution, preannealing conditions, annealing temperature, annealing time, annealing sequence, annealing ambient, impurity and dopant concentration, impurity and dopant distribution, point defect concentration, extended structural crystal defects (dislocations, twins, etc.), and wafer surface conditions.

The earliest studies of defect generation during low-temperature (450–1000 °C) annealing of Cz-grown wafers were based on electrical measurements[19,152,153] and IR spectroscopy.[19,154,155] At the beginning the major interest was devoted to oxygen-related donor states formed upon annealing. Structural characterization of the lattice defects formed during single-step thermal treatments started to be important at the end of the 1970s. During the 1980s, a much more comprehensive study of the oxygen precipitation process occurring upon complex annealing sequences [such as, for example, that simulating complementary metal-oxide-semiconductor (CMOS) process] was performed by several authors.[156,157]

Commercial Cz silicon wafers always undergo a donor killing treatment by the manufacturer, and even more cooling of ingots during the crystal pulling corresponds to a low-temperature treatment for several hours. All these procedures differ from one manufacturer to another. Therefore, the thermal history of "as-received" wafers can significantly differ and this explains the large spread in the results of different studies.

In spite of the mentioned scattering in the characterization results, related to the high number of parameters influencing oxygen precipitation, some general trends have been found and are worth illustrating as a "phenomenology" of oxygen precipitation in silicon. We first consider the effects of thermal treatments and then the effects of different impurities and dopants present in the silicon crystals.

1. Thermal history effect

Device producers are extremely concerned about the amount of precipitated oxygen and the rate of precipitation for a given range of initial oxygen concentration.[158] It is often found that in wafers cut from the same crystal with equal initial oxygen concentration and subjected to the same heat treatment oxygen precipitation can take place in different ways. Several authors have shown[159,160] that oxygen precipitation is significantly affected by the thermal history of the sample. The thermal history is generally understood as the *in situ* annealing to which Cz crystals are subjected after solidification in the crystal puller, varying along the crystal axis. The temperature variation along a silicon crystal during pulling is due to the fact that the seed-end portion of a crystal spends more time at a given temperature than the tang-end portion. This variation in thermal history along the grown crystal affects the amount of oxygen which precipitates,[160,161] the formation of microdefects,[162] the minority-carrier lifetime,[163] and, therefore, the device yield[164] (see Sec. V). Thermal history of the crystal also depends on the diameter and the length of the ingot, the shape of the ingot bottom, the pulling rate, the puller type, the hot-zone configuration, and the time that the ingot remains inside the puller in the course of growth process. An illustration of the temperature distribution along the ingot and in the puller during crystal growth is given in Fig. 44 as obtained by computer simulation of thermal history by Virzi and Porrini.[165] The thermal history effect is always present: It is often enhanced by the high oxygen content in the seed-end portion of the ingot, and is influenced by the high tang-end impurity concentrations. As an example, an ingot with a higher carbon content may show a lower thermal history dependence with respect to one with lower carbon content, due to the fact that carbon is a possible factor of oxygen precipitation enhancement.[135] Whether the thermal history influences oxygen precipitation in the wafers after a subsequent thermal treatment depends also on the initial interstitial oxygen content C_0, and on the amount of oxygen that precipitates ΔC_{ox} during the thermal treatment. In other words, it depends on the function $\Delta C_{ox} - C_0$ vs C_0 for the particular heat cycle.[166]

In order to reduce the influence of thermal history and improve the axial homogeneity of oxygen precipitation, several different approaches were found and are recommended. As shown by Fraundorf *et al.*[160] the thermal history effect can be erased to a large extent by a high-temperature anneal-

Downloaded 21 Apr 2008 to 146.186.238.16. Redistribution subject to AIP license or copyright; see http://jap.aip.org/jap/copyright.jsp

SIONYX1403000026.0062

SAMSUNG EX. 1002 - 2527/4148